NATIONAL AERONAUTICS AND SPACE ADMINISTRATION

Technical Report 32-1526

Volume XVI

The Deep Space Network

Progress Report
For May and June 1973

JET PROPULSION LABORATORY
CALIFORNIA INSTITUTE OF TECHNOLOGY
PASADENA, CALIFORNIA

August 15, 1973

NATIONAL AERONAUTICS AND SPACE ADMINISTRATION

Technical Report 32-1526

Volume XVI

The Deep Space Network

Progress Report
For May and June 1973

JET PROPULSION LABORATORY
CALIFORNIA INSTITUTE OF TECHNOLOGY
PASADENA, CALIFORNIA

August 15, 1973

Prepared Under Contract No. NAS 7-100
National Aeronautics and Space Administration

Preface

This report presents DSN progress in flight project support, TDA research and technology, network engineering, hardware and software implementation, and operations. Each issue presents material in some, but not all, of the following categories in the order indicated:

Description of the DSN

Mission Support
- Interplanetary Flight Projects
- Planetary Flight Projects
- Manned Space Flight Projects
- Advanced Flight Projects

Radio Science

Supporting Research and Technology
- Tracking and Ground-Based Navigation
- Communications, Spacecraft/Ground
- Station Control and Operations Technology
- Network Control and Data Processing

Network Engineering and Implementation
- Network Control System
- Ground Communications
- Deep Space Stations

Operations and Facilities
- Network Operations
- Network Control System Operations
- Ground Communications
- Deep Space Stations
- Facility Engineering

In each issue, the part entitled "Description of the DSN" describes the functions and facilities of the DSN and may report the current configuration of one of the five DSN systems (Tracking, Telemetry, Command, Monitor and Control, and Test and Training).

The work described in this report series is either performed or managed by the Tracking and Data Acquisition organization of JPL for NASA.

PAGE MISSING FROM AVAILABLE VERSION

Contents

DESCRIPTION OF THE DSN

MISSION SUPPORT

Planetary Flight Projects

SUPPORTING RESEARCH AND TECHNOLOGY

Tracking and Ground-Based Navigation

Contents (contd)

Communications, Spacecraft/Ground

Station Control and Operations Technology

Contents (contd)

Network Control and Data Processing

NETWORK ENGINEERING AND IMPLEMENTATION

Deep Space Stations

OPERATIONS AND FACILITIES

Deep Space Stations

Contents (contd)

DSN Functions and Facilities

N. A. Renzetti
Mission Support Office

The objectives, functions, and organization of the Deep Space Network are summarized. The Deep Space Instrumentation Facility, the Ground Communications Facility, and the Network Control System are described.

The Deep Space Network (DSN), established by the National Aeronautics and Space Administration (NASA) Office of Tracking and Data Acquisition under the system management and technical direction of the Jet Propulsion Laboratory (JPL), is designed for two-way communications with unmanned spacecraft traveling approximately 16,000 km (10,000 mi) from Earth to planetary distances. It supports or has supported, the following NASA deep space exploration projects: Ranger, Surveyor, Mariner Venus 1962, Mariner Mars 1964, Mariner Venus 67, Mariner Mars 1969, Mariner Mars 1971, Mariner Venus–Mercury 1973 (JPL); Lunar Orbiter and Viking (Langley Research Center); Pioneer (Ames Research Center); Helios (West Germany); and Apollo (Manned Spacecraft Center), to supplement the Spaceflight Tracking and Data Network (STDN).

The Deep Space Network is one of two NASA networks. The other, STDN, is under the system management and technical direction of the Goddard Space Flight Center. Its function is to support manned and unmanned Earth-orbiting and lunar scientific and communications satellites. Although the DSN was concerned with unmanned lunar spacecraft in its early years, its primary objective now and into the future is to continue its support of planetary and interplanetary flight projects.

A development objective has been to keep the network capability at the state of the art of telecommunications and data handling and to support as many flight projects as possible with a minimum of mission-dependent hardware and software. The DSN provides direct support of each flight project through that project's tracking and

data system. This management element is responsible for the design and operation of the hardware and software in the DSN which are required for the conduct of flight operations.

Beginning in FY 1973 a modified DSN interface has been established with the flight projects. In lieu of the SFOF, a multimission Mission Control and Computing Center (MCCC) has been activated as a separate functional and management element within JPL. This function, as negotiated with each flight project, will provide all computing and mission operations support for missions controlled from JPL. DSN computing support will be provided separately by the DSN. Radio metric, telemetry, and command data interfaces with the DSN are a joint DSN, MCCC, and flight project responsibility. The organization and procedures necessary to carry out these new activities will be reported in this document in the near future.

The DSN function, in supporting a flight project by tracking the spacecraft, is characterized by five network systems:

(1) DSN Tracking System. Generates radio metric data; i.e., angles, one- and two-way doppler and range, and transmits raw data to mission control.

(2) DSN Telemetry System. Receives, decodes, records, and retransmits engineering and scientific data generated in the spacecraft to Mission Control.

(3) DSN Command System. Accepts coded signals from mission control via the GCF and transmits them to the spacecraft in order to initiate spacecraft functions in flight.

(4) DSN Monitor and Control System. Instruments, transmits, records, and displays those parameters of the DSN necessary to verify configuration and validate the network. Provides operational direction and configuration control of the network and primary interface with flight project Mission Control personnel.

(5) DSN Test and Training System. Generates and controls simulated data to support development, test, training and fault isolation within the DSN. Participates in mission simulation with flight projects.

The facilities needed to carry out these functions have evolved in three technical areas: (1) the Deep Space Stations (DSSs) and the telecommunications interface through the RF link with the spacecraft is known as the Deep Space Instrumentation Facility (DSIF); (2) the Earth-based point-to-point voice and data communications from the stations to Mission Control is known as the Ground Communications Facility (GCF); (3) the network monitor and control function is known as the Network Control System (NCS).

I. Deep Space Instrumentation Facility

A. Tracking and Data Acquisition Facilities

A world-wide set of Deep Space Stations with large antennas, low-noise phase-lock receiving systems, and high-power transmitters provide radio communications with spacecraft. The DSSs and the deep space communications complexes (DSCCs) they comprise are given in Table 1.

Radio contact with a spacecraft usually begins when the spacecraft is on the launch vehicle at Cape Kennedy, and it is maintained throughout the mission. The early part of the trajectory is covered by selected network stations of the Air Force Eastern Test Range (AFETR) and the STDN of the Goddard Space Flight Center.[1] Normally, two-way communications are established between the spacecraft and the DSN within 30 min after the spacecraft has been injected into lunar, planetary, or interplanetary flight. A compatibility test station at Cape Kennedy (discussed later) tests and monitors the spacecraft continuously during the launch checkout phase. The deep space phase begins with acquisition by 26-m DSSs. These and the remaining DSSs listed in Table 1 provide radio communications until the end of the mission.

To enable continuous radio contact with spacecraft, the DSSs are located approximately 120 deg apart in longitude; thus a spacecraft in deep space flight is always within the field-of-view of at least one DSS, and for several hours each day may be seen by two DSSs. Furthermore, since most spacecraft on deep space missions travel within 30 deg of the equatorial plane, the DSSs are located within latitudes of 45 deg north and south of the equator. All DSSs operate at S-band frequencies: 2110-2120 MHz for Earth-to-spacecraft transmission and 2290-2300 MHz for spacecraft-to-Earth transmission. An X-band capability is being readied for future missions beginning in 1973.

[1]The 9-m (30-ft) diam antenna station established by the DSN on Ascension Island during 1965 to act in conjunction with the STDN orbital support 9-m (30-ft) diam antenna station was transferred to the STDN in July 1968.

To provide sufficient tracking capability to enable returns of useful data from around the planets and from the edge of the solar system, a 64-m (210-ft) diam antenna subnet will be required. Two additional 64-m (210-ft) diam antenna DSSs are under construction at Madrid and Canberra and will operate in conjunction with DSS 14 to provide this capability. These stations are scheduled to be operational by the middle of 1973.

B. Compatibility Test Facilities

In 1959, a mobile L-band compatibility test station was established at Cape Kennedy to verify flight-spacecraft/DSN compatibility prior to the launch of the Ranger and Mariner Venus 1962 spacecraft. Experience revealed the need for a permanent facility at Cape Kennedy for this function. An S-band compatibility test station with a 1.2-m (4-ft) diameter antenna became operational in 1965. In addition to supporting the preflight compatibility tests, this station monitors the spacecraft continuously during the launch phase until it passes over the local horizon.

Spacecraft telecommunications compatibility in the design and prototype development phases was formerly verified by tests at the Goldstone DSCC. To provide a more economical means for conducting such work and because of the increasing use of multiple-mission telemetry and command equipment by the DSN, a Compatibility Test Area (CTA) was established at JPL in 1968. In all essential characteristics, the configuration of this facility is identical to that of the 26-m (85-ft) and 64-m (210-ft) diameter antenna stations.

The JPL CTA is used during spacecraft system tests to establish the compatibility with the DSN of the proof test model and development models of spacecraft, and the Cape Kennedy compatibility test station is used for final flight spacecraft compatibility validation testing prior to launch.

II. Ground Communications Facility

The GCF provides voice, high-speed data, wideband data, and teletype communications between the Mission Operations Center and the DSSs. In providing these capabilities, the GCF uses the facilities of the worldwide NASA Communications Network (NASCOM)[2] for all long distance circuits, except those between the Mission Operations Center and the Goldstone DSCC. Communications between the Goldstone DSCC and the Mission Operations Center are provided by a microwave link directly leased by the DSN from a common carrier.

Early missions were supported by voice and teletype circuits only, but increased data rates necessitated the use of high-speed and wideband circuits for DSSs. Data are transmitted to flight projects via the GCF using standard GCF/NASCOM formats. The DSN also supports remote mission operations centers using the GCF/NASCOM interface.

III. Network Control System

The DSN Network Control System is comprised of hardware, software, and operations personnel to provide centralized, real-time control of the DSN and to monitor and validate the network performance. These functions are provided during all phases of DSN support to flight projects. The Network Operations Control Area is located in JPL Building 230, adjacent to the local Mission Operations Center. The NCS, in accomplishing the monitor and control function does not alter, delay, or serially process any inbound or outbound data between the flight project and tracking stations. Hence NCS outages do not have a direct impact on flight project support. Voice communications are maintained for operations control and coordination between the DSN and flight projects, and for minimization of the response time in locating and correcting system failures.

The NCS function will ultimately be performed in data processing equipment separate from flight project data processing and specifically dedicated to the NCS function. During FY 1973, however, DSN operations control and monitor data will be processed in the JPL 360/75 and in the 1108. In FY 1974 the NCS data processing function will be partly phased over to an interim NCS processor, and finally, in FY 1975, the dedicated NCS data processing capability will be operational. The final Network Data Processing Area will be located remote from the Network Operations Control Area so as to provide a contingency operating location to minimize single point of failure effects on the network control function. A preliminary description of the NCS appears elsewhere in this document.

[2]Managed and directed by the Goddard Space Flight Center.

Table 1. Tracking and data acquisition stations of the DSN

DSCC	Location	DSS	DSS serial designation	Antenna		Year of initial operation
				Diameter, m (ft)	Type of mounting	
Goldstone	California	Pioneer	11	26(85)	Polar	1958
		Echo	12	26(85)	Polar	1962
		(Venus)[a]	13	26(85)	Az-El	1962
		Mars	14	64(210)	Az-El	1966
Tidbinbilla	Australia	Weemala (formerly Tidbinbilla)	42	26(85)	Polar	1965
		Ballima (formerly Booroomba)	43	64(210)	Az-El	1973
–	Australia	Honeysuckle Creek[b]	44	26(85)	X-Y	1973
–	South Africa	Hartebeesthoek	51	26(85)	Polar	1961
Madrid	Spain	Robledo	61	26(85)	Polar	1965
		Cebreros	62	26(85)	Polar	1967
		Robledo	63	64(210)	Az-El	Under construction

[a]A maintenance facility. Besides the 26-m (85-ft) diam Az-El mounted antenna, DSS 13 has a 9-m (30-ft) diam Az-El mounted antenna that is used for interstation time correlation using lunar reflection techniques, for testing the design of new equipment, and for support of ground-based radio science.

[b]To be shared with STDN until January 1974.

The Use of an Extended Mini-Computer as a Compatibility Test System Controller

A. I. Bryan
DSN Systems Engineering Office

The transfer of the Digital Instrumentation Subsystem from the Spacecraft Compatibility Station in Cape Kennedy to Deep Space Station 61/63 in the Madrid Deep Space Communication Complex necessitated the fabrication of a new system to utilize as a controller for the Compatibility Test System. An automatic data processing equipment acquisition plan for category B equipment was submitted in July 1972 for this purpose. Implementation of the new Compatibility Test System hardware and a discussion of the functional design considerations is presented.

I. Introduction

The Compatibility Test System (CTS), at the Spacecraft Compatibility Station in Cape Kennedy, Florida, utilizes an Interdata Model 4 mini-computer for controlling the spacecraft/Deep Space Network compatibility test function. The test function consists of the following subsets:

(1) Ground receiver frequency control

(2) Ground exciter frequency control

(3) Received signal amplitude control

(4) Transmitted signal amplitude control

(5) Automatic ranging control

(6) Telemetry spectrum analysis and control

(7) Subsystem monitoring

(8) Real-time display information

(9) Test analysis

(10) Operator alert information

(11) Closed-loop RF link control

The compatibility test function was formerly controlled by the Digital Instrumentation Subsystem (DIS II), prior to the transfer of this equipment to DSS 61/63 (Madrid DSCC, Spain) in August 1972 to support the 64-m-diam antenna site. In order to maintain the CTS capability and to minimize cost, it was decided to utilize the Data Decoder Assembly (DDA) spare model 4 mini-computer to satisfy the requirement. An automatic data processing equipment (ADPE) acquisition plan was submitted to procure the necessary additional hardware and peripheral equipment required to implement the new system.

II. CTS Implementation

To maintain existing CTS integrity and to allow for future expansion, the new system consists of the following equipments:

(1) An Interdata model 4 mini-computer with 16K bytes of core memory

(2) An additional 16 K bytes of core memory

(3) A 9-track magnetic tape drive and interface

(4) A card reader and interface

(5) A digital input/output (I/O) controller and interface

(6) A 32-channel analog-to-digital converter and interface

(7) An 8-channel digital-to-analog converter and interface

(8) A line printer and interface

(9) An I/O expansion chassis

(10) A floating point instruction set

The equipment is housed in three standard DSN 48 cm (19-in.) racks and interfaces with the S-Band receiver/exciter and ranging subsystems through standard connectors. The block diagram in Fig. 1 illustrates the hardware configuration of the compatibility test function.

III. CTS Functional Design

A memory expansion of 16K bytes and floating point instruction set are required to utilize the Interdata Fortran IV system. FORTRAN is the primary high-level language utilized in support of project requirements as it provides rapid response to changes in test specifications.

A magnetic tape drive and interface is required to support rapid data storage capabilities and to provide a high-speed loading device for entering large programs into the CPU.

A card reader and interface provides the capability of rapid assembly and compilation of programming. Utilization of cards also provides more efficient and economical updating and maintenance of existing software.

A digital I/O controller is required to provide an interface between the CPU and ancillary digital registers. This capability allows for the transfer of input and output information for controlling, monitoring and display.

Analog-to-digital (A-D) and digital-to-analog (D-A) converters and interfaces are required for monitoring numerous system checkpoints for computational and control purposes. The analog interface module is required to interface the A-D and D-A units to the CPU.

A line printer and interface is required to provide a hard copy of compatibility test results. The line printer outputs all pertinent test data and status results. The line printer also provides the capability of high speed listing during the assembly and compilation processes.

An I/O expansion chassis is required to house the additional I/O devices, converters, and extended memory.

IV. CTS Support Capabilities

The CTS provides the following capabilities:

(1) Control of the programmed exciter oscillator

(2) Control of the programmed receiver local oscillator

(3) Control of the programmed received signal amplitude attenuator

(4) Control of the programmed transmitted signal amplitude attenuator

(5) Control of the Ranging Subsystem

(6) Control of status and parameter displays

Control of all functions listed above is under software direction and is performed from the automated control console. From this position, one operator has the ability to control transmitted and received frequencies, simulate RF doppler for both up and down links, establish telemetry signal-to-noise ratios, automatically compute spacecraft ranging delays and RF spectrum analysis. This total capability is unique within the DSN.

Reference

1. *Systems Interface Manual,* Publication 29-003R02, Interdata, Inc., Oceanport, New Jersey, August 1969.

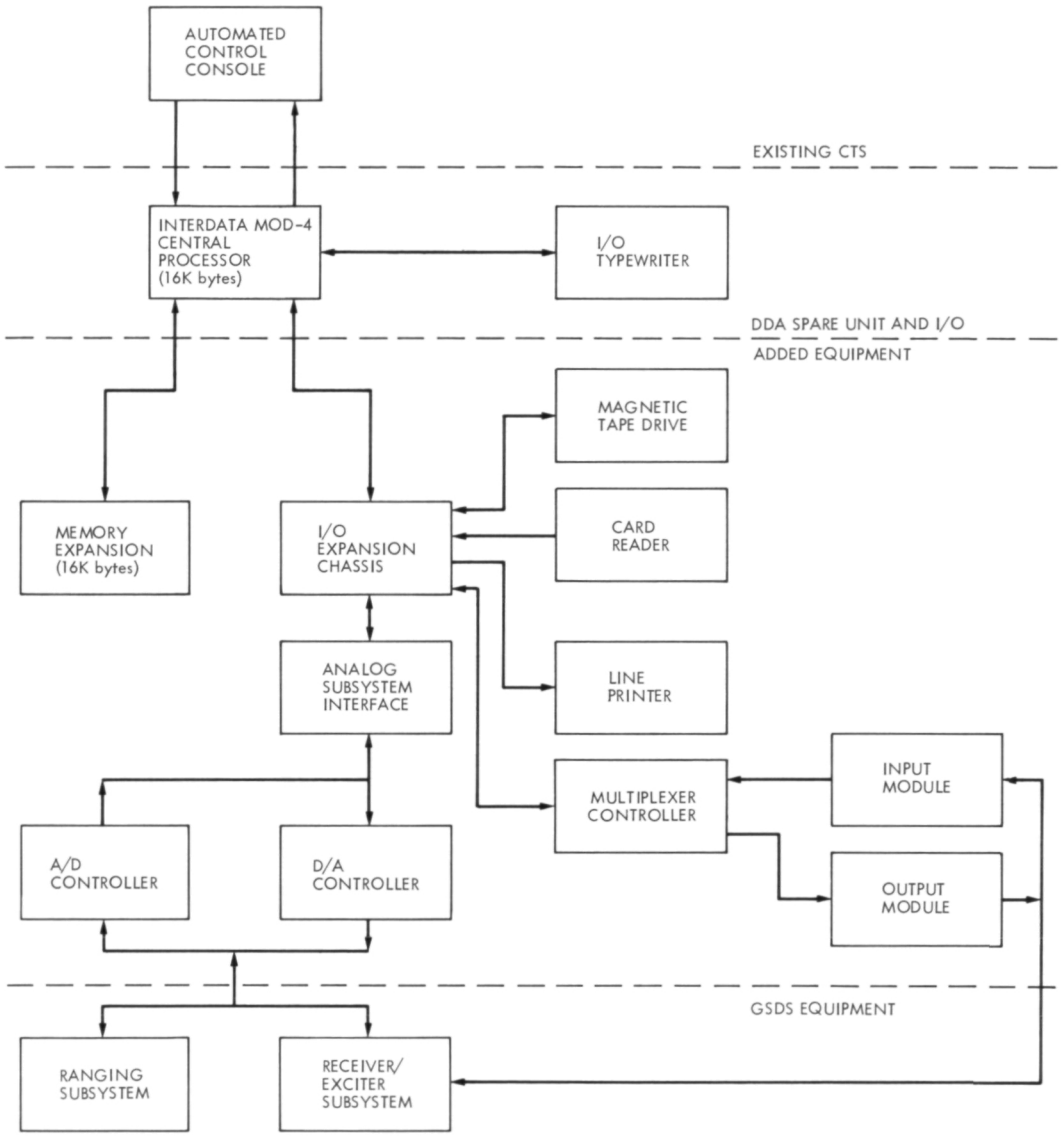

Fig. 1. Interdata Model 4 compatibility test system configuration

Mariner Venus/Mercury 1973 Mission Support

E. K. Davis
DSN Systems Engineering Section

During May and June 1973 the Deep Space Network concentrated on completion of open hardware and software implementation tasks. Particular attention was given to the Telemetry and Command Data Subsystem software problem reported in the previous article. DSN system testing was initiated and support was provided for Project Ground Data System tests.

I. Planning Activities

A. NASA Support Plan

The NASA Support Plan (NSP) for Mariner Venus/Mercury 1973 (MVM'73) is en route from NASA Headquarters, being returned for update prior to approval. Advanced verbal guidelines regarding the update were provided by NASA Headquarters during a visit to JPL in June 1973. Work on the required revision has been initiated.

B. DSN Operations Plan

The final version of the Network Operations Plan for MVM'73 was distributed to all users for comments and use during DSN test activities. Recommended changes are being incorporated in preparation for signoff in early July 1973.

C. DSN Support Team

The DSN Support Team for MVM'73 continued to meet every two weeks during this period. Primary attention was given to open implementation tasks and initiation of DSN Ground Data System testing using interim capabilities.

D. Mission Design and Sequence Planning Support

The DSN continued support for Project mission sequence design activities in preparation for the Mission Sequence Design Review held on June 27, 1973. The DSN Manager for MVM'73 presented Deep Space Station coverage plans which support the sequence design (Fig. 1). Deep Space Station configurations which represent limitations in tracking and data acquisition capabilities were also discussed (Table 1). The DSN Operations Manager served as a member of the Review Board. Concern was expressed regarding the serious conflicts which would result between MVM'73 and Pioneer 10 should the MVM'73 launch slip to late in the launch period. Deep Space Station configuration freezes for Pioneer 10 would preclude 64-m Deep Space Station coverage of MVM'73 Earth-moon TV calibrations during November 1973. Contingency planning has been initiated.

E. DSN-Spacecraft Compatibility Test Planning

The Ad Hoc committee for planning integrated spacecraft, DSN, and Mission Operations System tests during thermal vacuum testing at JPL in July 1973 held a final meeting at The Boeing Company on June 19, 1973. DSN detailed test procedures were distributed in May 1973 for review. Questions regarding procedures, schedules, and CTA 21 staffing plans were resolved. In view of CTA 21's two-shift staffing level, this will be a difficult support period. Split shifts and overtime are planned to provide 24-hour per day coverage for short periods. Actual test operations must be held close to the plan to avoid problems.

II. Program Control

A. Telemetry/Command Data Subsystem Software Acceptance Review

The subject review was conducted by the DSN on June 22, 1973 following transfer of software program DOI-5050-OP from development to operations on June 15, 1973. Presentations were made by DSN engineering and operations members of the Software Development Project in accordance with the agenda given in Table 2. Additional details are covered under Paragraph III, Implementation Activities.

B. Project Integrated Test and Training Schedule

The DSN has participated with other project elements to produce an integrated test and training schedule reflecting detailed plans for the June–November 1973 period. DSN, Ground Data System, Mission Operations System and Mission Control and Computing System test dates and cross support requirements have been phased to avoid conflicts between MVM'73 activities. This schedule shall serve as the top document for test control and status monitoring throughout the test period.

C. Spacecraft Pre-Shipment Review

The Project conducted the subject review at The Boeing Company June 19-20, 1973. Both spacecraft radios require some additional tests and rework to achieve flight certification and configuration. The 35-W traveling-wave tube (TWT) has not performed to specifications during bench tests; therefore, its inclusion in the radio configuration is questionable at this time. In the absence of major anomalies, the Review Board granted permission to ship the spacecraft.

III. Implementation Activities

A. GCF Status

Ground communication high-speed data implementation for MVM'73 has been completed. This includes high-speed data terminal equipment provided by the NASA Communications Network (NASCOM) for Project Remote Information Centers. Wideband coded multiplexer installation has been delayed approximately 30 days due to contractor manufacturing problems and as a result of work slowdown to meet GCF FY'73 cost ceilings. This slip has not impacted Project/DSN test activities, since existing wideband equipment was modified at CTA 21, DSS 14, and the Central Communications Terminal to provide interim test support. Implementation of the 230-kbits/s wideband circuit between DSS 14 and JPL is on schedule. The common carrier has supplied data sets and preliminary circuit tests are in progress.

B. DSS Status

Telemetry and command software development problems reported in the previous report have been resolved. Major implementation tasks required to achieve capabilities committed to be operational by July 1, 1973 are near completion. However, a number of minor tasks carried on Engineering Change Orders are behind schedule and are causing test/training difficulties at the Deep Space Stations.

1. Telemetry and Command Data Subsystem (TCD). The previous report discussed in detail TCD software development problems and actions taken to resolve this major red-flag item. During this reporting period, tasks were accomplished in accordance with the revised plan and schedule. An interim revision of the TCD software was provided for DSSs 12 and 14 test support by May 1, as planned. An updated interim package (DOI-5050-IN) was shipped to all Deep Space Stations on May 15, 1973. Early Ground Data System Tests were supported using this version; known anomalies did not preclude meeting most test objectives. Final acceptance tests were initiated on June 1, 1973 and completed on June 14, 1973 as scheduled. The development to operations formal transfer agreement was completed on June 15, and TCD program DOI-5050-OP was shipped to all Deep Space Stations. It should be noted that this program still contains certain minor anomalies and undesirable operational characteristics. Attachments to the transfer agreement categorize and assign priorities for these, subject to correction in subsequent updates. TCD original data record tape replay capability is listed as a major deficiency for

MVM'73. Correction of transfer agreement exceptions pertinent to MVM'73 are in progress and will be delivered in an update to DOI-5050-OP by July 27, 1973. However, it is not planned that the July update will have the capability to switch between low-rate engineering and medium-rate science without TCD program reload. The TCD Software Development Project estimates that this capability will not be incorporated until October 1973 due to conflicting Helios and Viking software development activities. The subject data rate switching without reload is required to be available for MVM'73 test/training by August 15, 1973. Development resources and Helios/Viking requirements are being negotiated to permit accomplishment on the required date.

2. Digital Instrumentation Subsystem (DIS). Completion of DIS software acceptance in April 1973 was not accomplished as planned due to delays in the implementation of hardware interfaces with the Tracking Data Handling Subsystem and Deep Space Station monitoring devices. Five separate Engineering Change Orders were involved. The problems encountered indicate a need for better integration and coordination of minor implementation tasks required to complete major system/subsystem development activities. Installation was completed at DSSs 12 and 14 in May 1973, permitting acceptance of the DIS monitor and tracking data handling software and transfer to operations. DIS program DOI-5046-OP was shipped to all DSSs in June 1973. Interface modifications at other DSSs are in progress in preparation for operations with DOI-5046.

3. Tracking Data Handling Subsystem (TDH). TDH hardware modifications are 30 days behind schedule primarily due to slips in contractor delivery of new sample-rate selector drawers. A wiring error caused initial units to be returned for rework. These units have now been provided for DSSs 12, 14, and 62. Delivery to other DSSs will proceed rapidly now that production errors have been corrected. Implementation of Planetary Ranging hardware continues on schedule. However, DSN development of associated software appears to be falling behind schedule. Approval of the Software Requirements and initiation of coding were not accomplished on June 1 as planned. Close attention is being directed to this item.

4. S/X-Band Equipment. Block IV Receiver/Exciter implementation required for DSS 14 S/X-band research and development (R&D) experiment support continues on schedule. Tests of the assemblies have been initiated at JPL. The Block IV Receiver/Exciter will be installed temporarily at CTA 21 in late July 1973 for additional tests and DSN-Spacecraft compatibility tests. Removal of the S/X cone assembly at DSS 14 was approved to facilitate dual uplink carrier intermodulation products tests. After reinstallation of the cone, certain alignment tests must be re-run, but this should not affect the S/X band development task. A plan for installation of the coherent reference generator at DSS 14 during the last week of July 1973 has been developed and coordinated.

IV. Test and Training Activities

The Ad Hoc committee for DSN Mission Operations System Spacecraft compatibility test planning has completed detailed procedures and schedules for conducting tests while the spacecraft is in the thermal-vacuum chamber at JPL. An intensive test period of approximately 150 hours is planned between July 18 and 31, 1973.

In June 1973, GCF/NASCOM engineering conducted training courses for DSN/DSS communication operations personnel. Installation, operation, and maintenance instructions were provided for new wideband data assemblies.

On-site training for DSSs supporting MVM'73 was initiated in May 1973 through viewing of video tapes and review of MVM'73 documentation. Upon receipt of interim and operational software programs, DSS System Performance Tests were initiated at DSSs 12, 14, 42, and 62 in accordance with DSN Standard Test Procedures. These Deep Space Stations have also supported a series of Project Ground Data System long-loop data transmission tests. Due to slips in software delivery, it was necessary to conduct Ground Data System tests in parallel with DSN System Performance tests. The purpose of GDS testing is to verify *technical* performance of the systems rather than *operator* performance. Consequently, limited operator proficiency/experience was expected and acceptable. It is recognized that this approach put the Deep Space Station personnel in a difficult support position. However, most DSN and GDS test objectives were eventually met, and the DSN is approaching a state of readiness to support the GDS Demonstration Test on July 2, 1973 and to initiate DSN Operational Verification Tests.

Table 1. MVM'73 mission sequence design review DSN coverage plans

	Configuration considerations
DSS 12	Two telemetry strings
DSS 62	Two telemetry strings
DSS 42/43	One telemetry string each plus one shared
DSS 61/63	One telemetry string each plus one shared
DSS 14	Two telemetry strings
DSS 14 to DSS 12	Microwave is possible
DSS 43 and DSS 63	No planetary ranging until Jan. 1, 1974
DSS 14	Only station with S/X-band capability
Fast acquisition requirements	

Table 2. TCD software status review (MVM'73) agenda

- Introduction
- Development review
  - System tape concept
  - Plan versus accomplishments
- Verification and acceptance testing
  - Anomaly reporting system
  - Test plans and procedures
  - Test results
- Outstanding anomalies
- Status of transfer to operations
- Future plans

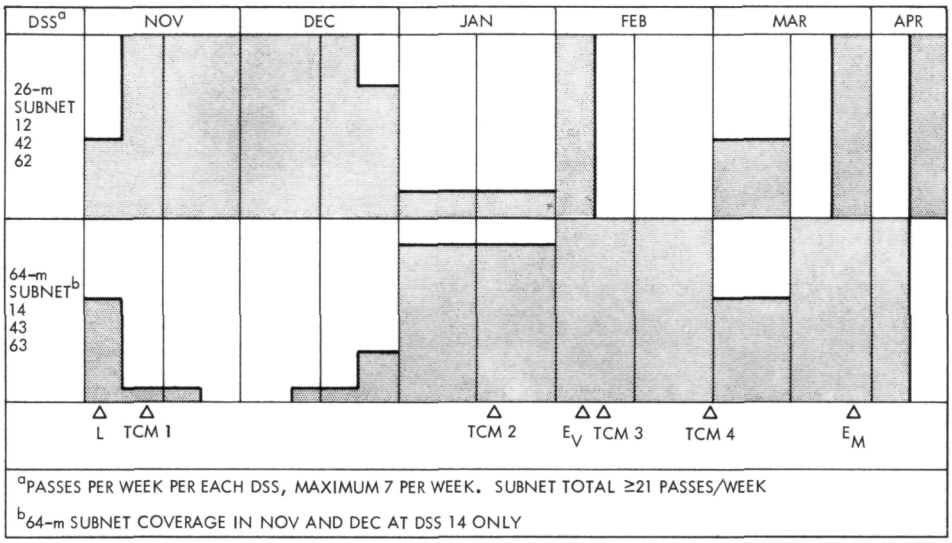

Fig. 1. MVM'73 mission sequence design review DSN coverage plan

Viking Mission Support

D. J. Mudgway
DSN Systems Engineering Office

D. W. Johnston
DSN Operations Office

The release of a preliminary version of the Deep Space Network Operations Plan for Viking has initiated the operations support for the Viking Mission. This article emphasizes the operations support in the planning phases of documentation, scheduling, training, and testing.

I. Introduction

As the DSN moves ahead into the hardware and software implementation phases of Viking support, operations activity moves into advanced planning stages. Using the network configurations described in previous articles, and the known peculiarities of the current Viking Mission design, the operations organization must start to develop procedures, strategies, and operational techniques by which the DSN resources can be deployed to achieve the desired mission support. This article is the first in which the operational planning activity is emphasized, and this approach will continue through the actual mission itself with the regular reporting of in-flight mission support.

II. Operations Documentation

The first operational milestone, the publication of the Network Operations Plan for Viking '75 Project, was completed on March 22, 1973. This preliminary version covered largely the DSN institutional facilities which will be used to support Viking '75. Its purpose was aimed mainly at project familiarization and education. The document covers Network Operations Support, Test and Training description, GCF Test and Training, GCF Configurations, and GCF Operations Procedures in detail. It will eventually cover detailed plans and procedures for test and training of the DSIF and Network Control System (NCS), configurations for the DSIF and NCS, and Network operations procedures.

In the past, the Network Operations Document has been divided into two separate sets of volumes for DSN operations and DSN test and training. The Network Operations Plan for Viking '75 incorporates a new philosophy in that everything is included in one document. This results in lower documentation costs by reducing the number of documents required from more than ten to just one. The document has been organized so as to facilitate locations of the various types of information .

III. Dual Carrier

The decision to adopt the two-station alternative for the requirement for simultaneous dual uplinks will have a larger effect on operations than originally anticipated. Without the dual capability at the 64-m stations, a second 26-m subnet is required to support the Project. It will be used to cover the approaching Spacecraft B following the separation of Orbiter A and Lander A.

Commitment of an additional 26-m-diam subnet requires that it be supplied with equipment to establish a Viking '75 configuration and that it be tested and trained in advance of the committed support. Test and training will be conducted after launch and thus reduce somewhat the overall test and training load. Although this second 26-m subnet will support the mission for only 30 days during cruise, the tests and training effort must be no less than that performed at the prime stations.

The fact that all stations in the DSN, with the exception of DSS 51, will be committed for Viking support during the 30-day period places a burden on the scheduling of support for the other flight projects.

Even though the dual carrier investigation is continuing, and the problems may be resolved by launch, planning continues on the assumption that this capability is required for mission enhancement only.

IV. Viking '75 Orbital Configuration

DSN Operations personnel have been working very closely with the DSN Manager and system engineers to produce a configuration which will allow a backup/failure strategy during orbital operations. As every item of available equipment will be utilized at the 64-m stations during orbital operations, a failure strategy becomes extremely important. By using equipment located at the conjoint stations in the case of DSSs 43 and 63 and at DSSs 11 and 14, a strategy has been formulated for a single-point failure. This strategy will be finalized and included in the Network Operations Plan following publication of the DSN Preparation Plan for Viking '75 Project.

V. Voltage-Controlled Oscillator (VCO) Requirement

A study has been conducted for the DSN Manager to determine the minimum number of VCOs required to support the Viking Mission. Since extreme doppler conditions during cruise will stress the standard VCOs to the limit of their operating capability, the study has included the possibility of a need for offset VCOs.

VI. Training

DSSs 11 and 14 are scheduled to support Viking '75 Flight Operations System (FOS) verification and demonstration tests during the first half of 1975. In order to support these tests, the stations must be fully equipped, trained, and manned to support orbital operations. As actual orbit operations do not begin until nearly one and a half years later, the training effort will need to be repeated following launch.

Several ways of solving the manning problem, in order to support the FOS tests, have been considered. One would be to borrow personnel from other stations for support of the tests and then, upon completion, return them to their respective stations. This would maintain the number of personnel at a set level but reduce the strength of the nonsupporting stations. To increase the number of personnel to support the FOS tests would imply manning for orbital operations one and a half years in advance of the actual need. This problem continues to be studied in conjunction with the actual definitions of the FOS test requirements.

VII. Viking Unique Procedures and Strategies

Work has started on several Viking unique strategies and procedures, particularly for lander acquisition and commanding. These will be reported in subsequent issues of this report.

Pioneer 10 and 11 Mission Support

R. B. Miller
DSN Systems Engineering

The Pioneer 10 and 11 encounters will place the greatest demands of any mission to date on total Ground Data System reliability. The encounter sequence and aspects of the spacecraft design which place demands on DSN performance are described.

I. Introduction

The Pioneer 10 Jupiter encounter will place the greatest demands on total Ground Data System reliability of any planetary mission supported by the Jet Propulsion Laboratory to date. This is principally because of the attempt to execute a complex encounter flyby sequence without the benefit of an on-board sequencer or an on-board data recording system. The encounter sequence, which lasts for a total of 60 days, will involve 14,000 ground commands, essentially all of which are time-critical. The vast majority of these commands are for the operation of a single instrument, the imaging photopolarimeter (IPP). Failure to transmit any of the encounter commands correctly on time will usually result in a loss of some of the science data from this instrument.

Since the science data are not recorded on board the spacecraft for later playback, outages in the real-time ground telemetry system can cause loss of science data from all eleven instruments on board the spacecraft. Such losses will be equal in length to the amount of time it takes to restore or replace the failed element in the ground system. The DSN objective for the critical encounter period is to be able to restore or replace a failed element in the telemetry or command system within 6 minutes.

II. The Imaging Photopolarimeter

The encounter sequence is dominated by the imaging photopolarimeter. The following description of that in-

strument is provided here so that the origin of the large number of commands required for encounter and their time-criticality may be understood.

The imaging photopolarimeter measures the intensity and polarization of visible light. The instrument consists of an optical telescope, beam-splitting optical prisms, two sets of filtering optics, two channeltron detectors, and signal processing logic and control. The beam-splitting prisms produce two orthogonally polarized beams. Passage through the filtering system results in two color channels, a red and a blue. The instrument has the following operating modes and instantaneous fields of view:

Mode 1, instrument on but not in use.

Mode 2, zodiacal light mode, 40×40 millirad.

Mode 3, polarimetry, 8×8 millirad.

Mode 4, imaging, 0.5×0.5 millirad.

The method in which the instrument scans in order to produce an image is shown in Fig. 1. Scan lines analogous to the horizontal lines in a video system are produced by the instrument looking in a fixed direction with respect to the spacecraft as the spacecraft spins. The start of each scan as the spacecraft rotates is controlled by a series of "spoke" commands which control the start with respect to the spin position or, alternately, the scan can be started by the limb of the planet using the "start data at threshold" mode. For encounter it is planned to use the "spoke" command mode almost exclusively. The equivalent of video vertical scanning is achieved by either stepping the instrument with respect to the spin axis 0.5 millirad between each rotation of the spacecraft or, during the nearest approach to the planet, holding the telescope in a fixed position and letting the relative motion of the spacecraft and Jupiter achieve the scanning. This means that during the closest approach the scan lines can be overlapping or have gaps between them depending upon the relative motion of the spacecraft and Jupiter.

In the imaging mode, the data are converted to 64 levels of intensities (6 bits) and stored in a 6144-bit buffer. The instrument will overwrite this buffer as it starts each "horizontal" scan with each rotation of the spacecraft. The memory read-in time is approximately one-half second and the spacecraft rotation rate is approximately 12 seconds, which means there are approximately 11 seconds available to read out the memory. In order to read out the 6144 bits in the 11 seconds available requires a data rate of 512 bps. The IPP instrument receives about 50% service rate on the spacecraft telemetry downlink, which means that a 1024-bps telemetry downlink from the spacecraft to Earth is the minimum data rate at which all the IPP data taken can be returned to Earth.

The 1024-bps telemetry rate for the time of encounter requires 64-m-diameter antenna coverage. Even with 64-m coverage it may be necessary to reduce the rate to 512 bps at low elevation angles. This will result in returning "horizontal" scans that are only half as long. In the event of a 64-m antenna failure that requires transferring the spacecraft to a 26-m antenna, the bit rate will have to be reduced to 128 bps, resulting in "horizontal" scan lines only one-tenth as long as would be possible at the maximum bit rate. The operation of the instrument in the polarimetry mode, Mode 3, is essentially identical to the above except that the field of view is 8×8 millirad and the automatic stepping is in 8-millirad steps. In addition to stepping the instrument at 0.5 or 8 millirad when in Mode 4 or 3, it is possible to slew the instrument to several fixed positions. The total range of look angles is 151 deg with respect to the spin axis. Between the stops at the limits of the 151 deg are 7 slew stops. The slew stops, referred to as slew angles 1 through 7, are each comprised of 2 stops 1 deg apart. When the instrument is slewed to a slew angle it stops at the slew angle position closest to the direction it is approaching from.

The IPP instrument has an automatic gain control feature. Because this feature does not operate properly on the Pioneer 10 spacecraft, more than twice as many commands will be required during the Pioneer 10 encounter than on the Pioneer 11 encounter.

III. The Imaging Photopolarimeter Encounter Sequence

It is intended to operate the IPP instrument on the order of 8 hours a day for periapsis ± 30 days and 24 hours per day for periapsis ± 8 days. Figure 2 depicts a typical 24-h IPP encounter sequence. This sequence and the periapsis sequence to be described later are both typical and not the final planned sequence. The chart portrays the look angle as a function of time. The three lines labeled Jupiter are the physical disk of the planet and show its change of position as a function of time. The sinusoidal lines labeled with a J and a Roman numeral depict the look angle of the moons of Jupiter that are in the field of view. The lines labeled SLA1 are the two stop positions of slew angle 1. The irregular line represents the instantaneous look angle of the IPP telescope. Note that this diagram represents only two dimensions in the operation of the instrument. Recall that the look angle is the angle

with respect to the spacecraft spin axis and is equivalent to the vertical axis in an ordinary video system. The control of the start of data taking with respect to the roll position of the spinning spacecraft, equivalent to the horizontal scan lines in an ordinary video system, is not depicted.

The basic strategy is to take repeating imaging scans of the disk of the planet, interrupted by slews to a slew angle for polarimetry whenever one of Jupiter's moons crosses a slew angle. Starting at the left of Fig. 1, the IPP instrument is at a slew angle taking polarimetry on Jupiter's second satellite. To get to position 1, 21 commands were required, 12 of which were to overcome the gain control problem. Between points 1 and 7 in the sequence, 5 additional gain control commands are sent at 30-min intervals. At point 7 in the sequence the instrument is commanded into the Mode 3 threshold mode where the instrument slews continuously until the limb is automatically detected. This point in the sequence involves 17 contiguous commands (sent at the maximum command rate of 1 command per 22 seconds), 13 of which are gain control commands to overcome the gain control problem. At point 8 in the sequence the instrument is commanded to the imaging mode (Mode 4) at the imaging rate of 0.5 millirad per spacecraft revolution. This point in the sequence involves 7 contiguous commands, 4 of which are gain control, and 2 are "spoke" commands. Point 9 in the sequence involves a single command to reverse the stepping direction of the telescope. Point 10 in the sequence involves 17 contiguous commands, 16 of which are gain control commands. The sets of commands at points 9 and 10, comprised of 1 and then 17 commands, are repeated at every similar point in the sequence that follows. Step 14 involves 26 contiguous commands, 23 of which are gain control commands, which place the instrument in the polarimetry mode at a slew angle for the crossing of Jupiter's third satellite. The commanding at point 15 in the sequence is identical to that at point 7 and the commanding at point 16 is identical to that at point 8. At point 19 in the sequence, 3 commands are sent which result in switching back to Mode 3 and stepping beyond slew angle 1. The commanding at step 20 reverses the slew to approach slew angle 1 from the correct side to stop at the position that the third satellite of Jupiter is now crossing and involves 32 contiguous commands, 23 of which are gain control.

The rest of the sequence depicted on this chart is built by repeating one of the command sequences already described at the appropriate time. In executing very similar sequences like those which were just described for 8 hours a day from periapsis −30 to +30 days, and 24 hours a day from periapsis −8 to +8 days, the origin of the requirement for 14,000 commands during the encounter sequence is understood.

The possible effects of ground command system problems can be understood by studying this portion of the encounter sequence. When the imaging on the planet is being performed, the look angle is controlled at all points in the sequence similar to 9 and 10 by the time of transmission of the ground commands. If an interruption to command capability occurred at point 9 in the sequence so that command did not leave, the instrument would continue to slew upward away from the disk of the planet. The recovery strategy would have to depend on the length of time it took to restore command capability. If command capability were restored a fairly short time after the schedule transmission time for the command, then the instrument would not have moved too far away from the disk of the planet and that same single command could then be sent to start slewing back toward the disk. A new time of transmission for the set of commands at point 10 in the sequence would have to be computed based on the slew rate and the new look angle that the instrument had to step through. If it took a long time to restore the system after the scheduled time of transmission for the command at point 9, then the instrument would have stepped a large number of degrees from the disk of the planet, and it would be wasting too much time to slew back to the disk. In this case it would be necessary to command the instrument back to the polarimetry mode and slew to slew angle 1 and execute the sequence of commands that would be used at a point such as 15 and 16 to get back to imaging on the disk of the planet.

In either failure case just described, clearly the instrument will end up out of phase with the rest of the planned sequence. When such failures occur, the sequence will have to be caught up at the next scheduled time for polarimetry on one of the satellites. The result will be a loss of some number of imaging scans across the disk of the planet or, to state it differently, the loss of some number of pictures. When the command failures occur near the scheduled time for a satellite observation, then that particular polarimetry viewing of the satellite may be lost.

The above paragraph describes the effect of command system outages on the encounter sequence. There is another category of command failure which has caused a great deal of concern, and that is false verification. False verification of a command means that all system and monitor indicators have indicated that the command was successfully transmitted error-free when in fact it was not.

The effect of false verification could be serious. For example, if the command at point 9 in the sequence was falsely verified, that would mean that the command to reverse scan direction was indicated as successfully transmitted but in fact was not, and the instrument would continue to scan upward away from Jupiter. The round-trip light time at this point in the mission is 90 min, which means that at point 10 in the sequence there would still be no indication that the command at point 9 was not received, and the set of commands at point 10 would be transmitted. At point 11 in the sequence, a round-trip light time would still not have occurred, and the result would be the execution of the mirror image of the planned sequence but up out of the field of view of the planet Jupiter.

It can be understood, then, why false verification is a greater concern for the encounter than detected interruptions to the command capability. In the course of Pioneer 10 and 11 mission support, nearly 30,000 commands have been transmitted and there have been three instances of false verification, the most recent one being in January 1973. The DSN is executing an implementation that will prevent the reoccurrence of the January incident of false verification. The previous two instances of false verification were caused by procedural errors. Since January, several failures which contributed to the previous two cases of false verification have occurred without resulting in a false verification. The DSN will continue to take steps to prevent any future occurrences of false verification.

Essentially the entire 60-day encounter sequence for the IPP instrument, with the exception of the periapsis pass, is built from the command sequences described above relating to Fig. 2. Figure 3 depicts a typical plan for the periapsis pass. Notice the rapidly changing look angle of the planet Jupiter and the satellite viewing in the near encounter. No further examination of the periapsis sequence will be offered here except to point out that, in Fig. 3, each discontinuity in the look angle of the instrument represents an average of about 15 to 20 contiguous time-critical commands.

IV. Conclusions

The DSN is making every effort, within resources, to insure that its portion of the command Ground Data System is as reliable as possible and to minimize the number of command system failures and the resultant loss of IPP data during the encounter sequence. However, there will be some interruptions in command capability during the encounter sequence because equipment and software do fail, and time is required to switch to redundant elements and to restore failed systems. It should be remembered that the command portion of the Ground Data System is comprised of two other elements besides the DSN (project personnel and equipment located at Ames Research Center and Mission Control and Computing Center equipment and personnel at JPL) and that failures in any one of the three elements of the Ground Data System can result in an interruption of command capability. The IPP data that will be lost because of Ground Data System outages during the 60-day encounter sequence is part of the price of flying a planetary encounter mission without an on-board sequencer in order to simplify the spacecraft design and the resulting spacecraft cost.

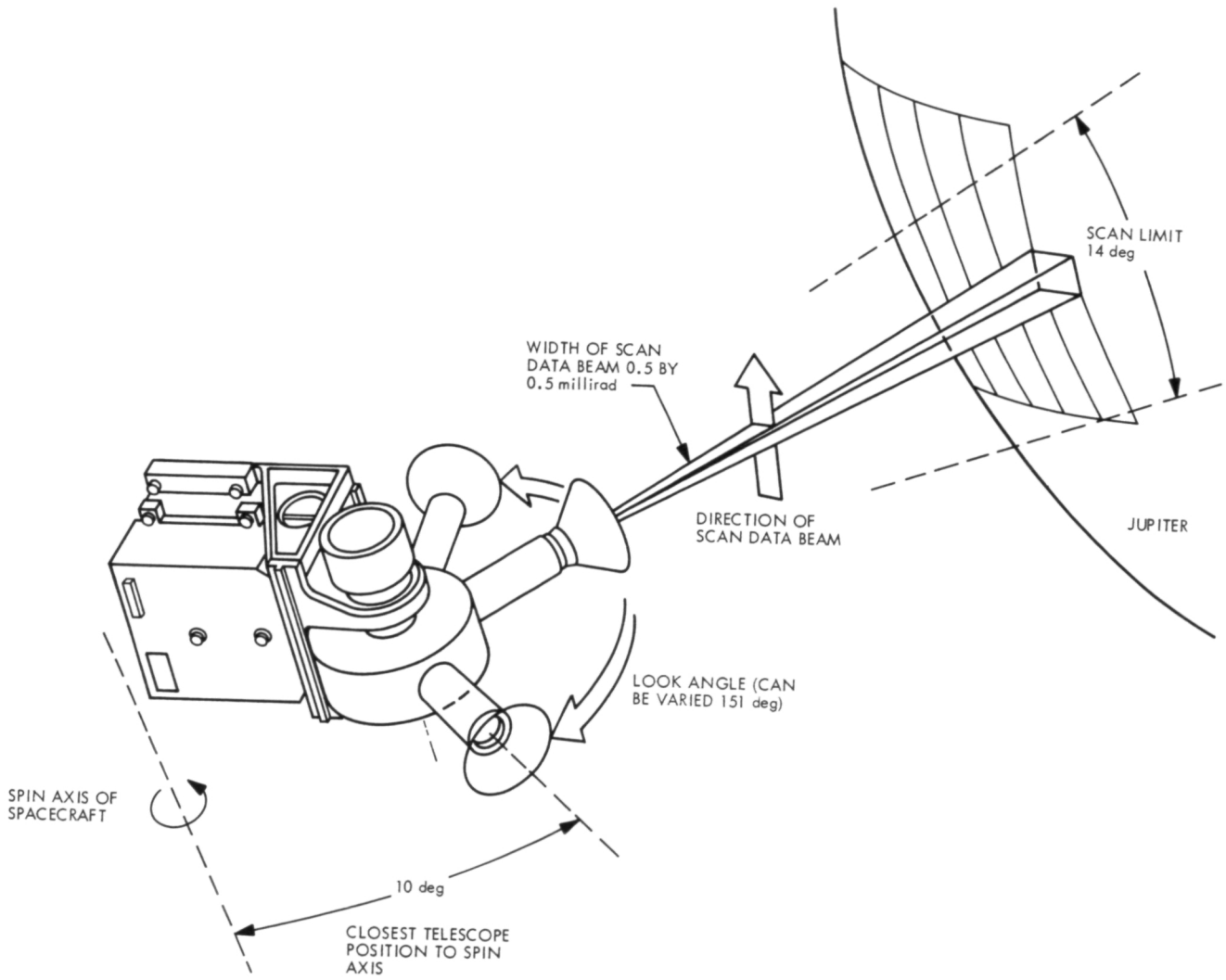

Fig. 1. The IPP imaging system

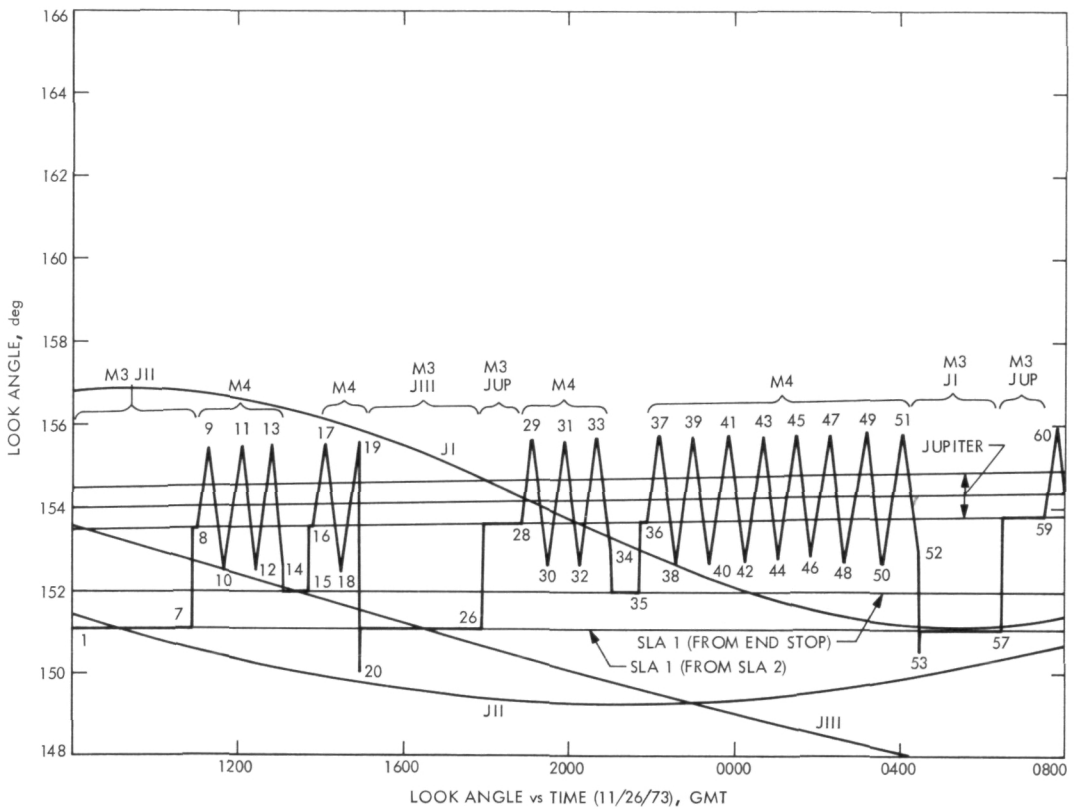

Fig. 2. Typical IPP 24-hour sequence

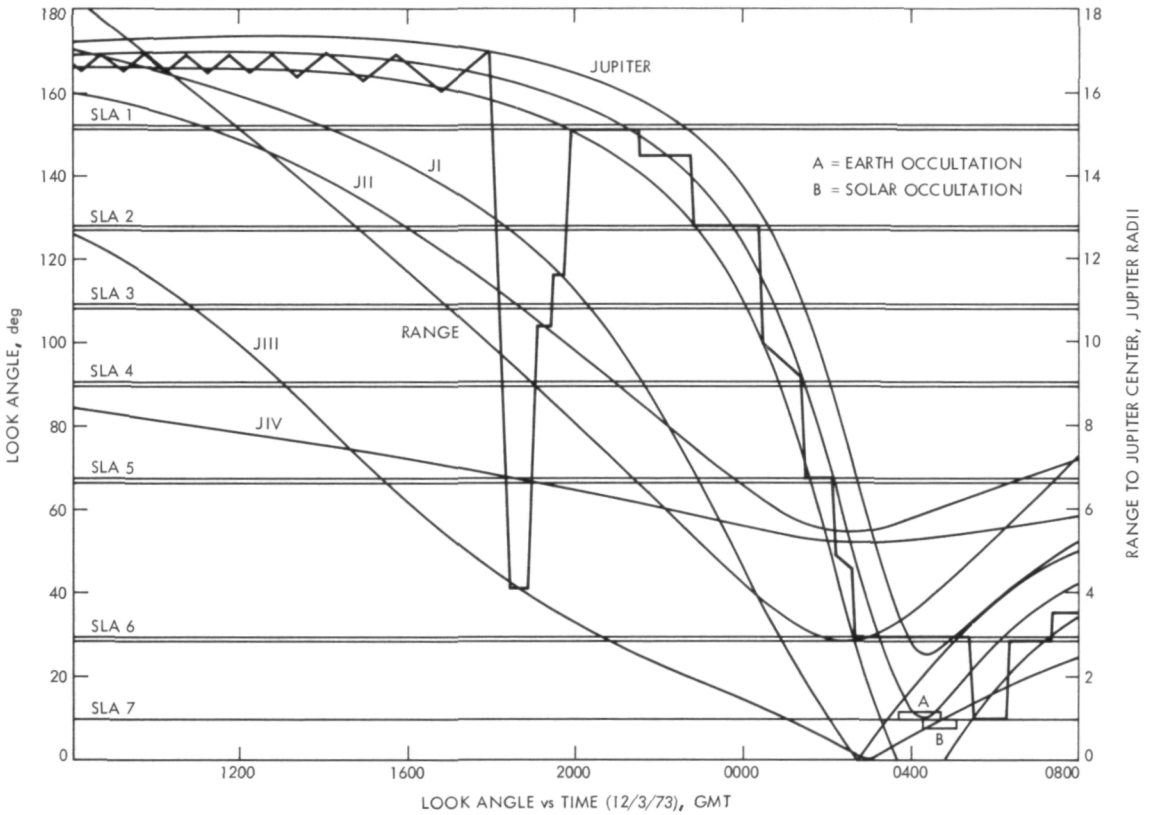

Fig. 3. Characteristic IPP periapsis sequence

Efficient Antenna Systems: Calibration of the Mars Deep Space Station 64-m Antenna System Noise Temperature Degradation Due to Quadripod Scatter

P. D. Potter
Communications Elements Research Section

In January 1973 extensive tests were performed of Mars Deep Space Station system noise temperature as a function of antenna elevation angle. These tests were performed under the ideal conditions of cold, dry weather, for which atmospheric absorption is well known. These data have been completely reduced and show a remarkably low residual to an elevation angle curve fit (less than 0.1 K). A new computer program has been developed which yields ground noise contribution as a function of antenna pointing direction and (known) direct feed system spillover. By subtracting the atmospheric and direct spillover effects out of the measured system temperature data, the noise temperature contribution of the quadripod scattering has been established to an accuracy of a few tenths of a kelvin. At low to moderate elevation angles, the effect is roughly twice as severe as at zenith. In this reporting, the data reduction procedure, computer program formulation and the results are presented.

I. Experimental Data

The extensive January 1973 tests performed on the DSS 14 reflex feed system have been previously described (Ref. 1). All four combinations of S- and X-band and reflex and non-reflex (standard) configurations were tested. As described in Ref. 1, the low-elevation angle noise temperature performance of the S-band reflex feed is superior to that of the standard S-Band Megawatt Transmit (SMT) (feed cone) performance. As will be described later in this article, the difference is predictable from the tricone geometry and the lower forward spillover of the S-band reflex systems. The observed effect has stimulated interest in the detailed noise temperature performance of the various feed systems.

The antenna gain was extensively tested, using radio source techniques. These gain tests were performed as a function of elevation angle by tracking a selected radio source (3C123) for a period of several hours, taking both on-source and off-source system temperature measurements. The off-source tests involved offsetting the

antenna pointing direction relative to source ephemeris position by a standard amount, typically 1 deg in azimuth. The noise adding radiometer (NAR)-determined system temperature and the station time were simultaneously printed on a digital recorder. From a knowledge of the source position and the time (printed to the closest second), the antenna elevation angle was accurately determined for the exact time the system off-source noise temperature was recorded, all without human error.

The measured temperature vs. elevation angle data so obtained was curve-fitted utilizing a JPL Scientific Computer Facility (SCF) cubic spline fitting program (Ref. 2). In reducing the data, the minimum number of spline breakpoints was used, compatible with a stable mean-square residual. Four days of data were available, 1/27/73 through 1/30/73, Universal Time. Each day's data (a single run) were separately curve fitted. The number of points per run varied from 26 to 72.

The largest data volume was for the S-band reflex configuration, with a total of 103 points (3 days of data) after combining the runs, with elevations from 8 to 85 deg. The RMS (i.e., 1 sigma) residual to the curve fit was 0.072 K. Spline breakpoints were used at 12, 22, 45, and 70 deg. The standard configuration (SMT feed cone) data consisted of 38 points (2 days), with elevations from 14 to 82 deg. Breakpoints were used at 45 and 70 deg, and an RMS (1 sigma) residual of 0.051 K relative to the curve fit was obtained.

The standard non-reflex X-band data were limited, unfortunately, to one run (1/30/73) of 17 points ranging from 50 to 84 deg elevation. No breakpoints were used and an RMS (1 sigma) residual of 0.012 K was obtained.

Interpretation of the X-band reflex data posed a special problem. Three runs were available: 1/28/73, 1/29/73, and 1/30/73. These data, when separately fitted, showed RMS residuals of 0.060, 0.050, and 0.093 K, respectively. However, the curve fits showed mean differences (for fixed elevation angles) between days of 0.5 to 1 K. If these large differences were ascribed to actual data noise, they would have to be interpreted as 10- to 20-sigma effects, which is statistically impossible. All tests were done by the same experimenters, offset from the same radio source and at the same times of day in each case. In all cases the weather was ideal: clear, dry, and cold. Thus it is virtually certain that either: (1) the receiving system changed between successive days, or (2) the NAR was not correctly adjusted in all cases. In no case is there evidence of a drift in the system temperature during a given run (several hours).

The above ambiguity cannot be resolved. After discussion with all of the parties involved, it was concluded that NAR misalignment was the most likely cause. The effect of such a misalignment is that all temperatures are incorrect by a fixed ratio close to unity. In combining the three X-band reflex data runs, therefore, two of them were multiplied by constant fixed ratios (2% and 5% different from unity) such that a minimum overall RMS of 0.080 K relative to the curve fit was obtained, a number comparable to the S-band data. The final X-band reflex data volume is 90 points, ranging from 8 to 85 deg elevation. The breakpoint values used were the same as for the S-band reflex data reductions.

Plots of the measured system temperature as a function of elevation angle were presented in Ref. 1 and are not repeated here. It is clear from these data that variations of several kelvins in antenna spillover effects occur as a function of elevation angle. The next section briefly describes a new computer program to analytically determine the effect of direct feed spillover upon noise temperature, as a function of feed design and antenna pointing direction.

II. Calculation of Direct Feed Spillover Noise Contribution

Figure 1 shows the ground noise contribution geometry. By a simple coordinate transformation it is found that the azimuthal angle, ϕ_E, corresponding to the horizon is given by

$$\cos \phi_E = \frac{\tan \alpha}{\tan \theta}, \qquad \theta \geq \alpha \tag{1}$$

where

α = antenna elevation angle

θ = polar angle in the antenna coordinate system

The ground noise contribution, $T_{AG}(\alpha)$, is given in kelvins by (Ref. 3):

$$T_{AG}(\alpha) = \frac{\iint_{\text{GROUND}} T_{\text{GND}}(\alpha,\theta,\phi)\, P(\theta,\phi) \sin\theta \, d\phi \, d\theta}{\iint_{\substack{\text{ALL} \\ \text{SPACE}}} P(\theta,\phi) \sin\theta \, d\phi \, d\theta} \tag{2}$$

where

$T_{GND}(\alpha,\theta,\phi)$ = ground brightness temperature, kelvins

$P(\theta,\phi)$ = relative power radiation pattern response of the antenna

It is seen from Eq. (2) that the antenna power pattern, $P(\theta, \phi)$, is merely a weighting function in the integration. Small errors in the pattern specification do not grossly affect the answer $T_{AG}(\alpha)$. Considering only direct feed spillover, and for DSN feed systems utilized to date, $P(\theta, \phi)$ is approximately independent of ϕ. Thus,

$$T_{AG}(\alpha) \approx \frac{\int_{\theta=\alpha}^{\theta=180^\circ} P(\theta)\sin\theta\, d\theta \int_{\phi=0}^{\phi=\phi_E(\alpha,\theta)} T_{GND}(\alpha,\theta,\phi)\, d\phi}{\pi \int_{\theta=0}^{\theta=180^\circ} P(\theta)\sin\theta\, d\theta} \tag{3}$$

where

$P(\theta)$ = the average power pattern

The brightness temperature of the ground, $T_{GND}(\alpha,\theta,\phi)$, is related to the ground physical temperature, T_{PHYS}, by

$$T_{GND}(\alpha,\theta,\phi) = T_{PHYS}\{1 - R^2[\psi(\alpha,\theta,\phi)]\} \tag{4}$$

where

$R[\psi(\alpha,\theta,\phi)]$ = magnitude of the ground voltage reflection coefficient

$\psi(\alpha,\theta,\phi)$ = ground grazing angle

If the antenna is circularly polarized,

$$T_{\substack{GND \\ CP}}(\alpha,\theta,\phi) = T_{PHYS}\left\{1 - \frac{R_V^2}{2}[\psi(\alpha,\theta,\phi)] - \frac{R_H^2}{2}[\psi(\alpha,\theta,\phi)]\right\} \tag{5}$$

where

$R_V[\psi(\alpha,\theta,\phi)]$ = ground reflection coefficient for vertical polarization

$R_H[\psi(\alpha,\theta,\phi)]$ = ground reflection coefficient for horizontal polarization

For dry desert terrain, values for $R_V[\psi(\alpha,\theta,\phi)]$ and $R_H[\psi(\alpha,\theta,\phi)]$ are given in Ref. 4. From geometry it can be determined that

$$\sin\psi(\alpha,\theta,\phi) = \cos\alpha\sin\theta\cos\phi - \sin\alpha\cos\theta \tag{6}$$

A simple computer program has been developed which evaluates Eq. (3) subject to Eqs. (5) and (6). The selected ground reflection coefficient is for DSS 14-type ground, based on the data in Ref. 4. The program input is the antenna radiation pattern, $P(\theta)$ (tabular data in JPL standard pattern format), and the ground physical temperature, T_{PHYS}. The next section describes computed results.

III. Results

For the DSN 64-m-diam antennas, calculation of direct forward spillover effects is slightly complicated by the tricone asymmetry. As shown in Fig. 2, the feedhorn axes are not parallel to the antenna axis. Consequently, for identical horn patterns and a given elevation angle, the forward ground spillover effect is more severe for the upper (SMT), Polarization Diversity S-Band (PDS) feed cone positions than it is for the lower X-Band Cassegrain Experimental (XCE) feed cone position. The direct rear spillover, which arises from the subreflector scatter characteristics, is approximately independent of tricone position for a given frequency and feedhorn pattern. Figures 3 through 6 show, among other things, the computed direct spillover noise contributions for the four possible systems, for a ground physical temperature of 15.5°C (60°F).

To determine the magnitude of the quadripod scatter effect, it was assumed that the system noise temperature was the sum of five components: (1) receiver/transmission line noise, (2) extra-atmospheric noise, (3) atmospheric noise loss, (4) direct spillover ground noise, and (5) quadripod scatter noise. At S-band, the atmospheric noise is not particularly dependent on humidity and has been very accurately determined as 2.2 kelvins (Ref. 5). At X-band, a zenith atmospheric noise contribution of 2.5 kelvins has been calculated by T. Otoshi of the Communications Elements Research Section for the clear, cold, dry conditions that prevailed for the January 1973 tests. The calculated atmospheric and direct spillover contributions were subtracted from the measured data described above, leaving a residual composed of items (1), (2) and (5). Items (1) and (2) are essentially elevation-angle independent; to determine their magnitude, it was assumed that the sum of items (4) and (5) have a value of 3.0 K at zenith. This value has been approximately determined experimentally (to within a few tenths of a kelvin) and was previously utilized in quadripod studies (Ref. 6). Using this information, the sum of (1) and (2) was determined, leaving only the quadripod component (5) as a residual. The resultant quadripod effect is shown

in Figs. 3 through 6 for the four systems. For the X-band reflex system, an additional component caused by dichroic plate reflection (Ref. 1) is present. The magnitude of this effect was determined (Fig. 6) by differencing out the quadripod effect determined for the nonreflex X-band operation.

Figure 7 shows the total ground noise contribution including direct spillover, quadripod scatter, and (for X-band reflex operation) dichroic plate scattering.

IV. Conclusion

By a combination of experimental data and computation, the DSS 14 quadripod-induced system noise temperature degradation has been determined as a function of antenna elevation angle. The magnitude is somewhat larger than that predicted for isotropic quadripod scattering (Ref. 6), but is in semiquantitative agreement. A possible technique for performance enhancement of the system by control of the quadripod scattering pattern has been previously suggested (Ref. 6).

References

1. Potter, P. D., "S- and X-Band Feed System," in *The Deep Space Network Progress Report*, Technical Report 32-1526, Vol. XV, pp. 54–62. Jet Propulsion Laboratory, Pasadena, Calif., June 15, 1973.
2. Hanson, R. J., "Computing Quadratic Programming Problems: Linear Inequality Constraints," Feb. 9, 1970 (JPL internal document).
3. Rusch, W. V. T., and Potter, P. D., *Analysis of Reflector Antennas*, pp. 71–73. Academic Press, New York, 1970.
4. Reed, H. R., and Russel, C. M., *Ultra High Frequency Propagation*, p. 97. John Wiley & Sons, New York, 1953.
5. Ho, W., et al., "Brightness Temperature of the Terrestrial Sky at 2.66 GHz," *J. Atmos. Sci.*, Vol. 29, pp. 1210–1212, September 1972.
6. Potter, P. D., "Antenna Study: Performance Enhancement," in *The Deep Space Network Progress Report*, Technical Report 32-1526, Vol. X, pp. 129–134. Jet Propulsion Laboratory, Aug. 15, 1972.

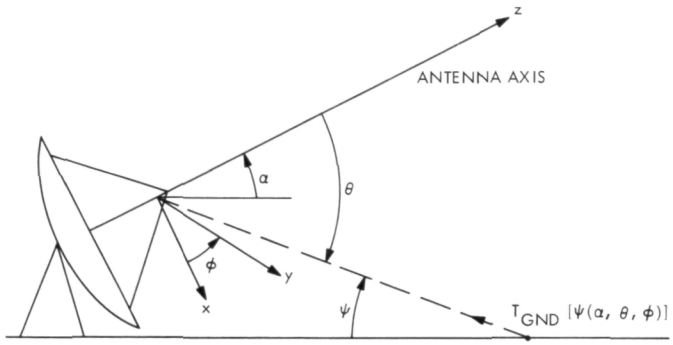

Fig. 1. Ground noise geometry

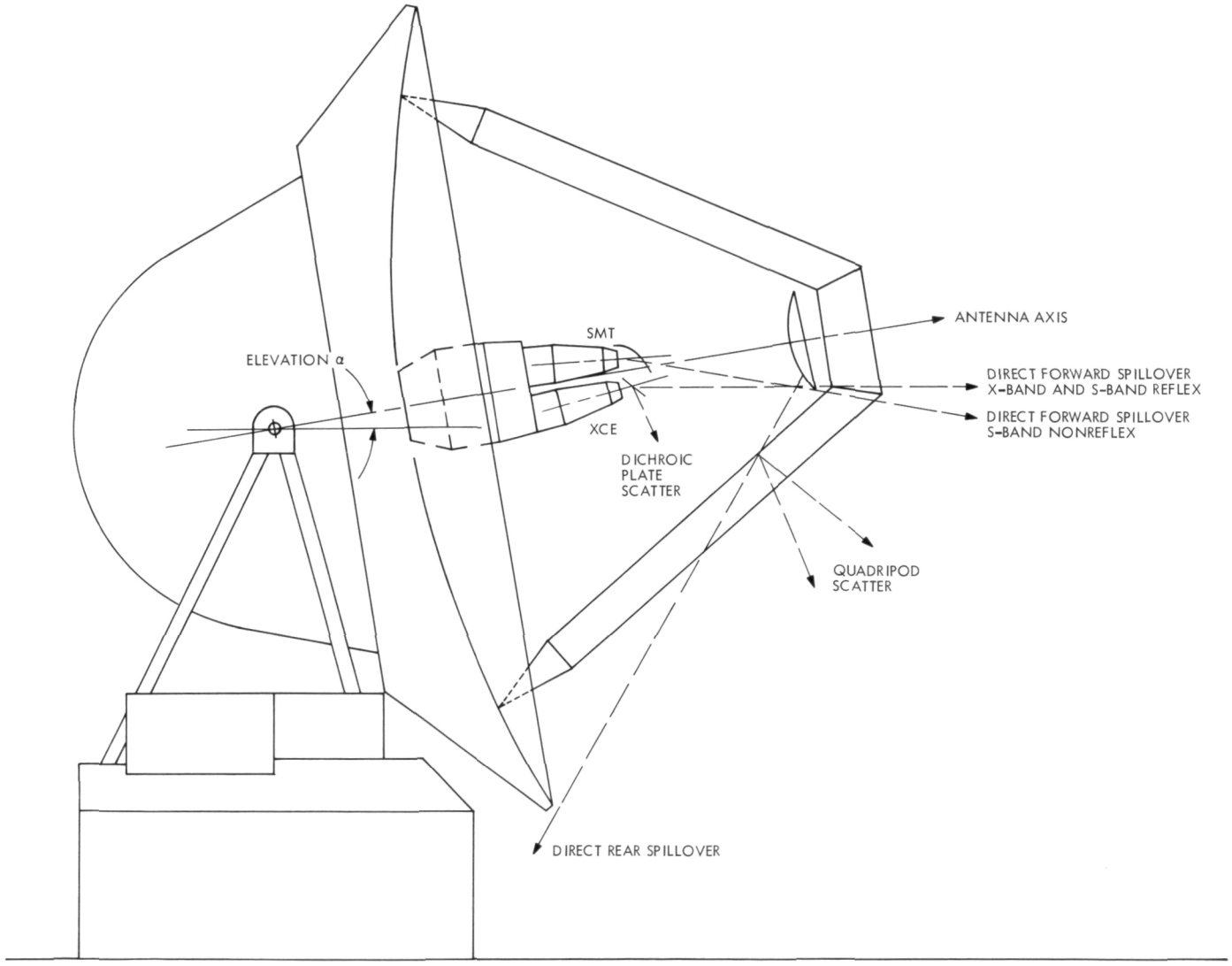

Fig. 2. DSS 14 spillover geometry

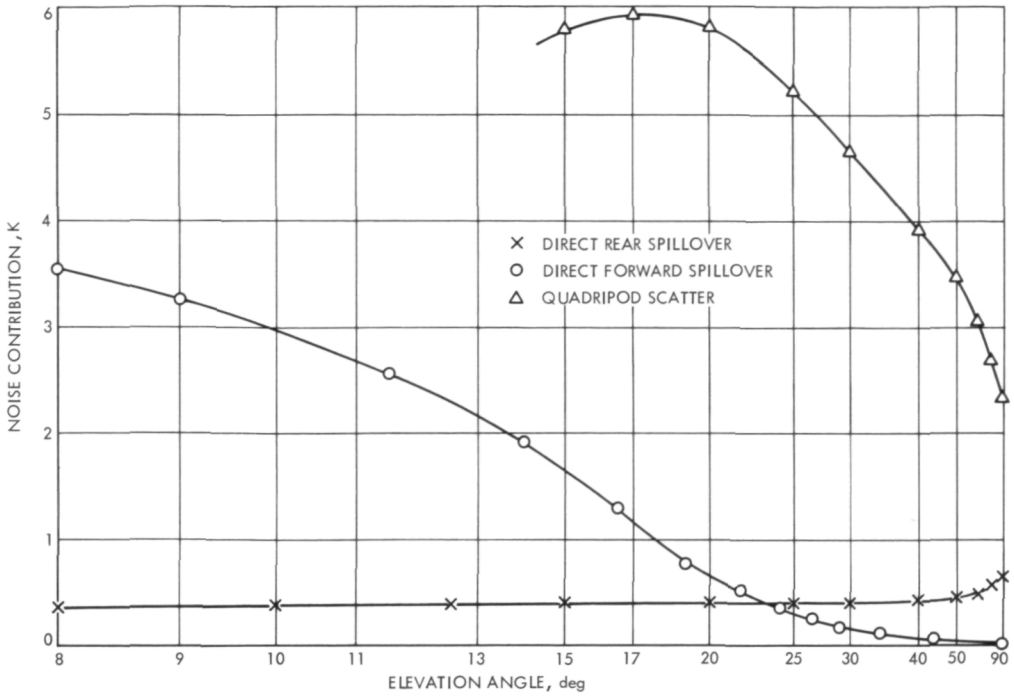

Fig. 3. DDS 14 dry ground noise contributions, S-band non-reflex (SMT)

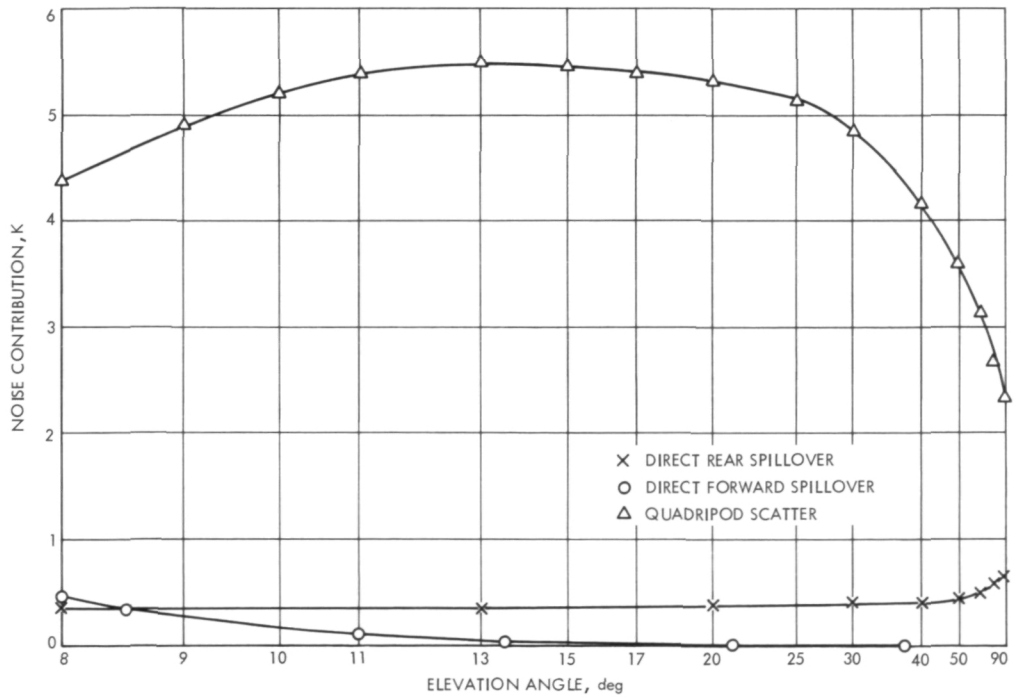

Fig. 4. DSS 14 dry ground noise contributions, S-band reflex

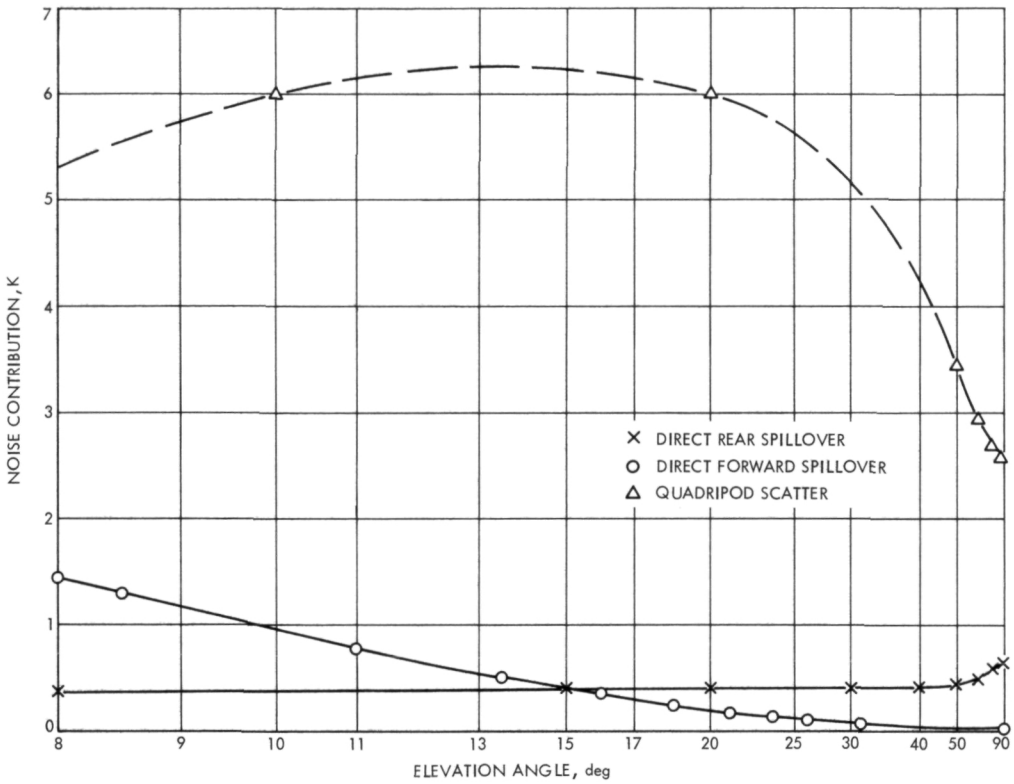

Fig. 5. DSS 14 dry ground noise contributions, X-band non-reflex, X-band Cassegrain Experimental (XCE))

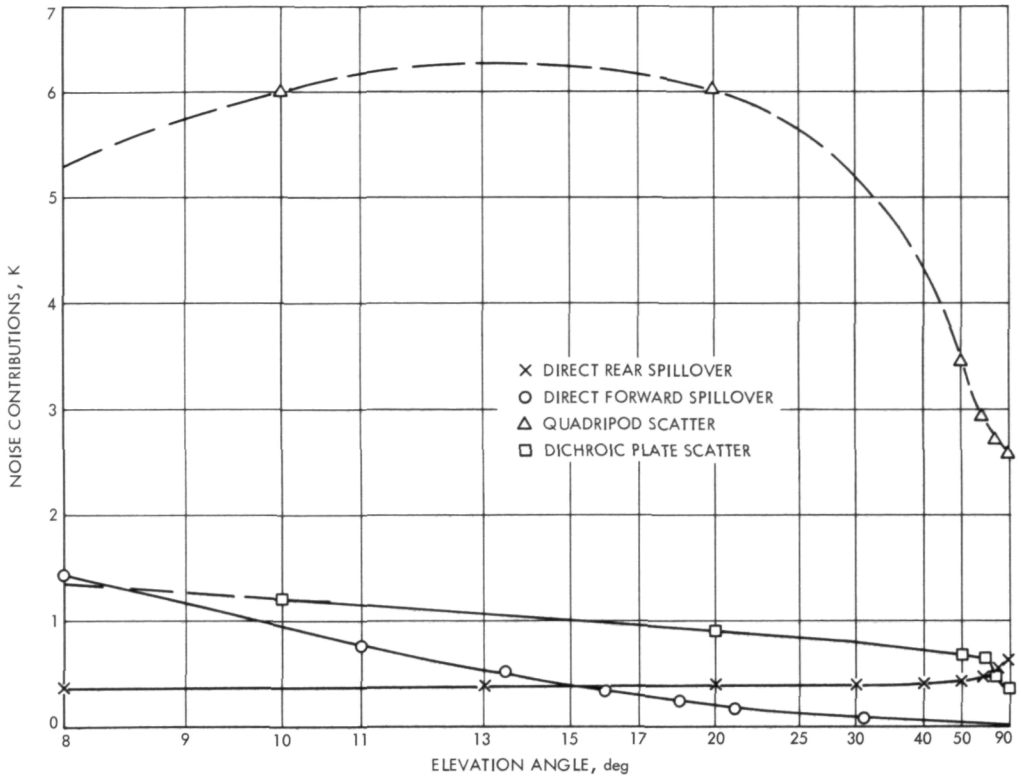

Fig. 6. DSS 14 dry ground noise contributions, X-band reflex

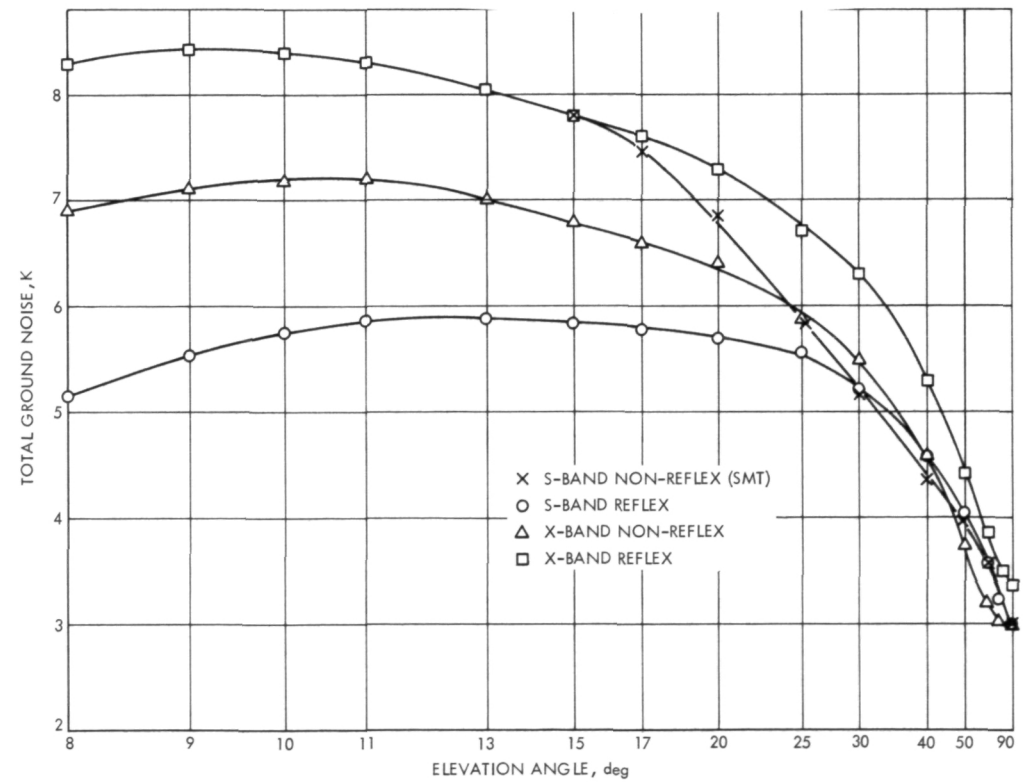

Fig. 7. DSS 14 dry ground total ground noise

Tracking Assistor for DSN Receivers

R. L. Sydnor and J. W. MacConnell
Communications Systems Research Section

The tracking assistor improves the performance of DSN receivers at fast doppler rate and high noise level by removing the stress in the phase locked loop of the receiver. The assistor is basically a down-up converter inserted in the 24-MHz feedback path of the receiver that removes the loop stress by subtracting the doppler, which is computed by a programmed local oscillator (Ref. 1). Since the input and output frequencies are nearly identical, special filtering and construction techniques are required to achieve the extremely high isolation necessary to prevent undesired phase modulation within the loop.

The synchronous assistor was employed during superior conjunction of MM'71. During this period it was possible to obtain ranging data, a measurement not possible with either of the receivers in their standard or third-order loop configuration.

I. Introduction

Tracking spacecraft with high doppler rates and low signal levels can cause receiver lock to be difficult or impossible to maintain. A solution to this problem is the use of a programmed oscillator (PO) to subtract the predicted doppler from the received signal. In such a configuration, the voltage-controlled oscillator (VCO) is only required to track the error between the calculated and actual doppler. When the doppler is predicted accurately, the VCO will not be required to track doppler rates or accelerations. Ideally, with such a system the VCO will always be operating at its rest frequency. The actual system resulted in the VCO operating between zero and 10 Hz from rest, while the conventional system without tracking assistance operated as high as 250 Hz from rest frequency. Large doppler accelerations (which often broke lock in the conventional system) were removed from the assisted receiver, thereby allowing a far more reliable lock when operating near the signal threshold.

II. System Description

The DSIF Block III receiver (Fig. 1) obtains its first local oscillator signal (S-band) by multiplying the VCO frequency by 96. When a doppler rate is present, the

VCO must move from its rest (center) frequency to provide the proper local oscillator (LO) frequency. By placing a mixer immediately following the VCO and subtracting the predicted doppler generated by a PO, the VCO will only be required to move from its rest frequency an amount ϵ (Fig. 1) equal to the difference between the actual and calculated doppler. To implement an assistor, a problem arises because the doppler frequency varies from zero to about 250 Hz. When the doppler is very small, it is extremely difficult to separate the VCO frequency from the desired VCO plus doppler frequency. The VCO leakage into the output must be at least 100 dB below the desired output to keep spurious phase modulation of the S-band LO less than one milliradian. The final solution utilized a down-up converter that reduced the undesired outputs to a negligible amount.

The Block IV receivers will contain a programmable synthesizer, which may be interfaced to a computer to form a PO. It is therefore unnecessary to implement any additional hardware for the Block IV receivers to obtain synchronous assist.

III. Electrical Description

As shown in Fig. 2, the VCO output (approximately 23.4 MHz) is first mixed with 18.4 MHz from a synthesizer referenced to the station frequency standard. The resultant 5 MHz is filtered in a six-section minimum-loss filter. This filter and the mixer attenuate the VCO and synthesizer signals about 90 dB below the 5-MHz output. The output from the PO contains the predicted doppler with a frequency bias of 18.4 MHz that mixes directly with the 5 MHz generated by the initial mixing of the VCO, thereby regenerating the 23.4-MHz VCO frequency. The second mixer provides an additional 30 dB of attenuation to any remaining VCO signal present on the 5-MHz signal, resulting in an overall attenuation of 120 dB from the VCO output. An auxiliary output is also provided for open-loop tracking by mixing the 5-MHz station reference with the 18.4 MHz plus doppler from the PO. Since these frequencies are nearly the same as in the main output, modules B and C are identical.

IV. Mechanical Considerations

In all the modules care must be taken to ensure good shielding between mixer inputs and output, filter sections, and power supply decoupling circuitry. Semirigid coax was employed throughout. Good coax is especially important between module A and module B in order to prevent the 5-MHz station reference from leaking in and causing undesired phase modulation. Well-shielded coax should be employed between this system and the peripherals (station standard, synthesizer, receiver VCO, and the PO) if 100 dB isolation is to be maintained.

V. Conclusion

The tracking assistor system was constructed and tested with Mariner Mars 1971 (MM'71) during superior conjunction. Ranging data were obtained during periods when it was impossible to get satisfactory data with any other available system.

The tracking assistor could be substantially simplified and the isolation requirements reduced if a VCO frequency several MHz from the desired output frequency were employed. The only isolation required in the system shown in Fig. 3 is between the two 30-MHz signals, while the present assistor requires high isolation in four main signal paths. The simplified assistor would require only two identical mixer modules, and the new PO bias frequency could easily be generated by the PO program.

Reference

1. Emerson, R. F., "Programmed Oscillator Software Development for High Doppler Rate Orbiting spacecraft," in *The Deep Space Network Progress Report,* Technical Report 32-1526, Vol. XIII, pp. 48–53, Jet Propulsion Laboratory, Pasadena, Calif., Feb. 15, 1973.

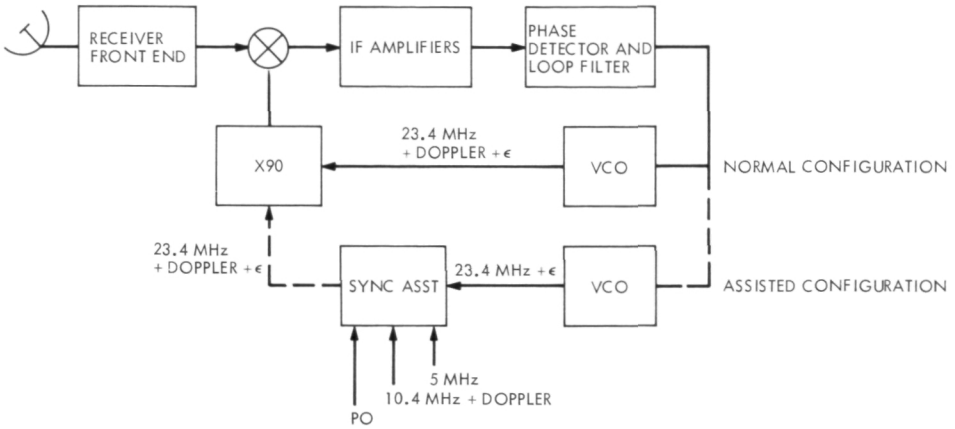

Fig. 1. Configuration modification of DSN receiver

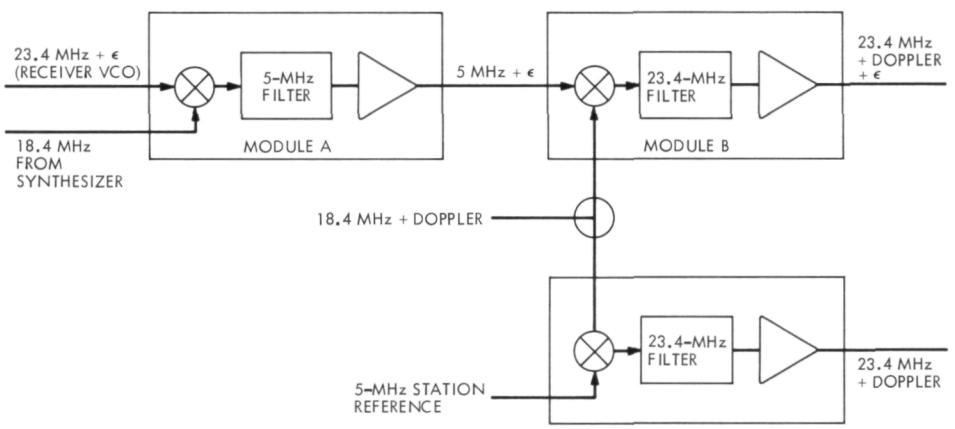

Fig. 2. Tracking assistor

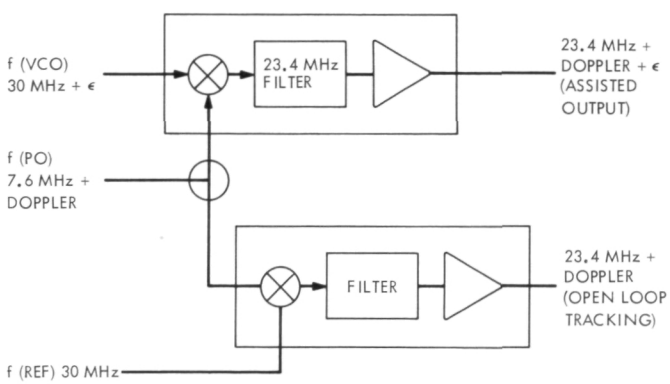

Fig. 3. Simplified assistor configuration

X-Band Filter

R. L. Leu
R.F. Systems Development Section

The need for additional filtering in the 400-kW S-band transmitter was established during compatibility testing between the 400-kW transmitter and the X-band traveling-wave maser receiver. The tests showed that ranging modulation on the S-band carrier resulted in side bands on the fourth harmonic (fourth harmonic is in X-band frequency range) that were approximately −145 dBm and in the passband of the X-band receiver.

I. Introduction

The need for additional filtering in the 400-kW S-band transmitter was established during compatibility testing between the 400-kW transmitter and the X-band traveling-wave maser (TWM) receiver. The tests showed that ranging modulation on the S-band carrier resulted in side bands on the fourth harmonic (fourth harmonic is in X-band frequency range) that were approximately −145 dBm and in the passband of the X-band receiver.

In order to eliminate interference from the S-band transmitter in the X-band receiver downlink for Mariner Venus/Mercury 1973 (MVM'73), a minimum of 30-dB attenuation is required for the fourth harmonic of the S-band uplink. To provide a safety margin the specification was written for a multimode 40-dB fourth harmonic filter. The basic specifications are given in Table 1.

Since this filter will be used in conjunction with the existing harmonic filter (described in Ref. 1), a rejection-type filter which is simpler for multimode filtering was designed. Also, the cooling requirements are minimal, as the power dissipation within the filter is a result of the passband insertion loss.

II. Summary

Varian Associates was awarded a contract to design, develop, fabricate, and test a filter capable of operation at

500-kW CW power in the 2.10- to 2.12-GHz fundamental frequency range. This filter was to provide in excess of 40-dB attenuation in the X-band (fourth harmonic) frequency range. Low-power tests show that the filter attenuation is greater than 45 dB (Figs. 1, 2, and 3). The filter is installed and operating at 400 kW with no degradation to the S-band system. Tests will be conducted to determine if the fourth harmonic interference has been eliminated in the X-band receiver.

III. Design

An important consideration in the design of the filter relates to the possible modes of propagation at the reject band frequencies. In the WR-430 waveguide, there are 29 possible modes of propagation at the fourth harmonic of the 2.10- to 2.12-GHz fundamental frequency range.

From a practical standpoint it would be extremely difficult to design a filter that would reject equally well 29 possible modes of propagation. However, at the 500-kW power level, it is not necessary to utilize a full-sized waveguide. Thus, it is possible to reduce waveguide dimensions in such a way as to greatly reduce the number of possible modes of propagation. For example, if the waveguide height (b dimensions) is reduced sufficiently, all TE_{mn} and TM_{mn} modes having $n > 0$ are eliminated. This is accomplished by making the TE_{01} mode cutoff frequency just above the fourth harmonic reject band frequency range, say, 8.50 GHz. To accomplish this it is necessary to reduce the b dimension. When this is done, the only modes that can propagate at the fourth harmonic frequency range are the TE_{10}, TE_{20}, TE_{30}, TE_{40}, TE_{50}, and TE_{60} modes.

The remaining six possible modes of propagation can be reduced to four by reducing the waveguide width from 10.9 to 8.8 cm (4.3 to 3.45 in.). The fundamental frequency band will still propagate efficiently since this is essentially a WR-340 waveguide. Thus, only the TE_{10}, TE_{20}, TE_{30}, and TE_{40} modes can exist at the fourth harmonic frequency range if a primary waveguide having cross-sectional dimensions of 8.8 by 1.75 cm (3.45 by 0.69 in.) is chosen.

It is necessary to consider the power-handling capability of this reduced-size waveguide. The theoretical breakdown power of a rectangular waveguide in terms of waveguide dimensions, frequency, and field strength can be written as

$$P = 1.33 \times 10^{-3}\, ab\, (\lambda/\lambda_g)\, E_{\text{rms}}^2$$

where

a and b = waveguide dimensions

λ = free space wavelength

λ_g = guide wavelength

E_{rms} = breakdown electric field strength

The practical breakdown power level for 8.8×1.75-cm (3.45×0.69-in.) cross-section waveguide taking into account all the derating factors is

$$P = 4.63\left(\frac{1}{2.10}\right)\left(\frac{1}{1.7}\right)\left(\frac{1}{1.25}\right)(0.73) = 445\,\text{kW}$$

This value is obviously unsatisfactory since the filter has to handle 500 kW.

However, this problem was circumvented by going to a configuration of two reduced-dimension waveguides in parallel. This is accomplished by placing a septum plate parallel to the broadwalls so that the waveguide dimensions on each side of the septum plate are 8.8×1.75 cm (3.45×0.69 in.).

Since there was an adequate safety factor in power-handling capability, the height of the waveguides on either side of the septum was reduced to 1.54 cm (0.605 in.) to improve coupling to the secondary waveguides. Secondary stubs having dimensions of 0.79×1.81 cm (0.312×0.711 in.) were chosen. Taking this into account in addition to the height reduction yields a calculated power handling capability of

$$P = 2\,(445)\left(\frac{0.605}{0.690}\right)\left(\frac{2.10}{2.54}\right) = 645\,\text{kW}$$

which is a 29% safety factor. Past experience has shown that these calculations are quite conservative so that this design was considered reasonable. The filter utilizes 56 secondary stubs on each side arranged in a four-across array spaced at 2.83 cm (1.113 in.), which is 3/4 guide wavelength for the TE_{10} and TE_{20} modes at the reject band frequency range. The short circuits for the stubs are adjustable and are locked mechanically in place after adjustment.

IV. Plans

In the next reporting period, tests will be conducted to determine the overall performance with the X-band TWM receiver.

Reference

1. Leu, R. L., "400-kW Harmonic Filter," in *The Deep Space Network Progress Report*, Technical Report 32-1526, Vol. VII, pp. 131–135. Jet Propulsion Laboratory, Pasadena, Calif., Feb. 15, 1972.

Table 1. X-band filter specifications

Passband:	
Frequency range	2.100–2.120 GHz
Insertion loss across frequency range	0.05 dB maximum
Input VSWR across frequency range	1.05:1 maximum
Power capacity	500 kW CW minimum
Stopband (fourth harmonic):	
Frequency range	8.400–8.480 GHz
Attenuation across frequency range (all modes)	40 dB minimum
Power level	1 W
Noise generation	Arcing, corona, breakdown, and other noise generating phenomena, excluding thermal noise, shall not exceed −180 dBm/Hz in frequency range 2.270–2.300 and 8.40–8.50 GHz

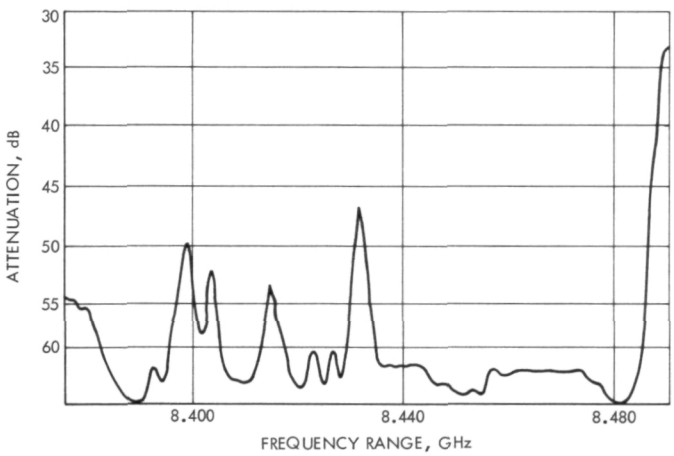

Fig. 1. Attenuation vs frequency TE_{20} mode

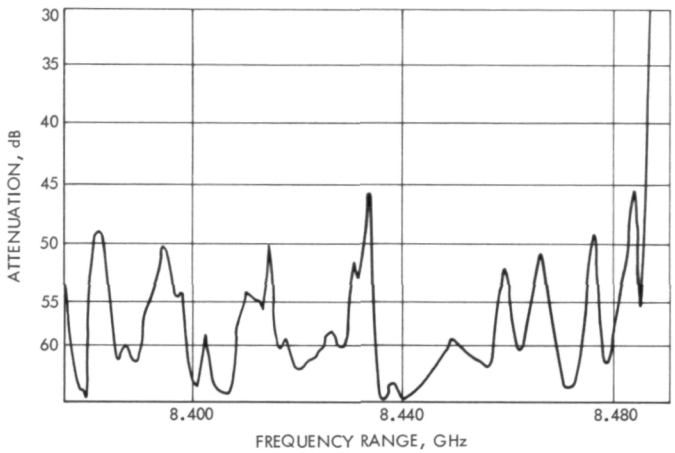

Fig. 2. Attenuation vs frequency TE_{10} mode

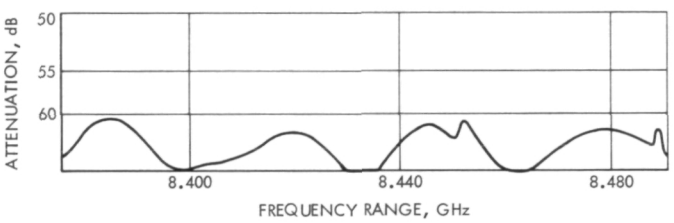

Fig. 3. Attenuation vs frequency TE_{01} mode

X-Band 250-kW Klystron

R. H. Smith
R.F. Systems Development Section

An X-band radar with an output of 400 kW is needed for future spacecraft mission planning. It will be used for planetary ranging of Saturn's rings, Mercury, Mars, the Jovian moons, and asteroids and to prepare for future spacecraft X-band uplink. To obtain this power level, two 250-kW klystrons will be combined for an output of 400 kW. The first 250-kW klystron has been tested by the contractor. Tests will shortly be conducted at the Goldstone High-Power Test Facility to determine the design of components for the 400-kW system.

I. Introduction

There is a need for improved (better-resolution) planetary radar mapping of Saturn's rings, Mercury, Mars, the Jovian moons, and asteroids. To fulfill this need an X-band radar is being developed. An X-band transmitter is being developed to deliver 400 kW of RF power at 8495 MHz. This transmitter will be used to demonstrate X-band operational capability for future spacecraft X-band uplink. The wider bandwidth at X-band allows improved ranging and altitude resolution. The transmitter power level is being produced by combining the output of two klystrons to produce an output power of 400 kW.

The first klystron has been tested by the contractor. An output power of 250 kW was achieved with an overall efficiency of 42% and, at 200 kW, an efficiency of 39%. This report covers the initial development stages of a 250-kW X-band klystron.

II. Description and Development

The klystron is a five-cavity beam modulated tube. It is being developed by Varian Associates of Palo Alto, California. Table 1 lists the requirements for the klystron performance. The output of each tube will be 250 kW, at a maximum voltage of 55 kV, operating at 8495 $\pm$25 MHz and a minimum saturated gain of 47 dB. The 50-MHz bandpass is required for the ranging modulation and to demonstrate operational capability of a klystron at this frequency with a 50-MHz bandpass that could be used at X-band DSN frequency.

III. Test Results

Tests were conducted on the first klystron at the contractor's facility. Table 2 lists the test results for 250-kW output saturated power. Table 3 lists the test results for

200-kW output at saturated power. At 53 kV the output power of 250 kW was achieved with a gain of 47 dB and an efficiency of 42%. At 50 kV, 200 kW was achieved with a gain of 46 dB and an efficiency of 39%. Figure 1 shows a group of output power curves vs frequency for varying beam voltages and constant drive. Figure 2 is a group of saturated power output curves vs beam voltage. The klystron was phase-modulated for 100% carrier suppression from 500 kHz to 1 MHz at 250- and 200-kW power levels with a body current increase of approximately 4 mA. Some other types of klystrons, when phase-modulated, had a 50% increase in body current. This increased body current exceeds the maximum limit (power dissipation in the klystron body).

IV. Future Plans

Three more klystrons are to be made and tested. The output power of two klystrons will be combined to produce an output power of 400 kW. Waveguide components will be tested at this level, the klystrons will be mounted in a cone, and the cone will be placed on the 64-m-diam antenna. Radar mapping of Saturn's rings and other experiments will be demonstrated.

Table 1. Klystron requirements

RF output power	250 kW CW
Operating voltage	55 kV maximum
Input frequency	8495
Bandwidth	±25 MHz at −1 dB Po
Efficiency at saturation	40% minimum
Saturated gain	47 dB minimum at 250 kW
Mounting	Any position
Coolant	Distilled water
Maximum VSWR	1.2:1

Table 2. Klystron performance (250 kW)

Frequency	8495 MHz
Beam voltage	53 kV
Beam current	11.2 A
Power output	250 kW
Gain	47 dB
Efficiency	42%
RF drive	5 W
Body current	25 mA
Bandwidth (−1 dB)	56 MHz

Table 3. Klystron performance (200 kW)

Frequency	8495 MHz
Beam voltage	50 kV
Beam current	10.3 A
Power output	200 kW
Gain	46 dB
Efficiency	39%
RF drive	5 W
Body current	25 mA
Bandwidth (−1 dB)	54 MHz

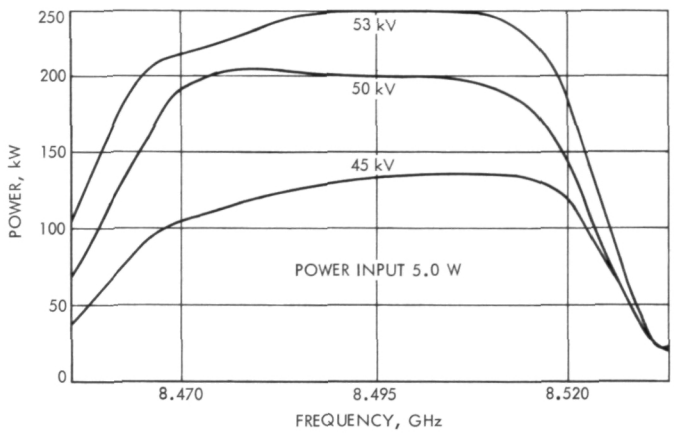

Fig. 1. Power output vs beam voltage

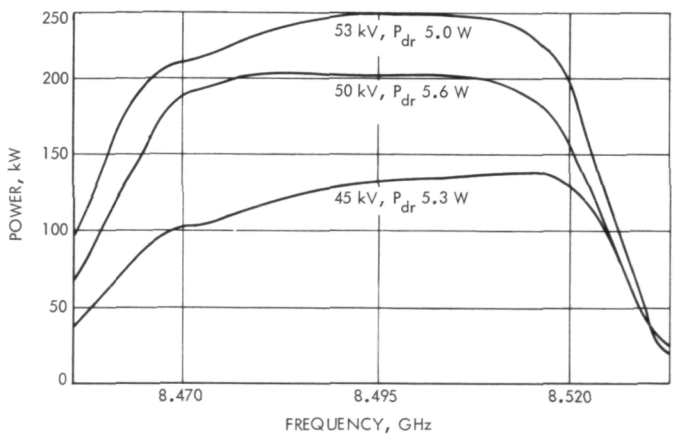

Fig. 2. Power output saturated vs beam voltage

X-Band Hybrid Combiner

R. W. Hartop
R.F. Systems Development Section

A four-port hybrid junction is being developed to combine the outputs of two 200-kW klystron amplifiers to achieve a 400-kW radiated signal at X-band. Progress to date in developing the hybrid under contract is reported.

I. Introduction

To achieve a 400- to 500-kW radiated signal at X-band for spacecraft uplink development and planetary radar applications, two 250-kW klystron tubes will be combined in phase. This technique avoids the costly and time-consuming development of a single klystron with the desired power output, but requires the development of a waveguide combiner that can handle the extreme power densities involved with high isolation, low voltage standing wave ratio (VSWR), and good balance.

Because of limitations on the dc power available, the expected maximum power level that the hybrid will experience will be 400 kW at 8495 MHz. System considerations require that the working isolation be at least 30 db to protect each tube window from coupled power from the other tube. Allowing for impedance mismatches on the antenna feed side of the hybrid, which effectively lower the isolation, a specification of 36 db was placed on hybrid isolation, with a design goal of 40 db.

II. Hybrid Development

As a result of a competitive procurement, Varian Associates was awarded a contract to develop the hybrid combiner. Delivery of two units is scheduled during the next reporting period. At the time of this report, development is essentially complete and some preliminary tests have been run on the first unit before hydrogen furnace brazing of the parts. The results are shown in Table 1.

The unbrazed hybrid made of oxygen-free copper is shown in Fig. 1. After brazing, the ends will be machined

to permit attachment of the waveguide flanges. The threaded boss in the center of the unit will provide for water cooling under power.

Figure 2 shows the top plate removed, revealing the water-cooling passages. The hybrid is symmetrical top to bottom as well as left to right, with another identical set of water passages underneath.

The waveguide passages and the coupling iris can be seen in Fig. 3, where the top wall has been removed. The two tubes in the center of the unit are posts that electrically determine the exact size of the coupling iris. They are hollow to permit water to flow through them.

III. Future Activities

During the next reporting period, final low-power tests will be performed on the first unit and the water passages will be vacuum tested to ensure their integrity. Preparations will begin for first stage high-power testing of the delivered unit using a single transmitter and multiple loads.

Table 1. Preliminary test results on hybrid No. 1 before brazing

Parameter	Frequency, MHz		
	8460	8495	8530
Isolation	$>$ 40 dB	$>$ 40 dB	40 dB
VSWR	1.015	1.015	1.03
Balance	$\pm$0.20 dB	$\pm$0.15 dB	$\pm$0.10 dB

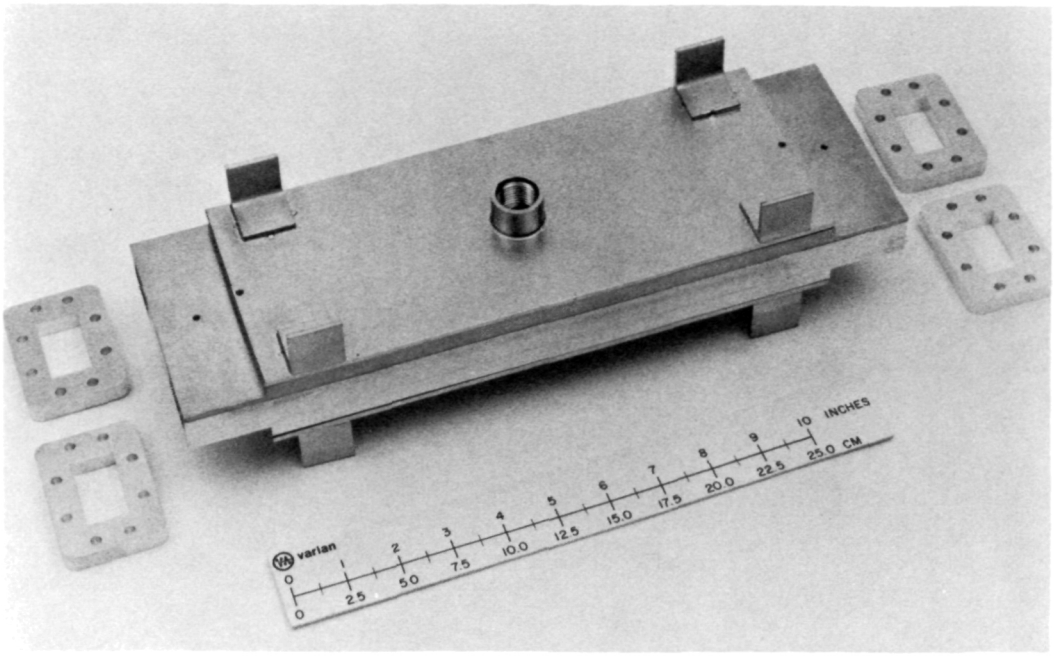

Fig. 1. Hybrid before brazing

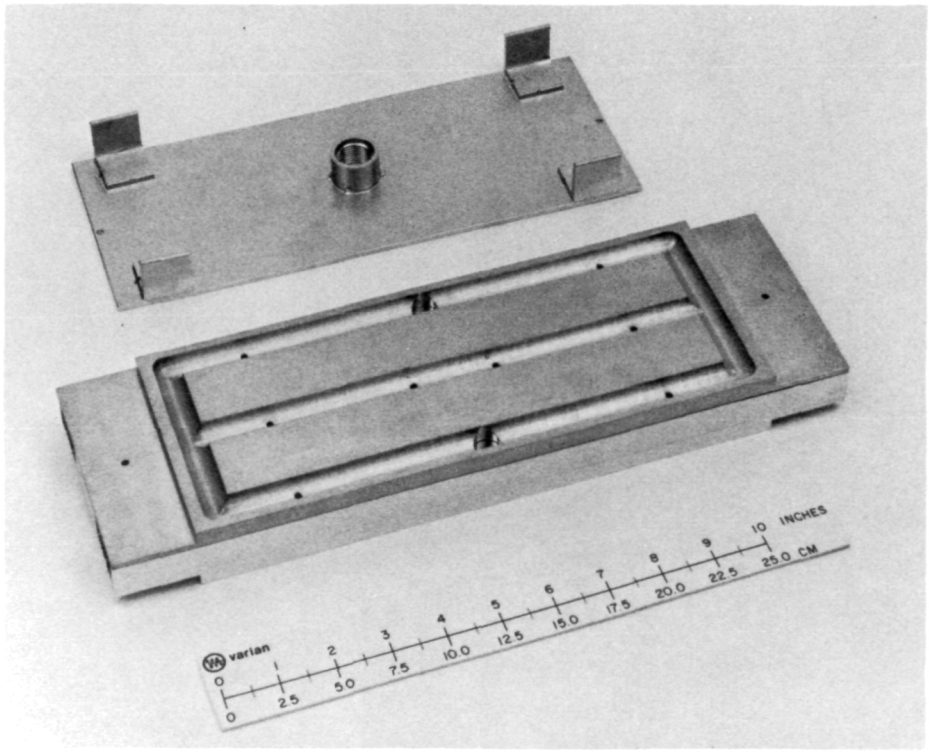

Fig. 2. Hybrid with top plate removed

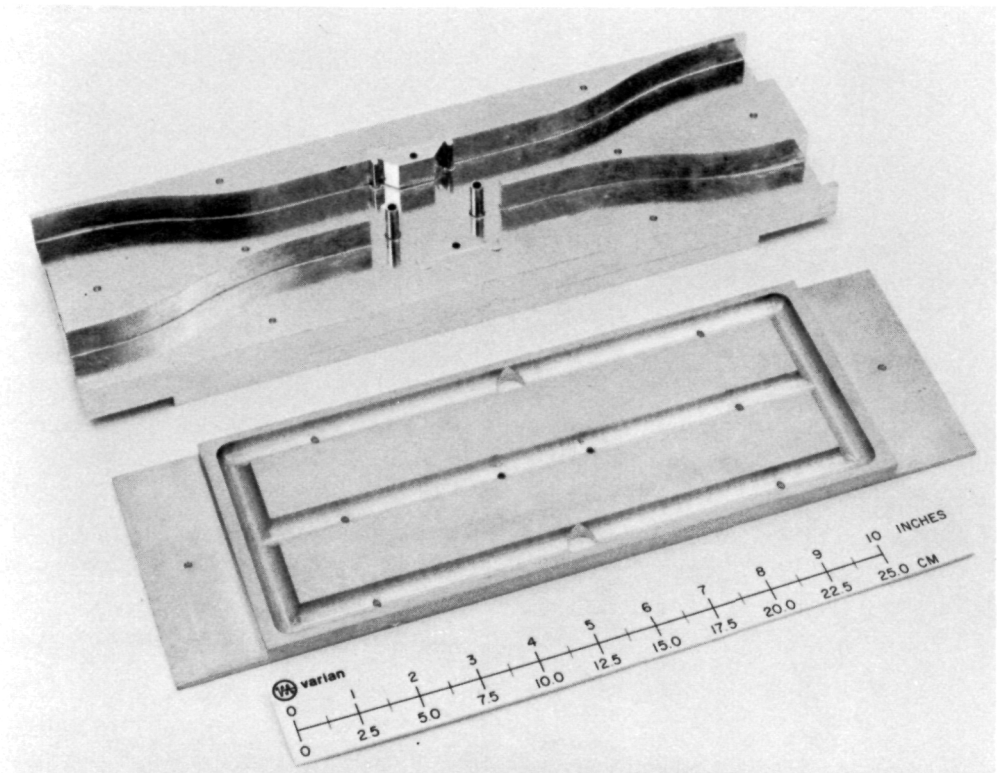

Fig. 3. Hybrid with top wall removed

An Analysis of Long Baseline Radio Interferometry, Part III

J. B. Thomas
Tracking and Orbit Determination Section

This article is the third installment in a series of articles presenting an analysis of long baseline radio interferometry. The practical data reduction steps that are required to extract fringe amplitude, fringe phase, and delay are described. These data reduction steps include bit stream manipulations, fringe stopping, Fourier analysis, and phase tracking. In addition, a detailed analysis is presented for the two-channel approach to bandwidth synthesis, a technique used for making accurate delay measurements.

I. Introduction

Two previous articles (Refs. 1, 2) were the first of a series of technical reports presenting an analysis of long baseline radio interferometry. In those reports, the cross-correlation function for a natural radio source was expressed in terms of fringe visibility, system temperatures, fringe phase and delay. In addition, an approximate mathematical model for the geometric delay (Ref. 1) was outlined. This report describes the practical steps in data reduction that are required to extract fringe amplitude, fringe phase, and delay. Fringe amplitude measurements can yield valuable information concerning source structure (Ref. 1). Delay and fringe phase measurements can lead to precise determination of geophysical parameters (polar motion, UT1, baseline vectors) and radio source locations. The data reduction steps described in this report include bit stream manipulations, fringe stopping, Fourier analysis, and phase tracking. In addition, the last section outlines two-channel bandwidth synthesis, a technique used for making accurate delay measurements.

II. Cross-Correlated Function

In long baseline interferometry measurements, the radio signal produced by a distant source is recorded simultaneously at two widely spaced antennas. These recorded signals are then cross-correlated to determine correlated amplitude as well as delay and fringe phase. In the present radio interferometry data reduction system, the first step in cross-correlation involves the multiplication of the voltage signals observed at the two antennas. One signal is offset in time to compensate for the difference in wave front arrival times.

Previous reports (Refs. 1, 2) derive the ensemble average of the voltage product for a natural source. This average voltage product, called the cross-correlation function (CCF), is given for analog signals by the expression (Ref. 2):

$$r_a(t, \tau_m) \equiv \frac{\langle V_1(t)\, V_2(t+\tau_m)\rangle}{\sqrt{\langle V_1^2\rangle \langle V_2^2\rangle}} = \gamma_v \sqrt{\frac{T_{R_1} T_{R_2}}{T_{S_1} T_{S_2}}} \frac{W_D}{W_B} \frac{\sin \pi W_D \Delta\tau_r}{W_D \Delta\tau_r} \cos \phi_f \tag{1}$$

where fringe phase is given by

$$\phi_f = (\omega_2 - \omega_1)\, t + \omega_2 \tau_m + \omega_a (\tau_g + \tau_I + \tau_c + \tau_t - \tau_m) + I_a + R_a + C_a$$

and where the "time delay error" is given by

$$\Delta\tau_r = \tau_g + \tau_I + \tau_c + \tau_t - \tau_m$$

In this expression,

$V_j(t)$ = voltage recorded at time t at station j, $j = 1, 2$

γ_v = fringe visibility

T_{R_j} = radio source temperature at station j

T_{S_j} = system noise temperature at station j

W_B = instantaneous recorded bandwidth

W_D = bandpass overlap after doppler shifting

ω_j = total effective mixing frequency at station j, $j = 1, 2$

ω_a = effective interferometer bandpass center after doppler shifting

I_a = total instrumental phase shift including mixing signal drifts

R_a = brightness transform phase shift

τ_m = model time delay, computed

τ_g = geometric time delay, actual

τ_I = total instrumental delay including clock synchronization error

τ_t = differential troposphere time delay

τ_c = differential charged-particle time delay at frequency ω_a

C_a = differential charged-particle phase shift at frequency ω_a

Note that transmission media effects have been included in the total delay and phase for completeness. This expression assumes a rectangular system bandpass with a linear phase-frequency response at each station. The model delay τ_m contains best estimates for the geometric and instrumental delays. In some cases, a troposphere model might be included in τ_m. In addition to these terms, the model delay always contains a time-independent offset τ_V which can be adjusted to "fine-tune" the alignment of the two bit streams.

The present JPL interferometry system is not analog but digital and records only the sign of the voltage signals. For such infinitely clipped signals, the cross-correlation function becomes (Refs. 2, 3):

$$r_a(t, \tau_m) \equiv \langle \tilde{V}_1(t)\, \tilde{V}_2(t+\tau_m)\rangle = \frac{2}{\pi} \sin^{-1} r_a(t, \tau_m) \tag{2}$$

where

$$\tilde{V}_j(t) = +1 \text{ if } V_j(t) > 0$$

$$\tilde{V}_j(t) = -1 \text{ if } V_j(t) < 0$$

In this report, we will consider only the weak source case ($r_a << 1$) for which

$$r_a(t, \tau_m) = \frac{2}{\pi} r_a(t, \tau_m) = A_f \cos \phi_f \tag{3}$$

where

$$A_f = \frac{2}{\pi} \gamma_v \sqrt{\frac{T_{R_1} T_{R_2}}{T_{S_1} T_{S_2}}} \frac{W_D}{W_B} \frac{\sin \pi W_D \Delta\tau_r}{\pi W_D \Delta\tau_r}$$

The cross-correlation function describes the average behavior of the voltage product. As indicated by Eq. (3), the cross-correlation function is a product of a sinusoidal factor $\cos \phi_f$ and an amplitude factor A_f. The phase of the sinusoidal factor describes the average phase behavior of the total system. The amplitude factor is a measure of the accuracy of time domain alignment and peaks if the model delay τ_m is sufficiently close to the actual total group delay ($W_D \Delta\tau_r << 1$). In addition, the amplitude depends on the source's correlated flux and system noise.

The next section will describe how, on the basis of this expected average behavior, the actual voltage products

are formed and manipulated so that amplitude, phase, and delay can eventually be extracted. Fringe amplitude measurements can yield valuable information concerning source structure (Ref. 1). Delay and fringe phase measurements can lead to precise determination of Earth orientation parameters, baseline vectors, and radio source locations.

III. Bit Stream Manipulations

The voltage signals at each antenna are sampled in time at the Nyquist rate $2W_B$, where W_B is the instantaneous recorded bandwidth. The volume of data generated by typical sampling rates (10^4–10^6 bits/sec) is too large to be manageable without compression. In addition, the noise on a single sample point on the cross-correlation function is generally too large for a single point to be informative when taken alone. Consequently, data compression techniques are employed in order to both reduce the volume of data and to collect statistics. The compressed data reveal the underlying characteristics of the cross-correlation function that are totally masked by noise over a few sample points. Typically, one data point in the compressed data (stopped fringes) contains 10^4–10^6 original sample points. Two stages are involved in the data compression procedure: presums and fringe stopping. The basic features of the initial steps in data reduction (signal multiplication and presums) will now be outlined. Fringe stopping is discussed in Section IV.

In a digital recording system, a positive voltage obtained at a given sample point is represented on tape by a bit with value 1 while a negative voltage is a 0 bit. Examples of two such bit streams, one for each antenna, are shown in Fig. 1. As indicated earlier, the time spacing between adjacent bits is $1/(2W_B)$ where W_B is the instantaneous bandwidth. After being read into a computer, bit stream 2 is offset relative to bit stream 1 by a model delay τ_m which partially compensates for the time delay of signal 2. The model delay is typically a sum of a time-varying geometric delay, a constant instrumental delay and an adjustable offset (τ_v). Because the time scale is quantized in bits, the total time offset τ_m can at best be rounded to the nearest bit. For typical experiments the quantized time offset ($\tilde{\tau}_m$) is constant over many bits in time before the model delay τ_m changes by one bit ($\dot{\tau}_m \lesssim 2\mu$bits/bit). Consequently, many bits require the same quantized time offset and may be aligned simultaneously by one shift operation. The bit streams are then multiplied together by means of an EXCLUSIVE OR, a digital logic operation that can operate simultaneously on all bits in a word of data (32 bits in an IBM 360). The fact that many bits may be shifted and multiplied simultaneously greatly reduces computation time. In the EXCLUSIVE OR operation the following rules are satisfied:

$$1*0 = 0 \qquad 1*1 = 1$$

$$0*1 = 0 \qquad 0*0 = 1$$

One can readily show that these relations produce a product with the proper sign when decoded under the bit conventions defined above. An example of bit multiplication for 8 bits is shown in Fig. 1 along with the corresponding sign interpretation for the process.

Since the time offset must be quantized and rounded to the nearest bit, the two bit streams can not be perfectly aligned for all bits. This roundoff misalignment in digital systems smears the "analog" delay curve. The resultant loss in peak amplitude is easily calculated by averaging the expected delay curve over ± 0.5 bits about the principal maximum. In this manner, one can readily show that a loss of peak amplitude of 3.4% results for an "ideal" $\sin(x)/x$ curve. In subsequent work, this slight roundoff smearing effect will be neglected.

After multiplication of the two bit streams, one has obtained over a limited time range a function that on the average is given by the cross-correlation function in Eq. (3). If the frequency $\dot{\phi}_f$ is small enough ($\approx 2 - 100$ Hz) and the recording rate is large ($\approx 10^4$ to 10^6 bits/sec) the CCF will be sampled many times (10^2 to 10^5) during one cycle of fringe phase as schematically indicated in Fig. 2. (The magnitude of the fringe frequency $\dot{\phi}_f$ may be greatly reduced by proper selection of mixing frequencies, ω_1 and ω_2, during the measurement.) Without loss of information concerning the CCF, one can sum adjacent sample points as long as the sum time interval is small (~ 0.1 cycle) compared to one cycle of fringe phase. These local sums are called presums. A simple example is given for 8 bits in Fig. 1. As indicated by the ostensibly random bits in this example, the systematic trends of the CCF are usually not evident over only a few bits due to poor SNR.

Because of the 0.1 cycle constraint, the presums for the present 48 kbits/s system cover time intervals ranging from one word (32 bits) to 50 words. Since the presums are carried over only a fraction of a cycle, each presum can be regarded as the value of the CCF at the middle of the presum interval multiplied by the number of bits in the presum. Thus, after signal multiplication and presum, the resulting CCF is identical to the original CCF (Eq. 3),

except for an amplitude increase, and is sampled less frequently. The presums $U_p(t, \tau_m)$ can formally be represented as

$$U_p(t, \tau_m) = \sum_{t' = t - \Delta t_p/2}^{t' = t + \Delta t_p/2} \tilde{V}_1(t')\, \tilde{V}_2(t' + \tilde{\tau}_m) \qquad (4)$$

where $\tilde{V}_j$ denotes infinitely clipped voltage and Δt_p is the presum time interval. All bit products within this time interval are included in the sum. The expected behavior of the presums is given by the expression

$$U_p(t, \tau_m) = N_t A_f \cos \phi_f + \text{noise} \qquad (5)$$

where N_t is the number of bits in the presum given by

$$N_t = 2 W_B \Delta t_p$$

Generally, the noise on the presums is too large for an individual presum to be useful. Therefore, the data must be compressed even more to reveal the cross-correlation function as indicated in the next section.

IV. Fringe Stopping

After obtaining the presums, the data can be compressed more by a process known as fringe stopping or phase counter-rotation. The first step in this process multiplies the presums by the cosine (or sine) of a model phase. (In the present system, the fringes are stopped with both the sine and cosine functions so that two statistically independent fringe compressions are obtained.) The model phase is computed from the expression

$$\phi_m(t) = -\varepsilon t + (\omega_2' - \omega_1')\, t + \omega_2' \tau_m \qquad (6)$$

where ω_1' and ω_2' are best estimates for the mixing frequencies ω_1, and ω_2 and τ_m is the model delay discussed in Section II. The frequency ε is a small analytical offset ($\approx 0.1 - 0.2$ Hz) of known sign and magnitude that will be discussed below. When the presums are multiplied by the cosine of the model phase, one obtains two terms

$$\begin{aligned} U_p(t, \tau_m) \cos \phi_m &= N_t A_f \cos \phi_f \cos \phi_m + \text{noise} \\ &= \frac{1}{2} N_t A_f \left[\cos(\phi_f - \phi_m) + \cos(\phi_f + \phi_m)\right] \\ &\quad + \text{noise} \end{aligned} \qquad (7)$$

The first term is of low frequency if the model phase closely approximates the actual phase ϕ_f. As indicated by Eqs. (1) and (6), this phase difference (stopped phase) is given by

$$\phi_f - \phi_m = \varepsilon t + \Delta\omega_a t + \omega_a \Delta\tau_r' + I_a + R_a + C_a \qquad (8)$$

where

$$\Delta\omega_a \equiv \omega_2 - \omega_1 - \omega_2' + \omega_1'$$

$$\Delta\tau_r' \equiv \tau_g + \tau_I + \tau_t - \tau_m$$

We have assumed the $(\omega_2 - \omega_2')\, \tau_m$ term is negligibly small, which is usually the case for typical frequency calibration accuracies ($\Delta f/f \approx 10^{-12}$).

Typically, residual frequencies in $\dot{\phi}_f - \dot{\phi}_m$ due to model errors in τ_m, ω_1' and ω_2' are less than 0.2 Hz at S-band. The second term in Eq. (7) has a frequency roughly equal to $2\dot{\phi}_f$ which typically falls in the range 5 to 200 Hz. Thus, a sum over time intervals that are small (~ 0.1 cycle) compared to the cycle time of $\phi_f - \phi_m$ will increase the amplitude of the first term but will leave it unmodified otherwise. However, such a sum will generally average the second term over enough cycles (~ 5) to make it negligibly small. These sum intervals are typically 0.1 to 1.0 seconds long. Fringe stopping can be formally represented as the sum

$$U_S(t, \tau_m) \equiv \sum_{t' = t - \Delta t_s/2}^{t' = t + \Delta t_s/2} U_p(t', \tau_m) \cos \phi_m(t') \qquad (9)$$

where Δt_s is the sum interval length. All presums within this interval are included in the sum. The expected form for these "stopped fringes" is given by the expression

$$U_S(t, \tau_m) = \frac{1}{2} N_S A_f \cos(\phi_f - \phi_m) + \text{noise} \qquad (10)$$

where $N_S = 2 W_B \Delta t_s$ is the number of bits in the interval Δt_s.

In the present system, the stopped fringes are divided by the "known" factor

$$K_N = \frac{1}{\pi} \frac{W_D}{W_B} N_s \qquad (11)$$

so that the maximum fringe amplitude depends only on correlated flux and noise temperatures. The normalized stopped fringes are computed by the expression

$$U_N(t, \tau_m) = U_s(t, \tau_m)/K_N \qquad (12)$$

The expected behavior of the normalized fringes is given by the expression

$$U_N(t, \tau_m) = A_N \cos(\phi_f - \phi_m) + \text{noise} \tag{13}$$

where

$$A_N = \gamma_v \sqrt{\frac{T_{R_1} T_{R_2}}{T_{S_1} T_{S_2}}} \frac{\sin \pi W_D \Delta\tau_r}{\pi W_D \Delta\tau_r}$$

With this normalization, the maximum fringe amplitude is theoretically given by

$$A_N|_{\max} = \gamma_v \sqrt{\frac{T_{R_1} T_{R_2}}{T_{S_1} T_{S_2}}} \tag{14}$$

and therefore depends only on the magnitude of the "correlated flux temperatures" relative to the system noise temperatures. Thus, the stopped fringes are sampled every Δt_s seconds (0.1 to 1 sec) and possess the "stopped" fringe frequency $\dot{\phi}_f - \dot{\phi}_m$ ($\lesssim 0.2$ Hz at S-band).

The stopped fringe frequency (See Eq. 8) is a sum of two components—the analytical offset ε and the residual fringe frequency $\Delta\nu_a$

$$\dot{\phi}_f - \dot{\phi}_m = \varepsilon + \Delta\nu_a \tag{15}$$

where

$$\Delta\nu_a \equiv \Delta\omega_a + \omega_a \Delta\dot{\tau}'_r + \dot{I}_a + \dot{R}_a + \dot{C}_a$$

The residual fringe frequency $\Delta\nu_a$ is the unknown frequency due to all physical effects that remain after the model $\omega_a \dot{\tau}_m$ (contained in $\omega_a \Delta\dot{\tau}'_r$) has been subtracted. The known offset ε is a computational artifact designed to resolve the frequency sign ambiguity. The sign ambiguity is a consequence of the fact that only the magnitude of frequency can be extracted from a sinusoid. The magnitude of ε is chosen so that it is larger than the maximum expected magnitude of the residual fringe frequency $\Delta\nu_a$ including all physical effects. If ε is this large, then the sign of $\Delta\nu_a$ can be determined by noting the sense of the total output frequency $|\dot{\phi}_f - \dot{\phi}_m|$ relative to $|\varepsilon|$. For example, assume that $\varepsilon = +0.2$ Hz. If $\Delta\nu_a$ is negative in Eq. (15), then it is subtracted from ε and $|\dot{\phi}_f - \dot{\phi}_m|$ is less than ε. If $\Delta\nu_a$ is positive, then $|\dot{\phi}_f - \dot{\phi}_m|$ is larger than ε. Therefore, if $|\dot{\phi}_f - \dot{\phi}_m| = 0.25$ Hz, then $\Delta\nu_a = 0.05$ Hz. If $|\dot{\phi}_f - \dot{\phi}_m| = 0.15$ Hz, then $\Delta\nu_a = -0.05$ Hz.

The various contributions to the residual frequency $\Delta\nu_a$ may be bounded as follows. As indicated earlier, the mixing frequencies are usually known to within 20 mHz at S-band. The residual frequency due to parameter errors in the model geometric delay can be bounded by means of the maximum values (Ref. 4) of the sensitivity partials[1] which for S-band observations over intercontinental baselines ($\approx 10{,}000$ km) are given by

$$\frac{\partial \nu_g}{\partial x} \sim 0.5 \text{ mHz/m} \qquad \frac{\partial \nu_g}{\partial \theta} \sim 20 \text{ mHz/arc sec} \tag{16}$$

where x and θ symbolize length and angle parameters, respectively. For example, if source location errors are less than 5 arc sec, the residual frequency due to this error source is less than 100 mHz. The single-raypath troposphere frequency effect ($\omega_a \dot{\tau}_t$) at S-band is less than 30 mHz for elevation angles greater than 10 deg. This transmission media effect can be largely eliminated (90%) by including existing troposphere models in τ_m. Ionosphere frequency effects at S-band are generally below 5 mHz.

An example of stopped fringes obtained over a Goldstone baseline with a 48 kbits/sec recording system[2] is shown in Fig. 3 for nine delay offsets. For the narrowband recording system in this example, the *a priori* delay was accurate enough to align the two bit streams within a fraction of a bit. Variations about the *a priori* delay were produced by assigning the adjustable offset τ_V the indicated values. Note that the amplitude variation of the fringes as a function of *time offset* fairly closely approximates the $\sin(x)/x$ width (≈ 40 μs) predicted by Eq. (13). As explained in Section VI, this amplitude variation versus model delay can be used to extract the single-channel delay observable. The frequency of the fringes (≈ 0.1 Hz) in this example is due mainly to the analytical frequency offset ε.

Thus, there are three primary observables to be obtained from the single-channel stopped fringes, fringe phase, maximum amplitude, and delay. The maximum amplitude (Eq. 14) leads to a determination of correlated flux or fringe visibility which can be used to investigate source structure. Single-channel fringe phase $\phi_f - \phi_m$ can only be determined to within an additive constant ($2n\pi$). For this reason, it only yields information concerning the time-varying components of the geometric delay, transmission media phase and instrumental phase. The third single-channel observable, the delay, is a sum of all group delay effects (geometric, transmission media, instrumental, clock synchronization). For sufficiently wide recorded bandwidths, the single-channel delay observable can yield useful information concerning all of these quantities.

[1] $\nu_g = \omega_a \dot{\tau}_g$

[2] Developed by D. S. Robertson and A. H. Legg of Weapons Research Establishment, Australia.

The techniques used to extract phase, amplitude, and delay will be discussed in the next three sections.

V. Fourier Analysis

After phase counter-rotation, the stopped fringes consist of sinusoidally varying curves of unknown frequency ($\approx \varepsilon$) and amplitude. Fourier analysis can be employed to extract these unknowns whenever the stopped fringes possess a sufficiently constant frequency and amplitude over the integration interval. The factors that cause the frequency and amplitude to vary will be discussed later in this section. Assume for the moment that the stopped fringes possess fairly constant amplitude and frequency so that Fourier analysis is useful.

Because of computation speed, the Fast Fourier Transform (FFT) is used for Fourier analysis. The FFT used in the present work can be expressed as the following discrete transform.

$$a_k = \frac{1}{2N}\sum_{t=0}^{N-1} g_t \exp\left(\frac{-i\pi \ell k}{N}\right) \qquad k = 0, 1 \cdots 2N-1$$

$$= \frac{1}{2N}\sum_{t=0}^{N-1} g_t \exp\left(-2\pi i f_k t_t\right) \tag{17}$$

where

$$t_t = \ell\,\Delta t_s$$

$$f_k = \frac{k}{2T}$$

$$T = N\Delta t_s$$

In these expressions, N is the number of fringe sample points in the integration interval T. The integration interval for the present 48-kbits/s recording system is usually the time span of one tape-pair (≈ 12 min). The input points g_t are given by the stopped fringe values computed in Eq. (12).

$$g_t = U_N(t_t, \tau_m) \qquad \ell = 0, 1 \cdots N-1 \tag{18}$$

where time (t_t) is measured relative to the beginning of the integration interval. Note that the frequency values (f_k) increment in steps of $1/(2T)$. (It should be noted that the normal FFT increments frequency in steps of $1/T$ which is sometimes inconveniently large. The normal FFT subroutines will perform the transform with twice the normal sample rate if the input array is doubled by filling the last N members with zeroes).

The single frequency response of the FFT can be determined by substituting a pure sinusoid with frequency f and phase β in Eq. (17).

$$g_t = A_T \cos(2\pi f \ell\,\Delta t_s + \beta) \qquad \ell = 0, 1, \cdots N-1 \tag{19}$$

The FFT modulus for this input function is given by

$$|a_k| \approx \frac{A_T}{4}\frac{\sin[\pi(k_f - k)/2]}{\pi(k_f - k)/2} \text{ for } |k_f - k| << 2N \tag{20}$$

where $k_f = 2fT$. Note that the frequencies k and k_f are in units of $1/(2T)$. As indicated by the $\sin(x)/x$ curve in Fig. 4, the FFT modulus $|a_k|$ peaks when k equals the input frequency. Note that the main lobe is four intervals wide. The first zeroes are separated from the principal maximum by $1/T$ in frequency. For a monochromatic input, the first side lobes should be attenuated by about $2/(3\pi)$ relative to the main lobe.

The data points in Fig. 4 are the FFT of the fringes in Fig. 3 for $\tau_V = 0$. The fact that the fringe FFT drops to zero within $1/T$ and also has side lobes of the correct size indicates that, at the spectral sensitivity of the transform ($\approx 200\ \mu$Hz), only one frequency is present.

After the FFT has been calculated for a given fringe curve, the FFT modulus is digitally searched for a maximum. After the main lobe is located, peak amplitude and center frequency are estimated by interpolation between the three main-lobe points or by a least-squares fit. In the least squares fit, the single-frequency response curve is typically fit to the points in the main lobe and two side lobes with the amplitude (A_T) and frequency (f) as solve-for parameters as indicated in Fig. 4.

Up to this point, we have assumed that the stopped fringes possess a constant amplitude and frequency over the integration period. In practice, both of these quantities change in time. The amplitude slowly changes because the radio source brightness transform and the system temperatures can sometimes change with time. Generally, these amplitude changes are negligible for integration times less than 10 min. The stopped fringe frequency, however, can change considerably in 10 min due to instrumental frequency instability, geometric delay model errors, and transmission media delays. If one of these factors causes frequency drifts across the integration interval (T) that are comparable to $1/T$, the FFT will spread out so that the FFT peak amplitude will underestimate the actual fringe amplitude. Expressed in terms

of phase, large phase deviations (~ 0.1 cycle) from linear behavior will cause loss of coherence in integration and therefore will diminish the peak response. If the frequency drifts are large compared to $1/T$, the FFT peak amplitude for weak sources can be so drastically reduced that the FFT signal is lost in the noise.

Rapid changes in frequency can sometimes be caused by rapidly changing troposphere delays at low elevation angles. This effect can generally be adequately removed by including an accurate troposphere correction in the model delay τ_m.

The magnitude of geometric frequency drifts can be bounded by means of the maximum values of the appropriate second partials, which for intercontinental observations at S-band are given by

$$\begin{aligned} \frac{\partial^2 \nu_g}{\partial x\, \partial t} &\lesssim \omega_e \left.\frac{\partial \nu_g}{\partial x}\right|_{\max} < 0.04\ \mu\text{Hz/m-sec} \\ \frac{\partial^2 \nu_g}{\partial \theta\, \partial t} &\lesssim \omega_e \left.\frac{\partial \nu_g}{\partial \theta}\right|_{\max} < 1.5\ \mu\text{Hz/(arc sec)-sec} \end{aligned} \tag{21}$$

where x, θ symbolize length and angle variables respectively and ω_e is Earth's rotation rate in radians/sec. For example, for a source error of 1 arc sec and an integration time of 100 sec, the geometric residual frequency would change by less than 0.15 mHz. Since the FFT single frequency response would be 10 mHz wide in this example, a frequency drift less than 0.15 mHz would only slightly decrease the FFT peak amplitude.

Instrumental instability can also cause frequency variations that reduce the FFT peak amplitude. Up to this point, we have only emphasized the largest component in the mixing signal, the linear term $\Delta\omega_a t$. In practice, actual mixing signals drift away from this ideal linear behavior by some amount, which has been collected in the phase term $I_a(t)$. These mixing signal drifts are usually due to frequency standard instabilities. One can easily estimate a typical phase (or frequency) drift for a given frequency standard if the stability specifications are available.

In summary, a Fourier transform of the stopped fringes serves two purposes in the present data reduction system. First, the FFT is used to detect the presence of fringes. The FFT reduces the detection problem to a simple search in the frequency domain. Secondly, once the FFT peak has been detected, the amplitude and frequency of the fringes can be estimated. These amplitude and frequency estimates are then used to initialize the phase tracking procedure, which will be described in the next section. The new estimates for amplitude and frequency produced by phase tracking are usually adopted as the final values. However, the FFT estimates for these quantities often serve as useful "quick-look" values.

VI. Phase Tracking

As indicated in the last section, FFT analysis can be used to determine the amplitude and frequency of the stopped fringes if they are "monochromatic" with constant amplitude over the integration interval. However, if nonlinear phase excursions are present, it is often desirable to extract the phase as a function of time. In addition, as we shall see, the two-channel approach to bandwidth synthesis requires phase extraction. Therefore, a technique called phase tracking was developed to extract the fringe phase. In this procedure, the time interval of interest (generally the FFT integration interval) is separated into subintervals with length Δt_ϕ (typically 1 to 100 sec). Each subinterval is fit successively by least squares with the sinusoid

$$f_s(t) = A_s \cos\left[2\pi\left(f_s t + \phi_s\right)\right] \tag{22}$$

where time t is zero at the beginning of each subinterval. With this definition, the phase ϕ_s denotes the phase at the beginning of the subinterval. In each subinterval, the amplitude (A_s), frequency (f_s), and phase (ϕ_s) are simultaneously varied in the least-squares fit. In the fit to each subinterval, the *a priori* amplitude and frequency are usually assigned the FFT values for the whole phase track period (≈ 10 min).

For the *first* interval, the *a priori* phase is determined by a least-squares search between 0–1 cycle with the amplitude and frequency fixed at the FFT values. After this initialization, a simultaneous least squares fit gives the amplitude, frequency, and phase (between 0–1 cycle) for the first interval.

For the *next and successive subintervals*, the *a priori* phase is found by adding the phase increment predicted by

$$\Delta\phi_s = f_{\text{FFT}}\, \Delta t_\phi \tag{23}$$

to the least-squares phase value for the preceding interval where f_{FFT} is the FFT frequency estimate. This projected phase estimate must be correct within about 0.2 cycle in order for the fit to succeed. (When frequency changes across the FFT integration interval are large, the frequency and phase of a given subinterval should be initialized with the least-squares frequency of the pre-

ceding subinterval provided the SNR is adequate.) After the simultaneous three-parameter fit for each subinterval, the parameter covariance errors are calculated on the basis of the actual RMS fringe residuals. Thus, the phase track output consists of the amplitude, frequency, phase, covariance errors, and RMS fringe residual for each subinterval.

The length of the subintervals should be made sufficiently small to reveal nonlinear trends in the phase. When nonlinear phase trends are present, the maximum subinterval length is defined by

$$\Delta t_\phi < \frac{\sigma_\phi}{\Delta f_s} \tag{24}$$

where σ_ϕ is the phase covariance error due to system noise, and Δf_s is the frequency change over the subinterval. That is, the phase effects of frequency drifts across a subinterval should be small compared to phase measurement precision. The minimum subinterval length is approximately equal to the time required for 0.5 cycle of fringe phase or by SNR limitations.

After the phase for each subinterval has been extracted, the phase values for the phase track period are given the proper sign by appropriately removing the analytical offset εt (see Eq. 8). The expected behavior of these corrected phase values, called residual phase $\Delta\phi_a$, is given by the expression

$$\Delta\phi_a = \Delta\omega_a t + \omega_a \Delta\tau_r' + I_a + R_a + C_a \tag{25}$$

If the delay model is sufficiently accurate and the frequency system is sufficiently stable, the residual phase will, to good approximation, vary linearly in time over the phase track interval (≈ 10 min). For this reason the residual phase values are fit by least squares with a straight line over the interval. In some cases, the fit slope, which is the "average" residual fringe frequency for the fit interval, is used as the "phase observable" for that interval. However, when large nonlinear phase excursions are present over a fit interval, the residual phase should be analyzed, since a single frequency clearly cannot describe nonlinear phase changes.

In some applications, when one source is observed more or less continuously for hours, the phase can be connected between phase track periods (in analogy with the phase projection described above) so that one obtains the connected phase over a long time interval (1 to 8 hours). When phase can be connected over hours, low magnitude (≈ 0.1 cycle) short term (≈ 10 min) phase excursions are less damaging. For example, local derivatives of the indicated excursions produce frequency noise of the order of 0.1 mHz which corresponds to 20 cm in equivalent baseline error for S-band observations. On the other hand, a grand fit to hours of connected phase data in this example will experience only 0.1 cycle (1 cm at S-band) of phase noise.

An example of a least-squares fit of a phase-track sinusoid is shown in Fig. 3 for several delay offsets. Only a fraction of the first subinterval (30 out of 50 sec) is displayed in the figure. Figure 5 shows the residual phase values obtained by phase-tracking the $\tau_V = 0$ fringes in Fig. 3 over 600 sec. Note that the 0.1-Hz analytical offset has been removed. The residual fringe frequency $\Delta\dot{\phi}_a$ is a consequence of all of the terms listed in Eq. (25). As one would require, there is excellent agreement between the fringe frequency values obtained by phase-tracking in Fig. 5 and by Fourier transform in Fig. 4 (after the FFT result has been corrected for the 100-mHz analytical offset). The amplitude values obtained by phase-tracking the fringes in Fig. 3 are shown in Fig. 6. The amplitude value for each delay offset τ_V is an average of the twelve amplitudes obtained from the twelve phase-track subintervals. Note the excellent agreement between the amplitudes obtained by phase-tracking ($\tau_V = 0$ case in Fig. 6) and by Fourier analysis in Fig. 4. As indicated in Fig. 6, the amplitude variation versus time offset has been fit with the $\sin(x)/x$ curve that would be generated by an ideal rectangular bandpass that is 24 kHz wide. The deviation of data points from the $\sin(x)/x$ curve is primarily due to the nonideal response of the actual system bandpass. In the least-squares fit, the center and amplitude of the $\sin(x)/x$ curve are used as solve-for parameters. The least-squares values for amplitude and center delay are a measure of the maximum amplitude and single-channel delay for the phase-track interval. (The delay and amplitude errors quoted for the example in Fig. 6 include the modeling error associated with the inadequate $\sin(x)/x$ curve. It should be noted that a more accurate delay curve model based on system bandpass measurements would improve the delay and amplitude precision considerably. For the example in Fig. 6, the delay uncertainty due to system noise alone would be about 150 nsec).

After a given time interval has been phase-tracked, the most important output quantities are the amplitude and phase for each subinterval. For the present 48 kbits/s system, only the phase values that are generated by the "peaked" fringes [i.e., $2W_B \Delta\tau_r < 1$] are retained for subsequent data analysis. (The slight statistical advantage gained by processing more delay offsets is greatly out-

weighed by the increased computation costs for this system). The fringe phase is an important observable containing valuable information concerning geometric quantities as well as transmission media and instrumental effects. As indicated in the next section, phase values measured for two separate channels can be combined by a procedure known as bandwidth synthesis to extract the delay. The amplitude values produced by the peaked fringes are retained for use in source structure calculations. If the fringes are phase-tracked or Fourier-analyzed for a range of delay offsets (τ_V), the amplitude variation as a function of delay can be analyzed to extract the single-channel delay.

VII. Bandwidth Synthesis

This section is devoted to a discussion of time delay measurements with emphasis on two-channel bandwidth synthesis.

As indicated in Section VI for a single band-limited channel, fringe phase can be determined over the phase-track interval except for an overall $2n\pi$ ambiguity. Therefore, with regard to single-channel phase, only the time-varying components carry information that may be readily analyzed. Since the z-component of the baseline (component along Earth's spin axis) enters the phase as a constant effect for a given source (Ref. 4), this $2n\pi$ phase uncertainty increases the difficulty of determining the z-component from single-channel phase. For this reason, delay measurements are desirable for three-dimensional baseline determination. Furthermore, the extra information carried by the delay observable strengthens the solution of the general multiparameter fitting procedure involving sources, baselines, and Earth orientation factors. For example, the delay observable removes the well-known singularity problem (unknowns > independent equations) and the zero-declination weakness associated with fits to fringe phase (or fringe frequency). For these reasons, a capability for precisely measuring delay becomes very desirable.

In general, the precision of delay measurements improves as the range of the observed frequencies increases (see Ref. 1 and Eq. 27). One way to increase the frequency range is to increase the recorded bandwidth. However, practical considerations regarding the size of the instantaneous record rate (cross-correlation cost and complexity, recorder availability) place the present system bandwidths at 2 MHz or less. Delay measurements with high precision (≈ 60 psec $\simeq 2$ cm) require much larger bandwidths than 2 MHz (Ref. 1). Therefore, in order to increase the frequency range further, a technique known as bandwidth synthesis has been employed. In this technique, one combines, either directly or indirectly, the phase information provided by a few band-limited channels whose separation in frequency is large compared to the single-channel bandwidth. In the original application of this technique (Ref. 5) six channels of radio noise were recorded in a time-shared mode. In that system the six channels equally share the total statistics allowed by the instantaneous record rate. However, the statistics associated with the two outer channels, separated by the greatest frequency interval, primarily determine the final precision of the delay observable. The inner channels serve mainly to resolve ambiguities in the delay determination. That is, with a six-channel experiment, the *a priori* delay can be much more uncertain than the *a priori* delay in a two-channel experiment with the same total frequency spread. However, in measurements that involve sufficiently precise *a priori* delay information, inner channels serve no function and are a waste of statistics.[3] In those cases, only the two outer channels should be measured, so all of the statistical strength of the measurement contributes to the final delay precision. An example of such a measurement situation would be a set of short baseline (< 200 km) experiments designed to frequently monitor small baseline changes due to tectonic motion. The delay observable is not greatly corrupted by transmission media because of differential cancellation over short baselines. Furthermore, delays for short baselines are less sensitive to angular errors in Earth orientation and source locations. Therefore, if sufficiently precise values for source locations and Earth orientation are gathered from other work, the *a priori* delay can be calculated with sufficient accuracy to allow two-channel ambiguity resolution. (If the baseline is fairly uncertain initially, one can make one or two preliminary measurements with closely spaced channels to lower the baseline uncertainty.) See Ref. 6 for a feasibility demonstration experiment for such a system. In some radio interferometry applications the two-channel approach is not adequate. An example would be a set of experiments that are corrupted by uncalibrated ionosphere delays that are large compared to the ambiguity level associated with the outer-channel separation.

In the remainder of this section, two-channel bandwidth synthesis will be analyzed. In principle, the multichannel system is also treated since the two-channel approach can be applied successively to channel pairs beginning with the two most closely spaced channels. That is, one can refine the *a priori* delay on the basis of the first two channels and proceed to the next larger sepa-

[3]This point was originally suggested by P. F. MacDoran.

ration and so forth. However, in the original application (Ref. 5) of the multichannel approach, the delay was obtained by summing the fringes of the various channels to obtain a delay response curve. This approach requires calibration of the relative phase of the various channels. As we shall see, the two-channel approach treats the instrumental phase as a solve-for parameter and thereby eliminates the need for relative phase calibration. That is, the only requirement placed on the instrumental phase by the two-channel technique is that the instrumental phase should exhibit stability with respect to some simple functional form—a constant, linear drift, etc.

An example of an instrumental configuration designed[4] for optimum phase stability in two-channel observations is shown in Fig. 7. In this system, a 10-MHz signal from the H-maser is converted to a 2240-MHz first local oscillator (LO) signal by using only multipliers: the standard $\times 4$ $\times 8$ multipliers and a new $\times 7$ multiplier. The $\times 7$ multiplier was designed and constructed[5] in order to avoid the use of a synthesizer. The $\times 7$ multiplier converts the input sinusoid to a square wave and then filters and amplifies the seventh harmonic.

In order to achieve maximum channel separation and better delay precision, the traveling wave maser (TWM) receiver bandpass was broadened by retuning the trim coil currents. In the retuned state, the receiver exhibited ample amplification over a 40-MHz interval (2270 to 2310 MHz) while maintaining an operating system noise temperature less than 30 K. Therefore, after mixing with the first LO signal at 2240 MHz, the edges of the receiver passband were placed at 30 and 70 MHz. However, this frequency spread exceeded the bandpass of the standard first mixer/preamp which possesses adequate gain only over 45 to 55 MHz. Consequently, the standard mixer/preamp was replaced with a similar module with a bandpass between 10 and 160 MHz, thereby making the system bandpass TWM-limited. The IF passband is then filtered into two channels—one centered at 30 MHz and the other at 70 MHz. Each channel is mixed with a 20-MHz signal derived from the hydrogen maser and each mixer response is appropriately filtered to place both channels at 50 MHz. At this point, each channel is transferred on alternate seconds to the video converter. The video converter mixes the input IF signal to baseband with a 50-MHz signal derived from the hydrogen maser. This time-shared baseband signal is passed through a 24-kHz bandpass for digital sampling and recording at a 48-kbit/sec rate. Note that the instrumental phase of this system relies exclusively on multipliers and H-maser frequency standards. [With this configuration, the differential phase noise was *less than* 0.008 cycles between the two channels for 700 second integration times (Ref. 6). Phase noise at the 0.008 cycle level corresponds to 200 psec (6 cm) of delay noise for a 40-MHz synthesized bandwidth.]

An example of stopped fringes generated by the above configuration is shown in Fig. 8. Note that alternate seconds clearly contain distinct fringes. The phase tracking technique outlined earlier can easily be modified to independently extract the phase of each fringe curve. Phase values obtained from the example fringes in Fig. 8 are shown in Fig. 9. The analytical offset ε has been removed after assigning the phase the proper sign. The small nonlinear phase excursions (≈ 0.03 cycle) could possibly be due to ionosphere effects. Note that the excursions are nearly identical in the two channels so that they nearly cancel in the delay calculation that follows. As indicated by Eq. (25), these phase values are theoretically represented by the expressions

$$\Delta\phi_a = \omega_a \Delta\tau_r' + R_a + \Psi_a + C_a \tag{26}$$

$$\Delta\phi_b = \omega_b \Delta\tau_r' + R_b + \Psi_b + C_b$$

where the subscript $a\,(b)$ denotes channel $a\,(b)$. In this expression, all instrumental phase effects have been included in Ψ_a and Ψ_b. The measured delay ($\Delta\tau$) may be extracted by combining the phase values as follows:

$$\Delta\tau \equiv \frac{\Delta\phi_a - \Delta\phi_b}{\omega_a - \omega_b} \tag{27}$$

In calculating $\Delta\tau$, one can assume that the frequency separation $\omega_a - \omega_b$ is essentially perfectly known ($\Delta f/f \approx 10^{-12}$). As described below, care must be taken to assign the correct value of $2n\pi$ to $\Delta\phi_a - \Delta\phi_b$. The expected behavior of $\Delta\tau$ is given by the expression

$$\Delta\tau = \Delta\tau_r' + \frac{\Psi_a - \Psi_b + C_a - C_b}{\omega_a - \omega_b} \tag{28}$$

We have assumed that the brightness transform phase R_a changes a negligible amount between channels.

The charged particle phase difference $C_a - C_b$ can be reduced to delay τ_c as follows. It can be readily shown that the charged-particle phase shift for channel x is given by expression (Ref. 7):

$$C_x = \frac{P_T}{\omega_x} \tag{29}$$

[4]This configuration was designed by D. J. Spitzmesser.

[5]Designed and constructed by R. L. Sydnor.

where

$$P_T = \frac{e^2}{2\pi m_e c}(N_1 - N_2)$$

In this expression, c is the speed of light and e and m_e are the charge and mass of the electron in mks units. Furthermore, $N_1 - N_2$ is the difference of the electron columnar content (number/area) along the two ray paths. The phase shift C_x is in cycles, and the frequency ω_x is in Hz. Based on Eq. (29), the charged-particle phase difference becomes

$$\begin{aligned} C_a - C_b &= \frac{P_T}{\omega_a} - \frac{P_T}{\omega_b} \\ &= -\frac{P_T}{\omega_a^2}(\omega_a - \omega_b) \text{ for } |\omega_a - \omega_b| << \omega_a \\ &= \tau_c(\omega_a - \omega_b) \end{aligned} \tag{30}$$

where $\tau_c = -P_T/\omega_a^2$ is the total delay due to charged particles. The expected behavior of the measured delay is then given by

$$\Delta\tau = \Delta\tau_r + \frac{\Psi_a - \Psi_b}{\omega_a - \omega_b} \tag{31}$$

where

$$\begin{aligned} \Delta\tau_r &= \Delta\tau_r' + \tau_c \\ &= \tau_g + \tau_I + \tau_c + \tau_t - \tau_m \end{aligned}$$

If the model delay is sufficiently accurate, and if the frequency systems are well calibrated, the measured delay $\Delta\tau$ will be constant (within the delay noise) over considerable time intervals (≈ 10 min). In this case, the delay values can be averaged over the interval. The delay values obtained from the phase plots in Fig. 9 are shown in Fig. 10 along with the average delay $\overline{\Delta\tau}$ for the whole 10-min interval. The delay error estimate in Fig. 10 is the uncertainty due to system noise.

When the phase values from the two channels are combined in Eq. (27), care must be taken to avoid $2n\pi$ ambiguities. That is, the difference $\Delta\phi_a - \Delta\phi_b$ must be assigned the proper number of integer cycles. A procedure with which $2n\pi$ ambiguities can be resolved will be discussed in the next four paragraphs.

Note that the phase difference is theoretically a sum of two terms.

$$\Delta\phi_a - \Delta\phi_b = (\omega_a - \omega_b)\Delta\tau_r + \Psi_a - \Psi_b \tag{32}$$

The instrumental phase term $\Psi_a - \Psi_b$ usually is not constant due to differences in the frequency systems at the two stations. If the frequency systems are very stable ($\Delta f/f \approx 10^{-14}$ for the better H-maser standards), this instrumental phase difference can be treated as a constant plus a linear drift in time. The linear drift is due primarily to the rate difference of the frequency standards. For good frequency standard calibration accuracies ($\Delta f/f \approx 10^{-12}$), the rate, $\dot{\Psi}_a - \dot{\Psi}_b$, will be about 40 μHz for a 40 MHz channel separation. At this rate, the instrumental phase difference will change only one cycle in 8 hours.

The maximum magnitude of the first term $(\omega_a - \omega_b)\Delta\tau_r$ is determined by the residual delay $\Delta\tau_r$, which may be estimated as follows. The maximum geometric delay errors are readily calculated using the maximum partial magnitudes and the *a priori* uncertainties in the geometric delay parameters (baseline, source location, UT1 etc.). The maximum values of the sensitivity partials (Ref. 4) for the geometric delay over an intercontinental baseline ($\approx 10{,}000$ km) are given by

$$\frac{\partial\tau_g}{\partial x} \sim 3 \text{ nsec/m} \qquad \frac{\partial\tau_g}{\partial\theta} \sim 150 \text{ nsec/arc sec} \tag{33}$$

where x and θ symbolize length and angle parameters respectively. For example, if the *a priori* source position is uncertain at the 2 arc sec level, this uncertainty will contribute less than 300 nsec to $\Delta\tau_r$. The magnitudes of transmission media calibration errors can usually be estimated once the calibration technique is selected. The terms in the delay that are constant at the level required for ambiguity resolution can be neglected at this stage. We will assume cable delays, bandpass group delays, etc., are constant at this level. These constant terms, as we shall see, are truncated or absorbed in the constant offset. After one has determined the maximum value of $\Delta\tau_r$ due to uncertainties in the variable components, the channel separation $\omega_a - \omega_b$, is selected so that, in the worst case, the term $(\omega_a - \omega_b)\Delta\tau_r$ is less than 0.2 cycle in magnitude. With this design, this first term will scatter more or less randomly between ± 0.2 cycle as one measures the delay for various sources in various directions.

Therefore, the phase difference $\Delta\phi_a - \Delta\phi_b$ consists of two terms—a slowly changing but continuous instrumental phase term plus a delay term that varies more or less randomly between ± 0.2 cycle when changing from source to source. Since the rate of the instrumental term is usually not exactly known, it may be treated as follows. We will assume for the moment that the rate is small ($\sim 40\ \mu$Hz). The average phase difference $\Delta\phi_a - \Delta\phi_b$ for the *first* radio source (1 to 10 minutes duration) is assigned the particular value of $2n\pi$ required to place $\Delta\phi_a - \Delta\phi_b$ between 0 to 1 cycle. This initialization procedure is justi-

fied by the fact that delay will always possess an unknown additive constant that will be a solve-for parameter. By this initialization, the level of the constant has been chosen to place the *first* delay value in a specified range. This delay truncation means that clock synchronization and constant instrumental delays cannot be determined by two-channel bandwidth synthesis unless elaborate instrumental phase and delay calibrations are performed to initialize the instrumental constant to within $2n\pi$. Once the first delay has been defined, care must be taken to assign the correct value of $2n\pi$ to subsequent delay values. If the instrumental phase, $\Psi_a - \Psi_b$, is slowly varying ($\sim 40\ \mu$Hz) then it will change by a fraction (~ 0.03) of a cycle before the next delay value is obtained a short time (≈ 10 min) later. If this is the case, the next phase difference must be within ± 0.2 cycle of the first difference provided the residual delay $\Delta\tau_r$ falls in the expected range. In this manner, the $2n\pi$ factor for each delay can be determined by comparison with the preceding phase difference.

Up to this point, we have assumed the instrumental rate $\dot{\Psi}_a - \dot{\Psi}_b$ is small ($\sim 40\ \mu$Hz). When this assumption is not satisfied, several courses of action are available. The most reliable but time-consuming frequency calibration involves an independent multiparameter fit to the single-channel phase (fringe frequency) observables to obtain the frequency offset at RF. The resulting offset can be easily scaled from RF to the synthesized bandwidth. No time is wasted by this procedure, since an independent fringe frequency solution should normally be performed as a check on the delay solutions. Another easier frequency calibration technique is to use a well-known source as a calibrator provided other geometric fringe frequency uncertainties are sufficiently small. The frequency standard rate difference has to be determined to within only about 2 MHz at S-band to allow the ambiguity resolution steps to proceed for a 40-MHz synthesized bandwidth. Once the oscillator offset is approximately known, the phase differences, $\Delta\phi_a - \Delta\phi_b$, can be corrected to remove the rapid linear drift. The ambiguity resolution process can then be applied, as outlined above, to these more slowly varying corrected phase differences.

Once the single-channel phase values and delay values have been determined for all observations, these observables can be fit simultaneously by a weighted least-squares technique to determine the source locations, baseline and Earth orientation factors. If the delay model τ_m used in data reduction is considered inappropriate for the least-squares fit, then one can add τ_m to the measured delay $\Delta\tau$ to obtain the total measured delay free of theoretical models.

VIII. Summary

In this report, the practical aspects of the JPL long baseline interferometry data reduction procedure have been described. The steps include bit stream manipulations, fringe stopping, Fourier analysis and phase-tracking. The most important output of these steps is fringe amplitude and fringe phase. Fringe phase values measured for two separate channels are combined by a procedure known as bandwidth synthesis to precisely extract delay. For less precise delay measurements, fringe amplitude variation versus model delay can be used to extract single-channel delay. Peak fringe amplitude can yield valuable information concerning source structure.

References

1. Thomas, J. B., "An Analysis of Long Baseline Radio Interferometry," in *The Deep Space Network Progress Report*, Technical Report 32-1526, Vol. VII, p. 37. Jet Propulsion Laboratory, Pasadena, Calif., Feb. 15, 1972.

2. Thomas, J. B., "An Analysis of Long Baseline Radio Interferometry, Part II," in *The Deep Space Network Progress Report*, Technical Report 32-1526, Vol. VIII, Jet Propulsion Laboratory, Pasadena, Calif., April 15, 1972.

3. Van Vleck, J. H., and Middleton, D., "The Spectrum of Clipped Noise," *Proc. IEEE*, Vol. 54, No. 1, p. 2, January 1966.

4. Williams, J. G., "Very Long Baseline Radio Interferometry and Its Sensitivity to Geophysical and Astronomical Effects," in *The Deep Space Network*, Space Programs Summary 37-62, Vol. II, p. 49. Jet Propulsion Laboratory, Pasadena, Calif., March 31, 1970.

5. Rogers, A. E. E., "Very Long Baseline Interferometry With Large Effective Bandwidth for Phase-Delay Measurements," *Radio Sci.*, Vol. 5, No. 10, p. 1239, October 1970.

6. Thomas, J. B., et al., "Radio Interferometry Measurements of a 16-Kilometer Baseline with 4 Centimeter Precision" (to be published).

7. MacDoran, P. F., "A First Principles Derivation of the DRVID Charged Particle Calibration Method," in *The Deep Space Network*, Space Programs Summary 37-62, Vol. II, p. 28. Jet Propulsion Laboratory, March 21, 1970.

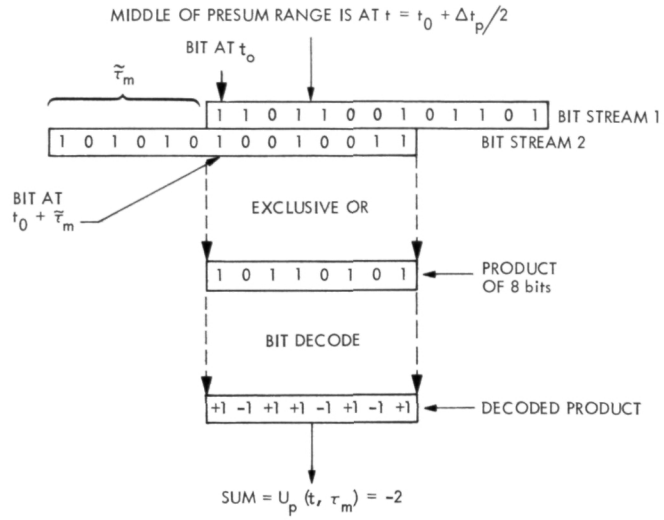

Fig. 1. Example of bit multiplication and presum

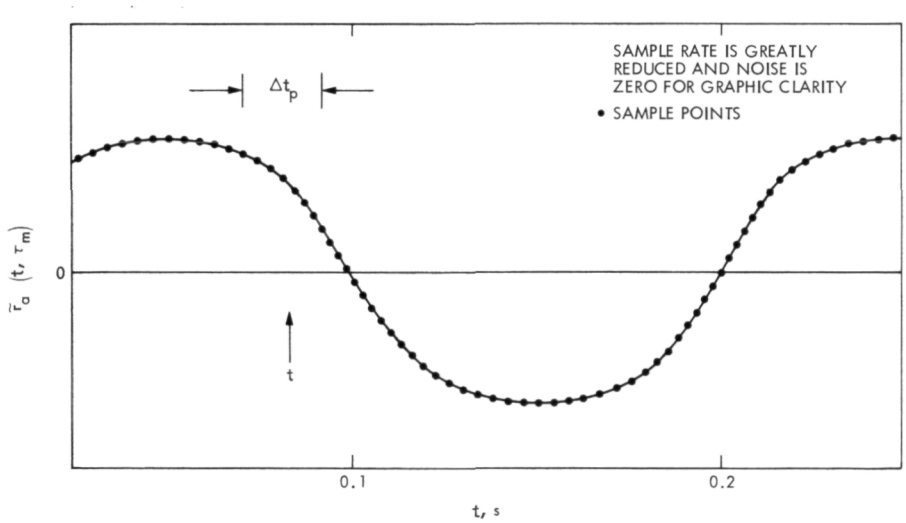

Fig. 2. Schematic example of presum time interval

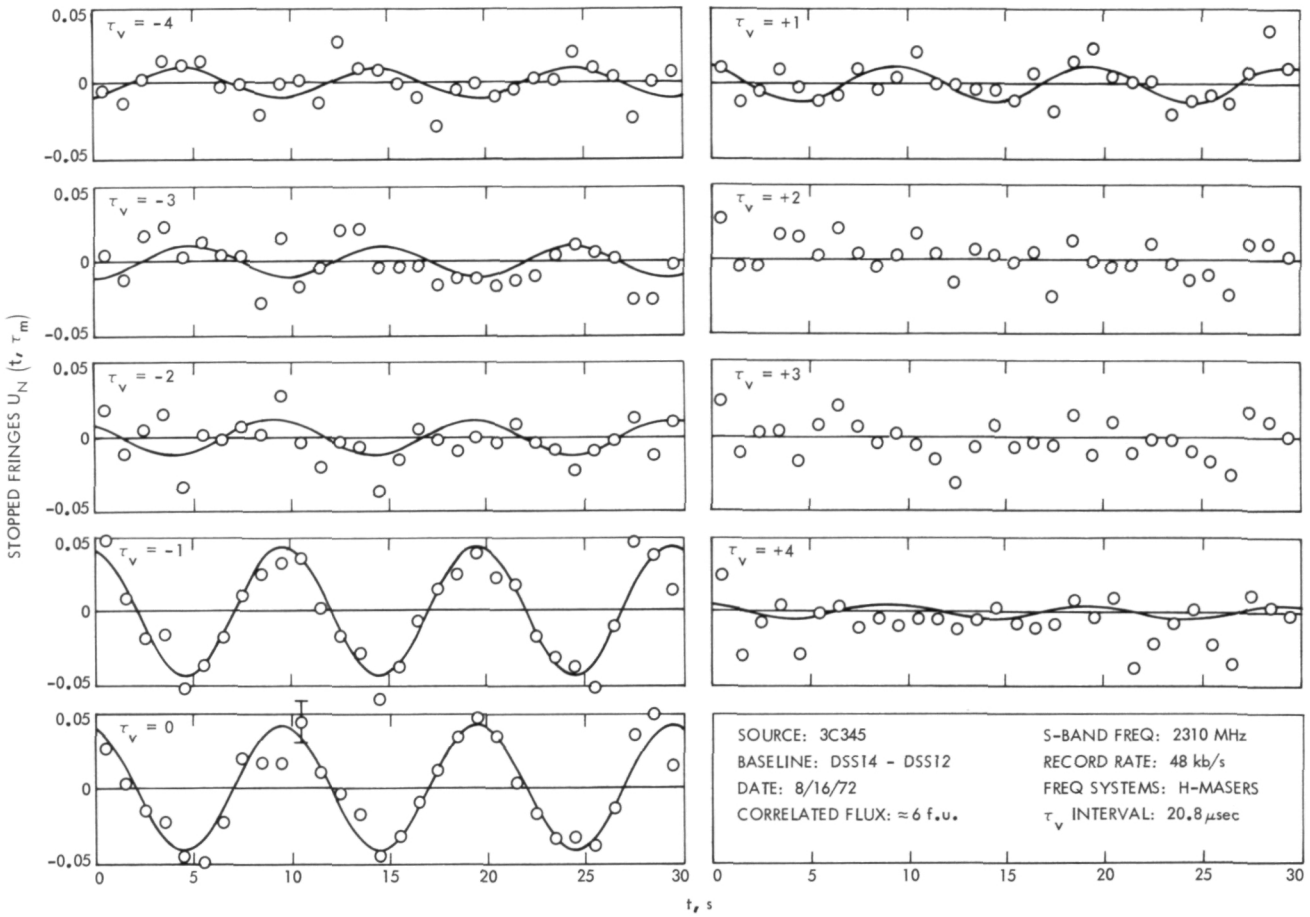

Fig. 3. Example of stopped fringes

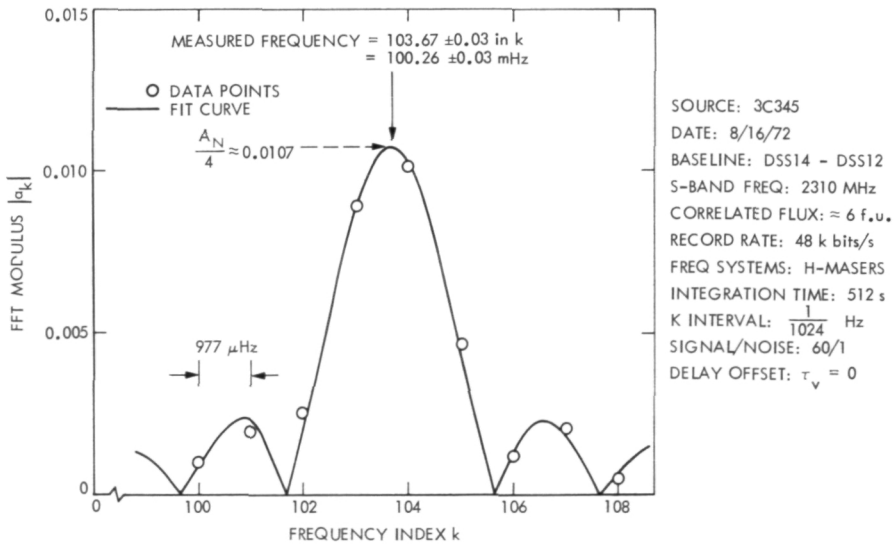

Fig. 4. Fourier transform of stopped fringes

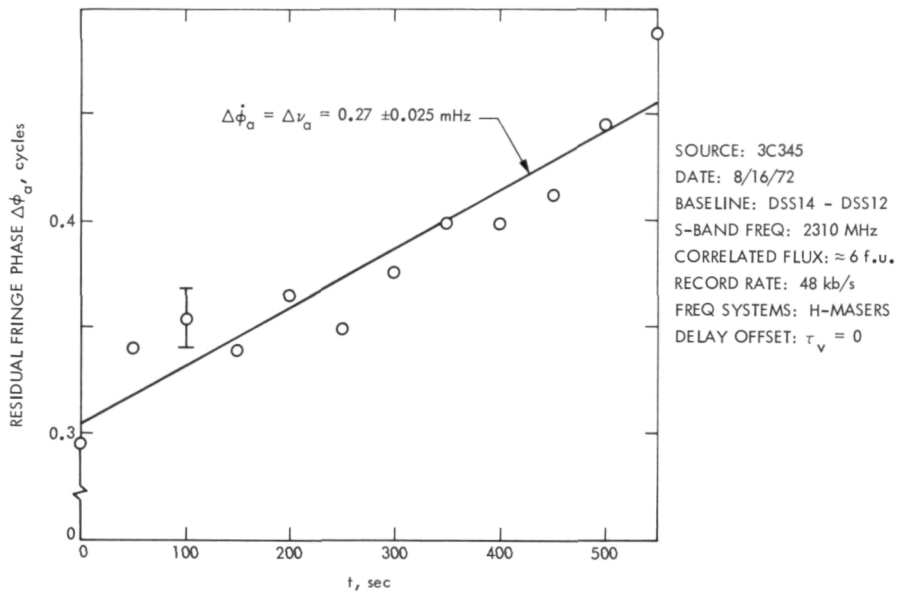

Fig. 5. Residual fringe phase plot

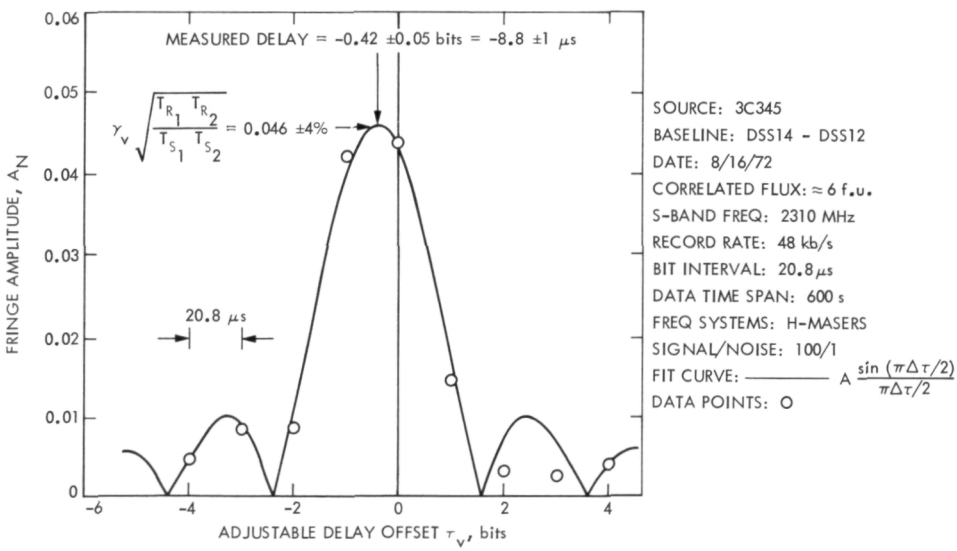

Fig. 6. Example of a delay curve

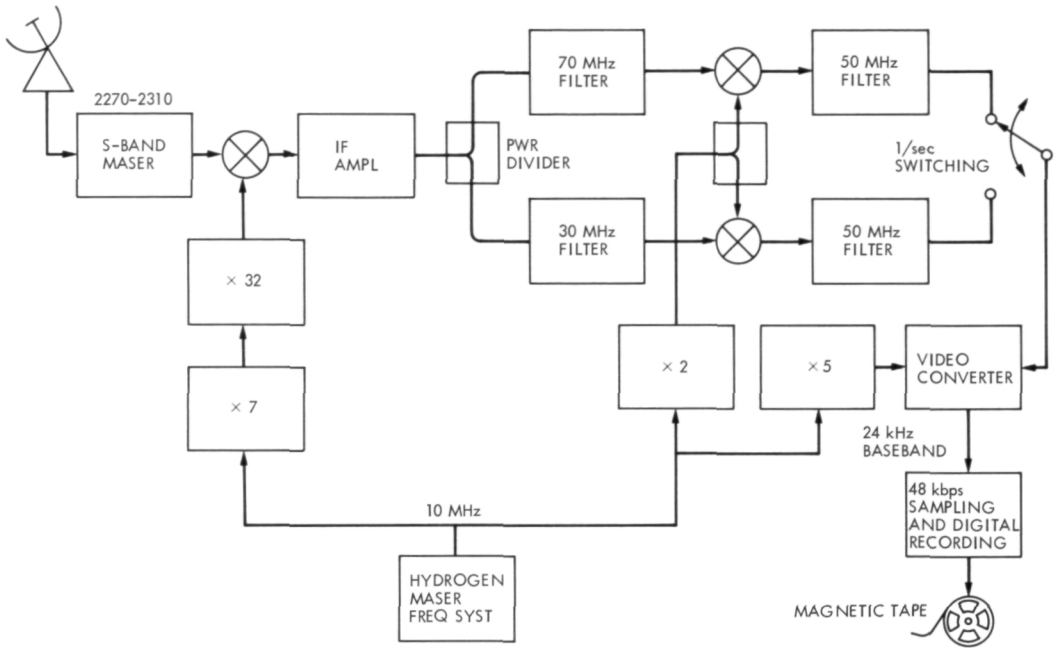

Fig. 7. Deep space station configuration for 40-MHz bandwidth synthesis

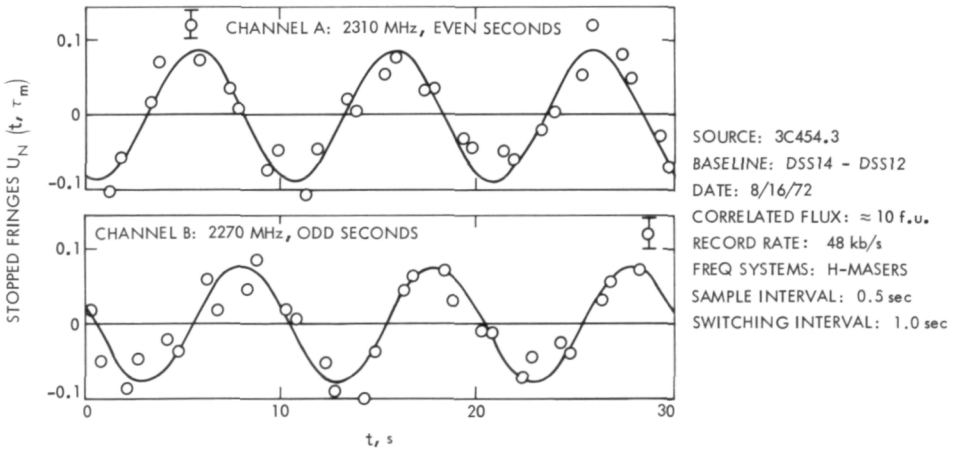

Fig. 8. Stopped fringes for two-channel bandwidth synthesis

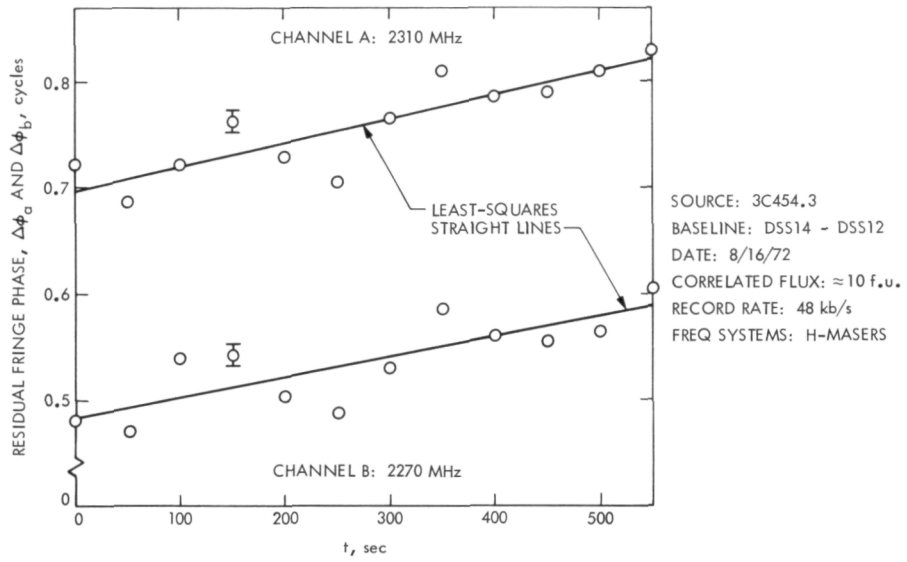

Fig. 9. Fringe phase values for two-channel bandwidth synthesis

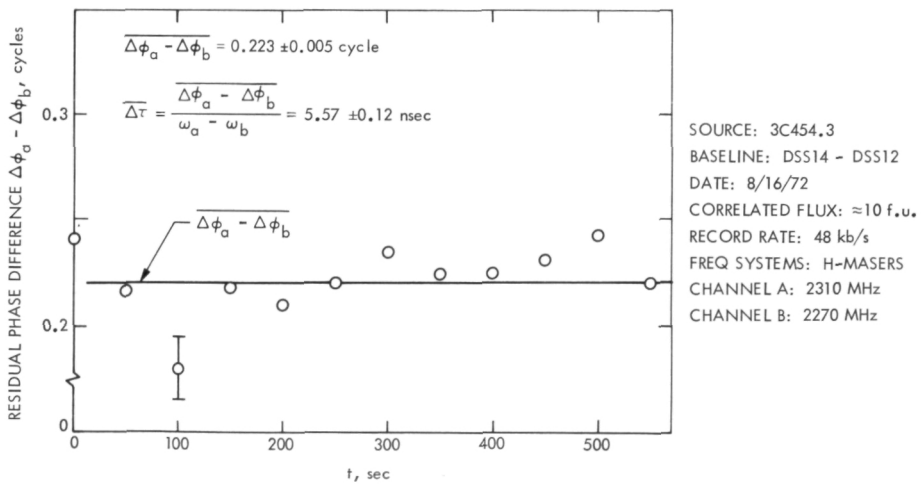

Fig. 10. Example of a delay calculation with two-channel bandwidth synthesis

Candidate Extragalactic Radio Sources for Differenced VLBI Tracking With Deep Space Probes

N. A. Mottinger
Tracking and Orbit Determination Section

The application of the ΔVLBI or VLBI switching technique for tracking extragalactic radio sources (ERS) and spacecraft which are at 10 deg or less angular separation offers a method for augmenting the current doppler navigation system. From general radio source catalogs, ERS have been selected which have promising spectral features and correlated flux values suitable for ΔVLBI tracking using the antennas in the Deep Space Network. A computer program has been written which reduces this list to those occurring in a specific region of the celestial sphere near the track of a deep spacecraft. Surveying two current missions, Pioneers 10 and 11, and two future missions, Mariner Venus/Mercury and Viking, reveals numerous opportunities for ΔVLBI.

I. Introduction

The technique of very long baseline interferometry (VLBI) has applications that range from the determination of the radio source positions to the measurement of the separation and orientation of the stations comprising the interferometer. Since it is possible to track man-made radio sources, e.g., a deep spacecraft, in the interferometric mode, the VLBI technique is being adapted for use as a new method for deep space navigation. This method (suggested by I. I. Shapiro of MIT) involves VLBI tracking which switches between spacecraft and radio sources when the angular separation between the two is approximately 10 deg or less. This technique, which will be referred to as ΔVLBI tracking, enables one to determine the angular position of the spacecraft relative to the natural radio source by analyzing the differenced VLBI observables. The purpose of this article is to show the results of an investigation to determine opportunities for ΔVLBI tracking using several deep space missions, some currently in progress (Pioneers 10 and 11) and two to be launched (Mariner Venus/Mercury and Viking).

II. Discussion of VLBI Navigation

If, in terms of small angular separation, a spacecraft were to "flyby" a natural extragalactic radio source (ERS), it is proposed that VLBI switching or ΔVLBI between the two can lead to accurate determination of the position of the spacecraft with respect to the ERS.

This technique offers a new means for spacecraft navigation and in addition assists in reducing the uncertainty in tracking stations locations, which is a limitation to navigation capability.

The ΔVLBI technique enables one to determine the position of the spacecraft any time it passes near an extragalactic radio source. The fact that the spacecraft position can be determined implies that the ΔVLBI system can augment the existing doppler tracking system and improve the overall navigation capability during the mission. Also, this ability to fix the position of the probe in space is similar to the situation where a spacecraft encounters one of the planets in the solar system. Both circumstances lead to the determination of the position of the spacecraft, from which it is then possible to obtain tracking station locations. As will be shown by the study done, there are numerous ERS "encounters" during a mission's Earth-to-target body phase, thereby increasing the number of opportunities from 1 per mission to several per mission when it is possible to determine the spacecraft location with respect to another object.

Implementation of the ΔVLBI method for navigation will require significant amounts of work. First, a catalog of extragalactic radio sources must be established that defines the coordinate system in which the planetary positions will be defined. The ERS are especially attractive for this work since they have essentially zero proper motion and hence should be the best references to date for defining an inertial frame. The entire operation can only succeed when the two reference frames, ERS and planetary, are precisely aligned.

Another important part involves the selection of specific ERS for use in the ΔVLBI measurements. To help with this, a computer program has been written which selects ERS from a catalog compiled by J. G. Williams of the Tracking and Orbit Determination Section of JPL and plots them along with trajectories of various deep space missions. Sources that are within 10 deg of the spacecraft trajectory are candidates for the ΔVLBI measurements. Although the sources maintained by Williams in his catalog have been specifically selected from more general radio source catalogs on the basis of promising spectral features and correlated flux values, it is not until they are actually analyzed by the interferometer that proof of their suitability is made. The computer program is useful in limiting the selection of ERS to those which are "encountered" by the spacecraft and therefore worthy of detailed study.

III. Results

Figures 1 and 2 show the results of the studies done using Williams' catalog for selecting sources near the the Pioneers 10 and 11, Mariner Venus/Mercury, and Viking trajectories. There are approximately nine sources in Fig. 1 which involve all but the Viking missions. Encompassed are the cruise and encounter phases of Pioneers 10 and 11 and the Venus and first Mercury encounter for MVM'73. It is interesting to note that Pioneer 10 oscillates between several ERS prior to encounter. Pioneer 11 will fly through the same area, but after periods of retrograde motion which take it beyond the limits of this plot, it returns to a portion of the sky near the occurrence of the first Mercury encounter of MVM'73. This is interesting since it shows that spacecraft flying by different bodies of the solar system do sometimes have a common ERS background. The second and successive MVM'73 Mercury encounters are not shown in this report. However, studying these in the same manner reveals numerous additional sources which will be near its flight path.

The Viking spacecraft do not fly against the ERS sources of Fig. 1 during their Earth-Mars transfer periods. However, Viking missions A and B do themselves traverse the same general regions, passing more than a dozen ERS (Fig. 2). Following arrival at Mars these spacecraft will eventually traverse the region shown in Fig. 1 and in doing so will also pass many other ERS. However, for the primary purpose of assisting in the navigation during the cruise phase of all these missions, Figs. 1 and 2 do show sources which are of top priority for immediate study.

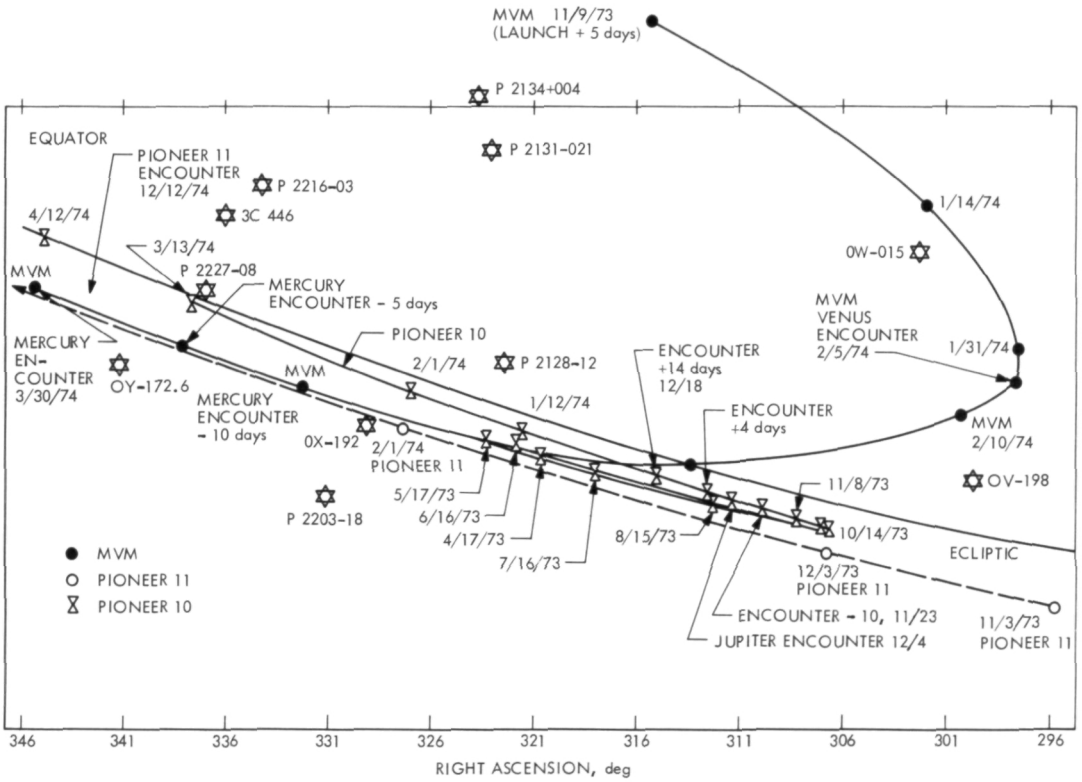

Fig. 1. Pioneers 10 and 11 and Mariner Venus/Mercury ΔVLBI source flybys

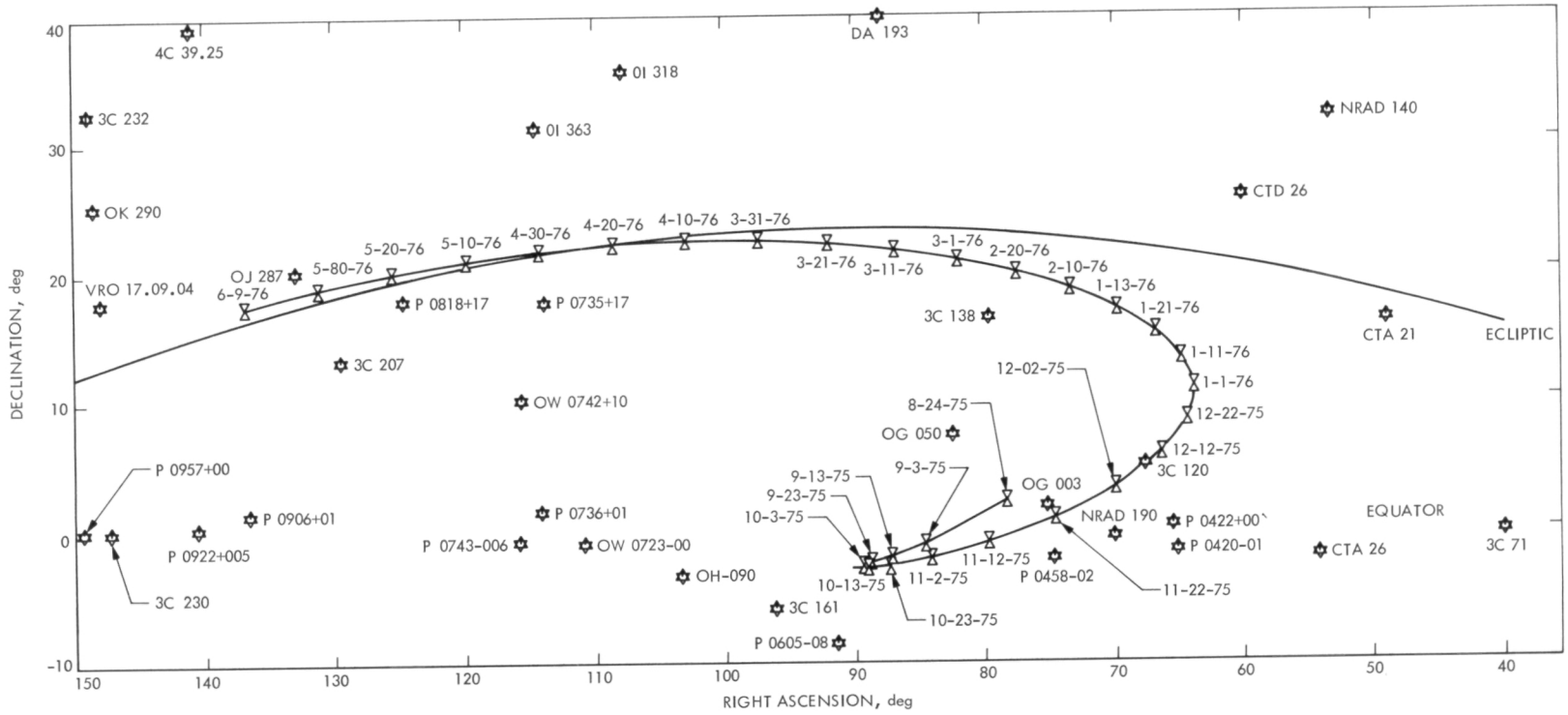

Fig. 2. Viking ΔVLBI source flybys

Frequency Generation and Control: Improved Vacuum Pump for the Atomic Hydrogen Frequency Standard

H. Erpenbach and P. Dachel
Communications Elements Research Section

This article describes the use of a turbo-molecular pump as an alternative to the getter-ion pumping systems normally used with the hydrogen maser; the preliminary results were excellent. The time required for pumpdown is about one-third that of the ion pump system. Argon, which is normally ion-pumped at a speed of about 5% of that of air, is removed at the same speed as air with the turbo-molecular pump.

The amount of maintenance required for a turbo-molecular is less than for an ion pump; ion pump elements have to be replaced once a year which means turning off the maser, installing new elements, and disturbing the maser, a process which requires several days. Turbo-molecular pump manufacturers claim 5 years or more without servicing.

I. Introduction

A turbo-molecular mechanical vacuum pump was tested as a substitute for an ion pump in a hydrogen maser. This vacuum pump does not operate on the positive displacement principle but rather on the principle of imparting momentum to gas molecules, preferentially in the direction of the desired flow.

In 1912 Gaede (Ref. 1) introduced a molecular-drag pump. In the molecular-drag pump (Ref. 2) there is an open passage from the inlet to outlet between which a pressure differential is maintained by the high velocity motion of one side of the passage relative to the housing of the pump, where the inlet and outlet are located. In Fig. 1 the principle of the molecular-drag pump is illustrated.

A number of alternative designs for molecular-drag pumps have been devised, but all of them had slow pumping speeds, about 20 liters/sec or less. In 1958 A. Pfeiffer introduced axial-flow molecular turbine pumps, now known as turbo-molecular pumps (Ref. 2). This type of pump has a series of rotating disks (all mounted on the central shaft) that are spaced alternately with stationary plates mounted in the housing. The disks and plates are

cut with slots set at an angle so that gas molecules caught in the slots of the moving disks are projected preferentially in the direction of the slots in the stationary plates. The pumping speed of one new-type turbo-molecular pump is consequently significantly higher, typically 500 liters/second at an inlet pressure of 133.3×10^{-6} N/m^2 (10^{-6} torr) with an outlet pressure of 133.3×10^{-3} N/m^2 (10^{-3} torr).

II. Application to System

A 12-year old turbo-molecular vacuum pump capable of 140 liters/sec was installed in place of the 200 liters/sec ion pump. The photograph of the prototype maser (Fig. 2) shows the details of the installation of the turbo-molecular pump.

The letter "A" in the photograph is the turbo-molecular pump; "B" is a 15-cm (6 in.) stainless steel bellows; "C" is the extension for the source to make it the same distance from the cavity as the original installation using the ion pump. The slight mechanical vibration of the pump was successfully isolated from the maser by the bellows and suitable shock mounts.

III. Performance

The turbo-molecular vacuum pump will evacuate a hydrogen maser in 30 minutes. An ion pump under the same condition would take at least 3 hours. The turbo-molecular pump has no high-voltage arcing problems. An ion pump operates on 5000 Vdc and has occasional internal flashovers in the pump which produce undesirable electrical noise.

It is not anticipated that the turbo-molecular vacuum pump will replace the ion pump in the near future, as much more time is needed for evaluation of the system.

References

1. Gaede, W., *Ann. Physik*, Vol. 41, p. 337, 1913.
2. Becker, Von W., "A New Molekular Pump," in *Vakuum-Technik*, pp. 149–152. Rudolf A. Lang, Berlin, October 1958.

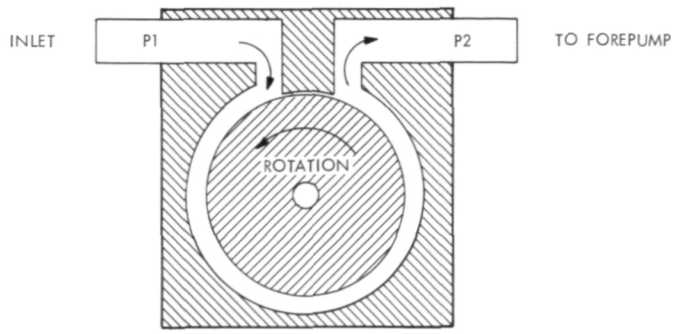

Fig. 1. Molecular drag pump schematic diagram

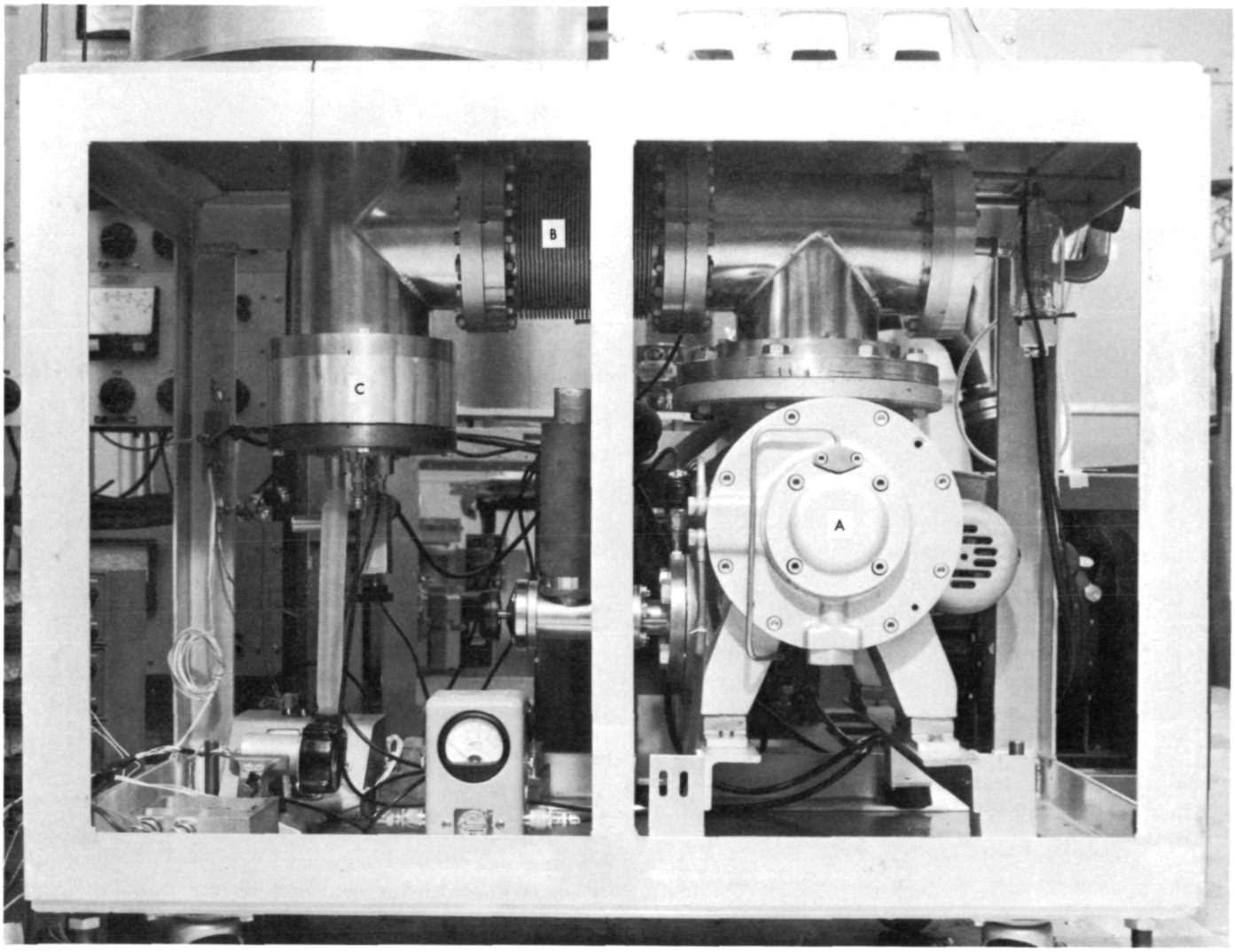

Fig. 2. Turbo-molecular pump vacuum system

Hydrogen Maser Frequency Standard Automatic Tuning Servo

C. J. Finnie and D. A. Norris
Communications Elements Research Section

This article describes the microwave cavity tuner control module for the DSN prototype hydrogen maser and details its operation.

This article describes the microwave cavity tuner control module for the DSN prototype hydrogen maser. A previous report (Ref. 1) described the general features and techniques employed in the tuning system. This report details the operation of the tuner control module.

The tuner control module (Figs. 1 and 2) can be operated in one of four modes (see front panel controls and displays, Fig. 1):

Tune: provides the control of hydrogen beam modulation, data acquisition, and filtering to control the tuning of the maser microwave cavity to the center of the atomic hydrogen resonance frequency (21 cm).

Track: allows automatic frequency tracking between the hydrogen maser and a reference oscillator with an adjustable offset.

Hold: allows the use of the frequency measuring techniques of the tuner system to be used as a malfunction monitor and alarm system.

Counter: allows the use of the tuner counters to calibrate the maser's internal test oscillator.

A block diagram of the control module is shown in Fig. 3. The *tune* mode operates as follows. The H-maser VCO is translated in frequency, by mixing it with a reference oscillator, to 0.01 Hz. The zero crossings of the 0.01-Hz beat frequency are very accurately detected and input to the tuner control module by a zero crossing detector in the H-maser receiver. These zero crossing events sequence a 3-bit binary counter, which in turn controls the following operating sequence.

The operator initializes the sequence with either the *reset* or *enter varactor* control, which sets the hydrogen flux modulation at a high flux level and the count direction of the sequence up-down counter (C1) upward. The arrival of the first zero crossing event enables C1, which counts a 1-kHz clock. The second zero event terminates the count, reverses the count direction and sets the hydrogen flux modulation to a lower level. The controller is inactive for the next period, as the physical system requires this delay to reach equilibrium. The third zero event enables a down count. If the count reaches zero before the arrival of the fourth zero event, the count

direction is reversed, and a negative error binary is set to flag the condition. The counter zero is detected by a digital comparator connected to the outputs of C1 and the front panel switch *error inhibit and alarm level*. With zero supply voltage to the comparator switch, the comparator operates as a zero detector. Because of the clocking mode of the particular counters used, the "greater than" output of the comparator is used to detect the zero count. Therefore, when the fourth zero event stops C1, the absolute value of the difference between the up count and the down count resides in C1, and the sign of the error has been stored. At this time, voltage is supplied to the comparator switch and the comparator output is used to set an "excess error" binary if the error residing in the counter exceeds the *error inhibit and alarm level* switch setting. Also at this time the value and sign of the error are strobed into the *period/period error* display. A running display of the counter operation is available at the *sequence* position of the *display* control. The latter position is primarily used for maintenance, trouble shooting, and operator orientation. After a 4-s delay, the count direction of C1 is set to down count, the comparator switch supply voltage is again set to zero, and the error is counted out of C1 at a 1-kHz clock rate. If the "excess error binary," previously described, has not been set, C2 counts a clock for the time it takes the error to count out of C1. If the error binary is set, an alarm line is set, and C2 does not count while the C1 error is being counted out. The clock rate of C2 is adjusted by the front panel control *time base*. The clock rates for C2 are 10 kHz, 1 kHz, and 100 Hz for switch positions of 0.001, 0.01 and 0.1 s, respectively. These positions correspond to module incremental gains of 0.1 V/s, 0.01 V/s, and 0.001 V/s, respectively, where time is the measured beat period error described in Ref. 1. If the period is 100 s and the oscillator reference frequency is 100 MHz, the incremental frequency error is 1 part in 10^{12} per second of measured period error. This entire tuning cycle is repeated after the next zero event, except that the first count is with the flux control in the low position and the second count is with the flux in the high position. This time reversal of the measurement sequence cancels the linear term of the reference oscillator drift. The C2 error count direction is reversed to compensate for the reversal of the count time sense.

The *track* mode uses a part of the *tune* mode counting sequence. The counter C1 is operator-initialized to the setting on the *period offset* front panel switch. The flux modulation is deactivated, and the counter control binary divider is automatically preset to the count cycle condition which exists after the second zero event of the *tune* mode. The first count of the tune mode has therefore been replaced with a settable constant. The first zero event starts a down count; the second zero event stops the count. The error sign, comparison, alarm, and transfer features are identical to those of the tuning mode. The cycle is automatically reset after each error transfer.

In the *hold* mode the sequence counter (C1) performs as it does for the tuning mode except that the error is not transferred to the varactor counter.

In the *counter* mode the hydrogen maser internal test oscillator replaces the clock of C1, and a 1-s gate derived from division of the control unit 100-Hz clock provides a 1-Hz resolution frequency counter with a 30-kHz maximum counting rate.

The *period offset* and *reset* control provides a manual reset for all control logic and C1, leaving the count in C2 and the varactor setting unchanged. The *enter varactor* control resets all functions including the varactor counter C2. Automatic reset occurs when the position of the mode switch is changed to prevent inadvertent changes in the varactor counter (C2). The *set varactor* digital switch initializes the varactor setting in the *tune* and *track* modes and is used for manual varactor entry in the *hold* mode.

The module is built in a standard four-width nuclear instrumentation module (NIM). The logic components are transistor-transistor logic (TTL) integrated circuits. Nand gates have been used for all gating functions to reduce package types. Two identical counter printed circuit boards are used, with the comparator integrated circuits (ICs) removed for C2. Two control printed circuit (PC) boards supply the 32 gating and binary ICs for the counter control functions. The counters consist of six single-digit integrated circuits and six 4-bit comparators for the C1 counter board. A second single-width NIM houses the 16-bit varactor digital-to-analog converter.

Reference

1. Finnie, C., "Tracking and Ground Based Navigation: Hydrogen Maser Frequency Standard Automatic Cavity Tuning Servo," in *The Deep Space Network Progress Report*, Technical Report 32-1526, Vol. XIV, pp. 56–59, Jet Propulsion Laboratory, Pasadena, Calif., April 15, 1973.

Fig. 1. External view of hydrogen maser cavity tuner control module

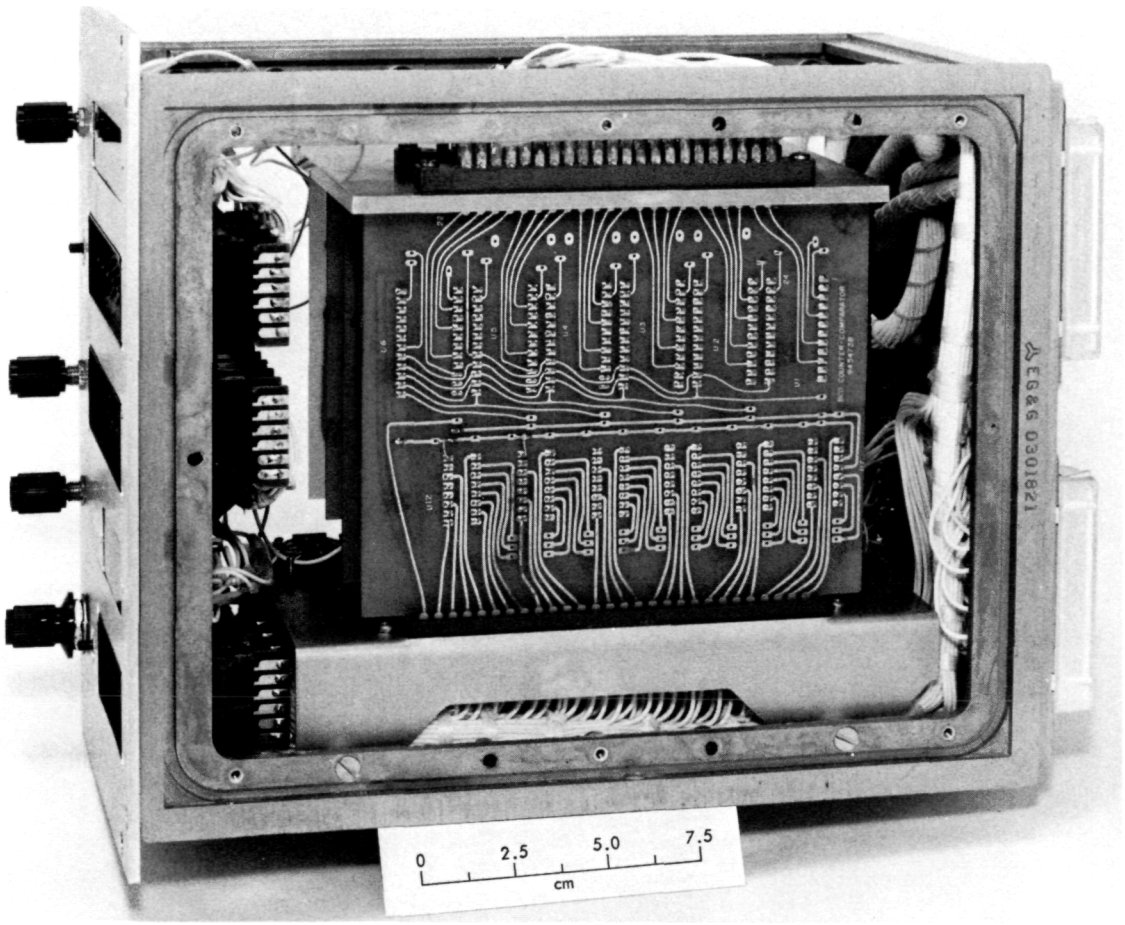

Fig. 2. Internal view of hydrogen maser cavity tuner control module

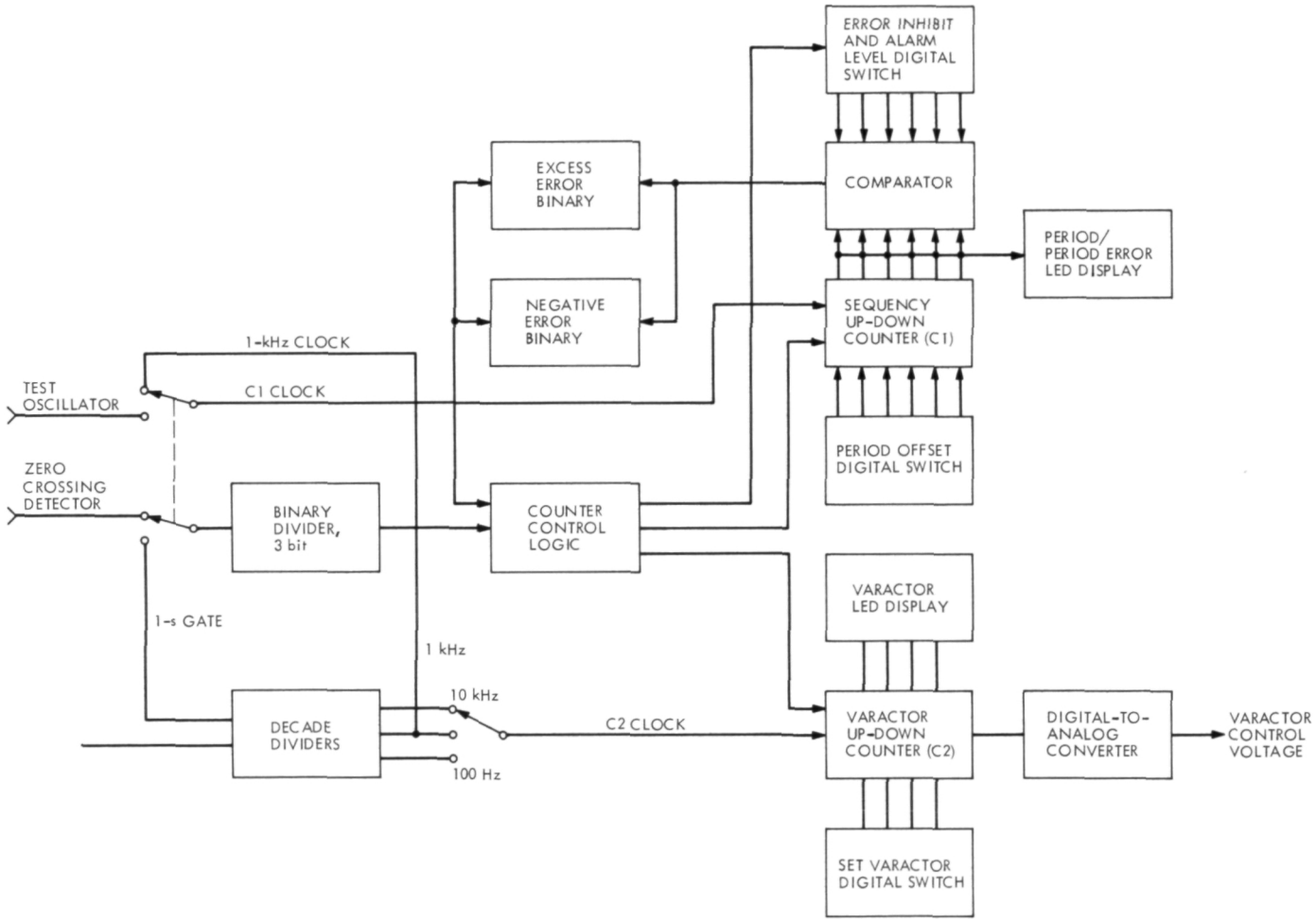

Fig. 3. Auto tuner control module block diagram

The Development of a New Broadband Square Law Detector

M. S. Reid, R. A. Gardner, and C. T. Stelzried
Communications Elements Research Section

A new broadband constant law detector has been developed for precision power measurements, radio metric measurements and other applications. It has a wider dynamic range and a more accurate square law response than has been available in the past. Other desirable characteristics are high-level dc output with immunity to ground loop problems, fast response times, ability to insert known time constants, and good thermal stability. This article briefly reviews the history of this development work and describes in detail the new detector and its performance.

I. Introduction

Broadband square law detectors are required for precision power measurement and a wide variety of other detector applications such as the Noise-Adding Radiometer (Ref. 1), the 64-m antenna servo boresighting system, antenna gain measurements, etc. All of the following detector characteristics are important and are desired in a single device:

(1) Wide dynamic range.

(2) Accurate square law response over the dynamic range.

(3) Good thermal stability.

(4) High-level dc output with immunity to ground loop problems.

(5) Ability to insert known time constants for radio metric applications.

(6) Fast response times compatible with computer-oriented systems.

No known commercial device has all of these characteristics in a single compact unit. Over the past ten years the Radio Frequency Techniques (RFT) Group (Section 333) has used two types of detectors in an attempt to fulfill the above requirements. Development proceeded slowly over the years, but recent work has culminated in a detector which has all of the above characteristics with acceptable accuracy. This article briefly reviews the history of this development work and describes in detail the new broadband square law detector and its performance.

II. The Early Models

Prior to 1965 a germanium diode detector (Type 1N198 or similar) was used which was matched to a 50-ohm input. Since no dc amplification was used, this detector fulfilled conditions (5) and (6) adequately, but the other conditions were not satisfied. The square law response varied from diode to diode and the accuracy obtained was seldom better than 10%. The detector law varied as much

as 20% with temperature. Due to the low operating voltages (about 10-mV maximum output), the dynamic range was restricted to less than 20 dB. The magnitude of ground loops often exceeded the dc output signal level. Figure 1 is a circuit diagram of one of these detectors and Fig. 2 shows its measured performance. Input power in −dBm is plotted against output voltage in mV in Fig. 2 for three different bandwidths. The response of this diode was not identical with CW and noise input signals (Refs. 2 and 3). In order to solve this problem for the CW power calibration program (Refs. 2 and 3), a different type of detector was used. This was the power meter detector.

Figure 3 is a photograph of the field model of this detector. The detector consists of a commercial power meter/thermistor combination and is still in use in the DSN. Square law response is excellent, and the higher operating voltages (about 1 V) result in immunity from most ground loops. Known time constants consist of simple RC circuits. The power meter detector still has the following severe problems:

(1) *Thermal drift.* The square law characteristic of the power meter relies on a balance between a detection thermistor and a reference thermistor. Any environmental temperature change upsets this balance and reduces the accuracy. The device, therefore, requires frequent zero adjustments.

(2) *Dynamic range.* This is limited to less than 10 dB unless scale changes are made.

(3) *Response time.* The response time, to 67.5% of full value, to an input level change is greater than 100 ms.

III. Recent Detector Development

When low-drift dc amplifiers became available, the construction of a diode detector with high-level output, good thermal stability, and good square law response became feasible. Several approaches were attempted before a practical device was developed. Figure 4 shows a block diagram of one of the recent detectors. The input is fed through step attenuators with an 80-dB range, a wide-band IF amplifier (1 to 110 MHz) with 45-dB gain, and into a detector/amplifier unit. The dc output from this unit is available through a variety of time constant and filter circuits, a typical example of which is shown in Fig. 4. Two outputs have time constants, one of which is variable; two outputs are fast, and the fifth has a frequency proportional to voltage.

Figure 5 is a detailed diagram of the diode detector and dc amplifier block in Fig. 4. This entire circuit is enclosed in a mumetal box for radio frequency interference (RFI) and magnetic shielding. The RF portion of this circuit is RFI-shielded from the remainder, as shown. All outputs from shielded enclosures are through capacitive feed-through connectors. The inner shielded box contains the diode and an isolation transformer. Considerable effort was expended in determining the best diode type from various manufacturers for this detector application. The objective was to find the optimum compromise between sensitivity, repeatability, square law characteristics, stability, drift, etc. A tunnel diode was chosen, type BD-3. The amplifier is an Analog Devices Model 234L.

The entire circuit is packaged in a standard chassis for rack mounting. Provision is made on the front panel for adjustment of the meter sensitivity and detector time constant as well as a dc bias offset. Figure 6 is a photograph of the engineering model.

IV. Performance

A. Dynamic Range and Square Law Response

The square law response of the detector is plotted in Fig. 7. Figure 7 shows output error in dB for a 1-dB input level change as a function of output level. A high-power broadband noise source was fed through a variable attenuator and a measured 1-dB step. The output from this step switch was connected to the input of the detector and the output was monitored in the usual way. The detector was taken over the whole range of its output voltage (0 to 2 V) by adjusting the variable attenuator. Each point on the curve was measured by switching the 1-dB step in and out. The response of a perfect detector would be a line parallel to the x-axis which intersects the y-axis at the 1-dB point. It may be seen from the figure that over the first 10 dB of detector dynamic range the deviation from square law is 0.009 dB, whereas over the whole of the measured dynamic range (60-mV to 2-V output) of 15.6 dB, the error is 0.032 dB. Figure 8 shows the detector square law response for a 30-dB input range. A true square law characteristic is shown by the straight line. This method of presenting the detector response does not have sufficient resolution to show the detector characteristics nor is it accurate, but is shown here for comparison with Fig. 2. It must be noted that the detector is more linear than the IF attenuator used to change the input signal level over the 30-dB range, and, therefore, this figure is more an attenuator characteristic than a detector characteristic. (This detector has been used in a program to measure IF attenuator characteristics; this is

reported elsewhere (Ref. 4)). The data of Figs. 7 and 9 were not taken this way. Each data point in these two figures was obtained by switching the same 1-dB step in and out. Thus neither the accuracy nor the linearity of this step affects the detector output data. With the above reservations in mind, the following departures from square law have been taken from Fig. 8: 0.25 dB over a 20-dB dynamic range and 0.35 dB over a 30-dB dynamic range.

B. Thermal Drift

The Model 234L amplifier shown in Fig. 5 is a chopper-stabilized dc amplifier with a specified drift of 0.1 μV/°C, referred to the input. For a gain of 200 the drift, referred to the output, is 20 μV/°C. Measurements have indicated that the total drift in field installations at Goldstone is less than 0.1 mV per week.

Figure 9 shows the effect of dc offsets on the detector performance. These data were taken and plotted in the same way as the data of Fig. 7. That is, the graph is a plot of detector output error against output signal level for a 1-dB step change in input signal. It may be seen from the figure that detection performance can be improved only over a small operating range by imposing a dc offset.

The time constant networks shown in Fig. 4 are made up of resistance–capacitance circuits and are inserted by using isolation amplifiers. Since these amplifiers operate at a gain of 1 or 5, thermal drifts are insignificant.

C. Ground Loops

Since the voltage levels in the detector are all about one volt, most ground loops are insignificant.

D. Response Time

Full voltage (to 99.9% output level) rise time is less than 300 μs. Faster low-drift amplifiers are now becoming available and it is expected that this response time will soon be lowered to less than 10 μs.

E. High-Level Output

The 0- to 10-V output shown in Fig. 4 is used for operation with an analog-to-digital converter for computer applications (Ref. 1). This output, therefore, has a low-pass filter to prevent clock feedback from the computer.

V. Thermal Stability

Figures 10 and 11 show the effect of temperature changes on the detector output. They are plots of output voltage drift as a function of detector chassis temperature.

The detector chassis was placed in an oven and the output voltages monitored with the input terminated. The oven temperature was changed in a series of step functions, and measured at a representative point on the detector chassis. The detector temperature and outputs were recorded on a strip chart recorder. Temperatures were allowed to stabilize for several hours before data were taken. When a step change was made in the oven temperature, the detector required some settling time before coming to a steady output voltage. For a 25°C step change in temperature, the detector settling time is approximately 60 min, and typical peak transient deviations are approximately 200 μV.

Figure 10 shows voltage drift data for a typical production model of the detector and Fig. 11 shows similar data for a selected good unit. In both figures the crosses are for the 10-V output, and the circles are for the 2-V V/F output. The output voltage scales for the two sets of data are, therefore, different. It must be noted that even in the production unit the use of the amplifier to yield a 10-V output does not seriously detract from the stability of the detector.

VI. Conclusion

A broadband constant-law detector has been constructed for precision power measurements, radio metric measurements, and other applications. It has a wider dynamic range, and a more accurate square law response over that dynamic range than has been available in the past. It has other desirable characteristics such as high-level dc output with immunity to ground loop problems, fast response times, ability to insert known time constants, and good thermal stability.

A subsequent article will discuss the operation of this detector in a programmable system which accounts for detector deviation from square law response to yield an instrument whose accuracy is 0.3%.

References

1. Batelaan, P. D., Goldstein, R. M., and Stelzried, C. T., "A Noise-Adding Radiometer for Use in the DSN," in *The Deep Space Network*, Space Programs Summary 37-65, Vol. II, pp. 66–69. Jet Propulsion Laboratory, Pasadena, Calif., Sept. 30, 1970.

2. Stelzried, C. T., and Reid, M. S., "Precision Power Measurements of Spacecraft CW Signal Level with Microwave Noise Standards," *IEEE Trans. Instrumentation and Measurement*, Vol. IM-15, No. 4, pp. 318–324, Dec. 1966.

3. Stelzried, C. T., Reid, M. S., and Nixon, D., *Precision Power Measurements of Spacecraft CW Signal With Microwave Noise Standards*, Technical Report 32-1066. Jet Propulsion Laboratory, Pasadena, Calif., Feb. 15, 1968.

4. Stelzried, C., Seidel, B., Franco, M., and Acheson, D., "Improved RF Calibration Techniques: Commercial Precision IF Attenuator Evaluation," in *The Deep Space Network Progress Report*, Technical Report 32-1526, Vol. XII, pp. 74–82. Jet Propulsion Laboratory, Pasadena, Calif., Dec. 15, 1972.

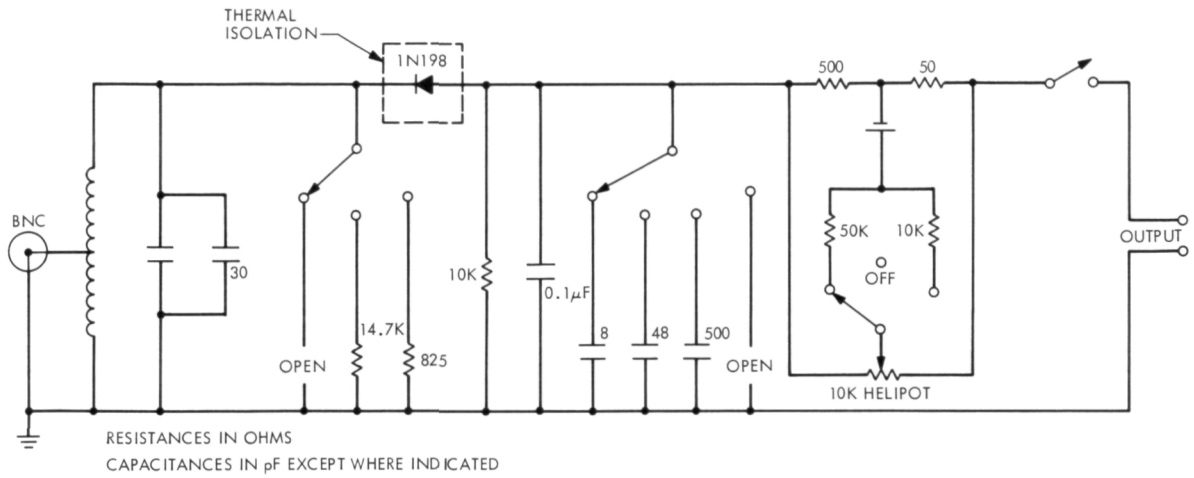

Fig. 1. Circuit diagram of early diode detector

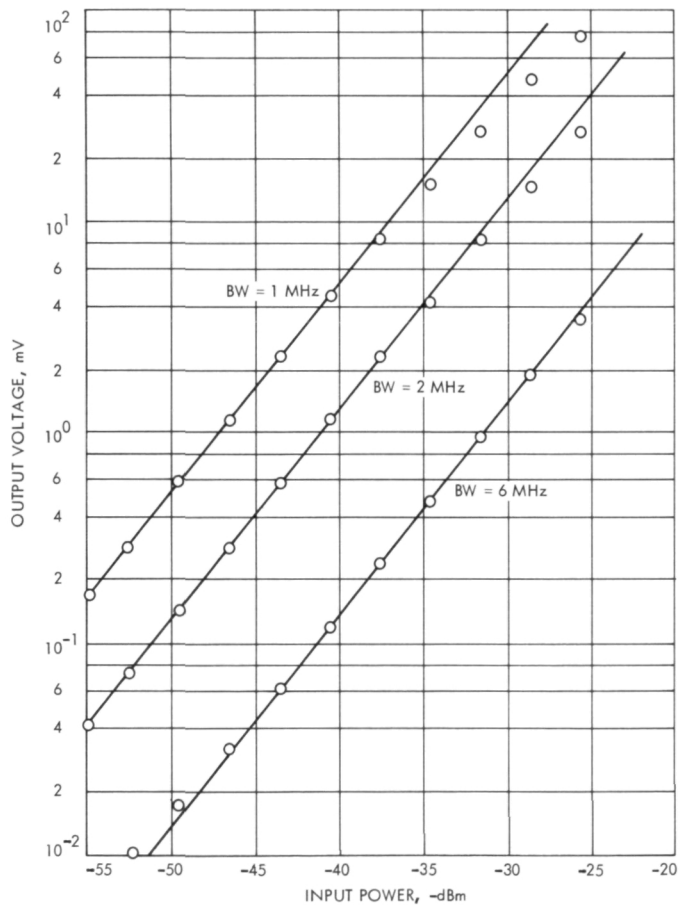

Fig. 2. Performance characteristics of an early detector

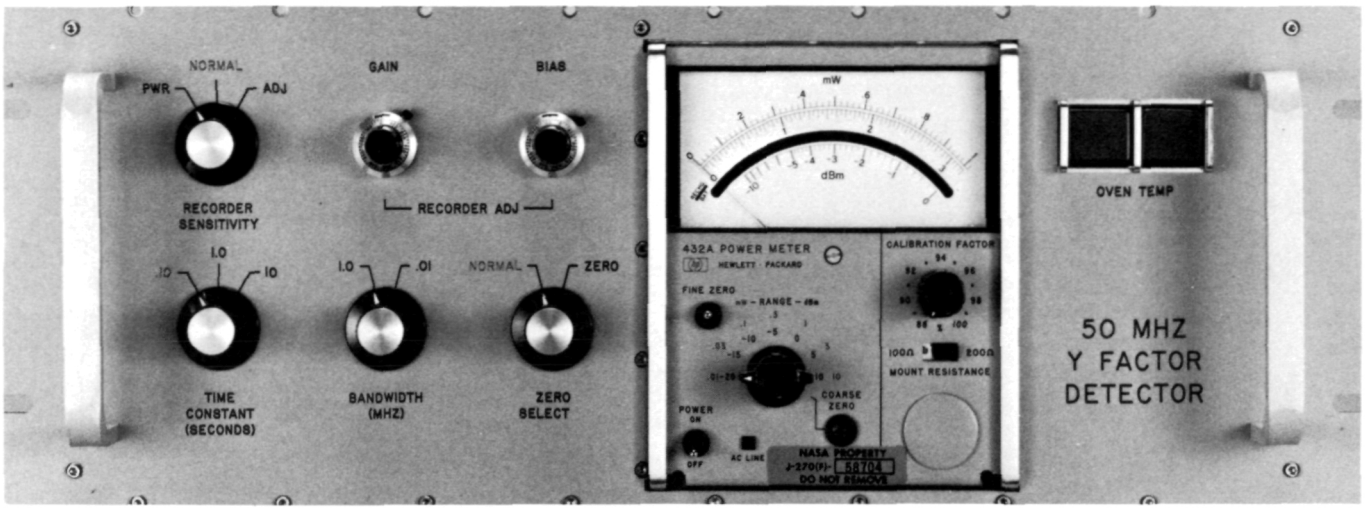

Fig. 3. Field model of the power meter detector

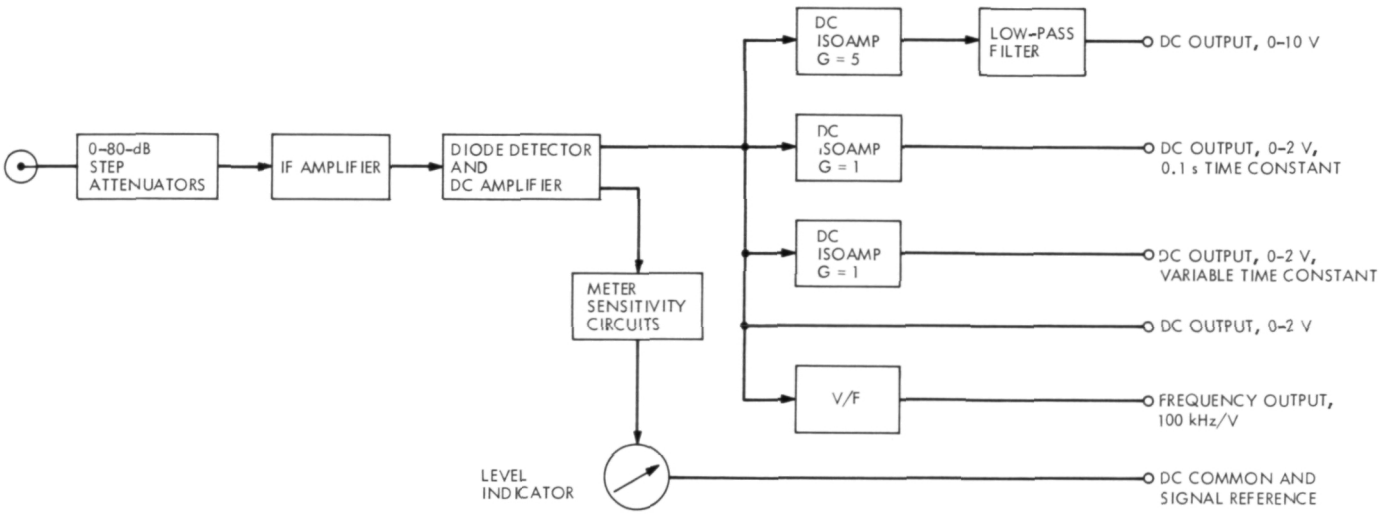

Fig. 4. Block diagram of the broadband square law detector

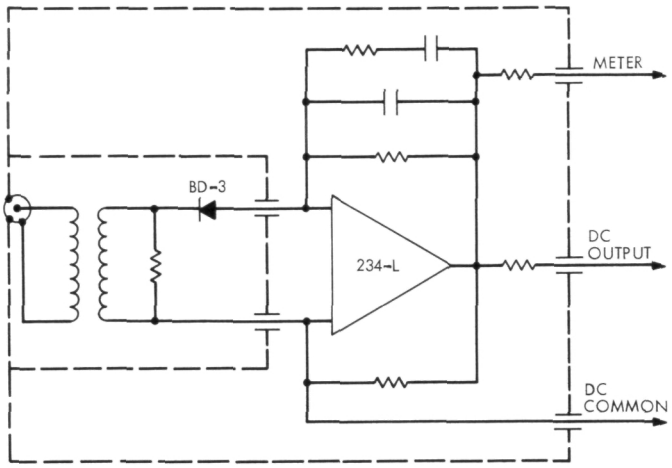

Fig. 5. Diode detector and dc amplifier

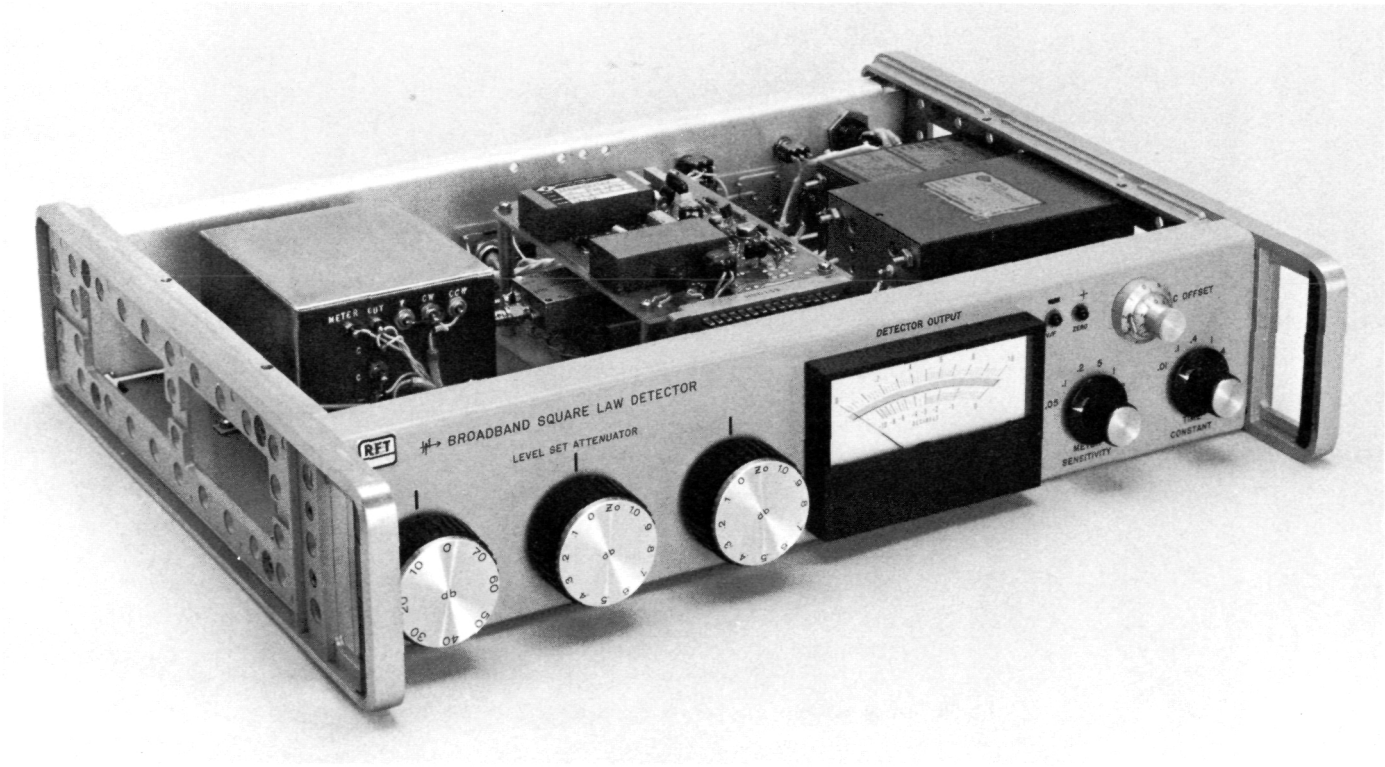

Fig. 6. Photograph of engineering model

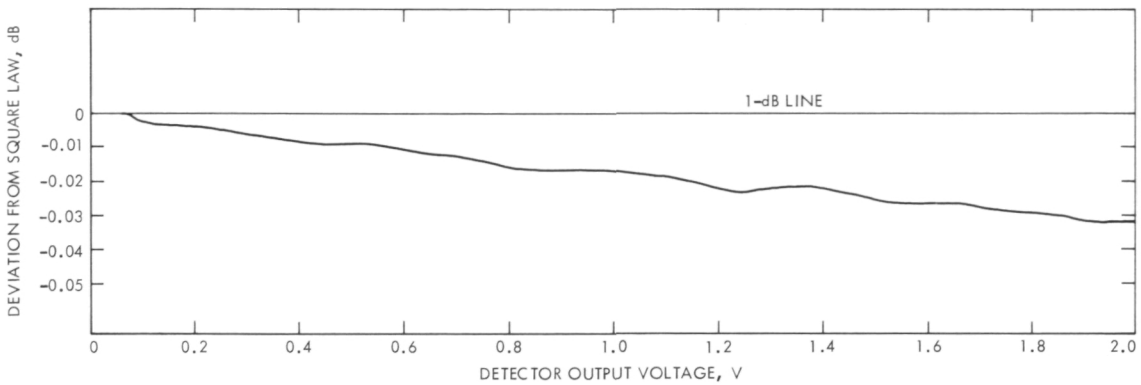

Fig. 7. Output error for 1-dB input level change as a function of output level

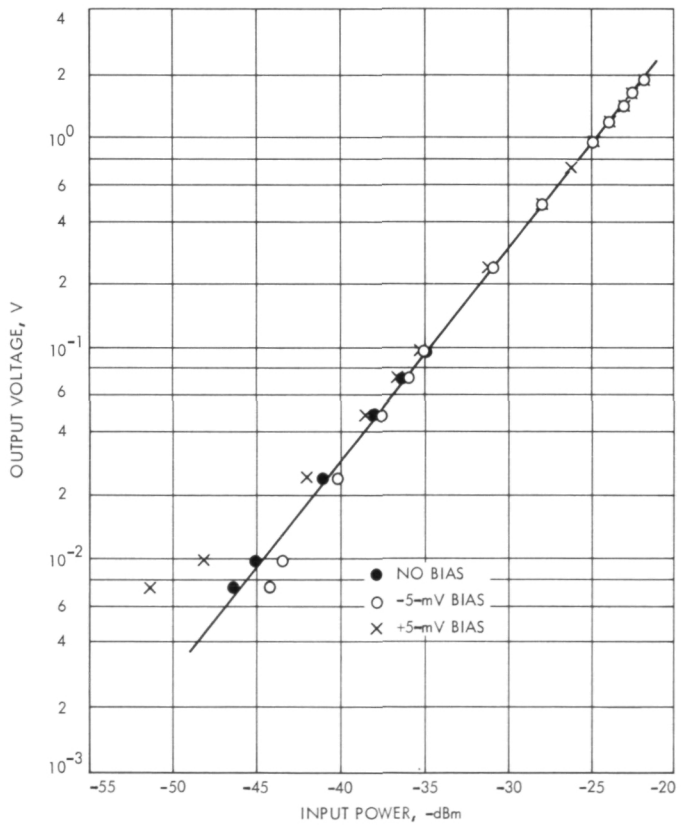

Fig. 8. Square law response for a 30-dB input range

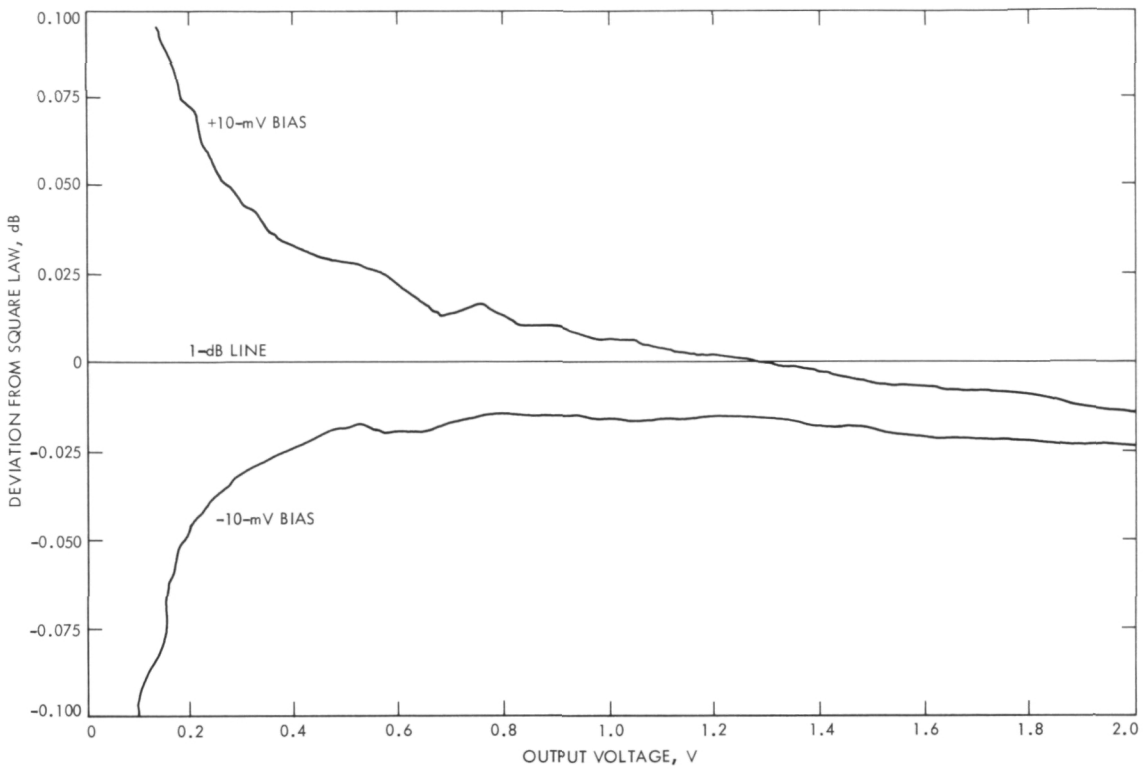

Fig. 9. The effect of dc offsets on the detector response

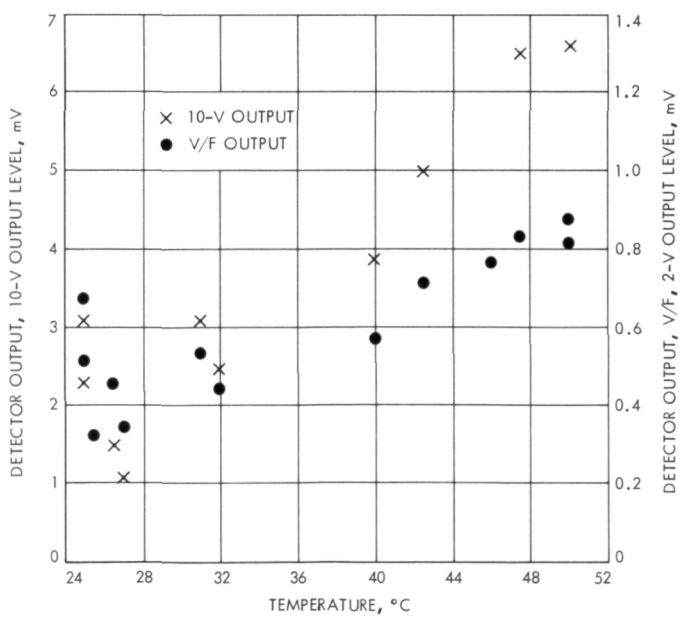

Fig. 10. Output drift as a function of temperature: typical production unit

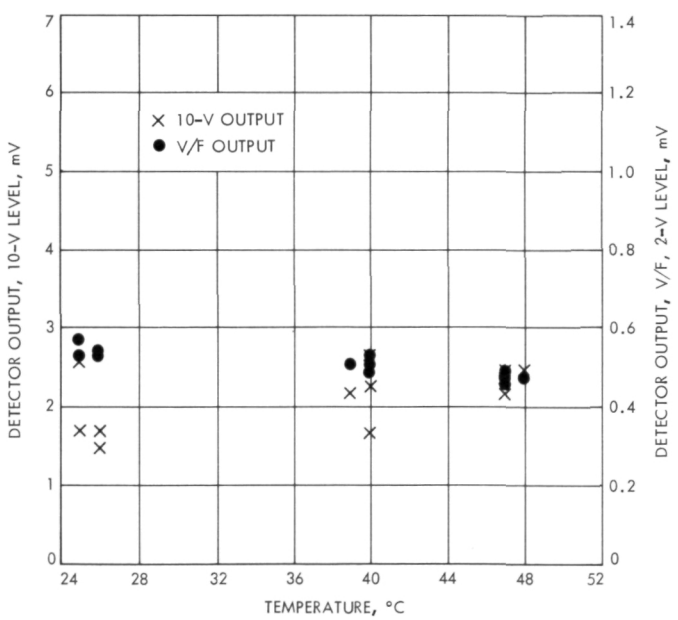

Fig. 11. Output drift as a function of temperature: selected unit

Faraday Rotation Observations During the 1970 Pioneer 9 Solar Occultation

A. R. Cannon
University of California, Berkeley

C. T. Stelzried
Communications Elements Research Section

J. E. Ohlson
Naval Postgraduate School

The Faraday rotation of the Pioneer 9 S-band signal was measured during the December 1970 solar occultation using the NASA/JPL 64-m Goldstone antenna. Steady-state Faraday rotation was significant over the region of 4–12 solar radii, reaching a maximum value of about 100 deg at 4 solar radii. Two transient Faraday rotation events were observed and related to solar phenomena. The Pioneer 9 steady-state Faraday rotation was similar to that observed during the November 1968 Pioneer 6 solar occultation. The first Pioneer 9 transient appears to be of the same form, magnitude, and duration as the three remarkable W-shaped Pioneer 6 transient events. The second Pioneer 9 transient was smaller in amplitude, had an S-shaped curve of longer duration, and in general was unlike the previous events. These two events occurred at approximately 6 solar radii. The Pioneer 6 observations did not extend beyond 12 solar radii, while Pioneer 9 was tracked to approximately 64 solar radii. No transient events were observed in this outer region.

The region of the solar corona from a few solar radii out to where the solar wind flow becomes super-Alfvenic at about 20–30 solar radii has been very difficult to study. An understanding of the processes occurring in this region is important because it is here that the solar wind is formed and many complex phenomena may occur. The recent advent of deep space probes and the completion in 1966 of the NASA/JPL 64-m parabolic dish at Goldstone, California, have greatly expanded our observational capabilities by enabling us to probe the corona with very narrow band continuous wave signals, of one or more distinct frequencies, and having definite polarizations. The present construction of other large antennas and the use of spacecraft like Helios, which are specifically designed to study the near-Sun region, promise to contribute significantly to our understanding of solar phenomena.

The solar occultation of Pioneer 6 in 1968 provided the first opportunity to observe the Faraday rotation of a linearly polarized S-band signal in the solar corona. Simultaneous measurements of polarization (Ref. 1) and

of spectral effects (Ref. 2) produced dramatic results and established the deep space probe as a valuable tool for studying the elusive coronal region near the Sun. The success of the Pioneer 6 experiment encouraged a major effort during the Pioneer 9 occultation in December 1970.

It has been shown (Ref. 3) that the net polarization rotation of a spacecraft signal traversing the solar corona is effectively given by the quasi-longitudinal approximation, in which the polarization rotation is proportional to the product of the electron density and the magnetic field component along the ray path, integrated along the entire line of sight from the probe to the observer:

$$\Omega_L = \frac{QL}{f^2}\int N(s)B_L(s)\,ds$$

where

Ω_L = Faraday rotation, deg

f = signal frequency, Hz

N = electron density, M^{-3}

B_L = longitudinal component of magnetic field, gauss

Q = 135.4816

L = units scaling factor for ds ($L = 1$ if ds in meters, $L = 6.9598 \times 10^8$ if ds in solar radii)

ds = element of length along ray path

Thus, a large Faraday rotation could result from either a high electron density or a large net longitudinal field component. On the other hand, high electron densities and strong magnetic fields could produce no net Faraday rotation if the field orientations are such as to cancel out in the integral.

The spacecraft is spin-stabilized with its antenna normal to the ecliptic plane. It transmits a linearly polarized S-band signal at 2.3 GHz, which was received on the 64-m Goldstone antenna. The polarization angle of the received signal was measured with the closed-loop tracking polarimeter developed for the Pioneer 6 occultation (Ref. 4). This polarimeter is very responsive and is capable of tracking the polarization angle to hundredths of a degree. It is uncertainties in the effect of Earth's ionosphere that really limit our ability to measure small Faraday rotation effects in the corona and prevent us from seeing the interplanetary medium far from the Sun (Ref. 5).

Figure 1 shows the orbits of both Pioneers 6 and 9 relative to a fixed Sun–Earth line. Tracking of Pioneer 9 was begun on October 2, 1970, when the spacecraft line of sight was 64 solar radii west of the Sun, and continued through January 28, 1971, when the line of sight was 24 solar radii east of the Sun. The Pioneer 9 observations were extended much farther from the Sun than Pioneer 6, but no coronal effects could be distinguished from the ionosphere in this outer region.

Daily averages of the observations referred to the plane of the ecliptic (Ref. 6) made within 12 solar radii of the Sun are shown in Fig. 2. These observations are uncorrected for the Earth's ionosphere. As the Pioneer 9 line of sight moved within 12 solar radii, the polarization measurements appeared to increase slightly above the maximum ionospheric effect. At 7.5 solar radii, the signal polarization angle dropped below 90 deg for the first time, and decreased steadily to about 100 deg below predicts when the spacecraft was lost at 4.3 solar radii. The last data points could be regarded as having ambiguities of multiples of 180 deg, since the polarization angle could have rotated by such amounts during the intervals between spacecraft set and spacecraft rise. The Pioneer 9 signal was reacquired 12 days later at 5.3 solar radii on exit with a polarization angle of 120 deg—again ambiguous by multiples of 180 deg. The polarization decreased steadily to 87 deg and then increased to the normal ionospheric level at about 12 solar radii.

The steady-state rotation observed during the Pioneer 9 occultation was remarkably similar in both sense and magnitude to that seen by Pioneer 6 two years earlier. The Pioneer 6 observations were analyzed in conjunction with coronal magnetic field constructions based on both solar magnetograph data and interplanetary spacecraft data. These efforts resulted in an electron density model for the corona at the time of the observations and provided a test of K. H. Schatten's coronal model (Ref. 7). A similar analysis is now being carried out on the Pioneer 9 data. This should provide a further comparison of coronal models and also provide some idea of the changes that occur during the solar cycle.

Two large transient events were also observed, one on Day 345 at 5.9 solar radii west of the Sun, and the other on Day 360 at 6.2 solar radii east of the Sun. Figure 3a shows the Pioneer 9 data for Day 345. Two periods of high system temperature caused by the antenna side lobe structure rotating across the Sun are apparent in the periods of high scatter at the beginning and end of the track. The system temperature rose to about 400 K during these periods and the receiver lock was very weak. Near the end of the track the polarization angle

decreased rapidly by about 45 deg, returned to its original level in about 30 min, and then was decreasing rapidly again as the spacecraft set. Due to the poor receiver lock, our classification of this as an event caused by the solar corona is based largely on operator confidence. The very large amplitude and negative direction eliminate the ionosphere as a possible source.

This event, insofar as it was observed, appears to be very similar to the three remarkable W-shaped impulsive events seen during the Pioneer 6 solar occultation in 1968. These are shown in Fig. 4. Each has an amplitude of about 40 deg and a duration of about 2 h. In view of the fact that these events occurred at such different distances from the Sun, and over a period of eight days, during which the Sun rotated by about 110 deg, thus changing the coronal regions probed by the ray path, it seems remarkable indeed that all three events should have the same sense of rotation, signature, amplitude, and period. The Pioneer 6 events also produced considerable broadening of the signal spectrum, observed simultaneously by R. M. Goldstein of JPL. Unfortunately no spectral measurements were made during the entry phase of the Pioneer 9 occultation.

The Pioneer 6 events have been associated with solar flares on or near the limb of the Sun nearest the signal ray path (Refs. 8 and 9). The average propagation speeds of the disturbances resulting from these identifications range from 80–340 km/s. The Pioneer 9 event is not so readily identified with possible flare sources due to the virtual absence of flares in western longitudes. The only flare occurring near the limb was a subflare which would require a disturbance speed of 22 km/s. There was a larger flare near the central meridian that would require a disturbance propagating across some 90 deg of solar longitude with an average speed of 1100 km/s. Of course, the event could have been caused by a flare which occurred beyond the limb, or might be due to sources not directly associated with optical flares. It is worth noting that several active regions which had previously produced a number of subflares were located just beyond the west limb, and there was very bright coronal green line emission on both the northwest and southwest limbs several hours before the Pioneer 9 transient.

There are a number of possible interpretations of these events. They could, for example, be caused by pairs of flares or by flares having two or more maxima. They could also be due to high-density clouds of electrons, kinks in magnetic field lines, or magnetic reconnection. One particularly interesting suggestion has been made by K. H. Schatten (Ref. 10), who pointed out that the events could be explained by a coronal magnetic bottle. A flare, occurring in a bipolar region, might carry field loops across the line of sight, until the tension in the field lines is finally able to contain the expansion and then contract back across the line of sight again. Such a bottle might explain many coronal phenomena, including the storage of cosmic ray particles.

The fact that the same type of event has been observed in four of the five Faraday rotation transients seen so far suggests that this may represent some fundamental characteristic of solar activity—as opposed to mere coincidence—and may provide a new insight into the mechanisms of such phenomena as flares.

A fundamentally different transient event was observed on Day 360. This is illustrated in Fig. 3b. The receiver lock was good during this event, but the event was still in progress when the spacecraft set. Even so, the observed duration (about 5 h) is much longer than any of the previous events. The amplitude is much less and the signature is quite different. The polarization angle decreased by about 7 deg and then increased to about 7 deg above the original level and appeared to be leveling off as the track ended.

There were several subflares and a flare near the west limb which might be considered as possible sources. The most likely candidate was a flare of importance 1N which occurred within 18 deg of the east limb and would require a disturbance velocity of 120 km/s, which is consistent with the Pioneer 6 identifications. There were two active regions beyond the limb which became visible on Day 361 and produced several subflares on succeeding days. There was very little green line emission during this period.

Again, there are several possible explanations, including a large kink in the field lines, a compression followed by a rarefaction as might occur in a shock wave, and an X-type configuration or closed magnetic loop that might result from magnetic reconnection. Fortunately, we also have measurements of the signal spectrum during this event. These measurements have yet to be analyzed, but it is hoped that the behavior of the spectrum will shed additional light on the mechanisms responsible for the event.

One of the intriguing questions still to be answered is "How far from the Sun can these transient events be

observed?" One of the reasons the Pioneer 9 observations were extended to such large distances from the Sun was to search for impulsive events in this outer region. The fact that no events were observed does not preclude the possibility of their existence since none may have occurred, or they may have been so diffuse as to be obscured by ionospheric effects. There were three flares and a number of subflares which occurred near the east limb during the exit phase without producing noticeable polarization effects. The disturbances may not have crossed the line of sight during our view periods or they may have passed unobserved due to the magnetic field geometry involved. At any rate, not every eligible flare produces an observable effect on the signal, particularly at distances beyond 10 solar radii. This suggests that perhaps some flare disturbances do not escape from the Sun. The physical interpretation of the transient events, or lack of events, as the case may be, is still in progress. It is hoped that these unique observations will provide some new insights into coronal processes and their effects on deep space (probe) tracking at small Sun–Earth–probe angles.

References

1. Levy, G. S., Sato, T., Seidel, B. L., Stelzried, C. T., Ohlson, J. E., and Rusch, W. V. T., "Pioneer 6: Measurement of Transient Faraday Rotation Phenomena Observed During Solar Occultation," *Science*, Vol. 166, pp. 596–598, 1969.
2. Goldstein, R. M., "Superior Conjunction of Pioneer 6," *Science*, Vol. 166, pp. 598–601, 1969.
3. Rusch, W. V. T., and Stelzried, C. T., "Net-field Polarization in a Magnetically Biased Plasma," *Radio Science*, Vol. 7, pp. 1131–1141, 1972.
4. Ohlson, J. E., Levy, G. S., Stelzried, C. T., "A Tracking Polarimeter for Measuring Solar and Ionospheric Faraday Rotation of Signals from Deep Space Probes," *IEEE Trans., Instrumentation and Measurement* (to be published).
5. Mulhall, B. D., and Stelzried, C. T., "The Ionospheric Electron Content as Determined From Faraday Rotation Measurements of an Earth Satellite and Deep-Space Probe," in *The Deep Space Network*, Space Programs Summary 37-64, Vol. II, pp. 21–24, Jet Propulsion Laboratory, Pasadena, Calif., Aug. 31, 1970.
6. Stelzried, C. T., Sato, T., and Abreu, A., "Transformation of Received Signal Polarization Angle to the Plane of the Ecliptic," *J. Spacecraft Rockets*, Vol. 9, No. 2, p. 69, Feb. 1972.
7. Stelzried, C. T., et al., "The Quasi-Stationary Coronal Magnetic Field and Electron Density as Determined from a Faraday Rotation Experiment," *Solar Physics*, Vol. 14, No. 2, Oct. 1970.
8. Schatten, K. H., "Flare Identification Associated with Coronal Disturbances," *Science*, Vol. 168, pp. 395–396, 1970.
9. Pintér, S., *Observations of Moving Solar Plasma Clouds at 10 Solar Radii*, Technical Report Geophysical Institute of the Slovak Academy of Science, Hurbanovo, June 1972.
10. Schatten, K. H., "Evidence for a Coronal Magnetic Bottle at 10 Solar Radii," *Solar Physics*, Vol. 12, p. 484, 1969.

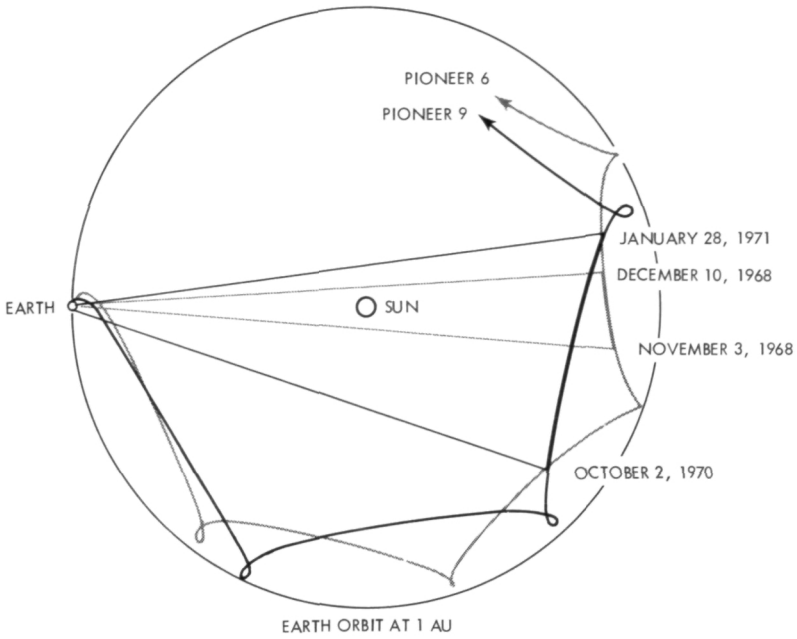

Fig. 1. Projection of fixed Sun–Earth line trajectories on plane of ecliptic

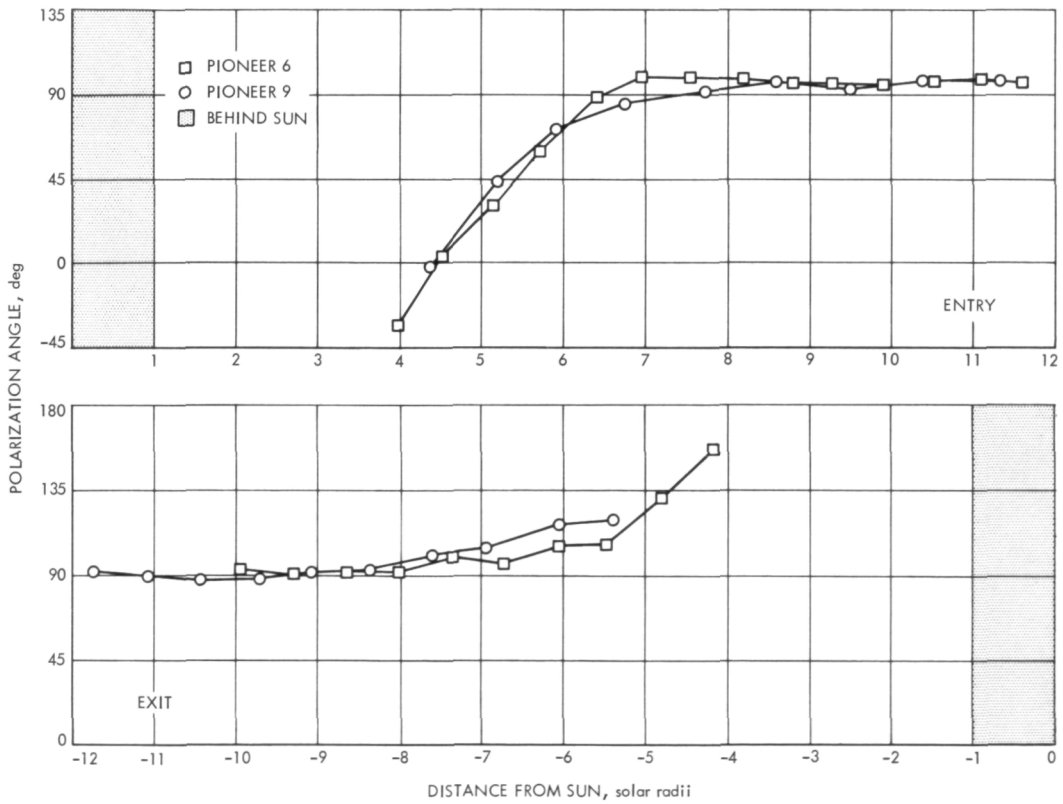

Fig. 2. Pioneer 6 and 7 polarization angles (referred to plane of ecliptic, uncorrected for ionosphere) vs distance from Sun

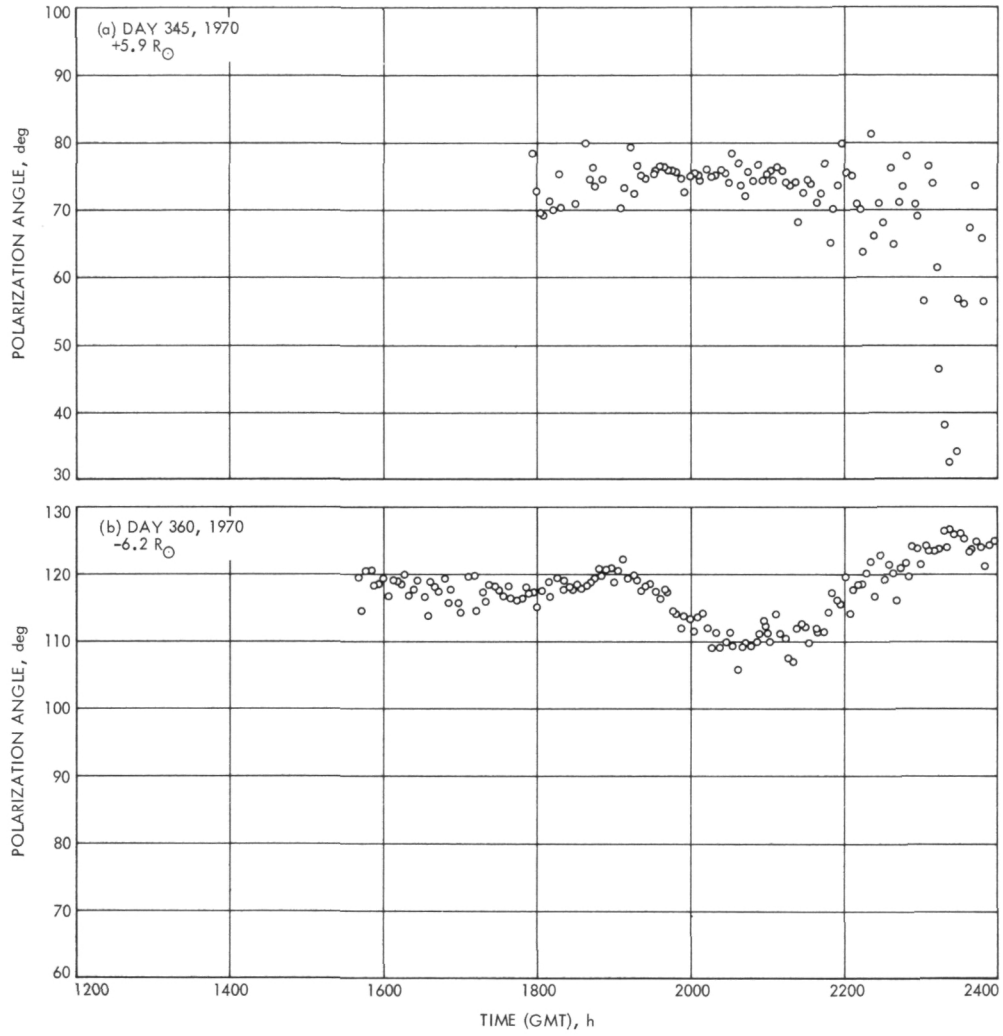

Fig. 3. Pioneer 9 signal polarization (200-s data points, referred to ecliptic, and uncorrected for ionosphere) vs time

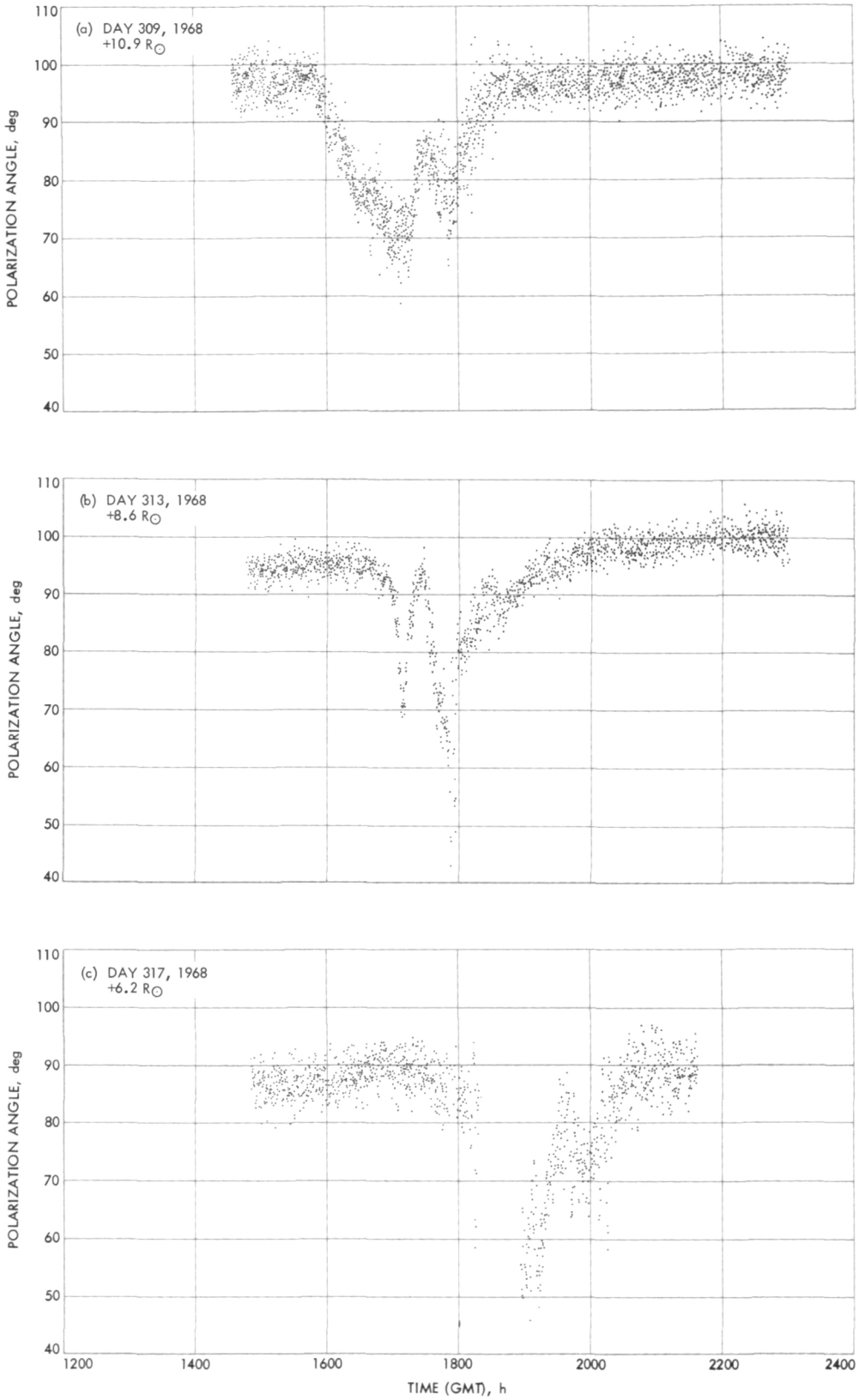

Fig. 4. Pioneer 6 signal polarization (10-s data points, referred to ecliptic, and uncorrected for ionosphere) vs time

Measurement of High Isolation

G. S. Palecki
R.F. Systems Development Section

A technique for measuring high isolation values of X-band components has been demonstrated. The test technique utilizes available commercial test equipment and provides swept-frequency data. Isolation up to 125 dB is readily measured.

The development and procurement of improved microwave components for the DSN continues to be an ongoing process. As performance specifications have become more stringent, acceptance test requirements placed on suppliers have also become more demanding. The reliable measurement of high microwave isolation is one such test that has been difficult to accomplish in the past utilizing commercial test equipment. The measurement requires equipment having high sensitivity and low internal noise for adequate resolution. This report describes an improved test technique which makes use of more recent commercial equipment. It is useful for measuring isolation values up to 125 dB. This technique was used for measuring waveguide switch isolation as reported in a previous article (Ref. 1).

A substitution technique was used to measure the isolation-vs-frequency characteristic of three WR-125 waveguide switches procured from Logus Manufacturing Corporation. The setup shown in Fig. 1 includes a swept-frequency X-band signal source, variable attenuators for calibration of isolation levels, a network analyzer for signal detection, and an X-Y recorder for data output. In addition, a traveling wave tube amplifier was used to increase the input signal level, and a tunnel diode amplifier was used to provide predetection gain and improve the system noise figure. All waveguide and coax connections were carefully checked before measurement to insure against leakage which could affect test results.

The measurement involves reference calibration of the setup with the switch under test in the through position and 90 to 120 dB of attenuation in the signal line. The switch is then moved to the bypass position and the attenuators are set to zero attenuation, allowing full power to flow through the switch into a load. The signal now measured by the detector is leakage through the waveguide switch.

Test results have shown this series of waveguide switches to exhibit isolations of at least 100 dB with a maximum isolation of between 120 and 125 dB at some frequencies (Ref. 1). This test setup has proven to be extremely useful because of the wide dynamic range and continuous sweep-frequency coverage, which readily identifies any anomalies in isolation characteristics.

Reference

1. Hartop, R. W. "X-Band Waveguide Switches," *Deep Space Network Progress Report*, Technical Report 32-1526, Vol. XV, pp. 48–50. Jet Propulsion Laboratory, Pasadena, Calif., June 15, 1973.

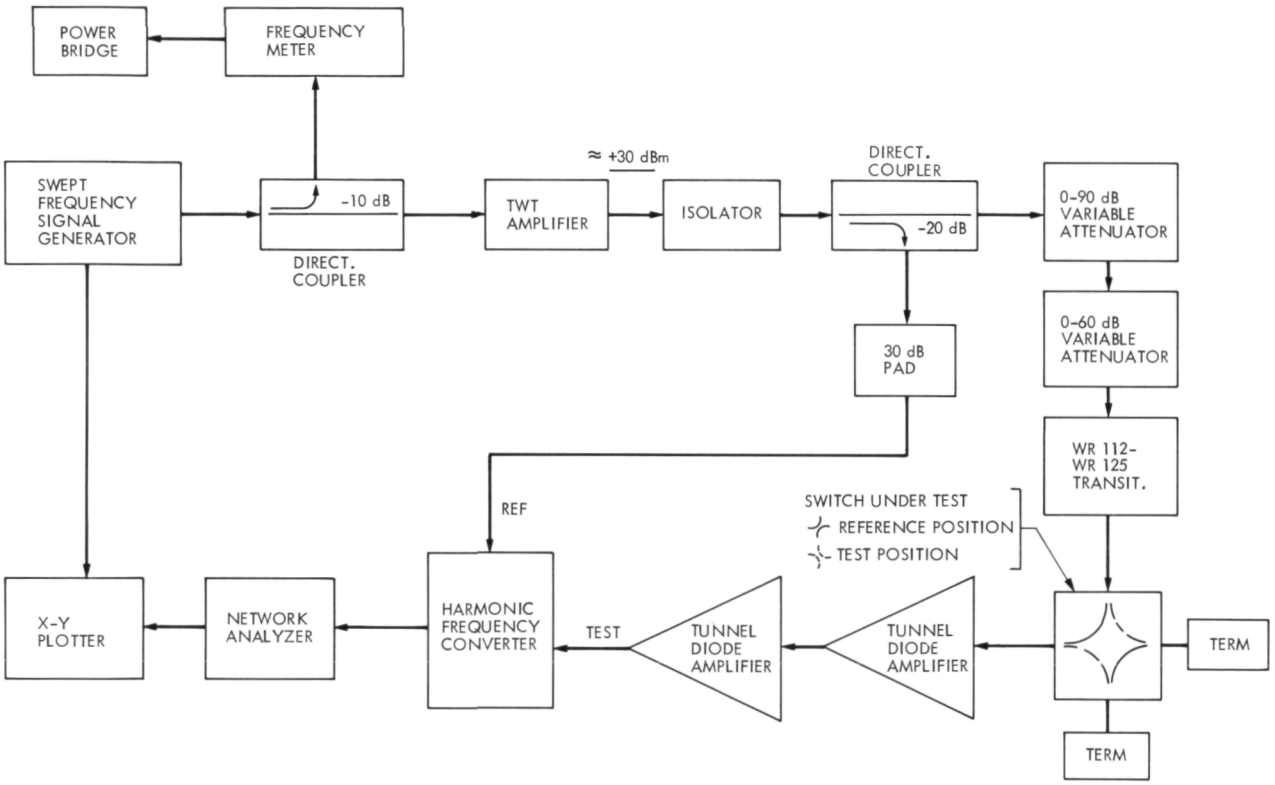

Fig. 1. Isolation test block diagram

Waveguide Installation Measurements at DSS 14

J. R. Loreman
R.F. Systems Development Section

The match of the DSS 14 waveguide installation has been affected by several waveguide changes necessitated by the installation of an additional X-band filter. A series of tests has been conducted as part of an effort to reduce transmitter back power.

An X-band filter has been recently added to the transmitter waveguide installation at DSS 14 (see "X-Band Filter," by R. L. Leu, in this issue of the DSN Progress Report). The purpose of the filter is to prevent X-band transmitter harmonics from affecting receiver operation for the Mariner Venus/Mercury 1973 (MVM'73) mission. The installation required several waveguide runs to be modified, changing their electrical length. Following the installation, station personnel began reporting high back power at certain of their operating frequencies. Reflected power data prior to the waveguide modifications is not available. High-power tests with and without the X-band filter show approximately the same reflected back power except with a shift in frequency. An investigation of the nature of the back power problem has been initiated.

As part of the investigation into reducing the back power, a series of swept-frequency waveguide voltage standing wave ratio (VSWR) measurements has been made. The VSWR measurements were made on all portions of the waveguide installation which affect the back power. Both the SMT and SPD cones were included. Figure 1 shows the waveguide runs and components associated with the high-power transmitter. The measurements were made by the installation of an S-band waveguide reflectometer and an S-band precision load, where appropriate, at selected points in the waveguide installation. Figure 2 shows the configuration of the test equipment used in the measurements. The network analyzer was used to measure the return loss of the reflected signal. The X-Y plotter provided a trace of return loss vs sweep generator frequency. The frequency band covered by the measurements was 2110 to 2120 MHz.

The test results of interest are presented in graphical form in Figs. 3 through 7. In these figures, the X-Y plot has been converted to directly show VSWR and theoretical transmitter back power at 400 kW. All measurements are referenced to the 400-kW transmitter output flange. Figures 3 and 4 show the results for the waveguide runs

to the inputs of the S-Band Megawatt Transmit (SMT) and S-Band Polarization Diversity (SPD) cones respectively. Figure 5 shows the results for the total waveguide run through the SMT cone. Figures 6 and 7 show the results for the total waveguide runs through the SPD cone for right circular polarization (RCP) and linear feed polarizations respectively.

The data indicates that the SPD configuration in particular should be investigated further to find means to improve the VSWR of the installation to a more acceptable limit. The next effort will be the development of a tuning device usable at the high powers employed in the DSN that can be used to improve the match of the waveguide and cones.

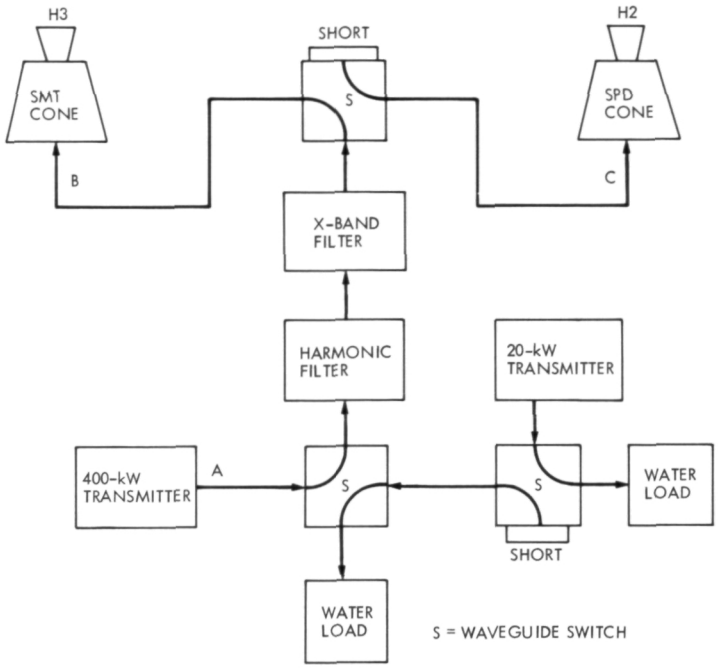

Fig. 1. Transmitter waveguide at DSS 14

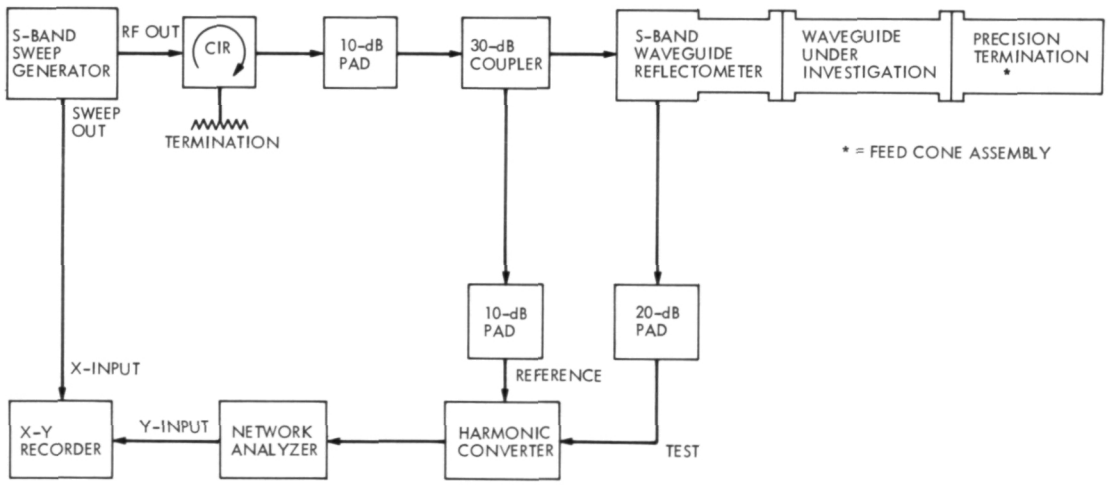

Fig. 2. Test equipment configuration swept-frequency waveguide VSWR measurements, 2110 to 2120 MHz

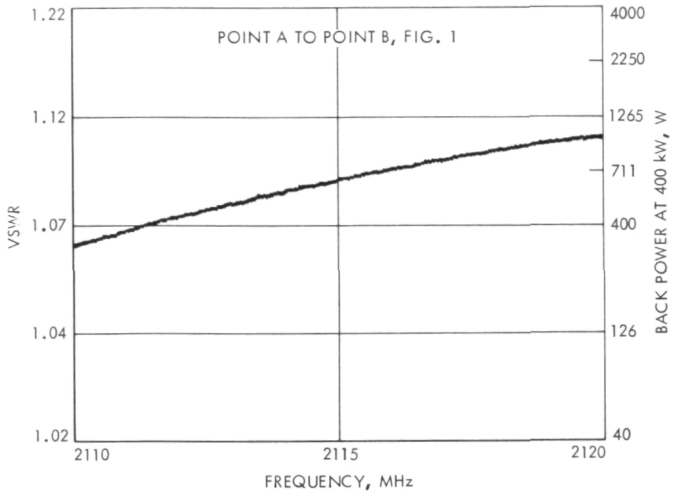

Fig. 3. VSWR, 400-kW transmitter to SMT cone input

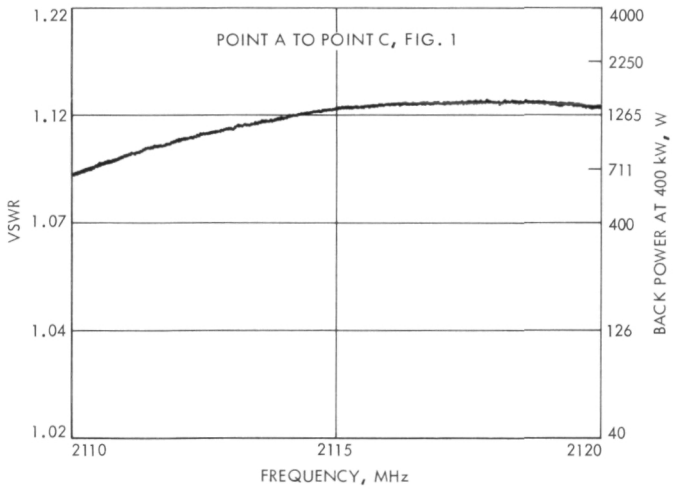

Fig. 4. VSWR, 400-kW transmitter to SPD cone input

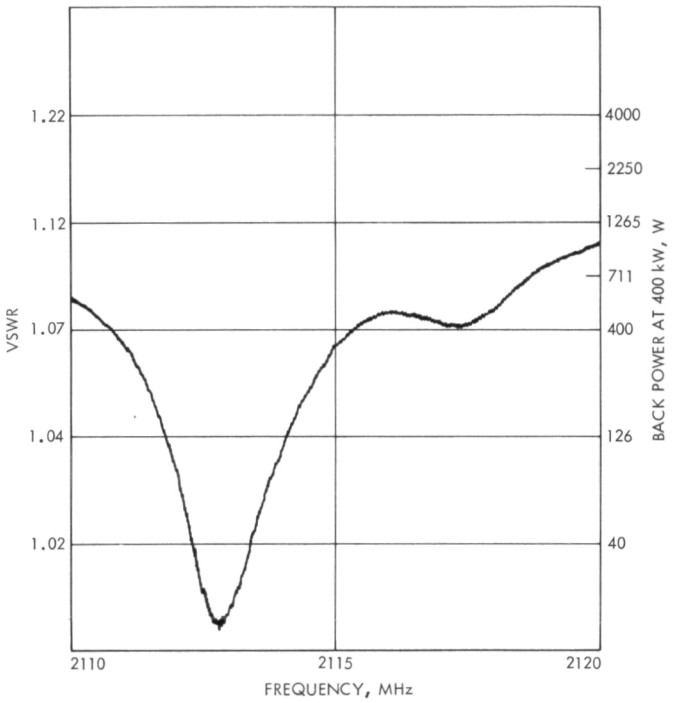

Fig. 5. VSWR, 400-kW transmitter through SMT cone

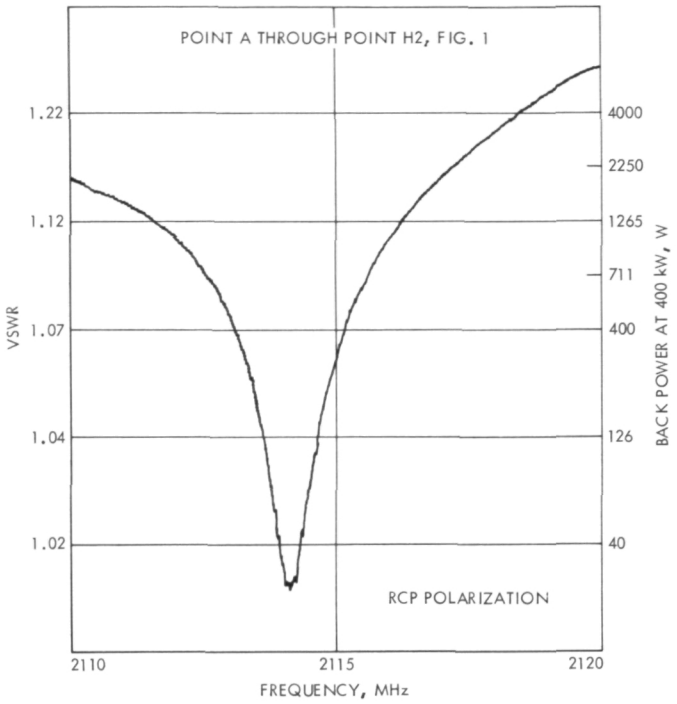

Fig. 6. VSWR, 400-kW transmitter through SPD cone

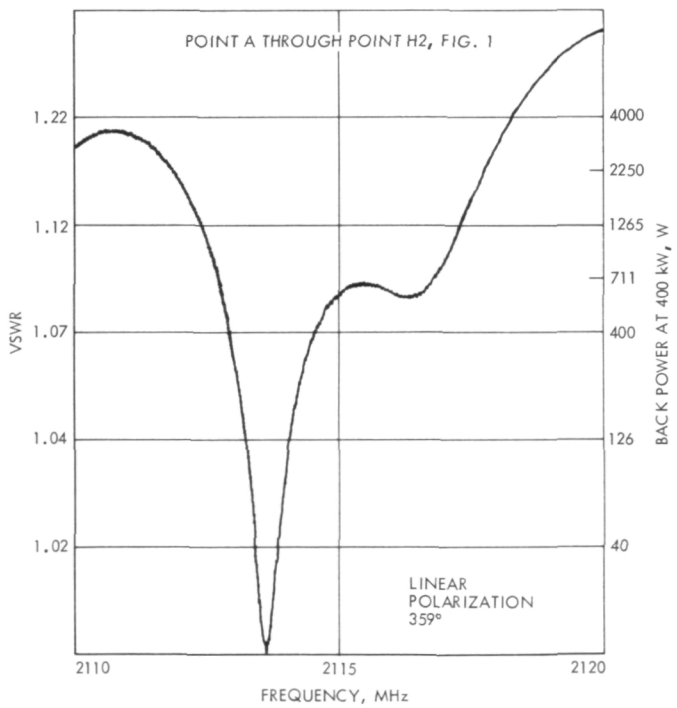

Fig. 7. VSWR, 400-kW transmitter through SPD cone

DSN Research and Technology Support

E. B. Jackson
R.F. Systems Development Section

The activities of the Development Support Group, at the Goldstone Deep Space Communications Complex, are discussed and progress noted on continuing efforts. Activities include planetary radar support for the Mariner Venus/Mercury 1973 Missions, preparation for a station automation demonstration, sky survey activity, dual-carrier activity on the 26-m-diameter antenna and progress thereof. Also discussed are changes in the Faraday rotation data collection system, repairs and support of the DSS 14 400-kW transmitter, and science support for later interpretation of the results from encounter observation of Jupiter by Pioneers 10 and 11.

During the two months ending June 15, 1973, the Development Support Group was engaged primarily in operation of the Venus station as the reduction of personnel effected in February 1973 gradually caused activities at the Microwave Test Facility (MTF) to cease. Only special tests in support of dual-carrier work and machine-shop support for the Venus 400-kW transmitter continued to be effected at the MTF.

I. In Support of Section 331

A. Planetary Radar

Continuing support of the Mariner Venus/Mercury 1973 spacecraft missions, eight Venus ranging missions, for a total of 56 h of range-data gathering, were performed. Difficulty was experienced with the DSS 14 programmed oscillator and development receiver. The programmed oscillator problem was solved by repair of broken and loose wiring and replacement of the synthesizer. The development receiver was removed, temporarily replaced by an older version, and moved to Venus station for repair.

B. Pulsar Automation Demonstration

Early in FY-74, it is planned to demonstrate station automation and remote control by configuring and operating the Venus station from JPL (Building 238). The mission planned for this demonstration is a pulsar track and, in preparation for this demonstration, personnel from Section 331 have been utilizing the Venus 26-m-diameter antenna, and the SDS-930 and SDS-910 computers and

associated receivers, expending 24 h in testing thus far. Also in preparation for this demonstration, a teletype circuit has been installed and tested between Building 238 and the Venus station. Station control during the demonstration will be exercised by a computer located in Building 238 using this teletype circuit as a communications link.

II. In Support of Section 333

Sky survey. Using automated data collection techniques, the 26-m-diameter antenna and associated receiver are used to perform sky surveys for long term testing of the equipment and techniques involved, obtaining radio-source data as a result of such testing. With the antenna placed in a fixed position (which is changed for each weekend's run), the system is started when the station is closed down for the weekend. As the Earth's rotation sweeps the antenna's beam, data are collected on radio sources within the beam. During this last two-month period, 452 h of data were thus collected and sent to Section 333 for analysis.

III. In Support of Section 335

A. Dual-Uplink Carrier Testing

With system cleanliness established and maintained (Ref. 1), "quiet" operation was continued until, after approximately two weeks, the system performance worsened again back to the −160 dBm region. Testing disclosed that the diplexer was at fault, even though it had undergone repair: particularly soft soldering of the matching posts to the waveguide walls was performed, and care was taken to form a fillet and avoid sharp edges. Since a replacement diplexer would not be available until early May, other tests, particularly tape tests, were scheduled.

Two kinds of tape are available for taping of the antenna surface joints, one of which is conductive and one of which has an insulating coating on the adhesive side. Testing the relative noise and intermodulation product generation characteristics of each, the insulated tape proved superior as long as the coating was not damaged by overly aggressive application.

In early May another diplexer, which had also undergone the soft soldering and filleting treatment, arrived and was installed. The system again became "quiet" (intermodulation products weaker than −180 dBm) and has remained so.

During this test period, which has involved a total of 323 h, a pair of rotary joints was also installed to verify its suitability for this type of low-noise service. It proved to be noise free and is still in the system. All of the elements that make up a feedcone (feedhorn, waveguide, switches, diplexers, filters, and rotary joints) have now been proven to be capable of noise- and intermodulation-product-free operation.

B. 400-kW Transmitter Automation Testing

In anticipation of automatic operation of the 400-kW transmitter by a PDP-11 minicomputer, interface testing and software development are underway, with testing being performed at the Venus station. The interface has been completed, a test program has been completed, and automatic startup, high-voltage runup, and partial operation has been achieved during 108 h of testing during the past two months.

IV. In Support of Section 391

Faraday rotation data collection. Data collection continues on a 24-h-per-day, seven-day-per-week basis, but the Stanford receiver has been reoriented to receive ATS-5, while the dual-channel phase-lock receiver continues to receive ATS-1. The data from both receivers continue to be punched onto paper tape and are sent to JPL for data reduction and analysis. The data are used to provide corrections to spacecraft ranging and doppler data to compensate for the effects of Earth's ionosphere. Such effects, if ignored, would cause probable location errors ranging from 5 km for a spacecraft at Venus encounter to 35 km for a spacecraft at Jupiter encounter.

V. In Support of Section 422

A. DSS 14 DSN 400-kW Transmitter Repair Support

In fulfillment of DSS 13's role as the "DSN High-Power Maintenance Facility," repairs have been made to a klystron socket tank for a 400-kW klystron. Additionally, a spare DSN 400-kW klystron has been received from Varian Associates and has undergone complete testing and parameter characterization at DSS 13. This tube was turned over to DSS 14 for installation as necessary. Testing was accomplished in the newly completed "test bed" built at DSS 13 for this purpose. Resembling a transmitter cabinet in general appearance, this device is especially designed to enable versatile testing of all components, such as klystrons, socket tanks, directional couplers, and arc detectors, which make up a 400-kW transmitter.

B. DSN Spares Tabulation

Working during the midnight shift when the Venus station is normally closed, personnel from Section 422 have been utilizing our SDS-930 computer, which has been temporarily equipped with four magnetic-tape units, to update a master listing of DSN spares. This effort is now complete and required 176 h of usage to update the spares lists for changes required by installation of Engineering Change Orders (ECOs), deletion, and addition of equipment.

VI. In Support of Section 825

Science support. Use of the DSS 13 26-m-diameter antenna and Noise Adding Radiometer continues for collection of baseline data on the radiation from Jupiter. These data, taken at 2295 MHz, will be used to aid interpretation of the radiation measurements at Jupiter to be reported by Pioneers 10 and 11 spacecraft. Observation of Jupiter and several radio-source calibrators, such as 3C48, 3C123, 3C147, and 3C309.1, consumed a total of 160 h during the past two months.

Reference

1. Jackson, E. B., Price, A. L., and Kolby, R. B., "DSN Research and Technology Support," in *The Deep Space Network Progress Report*, Technical Report 32-1526, Vol. XV, pp. 138–141. Jet Propulsion Laboratory, Pasadena, Calif., June 15, 1973.

High Power Switching and Combining Technique

R. B. Kolbly
R.F. Systems Development Section

The X-band radar will radiate 400-kW of output power by paralleling two 250-kW klystron amplifiers. The klystron outputs will be summed into a single waveguide by properly phasing in a 3-dB short-slot hybrid. To obtain preliminary data on combining the outputs of two klystrons and switching the power between the antenna and water load, tests were conducted using two S-band 20-kW klystrons. These test results also apply at X-band since the hybrid is bilateral and linear.

I. Introduction

The X-band radar, described in Ref. 1, will radiate 400-kW of output power by paralleling two 250-kW klystron amplifiers (see article on *X-Band 250-kW Klystron*, by R. H. Smith, in this issue). The klystron outputs will be summed into a single waveguide by properly phasing in a 3-dB short-slot hybrid.

In addition, there is a requirement for long pulse modulation (i.e., 10 seconds on/10 seconds off). This type modulation, when applied to the beam voltage and/or RF drive on/off switching, drastically reduces the life of the klystron since the thermal time constant of the massive copper collector is approximately one second. One technique for maintaining the life expectancy of the klystron and providing the on/off modulation capability is to switch the phase of one input to the combiner by 180 deg as illustrated in Fig. 1. This switches the total output power of 400 kW to the water load. The residual power going to the antenna will be a function of the hybrid isolation, relative phase of the two inputs, and the voltage standing wave ratio (VSWR) at the outputs of the hybrid.

To obtain preliminary data on combining the outputs of two klystrons and switching the power between the antenna and water load (Fig. 1), tests were conducted using two S-band 20-kW klystrons. These test results also apply at X-band since the hybrid is bilateral and linear.

II. Summary

The test results indicate that using the combiner as a high power switch will provide at least a 30-dB isolation at the antenna port with very little difficulty. The total output power can be maintained within ±0.1 dB with a feedback loop on the phase controller. The relative input phase to the hybrid must be controlled within ±5 deg.

III. Test Procedure

As stated, the tests were to obtain preliminary data on using a short-slot hybrid as a power combiner and a high power switch. The tests were conducted using two S-band 20-kW klystrons (5K70SG) operating into a 90-deg 3-dB short-slot hybrid. The S-band hybrid is similar to the one designed for the X-band radar. For these tests the two output ports of the S-band hybrid were terminated with water loads, one load simulating the antenna. In order to combine the output of each klystron into water load 1 (WL 1), the relative phase at the hybrid inputs must be 90 deg, as shown in Fig. 2. The relative phase was controlled by adjusting the helix voltage on one of the TWT driver amplifiers. The following tests were conducted:

(1) Determine power variation at (summed port) WL 1 as a function of the relative phase of the two inputs.

(2) Determine power variation at WL 2 (difference port) as a function of the relative phase of the two inputs.

(3) Determine amplitude stability of the power in WL 1 as a function of time and without feedback control for phase correlation.

Both klystrons were tuned broadband, saturated at 10 kW, and operated at a frequency of 2115 MHz.

IV. Test Results

The results of the first test are shown in Fig. 3. The radar specification for amplitude variation is ±0.5 dB. As can be seen from the data, amplitude variation due to phase variation is about ±0.1 dB at ±10% relative phase change. Figure 4 shows the power level at WL 2 as the relative input phases are changed. The ratio of this power to the power at the sum port WL 1 is the measured isolation of the hybrid. The data show the isolation at the difference port (WL 2) to be between 26 dB and 30 dB for a ±5-deg relative change.

One point to consider is that the S-band hybrid used for these tests has 7 dB less isolation than the X-band hybrid when tested (low power) with matched loads.

A three-hour stability test was run monitoring the total power at the summed port (WL 1) with no feedback loop to the phase controller. The power variation at WL 1 was less than 0.1 dB, indicating from Fig. 3 that the relative phase variation was less than ±10 deg. However, the relative phase stability required to maintain minimum power at the difference port, whether it be the antenna or water load as shown in Fig. 1, requires a maximum relative phase change of ±5 deg. Therefore, it appears that a closed loop system for the phase controller is required.

Figures 5 and 6 give the performance of the hybrid as a result of changing various parameters in the 5K70SG klystron. These data were obtained by using the standard transmitter drive and output monitoring circuitry in connection with the network analyzer connected to the input and output RF sample ports shown in Fig. 2. Figure 5 gives drive, relative phase shift, and output power as a function of beam voltage for saturated operation. Figure 6 shows power output and relative phase shift as a function of drive level at a fixed beam voltage.

Reference

1. Wiggins, C. P., "X-Band Radar Development," in *The Deep Space Network Progress Report,* Technical Report 32-1526, Vol. XII, pp. 19–21. Jet Propulsion Laboratory, Pasadena, Calif., Dec. 15, 1972.

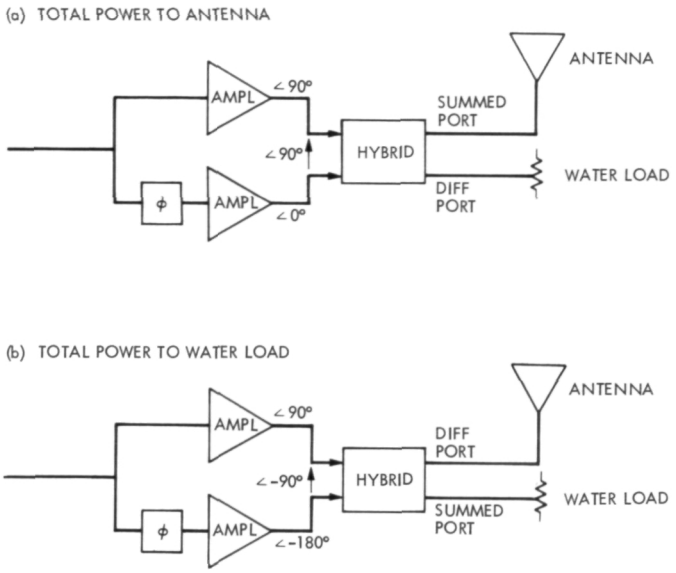

Fig. 1. Illustration of switching output power between antenna and water load

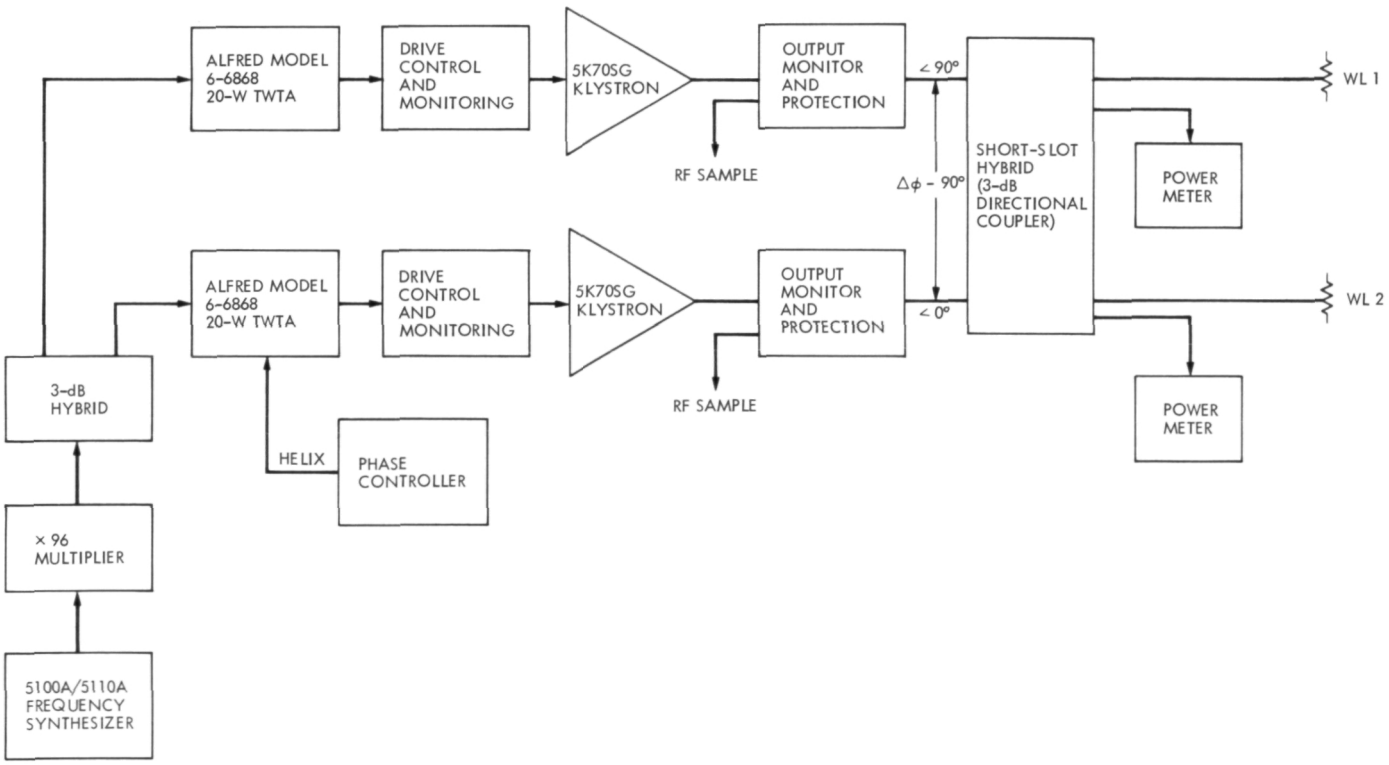

Fig. 2. Phased-transmitter test configuration

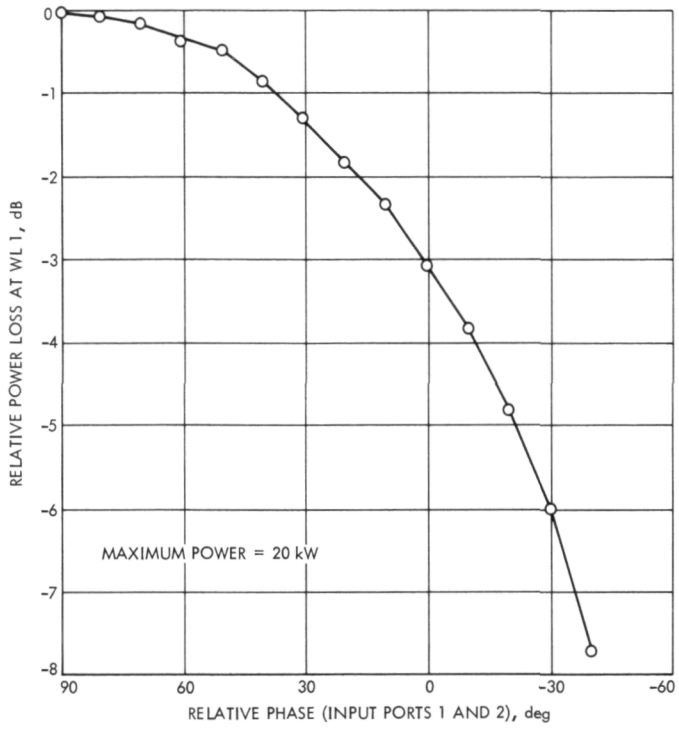

Fig. 3. Results of first test

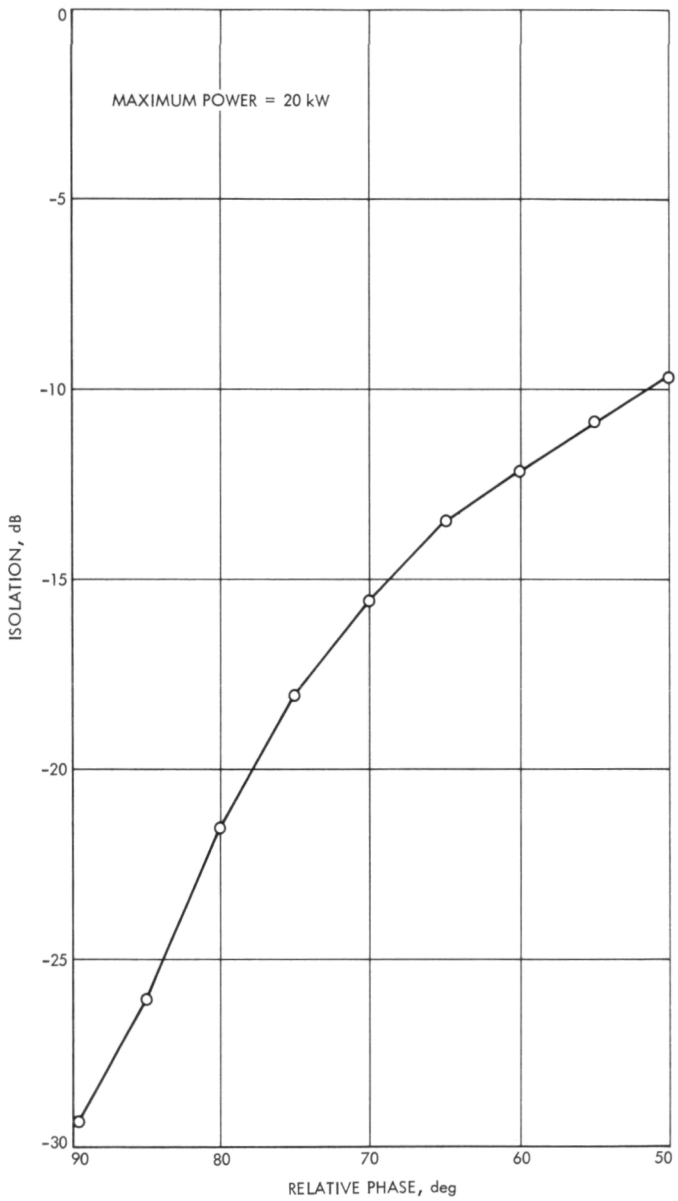

Fig. 4. Power level at WL 2 as relative input phases are changed

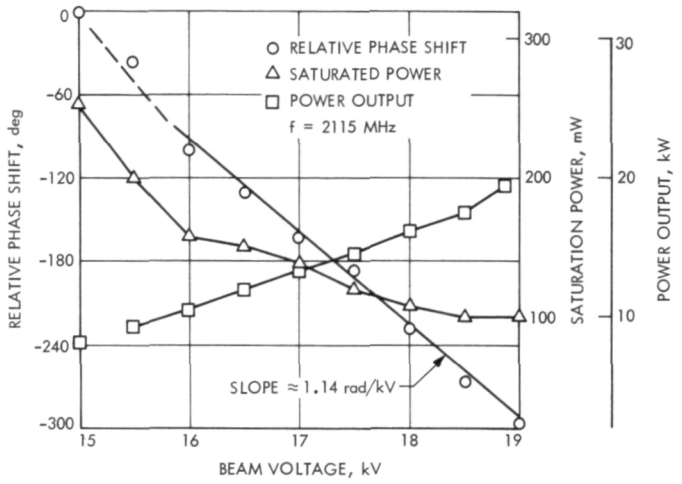

Fig. 5. Performance of 5K70SG klystron for saturated operation

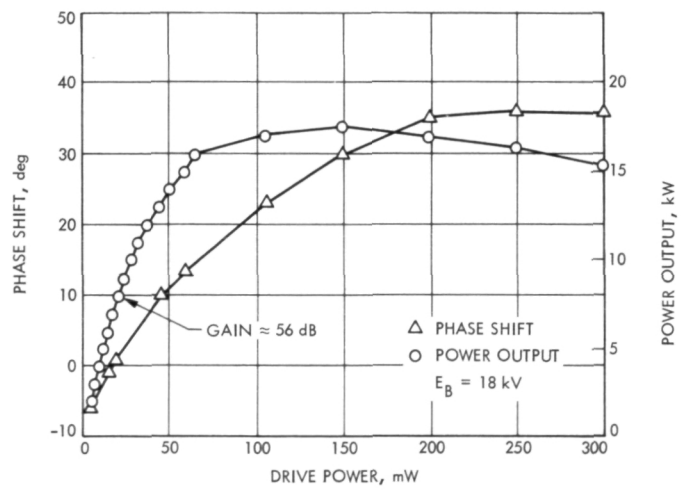

Fig. 6. Performance of 5K70SG klystron at fixed beam voltage

A Universal Dump Program for Minicomputer Software Debugging

C. C. Klimasauskas
Communications Systems Research Section

Low-cost minicomputers in wide variety are finding application in control and monitoring tasks ranging from laboratory testing to network operation. One significant problem which arises from this circumstance is that a significantly larger minicomputer system than is needed to perform the primary tasks must be acquired to do convenient software development. Consequently, work has been underway for some time to facilitate software development for the minimal configuration minicomputer using the Medium-Scale Xerox Data Systems Sigma 5. This article describes a general-purpose memory display program which runs on the Sigma 5 to dump memory images of minicomputer software to a printer or other man-readable device. The dump is formatted, as specified by control-card options, into machine-language instructions, character strings, or virtually whatever word/byte/field format is meaningful to the current problem.

I. Introduction

Low-cost minicomputers in wide variety are finding application in control and monitoring tasks ranging from laboratory testing to network operation. One significant problem which arises from this circumstance is that a significantly larger minicomputer system than is needed to perform the primary tasks must be acquired to do convenient software development. Consequently, work has been underway for some time to facilitate software development for the minimal configuration minicomputer using the Medium-Scale Xerox Data Systems Sigma 5. A general introduction to this activity may be found in Ref. 1. We expect ultimately to provide direct-coupled support where the minicomputer software is generated on the larger machine and is then loaded into the minicomputer and exercised via intercomputer communication links. One debugging tool which is useful, even if tedious to use, is a memory dump or display. This article describes a general-purpose memory display program which runs on the Sigma 5 to dump images of minicomputer software to a printer or other man-readable device. The dump is formatted, as specified by control-card options, into machine-language instructions, character strings, or virtually whatever word/byte/field format is meaningful to the current problem.

II. An Overview of the Processor

The universal dump program (UDP) looks at each record of the core dump (CD) as a single bit string. The user partitions this bit string into smaller units called words. Each word is partitioned further into fields (contiguous bit strings). Associated with each field is a field number and with that number a field conversion mode. Each word is indexed by an address which is specified dynamically by telling the UDP where to find the first address of the word or statically through specification. The address may be incremented by one or the number of bytes per word as specified through the addressing mode. The user has the option of indicating the conversion mode for the address, and the word, in addition to each field.

The first step in this process is description of the target machine. This phase generates tables which describe word size, byte size, field characteristics, conversion modes and all other data required to generate the dump. This phase produces syntax error messages and warnings. The following sections give a detailed description of the syntax of target machine description and listing format specification.

The next phase analyzes the tables for consistency and interpolates where possible to produce a complete set of consistent tables to drive the actual dump generator. This phase may find fatal specification errors which will prevent further execution. It also produces warning messages for nonfatal errors. A following section contains a complete description of all error messages.

Phase three is the actual routine for producing the dump listing. This program acts as a set of table-driven subroutines under the control of a single control routine. Figure 1 describes these program steps diagramatically. The program is implemented in Xerox Data Systems META-SYMBOL on the Sigma 5 computer to be run under the Batch Processing Monitor. On the right-hand side of Fig. 1 is the overlay structure of the program. Each of the files to produce this resides on magnetic tape in the standard Xerox Data Systems 7-track labeled-tape format. The source file for each overlay is followed by its corresponding binary file (in parentheses).

III. Conventions for Syntax Definition

This section presents some general comments which describe the meaning of the constructions used in defining syntax.

(1) The bracket construction:

[ ] indicates that those items contained within the brackets are optional

[. . .] indicates indefinite continuation of the optional construction in which this is imbedded.

(2) The brace construction:

$$\left\{\begin{array}{l}\text{option 1}\\ \text{option 2}\\ \quad .\\ \quad .\\ \quad .\\ \text{option}\end{array}\right\}$$ indicates that exactly one of the options indicated *must* be chosen.

(3) Upper case literals and symbols:

These are key words and delimiters which *must* occur exactly as shown.

(4) Lower case phrases and letters:

These are representative of other constructions which must be supplied according to elsewhere defined syntax. For instance, the phrase "usgc" occurs many times in the description of the syntax. This phrase represents a numeric constant and has the syntax described at the beginning of Section IV.

(5) Blanks or spaces:

Unless specifically noted, blanks are *not* allowed between characters. Three exceptions:

(a) ␣ signifies that exactly one blank is mandatory.

(b) ^ signifies that one or more blanks are optional.

(c) The blank occurs as part of a string as defined for the syntax of the particular statement. For example, see "constant literal field" under PRTDEF in Section IV.

IV. The Syntax of Machine Description and Listing Format Specification

Before describing the syntax, some general comments about constants, control cards, and comment cards are presented.

There are two classes of constants: (1) explicit or specified and (2) implicit. The explicit or specified constant will be denoted by "ussc" and the implicit constant by "usgc." The syntax of each of these is given below:

$$\text{usgc::}\left\{\begin{array}{ll}\text{[blank]} & \text{decimal digit [decimal digit [. . .]]}\\ \text{D} & \text{decimal digit [decimal digit [. . .]]}\\ \text{O} & \text{octal digit [octal digit [. . .]]}\\ \text{X} & \text{hexadecimal digit [hexadecimal digit [. . .]]}\end{array}\right\}$$

$$\text{ussc::} \left\{ \begin{array}{l} \text{decimal digit [decimal digit [...]]} \\ \text{octal digit [octal digit [...]]} \\ \text{hexadecimal digit [hexadecimal digit [...]]} \end{array} \right\}$$

as specified by the syntax of the statement.

Control cards must always have an asterisk in column one. Blanks are not allowed in control cards except where specifically noted. If the definition of a control card requires more than one physical card, continuation cards must not have an asterisk in column one. All other cards will be printed exactly as punched and may be used for documentation purposes.

As we consider in detail the syntax of each statement, we will first define its purpose and make general comments, then give the actual syntax and describe the various options which are possible. As we proceed, it may be helpful to study the decks and resulting dumps shown in Figs. 2 and 3.

A. WORD Specification (Target Machine Description)

This statement simply describes the length in bits of each word of the target machine. Since these are partitions of a continuous bit string, they are referred to as p-words or "partion words." (When each p-word is printed, first the address of the word is printed, then the contents, then the alphanumeric representation of the contents, and finally the user-defined fields). The syntax is as follows:

$$\text{*WORD} = \text{usgc}$$

where usgc is the number of bits per target machine word.

B. BYTE Specification (Target Machine Description)

This card is optional and is used for the purpose of computing the target machine address of the current p-word. This card must be used if byte addressing is specified. (See ADDRESS specification.) The syntax is as follows:

$$\text{*BYTE} = \text{usgc}$$

where usgc is the number of bits per target machine byte.

C. ADDRESS Specification (Target Machine Descriptor and Listing Format Specification)

This card defines the addressing mode of the target machine for the purpose of generating a pseudoaddress for the current p-word on the dump listing. Two modes are available: Byte and Word (default) addressing. Byte addressing increments the listing location counter by the number of bytes per word for each successive instruction. The conversion mode for the address can be optionally specified. The syntax is as follows:

$$\text{*ADDRESS} = \left\{ \begin{array}{l} \text{BYTE} \\ \text{WORD} \end{array} \right\} \left[, \left\{ \begin{array}{l} \text{HEX} \\ \text{DEC} \\ \text{OCT} \end{array} \right\} \right]$$

D. CHAR and SPECIAL Specifications (Target Machine Descriptors)

The CHAR card defines the actual width of a character and the number of right-justified significant bits needed to decode the character. For instance, ASCII characters are eight bits wide; however, the right seven bits actually contain all the character information. Three widely used character codes have been incorporated into the program. Provision is made for user-defined character conversion codes. The syntax of the CHAR specification is as follows:

$$\text{*CHAR} = \left\{ \begin{array}{c} \text{ANSCII} \\ \text{ASCII} \\ \text{EBCDIC} \\ \text{BCD} \\ \text{SPCL} \end{array} \right\} [(\text{usgc}_1,\text{usgc}_2)]$$

where

$\text{usgc}_1 \equiv$ the width of a character in bits.

$\text{usgc}_2 \equiv$ the number of right-justified significant bits per character.

If SPCL is specified, the actual binary-to-character conversion table must be specified. This is done through the SPECIAL card. The syntax is as follows:

$$\text{*SPECIAL} = \text{usgc}$$
$$\text{␣ character string}_1$$
$$\text{␣ character string}_2$$
$$\vdots$$
$$\text{␣ character string}_4$$

where

usgc ≡ the number of characters per character string. Because of the physical limitations of a card, this is at most 79.

␣ ≡ a required space. The first column must be blank.

character string$_i$ ≡ the ith contiguous string of characters in the binary-to-alphanumeric conversion vector. The jth character[1] in the character conversion vector should be (a) a period, if no valid extended alphanumeric character corresponds to the target machine's internal binary representation of j or if the character is not printable, or (b) the actual character if the target machine's internal binary representation of j corresponds to that character. (For example: in EBCDIC, for $j = 253$, the internal binary representation of j is 1111 1101 and does not correspond to a valid character, so the 253rd character in the conversion vector is a period. For $j = 240$, the internal binary representation of j is 1111 0000. This corresponds to the character "∅"; hence, the 240th character in the conversion vector is ∅.)

E. ROTATE Specification (Target Machine Preprocessing Descriptor)

In certain modes of operation, the halfwords may be swapped due to the method of transmission. This occurs, for instance, in the I/O processes of the PDP-11. It may also be desirable to rotate the contents of each word before breaking it into fields and decoding it. The ROTATE specification causes each p-word to be rotated right the number of bits specified. This occurs before any other procession on a record is done. The syntax is as follows:

*ROTATE:usgc

where

usgc is the number of bits to right-rotate each p-word before processing.

F. INSDEF Specification Card (Listing Format Specification)

INSDEF partitions the word into contiguous fields of bits. Each field has a corresponding field number which associates it with a print field (see PRTDEF). The syntax is as follows:

*INSDEF: ^ $f_1 f_2 f_3 \ldots f_r$

where

f_i is the ith contiguous string of bits corresponding to a print field; f_i itself is a contiguous string of digits (all the same) in the form dddd...d, where d takes on values 0–9. When $d = 0$, the field is ignored. When $d \neq 0$, the field corresponds to the dth print field and will be connected for printing according to the attributes of the dth print field. If $\ell(f_i)$ represents the number of bits in field

$$i, \sum_{i=1}^{r} \ell(f_i)$$

must equal the number of bits per p-word. Hence $f_1 f_2 \ldots f_r$ partitions the p-word into bit fields.

^ is an optional string of blanks.

G. PRTDEF Specification Card (Listing Format Specification)

PRTDEF specifies the type of conversion to perform when printing the bit fields of a p-word. It allows for inclusion of unchanging literals, conversion mode specifies, and zero width field delimiters. The syntax is as follows:

*PRTDEF: $f_1 f_2 \ldots f_r$

where

f_i is a field of one of three types:

(1) An unchanging literal field. This field is always printed exactly as it appears on the PRTDEF card, with the exceptions noted under the SKIP and NULL attributes described later. This field may *not* contain any of the following characters: M,X, O,D,B,C,L,:.

(2) A conversion mode field. The jth conversion mode field is the dth print field ($j = d$) described under INSDEF. This field describes the mode of conversion (X-hexadecimal, O-octal, D-decimal, B-binary, C-character, M-mnemonic, L-literal) and the number of print positions allocated to printing the field. (Note: the rightmost characters of the field are always printed. Truncation always occurs to the left.) The general format of the field is $S_1 S_2 \ldots S_n$ where $S_1 = S_2 = \ldots = S_n = S$, and S

[1]The index j starts at zero and goes through 2** (number of significant bits/character) −1 in steps of one.

defines the conversion mode as above; n is the width of the field in characters. For all but literal and mnemonic conversion, the maximum width is 12. For literals and mnemonics, the maximum is 4. There may be only *one* mnemonic field.

(3) A zero-width field delimiter. This is simply the character ':'. It serves to delimit two fields with the same conversion mode.

H. HEAD Specification Card (Listing Format Specification)

This card allows the user to put a heading at the top of each column of each page of listing. The header appears above the user-defined print fields. The first character after the colon appears immediately above the first character following the colon on the PRTDEF card (see PRTDEF). The syntax is as follows:

*HEAD: literal string

where 'literal string' is the user-defined header.

I. PARAM Specification Card (Listing Format Specification)

The PARAM card allows the user to modify the conversion mode of a print field when it is undesirable to print it. This card also is used to enter the literal table if the literal conversion mode was specified on the PRTDEF card. The syntax is as follows:

$$*\text{PARAM: usgc}_1\left[=\left(\left\{\begin{matrix}\text{SKIP}\\ \\ \text{NULL}\end{matrix}\right\}\left[,\left\{\begin{matrix}\text{SKIP}\\ \\ \text{NULL}\end{matrix}\right\}\right]\left[\left\{\begin{matrix}>\\ <\\ =\\ \neg\end{matrix}\right\}\left[\left\{\begin{matrix}>\\ <\\ =\\ \neg\end{matrix}\right\}\right]\text{usgc}_2\right]\right)\right]$$

$$[,\text{LIT}=\text{lit}_0,\text{lit}_1,\text{lit}_3,\ldots,\text{lit}_n]$$

where:

usgc_1 is the print field to be modified.

SKIP indicates that, following the current conversion mode field, blanks should be inserted to the end of the line and no further conversions made. This will occur if the SKIP-NULL condition is satisfied (see below); i.e., if the SKIP-NULL condition is satisfied, skip to the end of the line.

NULL indicates that the current conversion mode field and the preceding unchanging literal field should be blanked out. This will occur if the SKIP-NULL condition is satisfied.

SKIP-NULL condition: The relation operators in conjunction with usgc_2 form the SKIP-NULL condition. There may be a linear combination of at most two relational operators. If the relation thus defined between the contents of the current field and usgc_2 holds, the SKIP-NULL condition is '=0'. For the mnemonic conversion mode, the SKIP-NULL condition is implicitly satisfied if the operation code has not been assigned a mnemonic. In this case, an implicit NULL is performed, regardless of specification.

$\text{lit}_0,\text{lit}_1,\ldots,\text{lit}_n$ is the literal conversion vector for the current field if the literal conversion mode is specified. There are $n = 2^r - 1$ literals in this vector, where r is the bit width of the print field. Commas are used to delimit the literals. The ith literal corresponds to the internal binary representation of i (i takes on values 0 through $2^r - 1$).

J. OPS Specification (Listing Format Specification)

This card makes a one-to-one correspondence between machine operation codes and mnemonics. It builds the table for the mnemonic conversion field specified on the PRTDEF card. The syntax is as follows:

$$*\text{OPS} = \left\{\begin{matrix}\text{HEX}\\ \text{DEC}\\ \text{OCT}\end{matrix}\right\}$$

ussc_1, literal string_1

ussc_2, literal string_2

.

.

.

ussc_r, literal string_r

ussc_n, literal string_n

where

$ussc_i$ is the opcode for some instruction. $ussc_i$ is decoded as if it were in the mode specified by the 'OPS='card.

literal $string_i$ is the mnemonic corresponding to opcode $ussc_i$.

This card must follow the PRTDEF card.

K. BIN Specification (Listing Format Specification)

This card defines the mode of conversion for printing the contents of the entire p-word. (When each p-word is printed, first the address of the word, then its contents, in the mode specified by the BIN card, then the alphanumeric equivalent of the contents, and finally the user-defined fields are printed.) The syntax is as follows:

$$*\text{BIN} = \begin{Bmatrix}\text{HEX}\\ \text{DEC}\\ \text{OCT}\end{Bmatrix}$$

L. START and NEWLOC Specification (Listing Format Specification)

The purpose of START is to establish the initial value of the location counter for the address of the first p-word of the first record. If no NEWLOC card is present, the location counter is incremented for following records as if they were contiguous with the first. (This assumes that the core dump consists of more than one physical record.) This value may be explicitly stated or the program may be told where to find it in the first record. The syntax to do this is as follows:

$$*\text{START} = \begin{Bmatrix}\text{usgc}_1\\ \text{REC}[+\text{usgc}_2]:f_1f_2f_3[\{\pm\}\text{usgc}_3]\end{Bmatrix}$$

where

$usgc_1$ is the initial value of the location counter for listing purposes. REC indicates that the initial location will be found within the record. $usgc_2$ indicates the offset of the word in the record which contains the initial value of the location counter. (The word accessed is $usgc_2+1$.) $f_1f_2f_3$ forms a mask for extracting the location from the word. f_1 and f_3 are strings of zeros indicating bits to ignore. Either may be null. f_2 is the mask for extracting the bits which represent the initial location. It consists of a string of Ns. The total length of the three strings must be the number of bits per p-word. $usgc_3$ is an offset to be added to the address extracted, before using it as the initial value of the listing location counter.

NEWLOC performs exactly the same function as START and has the same syntax. However, NEWLOC applies to the second and each succeeding record. If the record mode is specified, it is assumed that each record is treated exactly the same as if it were the first record and START where specified with these parameters. If an absolute starting location is given under NEWLOC, this applies to the second record only, and each succeeding record is treated as if it were contiguous to the preceding record and the location counter is incremented appropriately. The syntax of NEWLOC is as follows:

$$*\text{NEWLOC} = \begin{Bmatrix}\text{usgc}_1\\ \text{REC}[+\text{usgc}_2]:f_1f_2f_3[\{\pm\}\text{usgc}_3]\end{Bmatrix}$$

where each symbol has the same meaning as for START.

Table 1 gives an incidence matrix which shows those cards that are necessary and any cards which they must precede. Those items in the left column must either precede, follow, or are optional with respect to the items across the top. This table should be helpful to the user for setting up a deck. If a card is optional, except in the presence of another, this is also noted. For instance, BYTE must precede the ADDRESS specification if used.

M. END Specification

The END card delimits the description deck and calls in the consistency analyzer. This must be the last card in the description deck. The syntax is as follows:

*END

This concludes the discussion of the syntax of target machine description and listing format specification. Actual examples of each of the statements are shown in Figs. 2 and 3.

V. Program Limitations and Diagnostics

The Universal Dump Program is aimed at minicomputers, and this is reflected in some design limitations. Even so, it is very flexible, and should provide no insurmountable limitations to the user. Table 2 describes its characteristics and limitations.

The initial phases of the program produce a considerable quantity of diagnostics designed specifically to aid the user in quickly identifying and correcting control-deck errors. Because of this, and the philosophy that a program should be executed if at all possible, most diagnostics do not prevent continued execution of the program. In the initial syntax analysis section, diagnostics do not prevent continued execution, although a FAILURE will terminate processing of that statement. All consistency checks will be made on the tables, even though fatal errors in consistency may be discovered. Fatal errors prevent execution of the listing phase and termination will occur. Nonfatal errors (WARNINGS) have no effect on continued execution and are merely to call the user's attention to unusual conditions. Table 3 lists possible errors, their probable cause, and fatality.

VI. Two Examples of Use

In this section we consider two examples to illustrate use of the program. The first decodes a dump of part of the monitor program for the XDS 930 computer, which is a second-generation machine that uses word addressing. The word is 24 bits, character code BCD, and usual listing mode OCTAL. The first record is a bootstrap which loads into location 2. Each following record is in absolute loadable binary form, with load location information in the second word. The instruction format is shown in Fig. 4. For a further description of the 930, see the *XDS 930 Computer Reference Manual.* Figure 2 illustrates how this information was used to generate a machine description deck. Figure 2 also shows the resulting dump.

The second example is from a considerably different machine, the PDP-11, manufactured by Digital Equipment Corporation. The PDP-11 is a medium-speed, third-generation minicomputer. It has 16-bit words, which are byte-addressable, and uses the ASCII character set. The usual listing mode is octal. The example here is a dump of an I/O routine in the standard PDP-11 absolute dump format. This format swaps the low- and high-order bytes in each word, making it necessary to reverse them before analyzing a record. This was done by means of the ROTATE command. Address information is contained in the third word of each record. The PDP-11 uses the first four bits of each word as an op-code, and for the op-codes '00' and '10', other bits in the word are used as modifiers. This condition is indicated by using the mnemonics SPCL and SPLB, respectively. The PDP-11 instruction format is shown in Fig. 5. For a further description of the PDP-11 instructions, see the *PDP-11/20 Processor Handbook* (Digital Equipment Corp.). Figure 3 shows the actual specification deck and dump listing for the I/O routine.

Reference

1. Layland, J. W., "An Introduction to Minicomputer Software Support," Klimasauskas, C. C., "The X930 Program Set for Sigma 5 Assembly," Erickson, D. E., The SAPDP Program Set for Sigma 5 Assembly," *The Deep Space Network Progress Report*, Technical Report 32-1526, Vol. VII, pp. 84–96, Jet Propulsion Laboratory, Pasadena, Calif., Feb. 15, 1972.

Table 1. The order of heirarchy of specification cards

O—may optionally precede or follow
P—must precede the statement on the top of the matrix
F—must follow the statement on the top of the matrix
blank—optional card

	WORD	BYTE	ADDRESS	CHAR	SPECIAL	ROTATE	INSDEF	PRTDEF	HEAD	PARAM	OPS	BIN	START	NEWLOC
WORD	–	P	P	P	P	P	P	P	O	P	P	O	P	P
BYTE		–	P[a]											
ADDRESS			–											
CHAR	O	O	O	–	O	O	O	O	O	O	O	O	O	O
SPECIAL				F[b]	–									
ROTATE						–								
INSDEF	F	O	O	O	O	O	–	O	O	P	P	O	O	O
PRTDEF	F	O	O	O	O	O	O	–	O	P	P	O	O	O
HEAD									–					
PARAM	F	O	O	O	O	O	F	F	O	–	O	O	O	O
OPS	F	O	O	O	O	O	F	F	O	O	–	O	O	O
BIN												–		
START	F	O	O	O	O	O	O	O	O	O	O	O	–	O
NEWLOC	F													–

[a]BYTE must be specified before address if byte addressing mode is used.

[b]SPECIAL must be used if and only if SPCL is specified for character type.

Table 2. Characteristics and limitations on the Universal Dump Program

Characteristic	Minimum	Maximum
p-word length (bits)	2	32
Binary, octal, decimal, hexadecimal, character field width (print positions)	1	12
Literal and mnemonic field width (print positions)	1	4
Location counter characters (print positions)	5	5
Buffer size (bits) (current implementation)	2×10^5	5×10^5

Table 3. Error messages

Syntax errors (syntax analysis phase: nonfatal)

Message	Meaning
FAILURE: UNEXPECTED END OF LINE ENCOUNTERED	Syntax scan expected to see a character, but came to end of card first
WARNING: CARD WAS NOT COMPLETELY PROCESSED	Syntax scan ended and released card, yet nonblank characters still remain
WARNING: I/O ERROR-ABORT**	An irrecoverable I/O error has occurred and program has aborted (fatal)
WARNING: END CARD SUPPLIED—NO EXTRA CHARGE	End-of-file on card input was encountered before an *END card
FAILURE: ILLEGAL SIZE: MUST BE (1-32)	Self-explanatory
FAILURE: CANNOT REDEFINE WORD SIZE—ERROR	Attempt to redefine size of a p-word—ignored
FAILURE: ILLEGAL BYTE LENGTH	Length of byte is zero, greater than the length of a p-word, or p-word length has not been defined
FAILURE: CANNOT REDEFINE BYTE LENGTH	Attempt to redefine byte length has been made
WARNING: WORD IS NOT BYTE MULTIPLE	The p-word is not an even byte multiple
FAILURE: BYTE LENGTH: UNDEFINED—IGNORED	The byte length must be defined before the ADDRESS card is used
FAILURE: ILLEGAL PARAMS: WORD OR BYTE EXPECTED	Self-explanatory diagnostic of ADDRESS card
FAILURE: ROTATE OPTION ALREADY IN EFFECT	Self-explanatory
FAILURE: ROTATE BITS > = WORD LENGTH; OR WORD LENGTH = 0	Self-explanatory
FAILURE: ATTEMPT TO REDEFINE START/NEWLOC	Self-explanatory
FAILURE: ILLEGAL FIELD FMT (:) EXPECTED	Self-explanatory
WARNING: MASK AND WORD ARE UNEQUAL MASK ASSUMED RT JUSTIFIED	Self-explanatory in context of START/NEWLOC card
FAILURE: ATTEMPT TO REDEFINE INSTRUCTION	One or more INFDEF cards have already been processed
FAILURE: MUST HAVE WORD LENGTH BEFORE INSDEF—YOU LOSE	WORD card must precede INSDEF statement
WARNING: DEFINED INS LENGTH AND ACTUAL INS LENGTH DIFFER	Self-explanatory in context of INSDEF statement
WARNING: ILLEGAL FIELD DEF CHARACTER —SCAN ENDED	Self-explanatory
FAILURE: ONLY ONE PRTDEF CARD ALLOWED —THIS IGNORED	One or more PRTDEF cards have been processed
FAILURE: UNKNOWN CHAR TYPE: ANSCII, ASCII, BCD, EBCDIC, SPCL, EXPECTED	Self-explanatory in context of CHAR card
FAILURE: CANNOT REASSIGN CHARACTER TYPE	One or more CHAR cards have been processed
FAILURE: CHARACTERS ARE LONGER THAN ONE WORD	Self-explanatory
FAILURE: WORD IS NOT AN EVEN CHARACTER MULTIPLE	Self-explanatory
FAILURE: ILLEGAL CHARACTER, COMMA EXPECTED	Self-explanatory
FAILURE: MASK IS LARGER THAN CHARACTER	Self-explanatory
FAILURE: ILLEGAL CHAR, RT PAREN EXPECTED	Self-explanatory
FAILURE: NO SPECIAL CHARACTER TABLE NEEDED	SPCL was not an option on the CHAR card
FAILURE: MAX OF 79 CHAR/CARD EXCEEDED	Self-explanatory
FAILURE: NO CHAR NEEDED—WIDTH IS ZERO	SPCL card has occurred before CHAR card
FAILURE: UNEXPECTED END OF CARD	A control card was encountered before the character conversion vector was completed

Table 3 (contd)

Syntax errors (syntax analysis phase: nonfatal)

Message	Meaning	Message	Meaning
FAILURE: ILLEGAL TYPE: HEX,DEC,OCT EXPECTED	Self-explanatory in context of BIN card	FAILURE: NO MNEMONIC FIELD FOR INSTRUCTION.	PRTDEF card did not have a mnemonic field or has not been encountered yet
FAILURE: UNIDENTIFIED PARAMETER JUST ENCOUNTERED	SKIP/NULL expected while scanning PARAM card—not found	WARNING: OP OUT OF RANGE—IGNORED	An op-code greater than maximum found while processing OPS card
WARNING: MISSING PRNTDEF FIELD—WIDTH OF 4 ASSUMED	PARAM card precedes the PRTDEF card	FAILURE: DYNAMIC STORAGE ALL ALLOCATED—NONE LEFT	Insufficient core available to complete processing of description deck
WARNING: INCORRECT NUMBER OF LITERALS	The number of literals on the PARAM card is less than needed to complete the binary-to-literal conversion vector	WARNING: THIS IS THE END	Normal message indicating completion of syntax phase

Syntax errors (table analysis phase: FAILURES are fatal)

Message	Meaning	Message	Meaning
WARNING: ZERO BYTES/WRD—ONE ASSUMED	Self-explanatory	FAILURE: ZERO FIELD WIDTH—FIELD:XX	PRTDEF field, but no corresponding field on INSDEF card (i.e., too many PRTDEF fields)
FAILURE: ZERO WIDTH CHARACTERS FAILURE: IMPROPER CHARACTER FIELD WIDTH	An irrecoverable error occurred while processing the CHAR card, or field width specifications are in error	FAILURE: NO CONVERSION TYPE—FIELD:XX	Too many INSDEF fields and no corresponding PRTDEF field
WARNING: NO CHR OPT—EBCDIC ASSUMED	No CHAR card in description deck	WARNING: LIT ENTRY, BUT CNVRSN TYPE NOT LIT—FIELD:XX	LIT option specified on PARAM card, but conversion type from PRTDEF was not literal mode
FAILURE: SPECIAL CHARACTER TABLE IS NULL	SPCL was specified on the CHAR card, but no SPECIAL card was validly processed		
WARNING: TOTAL PRINT FIELD > 33 CHR—TRUNCATED	The number of characters required to print the location, contents, and user fields exceeds 33 characters	FAILURE: PARAMETER ENTRY AFTER END OF FIELD IN PSN:XX	Field specified on a PARAM card is greater than any PRTDEF field
FAILURE: NO PRTDEF CARD PRESENT	Self-explanatory	WARNING: EXTRACT MSK, BUT NULL FIELD—FIELD:XX	INSDEF field is not related to any PRTDEF field
FAILURE: NO INSDEF CARD PRESENT	Self-explanatory		
FAILURE: LIT/MNE, BUT NO LIT ENTRY—FIELD:XX	L or M specification on PRTDEF, but no 'LIT' on PARAM card or OPS card respectively	WARNING: LITS, BUT NULL FIELD—FIELD:XX	PARAM card for undefined PRTDEF field has LIT option
		WARNING: PARAMS, BUT NULL FIELD: FIELD:XX	PARAM card for undefined field

XX is the field number (1–9).

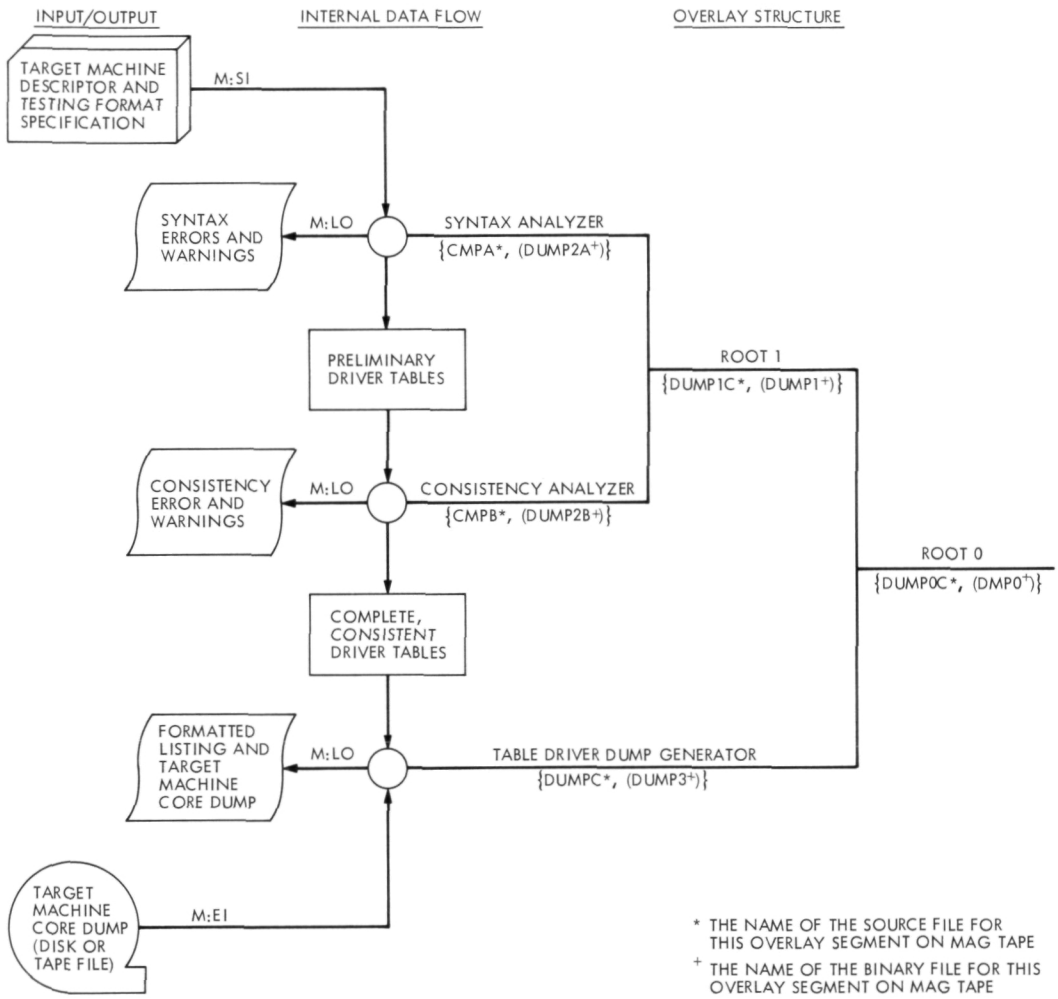

Fig. 1. Dump Program diagram

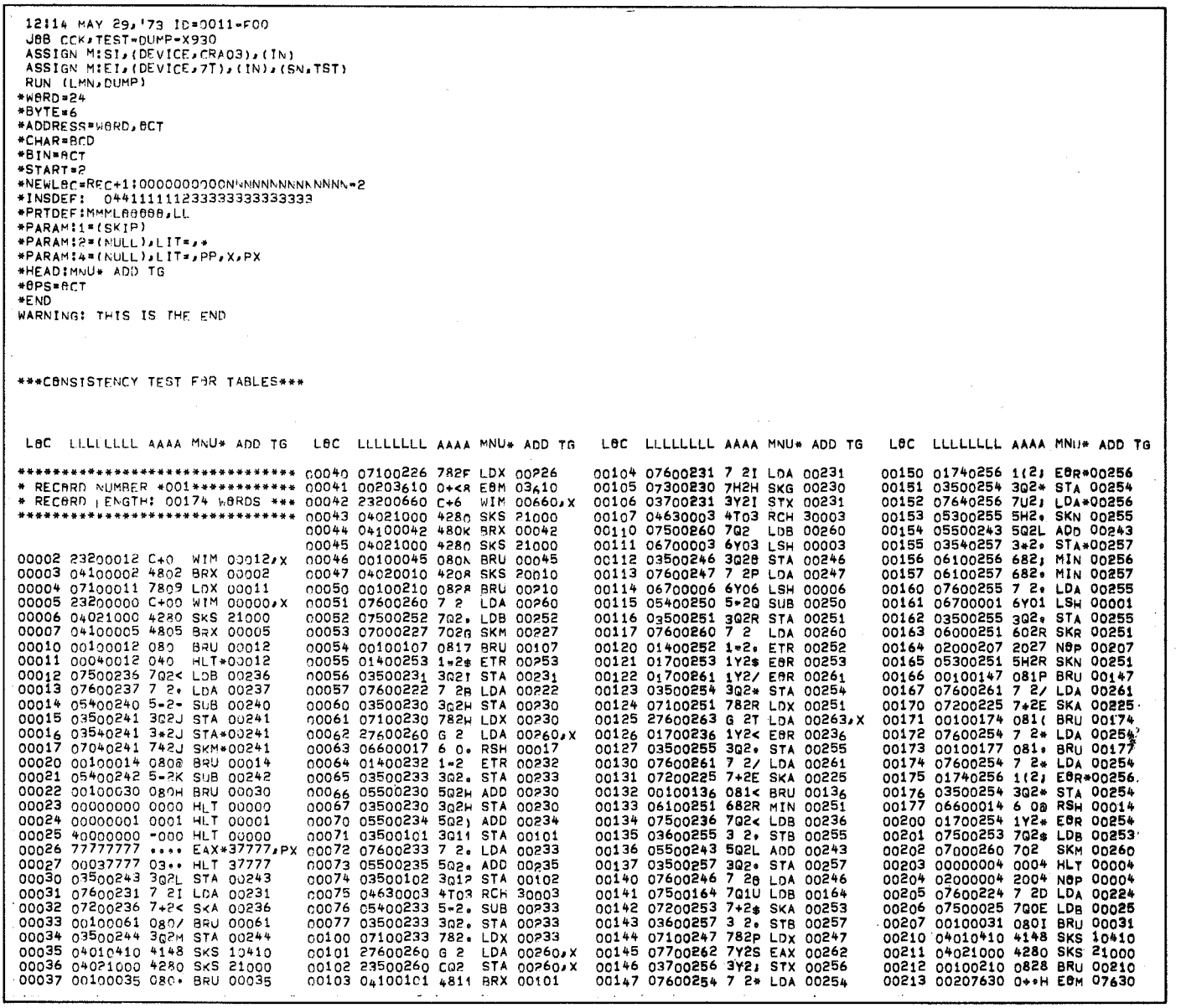

```
 12:14 MAY 29,'73 ID=0011-F00
 JOB CCK,TEST=DUMP=X930
 ASSIGN M:SI,(DEVICE,CRA03),(IN)
 ASSIGN M:EI,(DEVICE,7T),(IN),(SN,TST)
 RUN (LMN,DUMP)
*WORD=24
*BYTE=6
*ADDRESS=WORD,OCT
*CHAR=BCD
*BIN=OCT
*START=2
*NEWLOC=REC+1:000000000000NNNNNNNNNNNNN=2
*INSDEF:  04411111123333333333333
*PRTDEF:MMMLOOOOO,LL
*PARAM:1=(SKIP)
*PARAM:2=(NULL),LIT=,*
*PARAM:4=(NULL),LIT=,PP,X,PX
*HEAD:MNU* ADD TG
*OPS=OCT
*END
WARNING: THIS IS THE END



***CONSISTENCY TEST FOR TABLES***


 LOC  LLLLLLLL AAAA MNU* ADD TG   LOC  LLLLLLLL AAAA MNU* ADD TG   LOC  LLLLLLLL AAAA MNU* ADD TG   LOC  LLLLLLLL AAAA MNU* ADD TG

****************************** 00040 07100226 782F LDX 00226    00104 07600231 7 2I LDA 00231    00150 01740256 1(2; EOR*00256
* RECORD NUMBER *001********** 00041 00203610 0+<R EOM 03610  00105 07300230 7H2H SKG 00230    00151 03500254 3Q2* STA 00254
* RECORD LENGTH: 00174 WORDS *** 00042 23200660 C+6  WIM 00660,X 00106 03700231 3Y2I STX 00231  00152 07640256 7U2; LDA*00256
****************************** 00043 04021000 4280 SKS 21000    00107 04630003 4T03 RCH 30003    00153 05300255 5H2. SKN 00255
                               00044 04100042 4804 BRX 00042    00110 07500260 7Q2  LDB 00260    00154 05500243 5Q2L ADD 00243
                               00045 04021000 4280 SKS 21000    00111 06700003 6Y03 LSH 00003    00155 03540257 3*2. STA*00257
00002 23200012 C+0  WIM 00012,X 00046 00100045 080N BRU 00045  00112 03500246 3Q28 STA 00246    00156 06100256 682; MIN 00256
00003 04100002 4802 BRX 00002    00047 04020010 4208 SKS 20010  00113 07600247 7 2P LDA 00247    00157 06100257 682. MIN 00257
00004 07100011 7809 LDX 00011    00050 00100210 082R BRU 00210  00114 06700006 6Y06 LSH 00006    00160 07600255 7 2. LDA 00255
00005 23200000 C+00 WIM 00000,X  00051 07600260 7 2  LDA 00260  00115 05400250 5*2Q SUB 00250    00161 06700001 6Y01 LSH 00001
00006 04021000 4280 SKS 21000    00052 07500252 7Q2. LDB 00252  00116 03500251 3Q2R STA 00251    00162 03500255 3Q2. STA 00255
00007 04100005 4805 BRX 00005    00053 07000227 702G SKM 00227  00117 07600260 7 2  LDA 00260    00163 06000251 602R SKR 00251
00010 00100012 080  BRU 00012    00054 00100107 0817 BRU 00107  00120 01400252 1*2. ETR 00252    00164 02000207 2027 NOP 00207
00011 00040012 040  HLT*00012    00055 01400253 1*2$ ETR 00253  00121 01700253 1Y2$ EOR 00253    00165 05300251 5H2R SKN 00251
00012 07500236 7Q2< LDB 00236    00056 03500231 3Q2! STA 00231  00122 01700261 1Y2/ EOR 00261    00166 00100147 081P BRU 00147
00013 07600237 7 2. LDA 00237    00057 07600222 7 2B LDA 00222  00123 03500254 3Q2* STA 00254    00167 07600261 7 2/ LDA 00261
00014 05400240 5*2- SUB 00240    00060 03500230 3Q2H STA 00230  00124 07100251 782R LDX 00251    00170 07200225 7+2E SKA 00225
00015 03500241 3Q2J STA 00241    00061 07100230 782H LDX 00230  00125 27600263 G 2T LDA 00263,X  00171 00100174 081( BRU 00174
00016 03540241 3*2J STA*00241    00062 27600260 G 2  LDA 00260,X 00126 01700236 1Y2< EOR 00236  00172 07600254 7 2* LDA 00254
00017 07040241 742J SKM*00241    00063 06600017 6 0. RSH 00017  00127 03500255 3Q2. STA 00255    00173 00100177 081. BRU 00177
00020 00100014 0808 BRU 00014    00064 01400232 1*2  ETR 00232  00130 07600261 7 2/ LDA 00261    00174 07600254 7 2* LDA 00254
00021 05400242 5*2K SUB 00242    00065 03500233 3Q2. STA 00233  00131 07200225 7+2E SKA 00225    00175 01740256 1(2; EOR*00256
00022 00100030 080H BRU 00030    00066 05500230 5Q2H ADD 00230  00132 00100136 081< BRU 00136    00176 03500254 3Q2* STA 00254
00023 00000000 0000 HLT 00000    00067 03500230 3Q2H STA 00230  00133 06100251 682R MIN 00251    00177 06600014 6 0@ RSH 00014
00024 00000001 0001 HLT 00001    00070 05500234 5Q2) ADD 00234  00134 07500236 7Q2< LDB 00236    00200 01700254 1Y2* EOR 00254
00025 40000000 -000 HLT 00000    00071 03500101 3Q11 STA 00101  00135 03600255 3 2. STB 00255    00201 07500253 7Q2$ LDB 00253
00026 77777777 .... EAX*37777,PX 00072 07600233 7 2. LDA 00233 00136 05500243 5Q2L ADD 00243    00202 07000260 702  SKM 00260
00027 00037777 03.. HLT 37777    00073 05500235 5Q2. ADD 00235  00137 03500257 3Q2. STA 00257    00203 00000004 0004 HLT 00004
00030 03500243 3Q2L STA 00243    00074 03500102 3Q12 STA 00102  00140 07600246 7 2@ LDA 00246    00204 02000004 2004 NOP 00004
00031 07600231 7 2I LDA 00231    00075 04630003 4T03 RCH 30003  00141 07500164 7Q1U LDB 00164    00205 07600224 7 2D LDA 00224
00032 07200236 7+2< SKA 00236    00076 05400233 5*2. SUB 00233  00142 07200253 7+2$ SKA 00253    00206 07500025 7Q0E LDB 00025
00033 00100061 0807 BRU 00061    00077 03500233 3Q2. STA 00233  00143 03600257 3 2. STB 00257    00207 00100031 0801 BRU 00031
00034 03500244 3Q2M STA 00244    00100 07100233 782. LDX 00233  00144 07100247 782P LDX 00247    00210 04010410 4148 SKS 10410
00035 04010410 4148 SKS 10410    00101 27600260 G 2  LDA 00260,X 00145 07700262 7Y2S EAX 00262  00211 04021000 4280 SKS 21000
00036 04021000 4280 SKS 21000    00102 23500260 CQ2  STA 00260,X 00146 03700256 3Y2; STX 00256  00212 00100210 0828 BRU 00210
00037 00100035 080. BRU 00035    00103 04100101 4811 BRX 00101  00147 07600254 7 2* LDA 00254    00213 00207630 0+.H EOM 07630
```

Fig. 2. An application of the Universal Dump Program to the XDS 930 computer

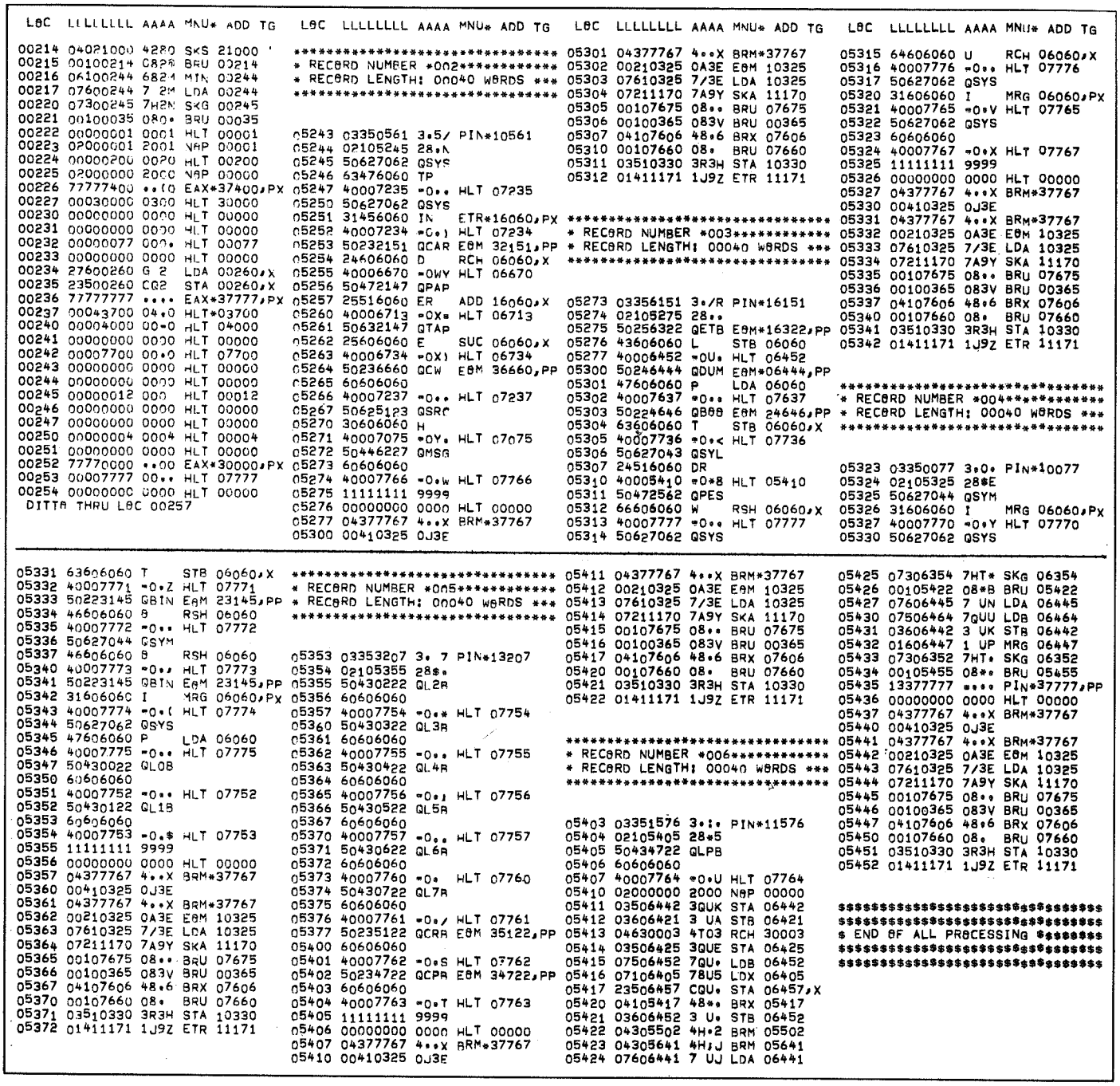

```
 LOC  LLLLLLLL AAAA MNU* ADD TG   LOC  LLLLLLLL AAAA MNU* ADD TG   LOC  LLLLLLLL AAAA MNU* ADD TG   LOC  LLLLLLLL AAAA MNU* ADD TG

00214 04021000 4280 SKS 21000 '  ******************************* 05301 04377767 4••X BRM*37767    05315 64606060 U    RCH 06060,X
00215 00100214 0828 BRU 00214    * RECORD NUMBER *002*********** 05302 00210325 0A3E E0M 10325    05316 40007776 =0•• HLT 07776
00216 04100244 6824 MIN 00244    * RECORD LENGTH: 00040 WORDS *** 05303 07610325 7/3E LDA 10325    05317 50627062 QSYS
00217 07600244 7 2M LDA 00244    ******************************* 05304 07211170 7A9Y SKA 11170    05320 31606060 I    MRG 06060,PX
00220 07300245 7H2N SKG 00245                                     05305 00107675 08•• BRU 07675    05321 40007765 =0•V HLT 07765
00221 00100035 080• BRU 00035                                     05306 00100365 083V BRU 00365    05322 50627062 QSYS
00222 00000001 0001 HLT 00001    05243 03350561 3•5/ PIN*10561    05307 04107606 48•6 BRX 07606    05323 60606060
00223 02000001 2001 NOP 00001    05244 02105245 28•A              05310 00107660 08•  BRU 07660    05324 40007767 =0•X HLT 07767
00224 00000200 0020 HLT 00200    05245 50627062 QSYS              05311 03510330 3R3H STA 10330    05325 11111111 9999
00225 02000000 2000 NOP 00000    05246 63476060 TP                05312 01411171 1J9Z ETR 11171    05326 00000000 0000 HLT 00000
00226 77777400 ••(0 EAX*37400,PX 05247 40007235 =0•• HLT 07235                                     05327 04377767 4••X BRM*37767
00227 00030000 0300 HLT 30000    05250 50627062 QSYS                                               05330 00410325 0J3E
00230 00000000 0000 HLT 00000    05251 31456060 IN   ETR*16060,PX ******************************* 05331 04377767 4••X BRM*37767
00231 00000000 0000 HLT 00000    05252 40007234 =0•) HLT 07234    * RECORD NUMBER *003*********** 05332 00210325 0A3E E0M 10325
00232 00000077 000• HLT 00077    05253 50232151 QCAR E0M 32151,PP * RECORD LENGTH: 00040 WORDS *** 05333 07610325 7/3E LDA 10325
00233 00000000 0000 HLT 00000    05254 24606060 D    RCH 06060,X  ******************************* 05334 07211170 7A9Y SKA 11170
00234 27600260 G 2  LDA 00260,X  05255 40006670 =0WY HLT 06670                                     05335 00107675 08•• BRU 07675
00235 23500260 CQ2  STA 00260,X  05256 50472147 QPAP                                               05336 00100365 083V BRU 00365
00236 77777777 •••• EAX*37777,PX 05257 25516060 ER   ADD 16060,X 05273 03356151 3•/R PIN*16151    05337 04107606 48•6 BRX 07606
00237 00043700 04•0 HLT*03700    05260 40006713 =0X• HLT 06713    05274 02105275 28••              05340 00107660 08•  BRU 07660
00240 00004000 00=0 HLT 04000    05261 50632147 QTAP              05275 50256322 QETB E0M*16322,PP 05341 03510330 3R3H STA 10330
00241 00000000 0000 HLT 00000    05262 25606060 E    SUC 06060,X  05276 43606060 L    STB 06060    05342 01411171 1J9Z ETR 11171
00242 00007700 00•0 HLT 07700    05263 40006734 =0X) HLT 06734    05277 40006452 =0U• HLT 06452
00243 00000000 0000 HLT 00000    05264 50236660 QCW  E0M 36660,PP 05300 50246444 QDUM E0M*06444,PP
00244 00000000 0000 HLT 00000    05265 60606060                   05301 47606060 P    LDA 06060    ******************************
00245 00000012 000  HLT 00012    05266 40007237 =0•• HLT 07237    05302 40007637 =0•• HLT 07637    * RECORD NUMBER *004*********
00246 00000000 0000 HLT 00000    05267 50625123 QSRC              05303 50224646 QB0B E0M 24646,PP * RECORD LENGTH: 00040 WORDS ***
00247 00000000 0000 HLT 00000    05270 30606060 H                 05304 63606060 T    STB 06060,X  ******************************
00250 00000004 0004 HLT 00004    05271 40007075 =0Y• HLT 07075    05305 40007736 =0•< HLT 07736
00251 00000000 0000 HLT 00000    05272 50446227 QMSG              05306 50627043 QSYL
00252 77770000 ••00 EAX*30000,PX 05273 60606060                   05307 24516060 DR                05323 03350077 3•0• PIN*10077
00253 00007777 00•• HLT 07777    05274 40007766 =0•W HLT 07766    05310 40005410 =0•8 HLT 05410    05324 02105325 28•E
00254 00000000 0000 HLT 00000    05275 11111111 9999              05311 50472562 QPES              05325 50627044 QSYM
 DITTO THRU LOC 00257            05276 00000000 0000 HLT 00000    05312 66606060 W    RSH 06060,X  05326 31606060 I    MRG 06060,PX
                                 05277 04377767 4••X BRM*37767    05313 40007777 =0•• HLT 07777    05327 40007770 =0•Y HLT 07770
                                 05300 00410325 0J3E              05314 50627062 QSYS              05330 50627062 QSYS

-------------------------------------------------------------------------------------------------------------------------------------

05331 63606060 T    STB 06060,X  ******************************* 05411 04377767 4••X BRM*37767    05425 07306354 7HT• SKG 06354
05332 40007771 =0•Z HLT 07771    * RECORD NUMBER *005*********** 05412 00210325 0A3E E0M 10325    05426 00105422 08•B BRU 05422
05333 50223145 QBIN E0M 23145,PP * RECORD LENGTH: 00040 WORDS *** 05413 07610325 7/3E LDA 10325    05427 07606445 7 UN LDA 06445
05334 46606060 8    RSH 06060    ******************************* 05414 07211170 7A9Y SKA 11170    05430 07506464 7QUU LDB 06464
05335 40007772 =0•• HLT 07772                                     05415 00107675 08•• BRU 07675    05431 03606442 3 UK STB 06442
05336 50627044 QSYM                                               05416 00100365 083V BRU 00365    05432 01606447 1 UP MRG 06447
05337 46606060 8    RSH 06060    05353 03353207 3• 7 PIN*13207    05417 04107606 48•6 BRX 07606    05433 07306352 7HT• SKG 06352
05340 40007773 =0•, HLT 07773    05354 02105355 28•.              05420 00107660 08•  BRU 07660    05434 00105455 08•• BRU 05455
05341 50223145 QBIN E0M 23145,PP 05355 50430222 QL2R              05421 03510330 3R3H STA 10330    05435 13377777 •••• PIN*37777,PP
05342 31606060 I    MRG 06060,PX 05356 60606060                   05422 01411171 1J9Z ETR 11171    05436 00000000 0000 HLT 00000
05343 40007774 =0•( HLT 07774    05357 40007754 =0•* HLT 07754                                     05437 04377767 4••X BRM*37767
05344 50627062 QSYS              05360 50430322 QL3R                                               05440 00410325 0J3E
05345 47606060 P    LDA 06060    05361 60606060                   ******************************* 05441 04377767 4••X BRM*37767
05346 40007775 =0•• HLT 07775    05362 40007755 =0•, HLT 07755    * RECORD NUMBER *006*********** 05442 00210325 0A3E E0M 10325
05347 50430022 QL0B              05363 50430422 QL4R              * RECORD LENGTH: 00040 WORDS *** 05443 07610325 7/3E LDA 10325
05350 60606060                   05364 60606060                   ******************************* 05444 07211170 7A9Y SKA 11170
05351 40007752 =0•• HLT 07752    05365 40007756 =0•, HLT 07756                                     05445 00107675 08•• BRU 07675
05352 50430122 QL1B              05366 50430522 QL5R                                               05446 00100365 083V BRU 00365
05353 60606060                   05367 60606060                   05403 03351576 3•:• PIN*11576    05447 04107606 48•6 BRX 07606
05354 40007753 =0•$ HLT 07753    05370 40007757 =0•. HLT 07757    05404 02105405 28•5              05450 00107660 08•  BRU 07660
05355 11111111 9999              05371 50430622 QL6R              05405 50434722 QLPB              05451 03510330 3R3H STA 10330
05356 00000000 0000 HLT 00000    05372 60606060                   05406 60606060                   05452 01411171 1J9Z ETR 11171
05357 04377767 4••X BRM*37767    05373 40007760 =0•  HLT 07760    05407 40007764 =0•U HLT 07764
05360 00410325 0J3E              05374 50430722 QL7R              05410 02000000 2000 NOP 00000
05361 04377767 4••X BRM*37767    05375 60606060                   05411 03506442 3QUK STA 06442    $$$$$$$$$$$$$$$$$$$$$$$$$$$$$$$
05362 00210325 0A3E E0M 10325    05376 40007761 =0•/ HLT 07761    05412 03606421 3 UA STB 06421    $$$$$$$$$$$$$$$$$$$$$$$$$$$$$$$
05363 07610325 7/3E LDA 10325    05377 50235122 QCRR E0M 35122,PP 05413 04630003 4T03 RCH 30003    $ END OF ALL PROCESSING $$$$$$$
05364 07211170 7A9Y SKA 11170    05400 60606060                   05414 03506425 3QUE STA 06425    $$$$$$$$$$$$$$$$$$$$$$$$$$$$$$$
05365 00107675 08•• BRU 07675    05401 40007762 =0•S HLT 07762    05415 07506452 7QU• LDB 06452    $$$$$$$$$$$$$$$$$$$$$$$$$$$$$$$
05366 00100365 083V BRU 00365    05402 50234722 QCPR E0M 34722,PP 05416 07106405 78U5 LDX 06405
05367 04107606 48•6 BRX 07606    05403 60606060                   05417 23506457 CQU• STA 06457,X
05370 00107660 08•  BRU 07660    05404 40007763 =0•T HLT 07763    05420 04105417 48•• BRX 05417
05371 03510330 3R3H STA 10330    05405 11111111 9999              05421 03606452 3 U• STB 06452
05372 01411171 1J9Z ETR 11171    05406 00000000 0000 HLT 00000    05422 04305502 4H•2 BRM 05502
                                 05407 04377767 4••X BRM*37767    05423 04305641 4H;J BRM 05641
                                 05410 00410325 0J3E              05424 07606441 7 UJ LDA 06441
```

Fig. 2 (contd)

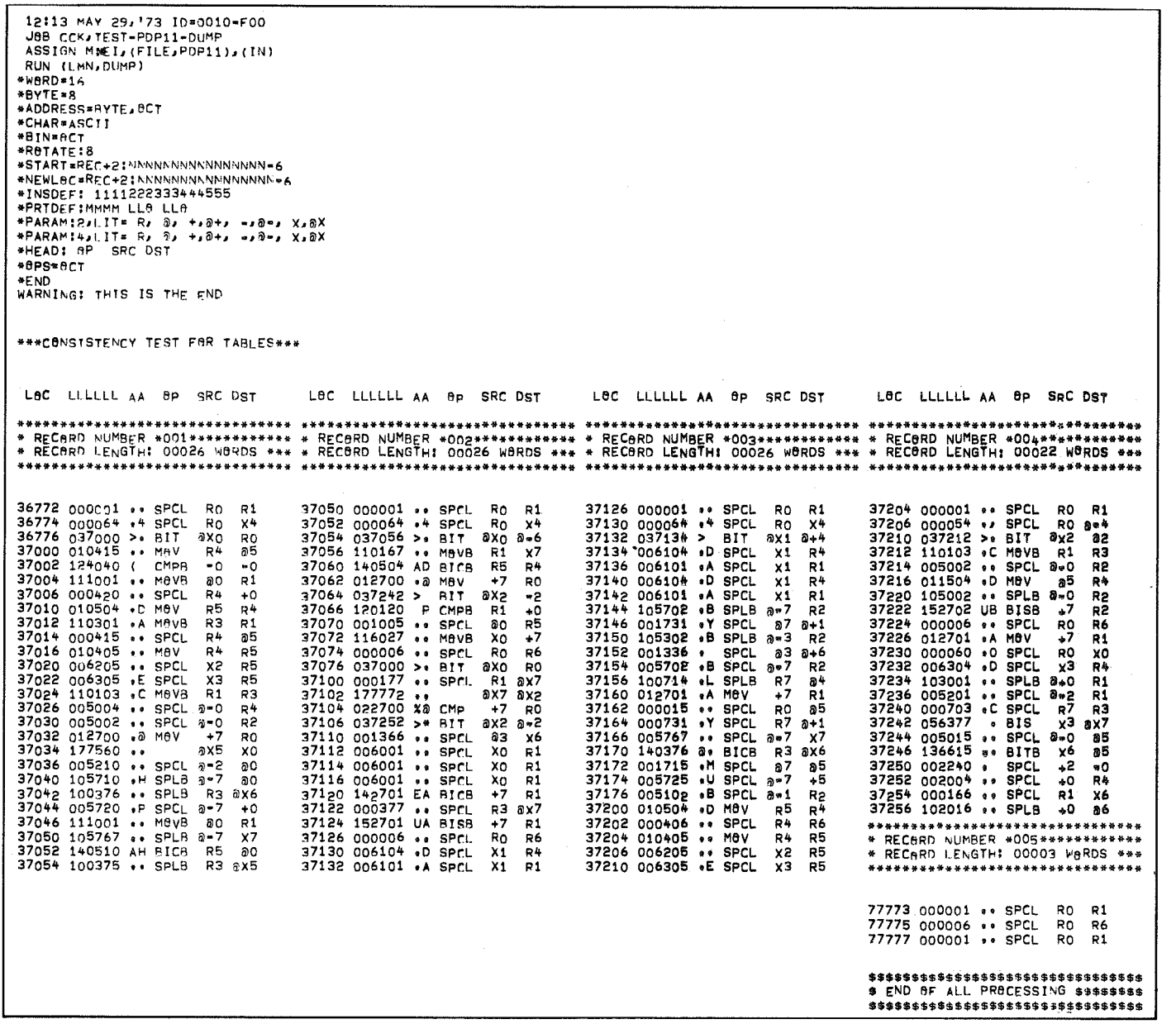

```
 12:13 MAY 29,'73 ID=0010=F00
 JOB CCK,TEST=PDP11=DUMP
 ASSIGN MMEI,(FILE,PDP11),(IN)
 RUN (LMN,DUMP)
*WORD=16
*BYTE=8
*ADDRESS=BYTE,OCT
*CHAR=ASCII
*BIN=OCT
*ROTATE:8
*START=REC+2:NNNNNNNNNNNNNNNN=6
*NEWLOC=REC+2:NNNNNNNNNNNNNNNN=6
*INSDEF: 1111222333444555
*PRTDEF:MMMM LLO LLO
*PARAM:2,LIT= R, @, +,@+, -,@-, X,@X
*PARAM:4,LIT= R, @, +,@+, -,@-, X,@X
*HEAD: OP  SRC DST
*OPS=OCT
*END
WARNING: THIS IS THE END


***CONSISTENCY TEST FOR TABLES***


 LOC  LLLLLL AA  OP  SRC DST      LOC  LLLLLL AA  OP  SRC DST      LOC  LLLLLL AA  OP  SRC DST      LOC  LLLLLL AA  OP  SRC DST

******************************** ******************************** ******************************** ********************************
* RECORD NUMBER *001*********** * RECORD NUMBER *002*********** * RECORD NUMBER *003*********** * RECORD NUMBER *004***********
* RECORD LENGTH: 00026 WORDS *** * RECORD LENGTH: 00026 WORDS *** * RECORD LENGTH: 00026 WORDS *** * RECORD LENGTH: 00022 WORDS ***
******************************** ******************************** ******************************** ********************************


36772 000001 .. SPCL  R0  R1     37050 000001 .. SPCL  R0  R1     37126 000001 .. SPCL  R0  R1     37204 000001 .. SPCL  R0  R1
36774 000064 .4 SPCL  R0  X4     37052 000064 .4 SPCL  R0  X4     37130 000064 .4 SPCL  R0  X4     37206 000054 ., SPCL  R0  @+4
36776 037000 >. BIT  @X0  R0     37054 037056 >. BIT  @X0 @+6     37132 037134 >  BIT  @X1 @+4     37210 037212 >. BIT  @X2  @2
37000 010415 .. MOV   R4  @5     37056 110167 .. MOVB  R1  X7     37134 006104 .D SPCL  X1  R4     37212 110103 .C MOVB  R1  R3
37002 124040 (  CMPB  -0  -0     37060 140504 AD BICB  R5  R4     37136 006101 .A SPCL  X1  R1     37214 005002 .. SPCL @+0  R2
37004 111001 .. MOVB  @0  R1     37062 012700 .@ MOV   +7  R0     37140 006104 .D SPCL  X1  R4     37216 011504 .D MOV   @5  R4
37006 000420 .. SPCL  R4  +0     37064 037242 >  BIT  @X2  -2     37142 006101 .A SPCL  X1  R1     37220 105002 .. SPLB @+0  R2
37010 010504 .D MOV   R5  R4     37066 120120  P CMPB  R1  +0     37144 105702 .B SPLB @-7  R2     37222 152702 UB BISB  +7  R2
37012 110301 .A MOVB  R3  R1     37070 001005 .. SPCL  @0  R5     37146 001731 .Y SPCL  @7 @+1     37224 000006 .. SPCL  R0  R6
37014 000415 .. SPCL  R4  @5     37072 116027 .. MOVB  X0  +7     37150 105302 .B SPLB @-3  R2     37226 012701 .A MOV   +7  R1
37016 010405 .. MOV   R4  R5     37074 000006 .. SPCL  R0  R6     37152 001336 .  SPCL  @3 @+6     37230 000060 .0 SPCL  R0  X0
37020 006205 .. SPCL  X2  R5     37076 037000 >. BIT  @X0  R0     37154 005702 .B SPCL @-7  R2     37232 006304 .D SPCL  X3  R4
37022 006305 .E SPCL  X3  R5     37100 000177 .. SPCL  R1 @X7     37156 100714 .L SPLB  R7  @4     37234 103001 .. SPLB @+0  R1
37024 110103 .C MOVB  R1  R3     37102 177772 ..       @X7 @X2     37160 012701 .A MOV   +7  R1     37236 005201 .. SPCL @-2  R1
37026 005004 .. SPCL @-0  R4     37104 022700 %@ CMP   +7  R0     37162 000015 .. SPCL  R0  @5     37240 000703 .C SPCL  R7  R3
37030 005002 .. SPCL @-0  R2     37106 037252 >* BIT  @X2 @-2     37164 000731 .Y SPCL  R7 @+1     37242 056377  . BIS   X3 @X7
37032 012700 .@ MOV   +7  R0     37110 001366 .. SPCL  @3  X6     37166 005767 .. SPCL @-7  X7     37244 005015 .. SPCL @-0  @5
37034 177560 ..       @X5 X0     37112 006001 .. SPCL  X0  R1     37170 140376 @. BICB  R3 @X6     37246 136615 =. BITB  X6  @5
37036 005210 .. SPCL @-2  @0     37114 006001 .. SPCL  X0  R1     37172 001715 .M SPCL  @7  @5     37250 002240 .  SPCL  +2  -0
37040 105710 .H SPLB @-7  @0     37116 006001 .. SPCL  X0  R1     37174 005725 .U SPCL @-7  +5     37252 002004 .. SPCL  +0  R4
37042 100376 .. SPLB  R3 @X6     37120 142701 EA BICB  +7  R1     37176 005102 .B SPCL @-1  R2     37254 000166 .. SPCL  R1  X6
37044 005720 .P SPCL @-7  +0     37122 000377 .. SPCL  R3 @X7     37200 010504 .D MOV   R5  R4     37256 102016 .. SPLB  +0  @6
37046 111001 .. MOVB  @0  R1     37124 152701 UA BISB  +7  R1     37202 000406 .. SPCL  R4  R6     ********************************
37050 105767 .. SPLB @-7  X7     37126 000006 .. SPCL  R0  R6     37204 010405 .. MOV   R4  R5     * RECORD NUMBER *005*************
37052 140510 AH BICB  R5  @0     37130 006104 .D SPCL  X1  R4     37206 006205 .. SPCL  X2  R5     * RECORD LENGTH: 00003 WORDS ***
37054 100375 .. SPLB  R3 @X5     37132 006101 .A SPCL  X1  R1     37210 006305 .E SPCL  X3  R5     ********************************


                                                                                                  77773 000001 .. SPCL  R0  R1
                                                                                                  77775 000006 .. SPCL  R0  R6
                                                                                                  77777 000001 .. SPCL  R0  R1


                                                                                                  $$$$$$$$$$$$$$$$$$$$$$$$$$$$$$$$
                                                                                                  $ END OF ALL PROCESSING $$$$$$$$
                                                                                                  $$$$$$$$$$$$$$$$$$$$$$$$$$$$$$$$
```

Fig. 3. An application of the Universal Dump Program to the PDP-11 computer

THE 930 INSTRUCTION:

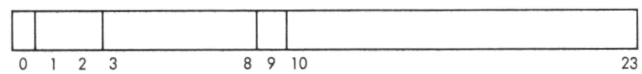

BIT	FUNCTION
0	UNUSED
1-2	TAG FIELD: BIT 1 SET, INDEXING IS USED BIT 2 SET, OPERATOR IS PROGRAMMED
3-8	OPERATION CODE
9	INDIRECT ADDRESSING BIT
10-23	ADDRESS OF OPERAND

Fig. 4. Instruction format for the XDS 930 computer

THE PDP-11 INSTRUCTION:

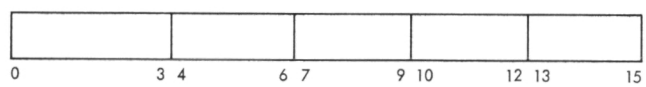

BIT	FUNCTION
0-3	OPERATION CODE
4-6	ADDRESSING MODE FOR SOURCE OPERAND
7-9	SOURCE OPERAND REGISTER
10-12	ADDRESSING MODE FOR DESTINATION OPERAND
13-15	DESTINATION OPERAND REGISTER

Fig. 5. Instruction format for the PDP-11 computer

The Golay-Viterbi Concatenation Scheme

E. R. Berlekamp[1]
Communications Systems Research Section

This article examines in detail the Golay-Viterbi concatenation scheme which has been proposed for use for the nontelevision scientific data portion of the Mariner Jupiter/Saturn telemetry. The simplest form of the scheme makes no use of the memory in the noise caused by the Viterbi decoder; in this article we will demonstrate that it is possible to utilize this memory to obtain improved performance.

It has been proposed that scientific data on the MJS'77 project be given more noise protection than the TV data and that this can be achieved by using the Golay code, interleaved to a depth of j ($j = 10$ to 25) to achieve an overall block length of $24j$. The $24j$ bits in any overall block may be conveniently arranged in j rows of 24 bits each, where each row is a code word in the Golay code. The bits are transmitted consecutively, column by column. The outer channel through which these blocks are transmitted contains a convolutional encoder and a Viterbi decoder. Even if the space channel over which the inner convolutional code is transmitted is memoryless, the phenomenon of error propagation in the Viterbi decoder will cause the outer channel to be bursty. However, the interleaved nature of the outer code distributes an error burst among the j different Golay codes, so that most bursts do not cause more than a few errors in any particular Golay code word. It is therefore possible to correct many common error patterns by decoding the outer code row by row.

Of course, there are some error patterns which this procedure will fail to correct. The most common such error patterns will cause one or more rows to be received as a word with highly improbable syndrome, corresponding to an error pattern of weight 4 or more with no simple burst explanation. When this rare event occurs, we suggest a refined algorithm for redecoding the entire block of $24j$ bits. This algorithm would probably be programmed on a computer rather than implemented in hardware. Since it would be used only on those rare blocks on which an error was detected by the Golay code, the refined algorithm need not be as fast as the conventional row-by-row decoding algorithm operating on the output of the Viterbi decoding hardware.

[1]Consultant to JPL from U. C. Berkeley.

The most effective attack is to go back to the original data and reexamine the decisions made by the Viterbi decoder in more detail. The goal of this reexamination is to erase those bits on which the decoding decisions were close. Once this has been done, it will be quite easy for the Golay code to correct the erasures as well as the small number of errors which might remain. It is well known that if there are no errors present, any linear binary code with minimum distance d can correct *all* patterns of $d - 1$ or fewer erasures, and hence, that the extended (24, 12) Golay code can correct any pattern of not more than 7 erasures. The easiest way to accomplish this erasure decoding up to minimum distance is to set all erasure bits to 0, try to decode, then set all erased bits to 1, and try to decode again. Of course, one attempt or the other must succeed in correcting an "error" pattern of weight less than $d/2$ in the erased positions.

It is less well known that linear codes typically have much greater erasure correction capabilities than indicated by the minimum distance. In particular, when there are no errors, the Golay code is not only capable of correcting *all* patterns of 7 erasures, it can also correct 322/323 of the patterns of 8 erasures as well as most patterns of 9 or 10 erasures, 286/323 of the possible patterns of 11 erasures and over half of the patterns of 12 erasures. In other words, erasures are *less* than half as difficult to correct as errors. A program for correcting the erasures need only solve simultaneous linear equations over GF(2).

We now comment on the problem of simulating a refined Viterbi decoder which will erase those message bits about which it is not too sure. Recall that the Viterbi decoder makes two kinds of errors, the so-called "decoding" errors, which arise when its estimate of the last bit in the encoder's shift register is incorrect, and "memory truncation errors," which arise because its memory of 4 or 5 constraint lengths is occasionally insufficient. The latter type of error appears to be considerably less frequent than the former, and if necessary could be further reduced by using a longer memory in the simulator.

To detect the "decoding" errors, one might design a modified Viterbi decoder in which each original register was replaced by a list of L registers holding the L most probable message sequences consistent with the appropriate hypothesis about the current contents of the encoder's shift register. Even with $L = 2$, this complicates the simulating program considerably, because *most* decisions made by the Viterbi decoder are very close. However, this is usually not because the decoder is on the verge of making an error, but because the decision is between two very improbable sequences somewhere in the trellis, and neither of these sequences is destined to reach the output anyway.

Since the original sequence will have already been processed by the Linkabit decoder anyway, the simplest way to simulate a decoder with list 2 would be to begin by re-encoding the sequence that was decoded on the first pass and subtract it from the original.

The simulator's task of finding good second-choice message sequences is now simplified by its a priori knowledge that the first choice will be the all-zero sequence. Because of this fact, the simulator need not differ from the conventional Viterbi decoder except in the number of its outputs. In addition to the estimated message sequence, which we know will be all-zero except in the rare events when the simulator is able to correct a memory truncation error, there are three other outputs which are of considerable importance. These are the likelihood of the message register containing the (first choice) all-zero sequence, the likelihood of the message register containing the (second choice) 1000 . . . 0 sequence, and the full previous message sequence corresponding to this second choice. This sequence represents the most probable error event under the hypothesis that the error event ends with the bit about to pass out of the message register.

When the likelihoods of the two candidates are close, then a likely error event has been detected and the appropriate bits of the decoded message sequence should be erased.

Of course, those error events which occur when two or more wrong paths are more probable than the correct one will not be erased by the algorithm just described. Such events would cause a decoding error even if the decoder were allowed a list of two candidates. When the rate of the code is sufficiently low (or, equivalently, if the signal-to-noise ratio is sufficiently high), then a list-of-two error of this type is much less probable than a conventional list-of-one error. However, when the rate of the code is sufficiently high (or, equivalently, the signal-to-noise ratio is sufficiently low), then most list-of-one errors are also list-of-two errors.

Fortunately, the three outputs of the simulator contain sufficient information to determine, with high probability, which type of error has occurred. When the likelihoods of both candidates are relatively high, then a list-of-two

error is very unlikely and a decoding error can almost surely be prevented by erasing the second-choice candidate message pattern. For example, if this is . . . 00010101, then only the three bits indicated by the ones need be erased. The two zero bits within the likely error event were decoded correctly, independently of whether this likely error event actually occurred. However, if the likelihoods of both candidates are relatively low, then the selected choice represents the best of a bad lot, and a list-of-two error is almost as likely as a list-of-one error. Very probably, the third-, fourth-, and fifth-place choices rank very close to the second. Under these circumstances, the only way the Viterbi simulator can be fairly sure of making no error is to erase *all* of the bits within the burst corresponding to the second choice, and possibly a few previous bits as well. I cannot think of any good simple algorithm to determine how far back to extend the erasure burst. One sophisticated approach would be to couple this simulator with another simulator which decoded the convolutional code *backwards in time*. Just as the outputs of the forward-in-time Viterbi simulator give good estimates of the probabilities of error events ending at each message digit, the outputs of the reverse-in-time Viterbi simulator would give good estimates of the probabilities of error events beginning at each message digit. By combining the two, a good estimate of the location and extent of list-of-two error events could be obtained. The message bits within such a span could then be erased.

There remains the problem of selecting the values of likelihoods which should cause the simulator to erase. The selection of these parameters should be governed by the erasure and error-correct capabilities of the outer code.

With 3 erasures in a block of length 24, the Golay code can still correct any pattern of two or fewer errors. A single error can be corrected in the presence of any pattern of 5 erasures and most patterns of 6 erasures. Hence, if the Viterbi simulator erases up to 15 to 25% of the bits in a long block, there is still an excellent chance that the outer interleaved Golay code will be able to correct these erasures and any error events that were undetected by the simulator as well. If the outer code still fails to correct the erased Viterbi output, then there are still further, even more complicated attacks that might be tried. For example, one might try to use the constraint that all bits in a candidate Viterbi error event corresponding to a likely second choice must be the same. However, the number of blocks not decoded correctly by the refined outer decoder when suitable bits of its input have been erased is so small that such further refinements may not be necessary.

Other work on causing the Viterbi decoder to output erasures has been done by Clark and Davis (Ref. 1).

Reference

1. Clark, G. C., Jr., and Davis, R. C., "Two Recent Applications of Error-Correction Coding to Communications Systems Design," *IEEE Trans. on Comm. Tech.*, Vol. 19, pp. 856–863, 1971.

Weight Distributions of Some Irreducible Cyclic Codes

L. D. Baumert
Communication Systems Research Section
J. Mykkeltveit
University of Bergen, Norway

Irreducible cyclic codes are one of the largest and most powerful known classes of block codes. For example, the celebrated Golay code now being studied for use on the Mariner Jupiter-Saturn Mission is an irreducible cyclic code. This article presents techniques for computing the weight enumerators of a large subclass of irreducible cyclic codes.

I. Introduction

Irreducible cyclic codes are binary and nonbinary block codes whose encoders are linear feedback shift registers, such that the polynomial that represents the feedback logic is irreducible. Irreducible cyclic codes have proved to be among the most useful block codes: the (32, 6) first-order binary Reed-Muller code currently in use on Mariner flight projects and the (24, 12) binary Golay code which has been proposed for a Mariner Jupiter/Saturn 1977 (MJS'77) concatenated coding system are both (essentially) irreducible cyclic codes. Nonbinary irreducible cyclic codes could be used to conserve bandwidth for low-rate, deep-space telemetry.

It is the object of this article to provide techniques for computing the weight enumerators of a large class of irreducible cyclic codes. The weight enumerator of a block code of length n is the polynomial

$$A(Z) = \sum_{i=0}^{n} A_i Z^i$$

where A_i denotes the number of words of weight i in the code. The enumerator $A(Z)$ provides valuable information about the performance of the code, and is needed to compute the error probability associated with proposed decoding algorithms.

The results of this paper enable one to compute the weight enumerator of all (n, k) p-ary irreducible codes for which the integer $N = (p^k - 1)/n$ is a prime congruent to 3 (mod 4) for which p has order $(N - 1)/2$.

II. Preliminaries

Let p be a prime, $q = p^k$, F_q the finite field with q elements and $T(\xi) = \xi + \xi^p + \cdots + \xi^{p^{k-1}}$, the trace of F_q/F_p. If n divides $q - 1$ and if θ is a primitive n-th root of unity in F_q, the set C of n-tuples

$$c(\xi) = (T(\xi), T(\xi\theta), \cdots, T(\xi\theta^{n-1})), \qquad \xi \text{ in } F_q$$

in a vector space over F_p that is closed under the cyclic permutation $S: (v_0, v_1, \cdots, v_{n-1}) \to (v_1, \cdots, v_{n-1}, v_0)$. C is called an (n, k) irreducible cyclic code over F_p. (Cyclic because it is S-invariant and irreducible because no subspace of C is S-invariant).

Let N be a positive integer not divisible by p and let $k = \text{ord}_N(p)$, i.e., k is the least positive integer such that $p^k \equiv 1$ modulo N. Associate with N and p the sequence of (n_m, km) irreducible cyclic codes with $n_m = (p^{km} - 1)/N$. R. J. McEliece and H. Rumsey (Ref. 1) have shown that the calculation of the weight distributions for this whole sequence of codes reduces to a single calculation (essen-

tially that of calculating the weight distribution for the case $m = 1$). Explicitly, they show that we want to determine the polynomial

$$H^{(1)}(x) = H(x) = \sum_{i=0}^{N-1} \eta_i x^i \tag{1}$$

where the numbers η_i are defined as follows: let Ψ be a primitive root of F_q such that $\Psi^N = \theta$ (thus $nN = p^k - 1$), let $\zeta = \exp(2\pi i/p)$ and let $\epsilon(\xi) = \zeta^{T(\xi)}$, then

$$\eta_i = \eta(\Psi^i) = \sum_{j=0}^{n-1} \epsilon(\Psi^i \theta^j) = \sum_{j=0}^{n-1} \epsilon(\Psi^{Nj+i}) \tag{2}$$

Thus

$$H(x) \equiv \sum_{0 \neq \alpha \epsilon F_q} x^{\mathrm{ind}(\alpha)} \epsilon(\alpha) \qquad (\text{modulo } x^N - 1) \tag{3}$$

where if $\alpha = \Psi^i$, $\mathrm{ind}(\alpha) = i$.

Baumert and McEliece (Ref. 2) have determined this polynomial in many of the simpler cases. In particular, when $k = \phi(N)/2$ they indicate methods that can be used to solve the problem (at least for those cases with $(p^k - 1)/(p - 1) \equiv 0$ modulo N, as it always is for $p = 2$). Here, when N is a prime number of the form $4t + 1$ the code weight distributions are particularly nice. These are all contained in Theorem 6 (Ref. 2). When N is a prime of the form $4t + 3$, things are a bit more difficult. In this note we establish a general formula for $H(x)$ that covers all such primes $N = 4t + 3$ with the single exception $N = 3$. Furthermore, the analogous polynomials $H^{(m)}(x)$ are also determined as well as the associated code weight distributions for the whole sequence of (n_m, km) irreducible cyclic codes. To accomplish this we make use of the rule (Ref. 1):

$$-H^m(x) \equiv (-H(x))^m \qquad (\mathrm{mod}\, x^N - 1) \tag{4}$$

III. Statement and Proof of the Results

Let $\beta = \exp(2\pi ij/N)$, $\beta \neq 1$, then it is a classical result that

$$H^{(m)}(\beta)\,\overline{H^{(m)}(\beta)} = q = p^{mk} \tag{5}$$

where the bar denotes complex conjugation. Furthermore,

$$H^{(m)}(1) = -1 \tag{6}$$

(proofs can be found in Ref. 2 as well as many other places). Since N is a prime number it follows that the $\eta_i^{(m)}$ (i.e., $H^{(m)}(x)$) can easily be determined from the coefficients a_i in

$$H^{(m)}(\beta) = a_0 + a_1 \beta + \cdots + a_{N-1} \beta^{N-1} \tag{7}$$

where, for definiteness, we fix $\beta = \exp(2\pi i/N)$.

Equation (5) shows that it is useful to know the highest power of p that divides $H(\beta)$; let this be p^a. Stickelberger (Ref. 3) provides us with a way of determining a. Let $t = t_0 + t_1 p + \cdots$ be the expansion of t in the base p and let $w_p(t) = t_0 + t_1 + \cdots$. Then, Stickelberger tells us that

$$(p-1)\,a = \min\{w_p(jn): 1 \leq j < N \text{ where } (j, N) = 1\} \tag{8}$$

Lemma (McEliece and Welch):

Let N and p be prime numbers, $N = 4t + 3$ and $3 \neq N \neq p$. Let $k = \mathrm{ord}_N(p) = (N-1)/2$ and let p^a be the highest power of p that divides $H(\beta)$, $\beta = \exp(2\pi i/N)$. Then

$$a = w_p(n)/(p-1) = \sum r_i/N \tag{9}$$

where the r_i are the quadratic residues of N.

Proof:

Note first that $r \equiv pj$ modulo N implies that $w_p(rn) = w_p(jn)$. For

$$jn = j_0 + j_1 p + \cdots + j_{k-1} p^{k-1} \tag{10}$$

$$pjn = 0 + j_0 p + \cdots + j_{k-2} p^{k-1} + j_{k-1} p^k$$

$$\equiv j_{k-1} + j_0 p + \cdots + j_{k-2} p^{k-1} \text{ modulo } nN\,(= p^k - 1)$$

But $pjn \equiv rn$ modulo nN as well, and since both of these are reduced modulo nN they must be equal. So $w_p(rn) = w_p(pjn) = w_p(jn)$ as asserted and

$$rn = j_{k-1} + j_0 p + \cdots + j_{k-2} p^{k-1} \tag{11}$$

In the case at hand p generates the quadratic residues modulo N and -1 is a quadratic nonresidue of N. So only $j = \pm 1$ need be considered in Eq. (8). We wish to show that $w_p(n) \leq w_p(-n)$. Let $r_i \equiv p^i$ modulo N ($i = 0, 1, \cdots, k-1$) and let $s_i \equiv -r_i$ modulo N. Then, it follows from Eqs. (10) and (11) that, using $j = 1$,

$$n \sum r_i = w_p(n)\,(1 + p + \cdots + p^{k-1})$$

$$= w_p(n)\,(p^k - 1)/(p-1) \tag{12}$$

and similarly

$$n \sum s_i = w_p(-n)\,(p^k - 1)/(p-1)$$

So

$$w_p(n) < w_p(-n) \text{ if } \sum r_i < \sum s_i$$

But, for primes $N = 4t + 3$, this is a famous result of Gauss (see Weyl, Ref. 4). So

$$a = w_p(n)/(p-1) = \sum r_i/N$$

as was to be proved.

Theorem:

Let N and p be prime numbers, $N = 4t + 3$ and $3 \neq N \neq p$. Let $k = \text{ord}_N(p) = (N-1)/2$, $a = w_p(n)/(p-1)$ and $\beta = \exp(2\pi i/N)$. Then for each integer $m \geqq 1$, there exist unique positive integers c_m, d_m prime to p, which satisfy the diophantine equation

$$c_m^2 + Nd_m^2 = 4p^{m(k-2a)} \tag{13}$$

and

$$H^{(m)}(\beta) = \pm p^{ma}\left(\frac{c_m + d_m + 2d_m \sum \beta^i}{2}\right) \tag{14}$$

where i runs over the quadratic residues modulo N. Further, the integers $\eta_i^{(m)}$ are given by:

$$\begin{aligned}
\eta_0^{(m)} &= \frac{\pm p^{ma} c_m (N-1) - 2}{2N} \\
\eta_1^{(m)} &= \frac{\pm p^{ma} (d_m N - c_m) - 2}{2N} \\
-\eta_{-1}^{(m)} &= \frac{\pm p^{ma} (d_m N + c_m) + 2}{2N}
\end{aligned} \tag{15}$$

and this determines $H^{(m)}(x)$ completely, since $\eta_{ip}^{(m)} = \eta_i^{(m)}$ (all i).

Proof:

Since $N > 3$, we have $k > 1$ and so $(p-1, N) = 1$. By the Corollary of Theorem 2 (Ref. 2) it follows that $H(\beta)$ is an algebraic integer of $Q(\beta)$; in fact, an integer of its unique quadratic subfield $Q(\sqrt{-N})$. (Q denotes the field of rational integers here.) Now, every algebraic integer of $Q(\sqrt{-N})$ has a unique representation in the form $(c + d\sqrt{-N})/2$ where c, d are rational integers and $c \equiv d$ modulo 2. Conversely, every such expression is an algebraic integer of $Q(\sqrt{-N})$. Let $\alpha = H(\beta)/p^a$ with a defined by Eq. (9) above. Then,

$$4\alpha\bar{\alpha} = c^2 + Nd^2 = 4p^{k-2a} \tag{16}$$

and α can be determined from among the solutions of this diophantine equation.

As a first step towards determining α, note that p divides α if and only if p divides c and p divides d. This is trivial except for $p = 2$, where the assumption c, d even requires special handling. Since $\alpha\bar{\alpha}$ is the norm of an algebraic integer it must be a rational integer. So $k - 2a \geqq 0$. But k is odd, so $k - 2a \geqq 1$. Furthermore, p generates the quadratic residues of N. In particular then, p is a quadratic residue of N. If $p = 2$, quadratic reciprocity tells us that $N \equiv -1$ modulo 8. So for $p = 2$, with c, d even, we find in examining Eq. (16) that $c^2 \equiv d^2$ modulo 8. Thus $c \equiv d$ modulo 4 and 2 does indeed divide α as asserted.

Since p^a was the highest power of p dividing $H(\beta)$, among the solution pairs c, d of Eq. (16) we are only concerned with those c, d not divisible by p. Consider the prime ideal factorization of the principal ideal generated by p in $Q(\sqrt{-N})$. Here $(p) = PQ$, where P, Q are complex conjugate prime ideals (i.e., $Q = \bar{P}$). So if $\gamma = (e + f\sqrt{-N})/2$ with e, f solutions of Eq. (16) and e, f prime to p, it follows that the ideal (γ) can only be P^{k-2a} or Q^{k-2a}. Thus γ or $\bar{\gamma}$ generates the same ideal that α does. Say $(\gamma) = (\alpha)$; this implies that $\gamma = u\alpha$, where u is a unit of the field $Q(\sqrt{-N})$. But, for $N > 3$, this field has only ± 1 as units. So there are only 4 possibilities for α:

$$\alpha = \pm\left(\frac{c \pm d\sqrt{-N}}{2}\right)$$

The $\pm$ sign for d corresponds to the choice between α and α which is of no consequence, as it merely reflects the ambiguity between $H(\beta)$ and $\overline{H(\beta)}$ and does not affect the answer materially. So we may stipulate without loss, that c and d are the unique positive integers, prime to p, that satisfy Eq. (16) and that $\alpha = \pm(c + d\sqrt{-N})/2$. The remaining $\pm$ ambiguity is critical and shows up in the formulas for the η_i's. Fortunately, the requirement that all the η_i's must be rational integers always resolves this final ambiguity.

So we have determined that

$$H(\beta) = \pm p^a\left(\frac{c + d\sqrt{-N}}{2}\right) = \pm p^a\left(\frac{c + d + 2d\sum \beta^i}{2}\right)$$

where i runs over the quadratic residues modulo N, as follows from Gauss' representation of $\sqrt{-N}$ in the field $Q(\beta)$. This, together with $H(1) = -1$, suffices to determine the η_i as given in Eq. (15); the theorem is proved for $m = 1$.

With $m > 1$, the above reasoning together with Congruence (4) taken at $x = \beta$, shows that p^{ma} is the highest power of p dividing $H^{(m)}(\beta)$. So the argument above determines $H^{(m)}(\beta)$ exactly as indicated in Eqs. (13), (14), and (15).

Recalling the definition, Eq. (2), of the η_i and the definition of a code word $c(\xi)$ in one of these irreducible cyclic codes, it is clear that the η_i's determine the distribution of the elements of F_p amongst the codewords of C. Thus:

Theorem:

Let N and p be prime numbers, $N = 4t + 3$ and $3 \neq N \neq p$. Let $k = \mathrm{ord}_N(p) = (N-1)/2$, let $a = w_p(n)/(p-1)$, let $q = p^{mk}$, and let c_m, d_m be the unique positive integers prime to p that satisfy the diophantine equation $c_m^2 + Nd_m^2 = 4p^{m(k-2a)}$. Then there are three distributions of elements of F_p that occur in the nonzero codewords of the associated (n_m, km) irreducible cyclic code: (caution if $m = 1$ and $k \neq \mathrm{ord}_n p$ this code is degenerate in that some codewords are repeated).

Class 0 (containing n_m codewords):

$$N_0 = \frac{2q - 2p \pm (p-1)\,p^{ma}\,c_m\,(N-1)}{2pN}$$

$$N_i = \frac{2q \mp p^{ma}\,c_m\,(N-1)}{2pN} \qquad i = 1, \cdots, p-1$$

Class 1 (containing $n_m(N-1)/2$ codewords):

$$N_0 = \frac{2q - 2p \pm (p-1)\,p^{ma}\,(d_m N - c_m)}{2pN}$$

$$N_i = \frac{2q \mp p^{ma}\,(d_m N - c_m)}{2pN} \qquad i = 1, \cdots, p-1$$

Class -1 (containing $n_m(N-1)/2$ codewords):

$$N_0 = \frac{2q - 2p \mp (p-1)\,p^{ma}\,(d_m N + c_m)}{2pN}$$

$$N_i = \frac{2q \pm p^{ma}\,(d_m N + c_m)}{2pN} \qquad i = 1, \cdots, p-1$$

Here N_i is the number of times the element i of F_p appears in the codeword.

IV. Some Examples

Example 1: $N = 7$, $p = 2$, $k = 3$, $n = a = c = d = 1$. This code is degenerate and its 7 (supposed nonzero) codewords are 1,1,1,1,0,0,0. Nevertheless our formulas are valid. They give $\eta_0 = \eta_1 = -1$, $\eta_{-1} = +1$; $H(x) = -1 - x - x^2 + x^3 - x^4 + x^5 + x^6$. Class 0 contains 1 codeword ($N_0 = 0$, $N_1 = 1$). Class 1 contains 3 codewords ($N_0 = 0$, $N_1 = 1$). Class -1 contains 3 codewords ($N_0 = 1$, $N_1 = 0$.

It can be shown that these codes are degenerate only when $m = 1$ (and not always then). So let us consider $m = 2$. Here $N = 7$, $p = 2$, $mk = 6$, $n_2 = 9$, $a = d_2 = 1$, $c_2 = 3$. Equation (15) yields $\eta_0^{(2)} = 5$, $\eta_1^{(2)} = 1$, $\eta_{-1}^{(2)} = -3$ so $H^{(2)}(x) = 5 + x + x^2 + x^4 - 3(x^3 + x^5 + x^6)$. Thus there are 9 codewords ($N_0 = 7$, $N_1 = 2$), 27 codewords ($N_0 = 5$, $N_1 = 4$) and 27 codewords ($N_0 = 3$, $N_1 = 6$).

Example 2: $N = 11$, $p = 3$, $k = 5$, $n = 22$, $a = 2$, $c = d = 1$. Equation (15) yields $\eta_0 = \eta_1 = 4$, $\eta_{-1} = -5$. Class 0 contains 22 codewords ($N_0 = 10$, $N_1 = N_2 = 6$). Class 1 contains 110 codewords ($N_0 = 10$, $N_1 = N_2 = 6$). Class -1 contains 110 codewords ($N_0 = 4$, $N_1 = N_2 = 9$).

Example 3: $N = 79$, $p = 2$, $k = 39$, $n = 6\,958\,934\,353$, $a = 17$, $c = 7$, $d = 1$. Thus $\eta_0 = 452945$, $\eta_1 = 59729$, $\eta_{-1} = -71343$. Class 0 contains n codewords ($N_0 = 3479693649$, $N_1 = 3479240704$). Class 1 contains $39n$ codewords ($N_0 = 3479497041$, $N_1 = 3479437312$). Class -1 contains $39n$ codewords ($N_0 = 3479431505$, $N_1 = 3479502848$).

References

1. McEliece, R. J., and Rumsey, H., "Euler Products, Cyclotomy and Coding," *J. Number Theory*, Vol. 4, No. 3, pp. 302–311, June 1972.
2. Baumert, L. D., and McEliece, R. J., "Weights of Irreducible Cyclic Codes," *Inform. Contr.*, Vol. 20, No. 2, pp. 158–175, March 1972.
3. Stickelberger, L., "Über eine Verallgemeinerung der Kreisteilung," *Math. Ann.* Vol. 37, (1890), pp. 321–367.
4. Weyl, H., *Algebraic Theory of Numbers*, pp. 199–200. Princeton University Press, Princeton, N.J., 1940.

Implementation of a Flutter Compensator for DSN Predetection Recording

A. G. Slekys
Communications Systems Research Section

Baseband recordings of simulated phase-shift-keyed signals were carried out at CTA 21 in a DSN-compatible environment with the purpose of estimating the data degradation (measured in (ST) symb/N_0) caused by the record/playback process. The major cause of the lower effective signal-to-noise ratio at playback is recorder time-base instability or flutter. Incorporating a digital flutter compensator in the playback scheme significantly reduces the instantaneous phase jitter and hence the overall record/playback degradation. Results of the tests, together with a description of the compensator, are presented.

I. Introduction

A practical scheme for predetection recording of spacecraft telemetry data for use in the DSN with existing standard hardware is described. Results of tests performed on a simulated phase-shift-keyed (PSK) telemetry IF signal at CTA 21 show an estimated data degradation of 5 to 10 dB (*ST* symb/N_0) introduced by the record/playback process, most of it due to recorder time-base instability at playback (Ref. 1). Addition of a digital flutter compensator in the playback hardware reduced the rms phase jitter by 2 orders of magnitude. Curves of the peak-to-peak and rms phase correction provided by the compensator at different tape speeds are presented.

II. Predetection Recording System

Figure 1 shows the experimental setup for performing baseband recording of 10-MHz telemetry IF. Required additional hardware is a low-pass filter for noise limiting and a linear mixer to add in a sine-wave sync signal at a frequency at least twice the baseband bandwidth. Since the record/playback speed ratio is unity, the tape speed at record is set to the value that provides sufficient bandwidth for accommodating the signal spectrum. Table 1 lists the available tape speeds and associated bandwidths for the Ampex FR 1400 tape units presently installed in the DSN.

Simulated PSK signals using equipment at CTA 21 with a range of 15 to 5 dB were recorded at 76.2 cm/s (30 ips). A medium rate uncoded data signal, at 1024 bits per second (BPS), with a 24-kHz subcarrier was used.

Figure 2 details the playback arrangement, with and without the flutter compensator.

The sync signal is bandpass-filtered from the output signal track and used to clock the data into the compensator. The balanced modulator in the Subcarrier Demodulator Assembly (SDA) retranslates either the compensated baseband signal or the uncompensated low-pass filtered baseband signal back to the 10-MHz IF frequency. The detected data output from the SDA is then sent on to the Symbol Synchronizer Assembly (SSA) and Telemetry and Command Processor Assembly (TCP) computer for calculation of data signal-to-noise ratio (SNR), measured in (ST symb/N_0).

Without the record/playback interruption, the SDA was able to indicate suitable lock at about 1 dB. Using the FR 1400-type unit for both recording and playback, the reproduced baseband was phase- and frequency-modulated to the extent that the SDA was unable to acquire suitable lock with the originally recorded 5-dB baseband signal, and showed only intermittent lock with the 15-dB signal during periods of more linear tape playback. The data degradation during the locked intervals ranged from 5 to 8 dB. The present DSN predetection recording policy involves recording on FR 1400 units with playback on the FR 2000 unit at CTA 21, with estimated degradations of only 1 to 2 dB. Measurements of data degradation with the addition of the compensator are incomplete as yet, although estimates are of 1- to 2-dB loss relating to observations of the correlation indication provided by the SDA when lock is achieved.

III. Flutter Compensator Design

Figure 3 is a block diagram of the flutter compensator, essentially a digital buffer with a variable frequency data rate in and a constant frequency data rate out. Clocking of the analog-to-digital conversion of the baseband signal is performed by the sine-wave sync signal, which on playback is flutter modulated equally with the data signal. The sampled signal is written into the digital buffer at the modulated rate and read out at a constant rate, equal to the frequency of the originally recorded sine-wave sync signal. The output is then passed through a digital-to-analog converter and low-pass filter with a cutoff frequency of half the sync-signal frequency, thus providing a reconstructed and compensated version of the baseband signal.

The present design[1] has a total buffer capacity of 1024 six-bit words, and employs a six-bit analog-to-digital converter with a maximum sampling rate of 200 kHz.

Since readout of data from the buffer commences only after it is half full, the limit on time variations introduced on the data signal by the record/playback process is 512 samples, which if exceeded causes buffer overflow.

IV. Evaluation of Flutter Compensator

Essentially the same record/playback setup was used as outlined in Figs. 1 and 2. The interfacing with the real-time CTA 21 equipment was not required, since a single-frequency sine wave at 50 kHz (coherent with the 200-kHz sync signal) replaced the aforementioned baseband telemetry signal. The originally recorded signal was compared with both the compensated and uncompensated versions of the reproduced signal, with the purpose of establishing peak-to-peak and rms phase differences. Figures 4, 5, and 6 show the instantaneous phase jitter correction provided by the compensator. Peak-to-peak and rms phase errors as measured on a strip-chart recorder connected to the output of a phase meter are plotted versus time for signals recorded at 76.2, 152.4, and 304.8 cm/s. It can be seen that the short-term time-base instability causes phase errors as large as ± 180 deg at several frequencies, corresponding to mechanical nonlinearities of the machine.

Compensated rms phase error plots show variations within 2 deg. The compensated rms phase error trace of Fig. 5 shows an "overflow" region, an interval of about 6 s duration when the time delay between the compensated and uncompensated signals exceeded half the buffer capacity or 512 words. This "drifting" or long-term speed instability of the recorder caused several overflows of duration typically around 10 s. The effect of an overflow is to cause multiple or overlapping versions of the sampled sinusoid to be reconstructed at the output. With a time constant of about 5 to 10 s, the speed servo loop built in the recorder slows up the playback speed sufficiently to allow the buffer to be emptied at a faster rate than filled, until the output/input ratio again approaches unity. In order to overcome this problem, buffer size must be increased by about 30%, or a feedback signal proportional to the output/input sample

[1]Use of breadboard model through courtesy of L. Jung, DSIF Digital Systems Development Section, JPL.

locations in the buffer must be provided as an additional error signal to the speed servo loop.

V. Conclusion

A practical scheme for predetection recording of telemetry with low SNR using existing DSN hardware has been described. Implementation of a flutter compensator in the playback setup allows for use of existing Ampex FR 1400 tape units exclusively, by improving rms phase jitter by 2 orders of magnitude. An advanced prototype designed with increased buffer memory will eliminate the overflow problem with the present breadboard model.

Reference

1. Slekys, A., "Predetection Recording and Dropouts," in *The Deep Space Network Progress Report*, Technical Report 32-1526, Vol. IX, pp. 115–118. Jet Propulsion Laboratory, Pasadena, Calif., June 15, 1972.

Table 1. Tape speed vs bandwidth and recording time for the Ampex FR 1400 tape unit

Tape speed, cm/s (in./s)	Recording bandwidth, kHz	Recording time, h
304.8 (120)	1500	0.25
152.4 (60)	750	0.5
76.2 (30)	375	1
38.1 (15)	187	2
19.05 (7½)	93	4
9.52 (3¾)	46	8
4.76 (1⅞)	23	16

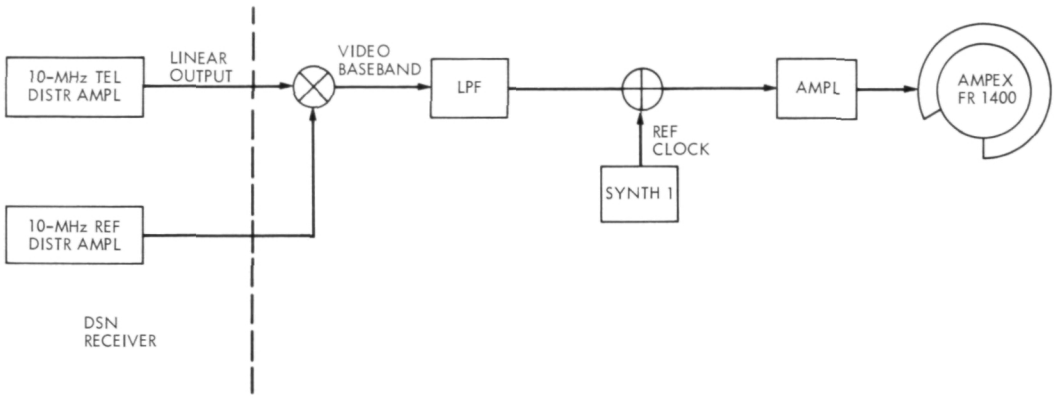

Fig. 1. Predetection recording system block diagram

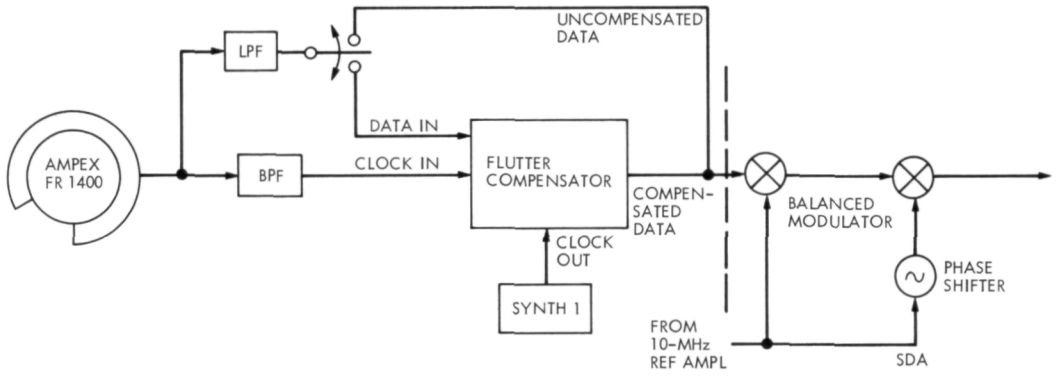

Fig. 2. Playback scheme with/without compensator

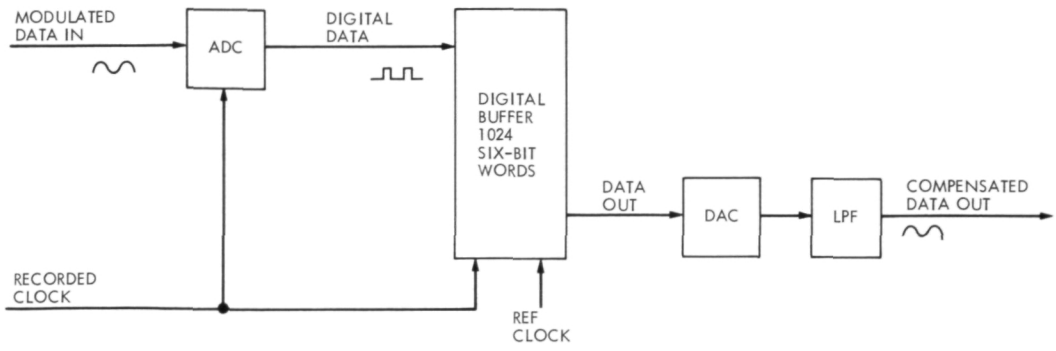

Fig. 3. Flutter compensator block diagram

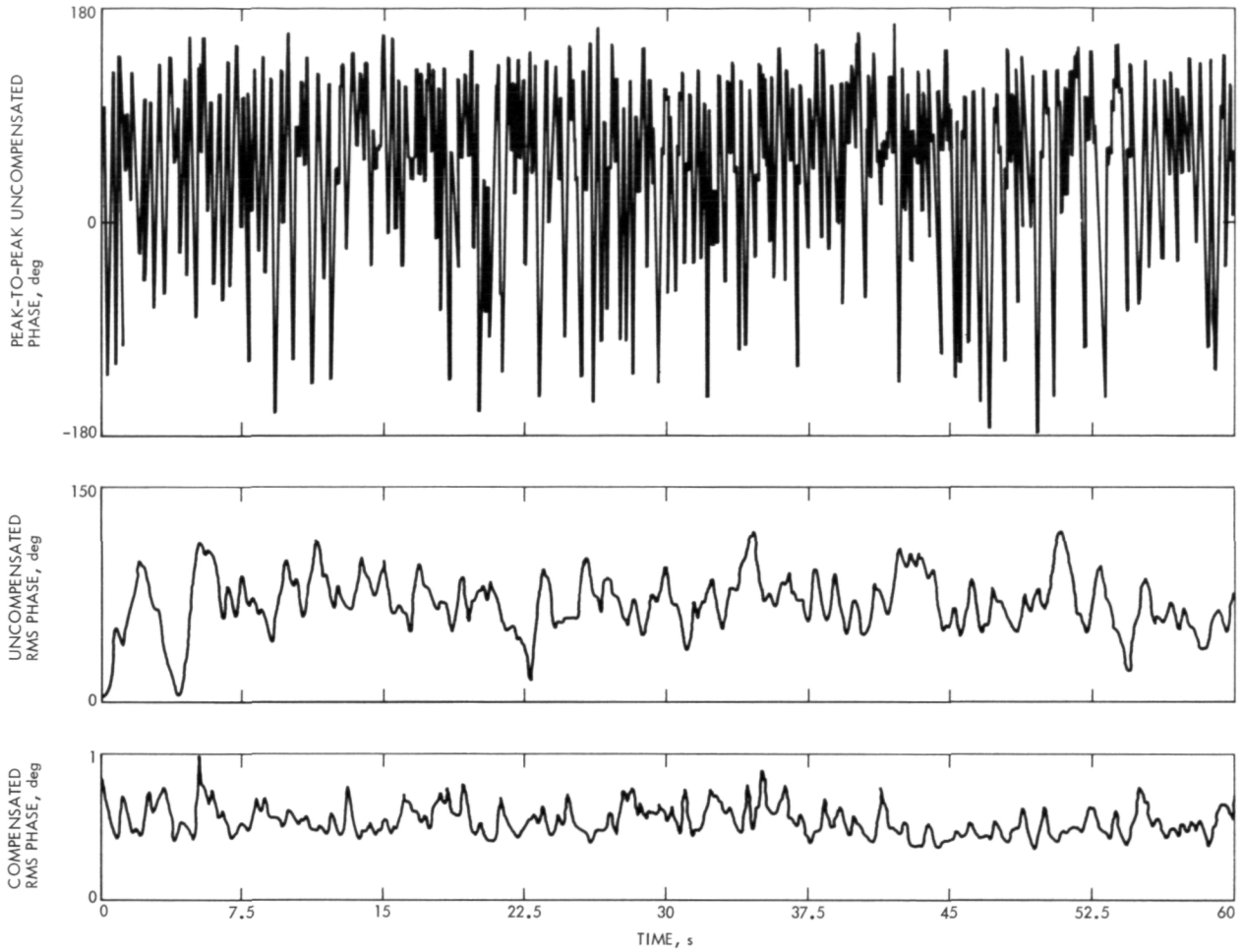

Fig. 4. Phase difference plots for signal reproduced at 76.2 cm/s (30 ips)

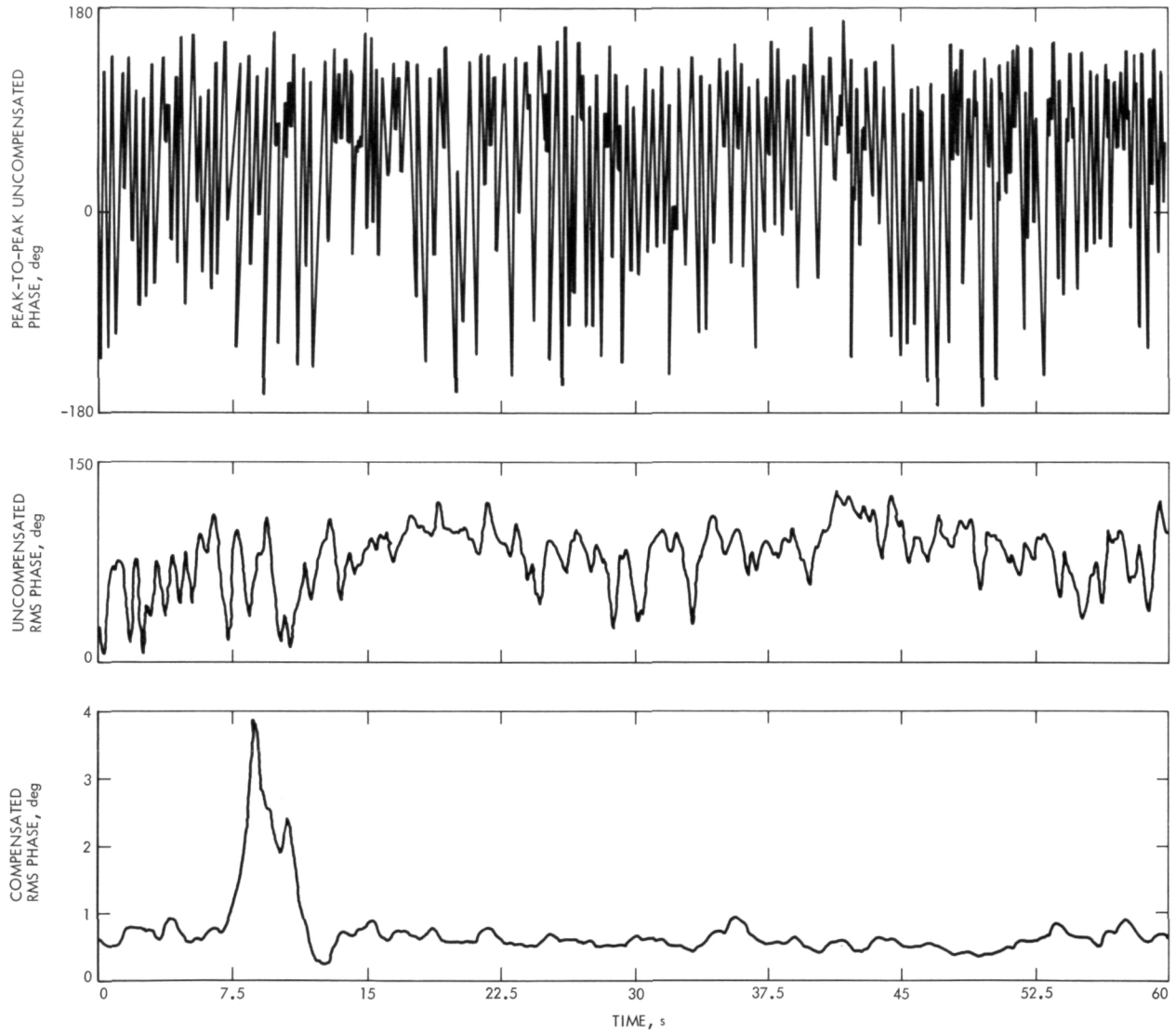

Fig. 5. Phase difference plots for signal reproduced at 152 cm/s (60 ips)

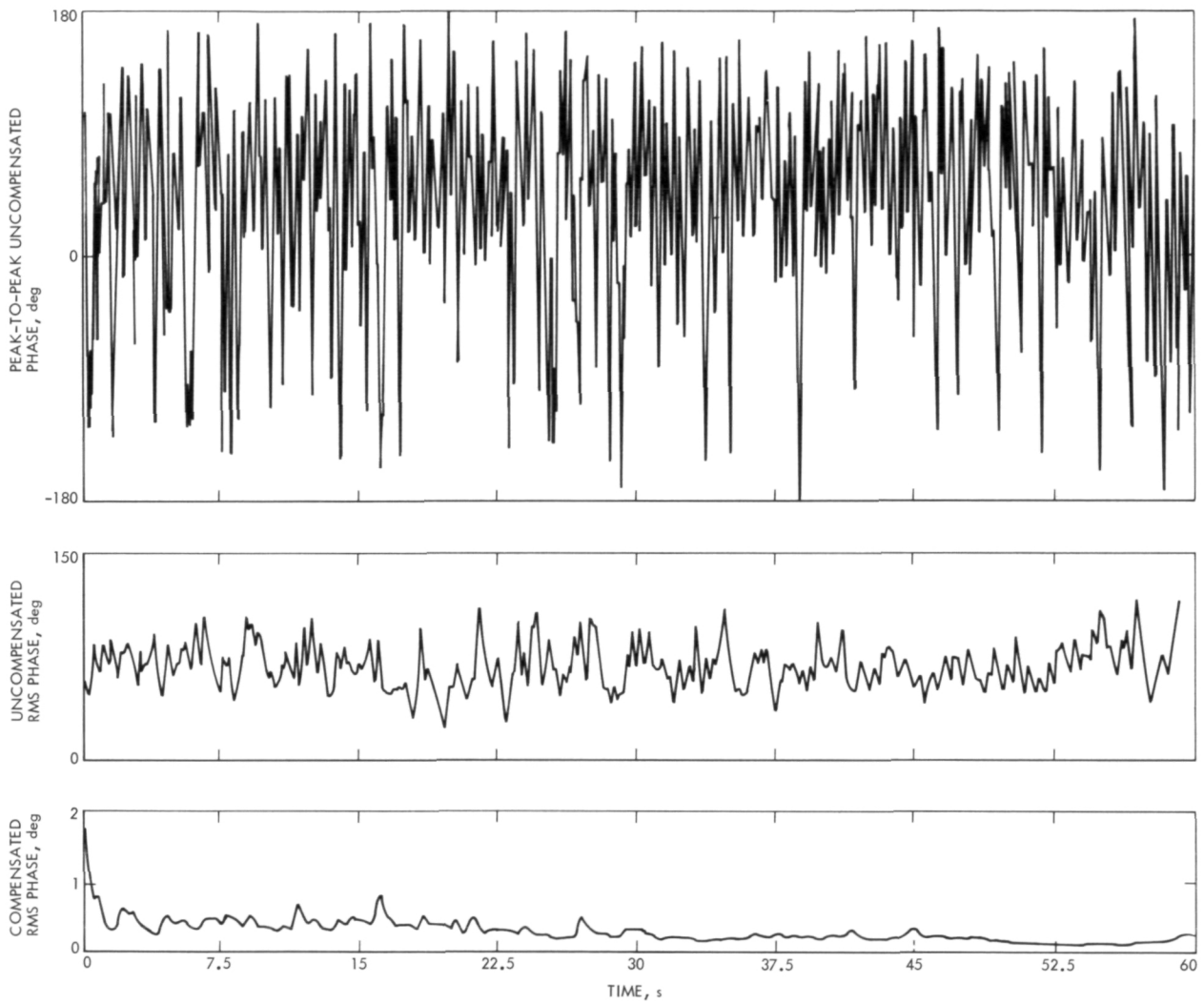

Fig. 6. Phase difference plots for signal reproduced at 304.8 cm/s (120 ips)

Block IV Subcarrier Demodulator Assembly Design

R. B. Crow
R.F. Systems Development Section

A design effort was undertaken during the past two years to design and build a Block IV Subcarrier Demodulator Assembly. The salient features that were to be incorporated were: (1) capability of manual or computer control, (2) small size, (3) higher data rate capacity (500,000 symbols/s), and (4) improved subcarrier tracking in the presence of high doppler rates. This report reviews the design and indicates the current status of the development project.

I. Introduction

The Block IV Subcarrier Demodulator Assembly (SDA) is a new assembly scheduled for incorporation into the DSN in FY 1975. The Block IV SDA is a second-generation development that has evolved from the basic development work done on the Block III SDA started in 1968. To appreciate the new design, a functional comparison between the Block III and Block IV SDA is listed in Tables 1 and 2 to illustrate the difference in the designs. Comments have been made where significant differences occur.

II. Block Diagram of Block IV SDA

It will be noted from the block diagram (Fig. 1) that the RF modules are designed for remote control (i.e., both the voltage variable attenuators and phase shifters are controlled from the control unit assembly) to allow either manual or computer control of the SDA.

This block diagram differs from the Block III SDA in that the error channel uses part of the quad intermediate-frequency (IF) channel. This reduces the required hardware and has the effect of improving the loop performance since the data and data estimate paths have more nearly equal time delays. A further improvement in path delay matching will be realized since increasing the package density has resulted in more of the signal path contained in each module and fewer system cables. Matching the time delay path (data and data estimate) is important since it directly affects the loop gain and therefore tracking performance.

III. Signal and Noise Level Profile for the Block IV SDA

The criteria utilized in this proposed design were as follows:

(1) Gain switching using combinations of 0-, 7-, 13-, and 20-dB attenuators is required before and after the phase switch in the quadrature generator to maintain maximum signal (and noise) level (consistent with linearity) vs subcarrier leakage at the phase switch. Gain switching is required due to the quadrature generator subcarrier leakage problem (i.e.,

the signals at the input to the quadrature generator are carrier times subcarrier times data, *and* subcarrier estimate. The output spectrum is not simply the product of the input, but is the product plus an unwanted additional component of the subcarrier estimate). A comparison was made between the Block III and Block IV performance for this problem and an improvement of 10 dB was achieved. This improvement was achieved by using devices with greater linear dynamic range.

(2) Bandwidth switching, after the quadrature generator, was implemented using six discrete bandwidths. Bandwidth selection was made using the criteria that

$$\frac{ST_{sy}}{N_o} = -1\,\text{dB}\ (\text{for}\ 5 \leqq R_{sy} \leqq 500\,\text{sps})$$

$$\frac{ST_{sy}}{N_o} = -4\,\text{dB}\ (\text{for}\ 500 \leqq R_{sy} \leqq 500\,\text{ksps})$$

determine the lower symbol rate allowed to guarantee system linearity. A 7-dB crest factor was allowed between the rms noise level and the 1-dB gain compression level for each system component.

Each bandwidth was chosen for its maximum symbol rate, through a filter with minimum tolerance bandwidth, according to $B_n = 9\,R_{sy}$ (noise bandwidth equals nine times symbol rate).

Filter noise bandwidths were also chosen such that a minimum number of filter bandwidths would cover the symbol rate range. The data estimate time constants (τ_D) were chosen in 1/3-decade increments so that IF filter bandwidth switching coincides with τ_D intervals.

IV. Phase-Locked Loop Design and SDA Performance Analysis

A. Design Characteristics

The subcarrier tracking loop shall be functionally configured as in Fig. 2 with the following design characteristics:

$$H(s) = \frac{G(s)}{1 + G(s)}$$

$$= \frac{1 + 2T_2 s + T_2^2 s^2}{1 + s\left(\frac{1}{G} + 2T_2\right) + s^2\left(\frac{2T_1}{G} + T_2^2\right) + s^3\left(\frac{T_1^2}{G}\right)}$$

where

$G(s)$ = open loop transfer function $= \dfrac{G\,(1 + T_2 s)^2}{s\,(1 + T_1 s)^2}$ (Ref. 1)

K_d = phase detector constant (V/cycle)

K_v = voltage-controlled oscillator (VCO) constant (Hz/V)

K_m = loop frequency multiplication factor

K_a = loop dc gain not included in loop filter

$G = \alpha_{sl}\,K_d\,K_v\,K_m\,K_a$

α_{sl} = loop gain suppression factor resulting from the effect of the bandpass limiter upon the amplitude error signal

$$= \text{erf}\left(\sqrt{\frac{(\alpha')^2\,\frac{S}{N_o}}{8\pi\,B_{if}}}\right) \text{for}\ \nu = 1/4$$

(see Fig. 1 and Ref. 2)

where ν is the fraction of the strong signal peak error voltage at which the limiter saturates (Ref. 2), and, for a 50% transition probability (Ref. 2),

α' = loop gain suppression factor resulting from the data estimate action upon the loop

$$= \left[0.769\left(0.887 + 0.2\left(\frac{ST_{sy}}{N_o}\right)^{1.2}\right)\Big/ \left(1 + 0.2\left(\frac{ST_{sy}}{N_o}\right)^{1.2}\right)\right] \text{erf}\left(\left(0.667\,\frac{ST_{sy}}{N_o}\right)^{0.5}\right)$$

B. Loop Design Implementation

Since the doppler offset (Ω, Hz), doppler rate (Λ, Hz/s), and mission time (t, s) are known, the SDA static phase error can be solved for by:

$$\Phi_{ss} = \frac{360\,(\Omega + \Lambda t)}{G} + \frac{720\,\Lambda\,T_1}{G}\,(\text{deg})$$

Given the configuration shown below, the loop can be designed to meet the required steady state phase error (Φ_{ss}) for a particular application.

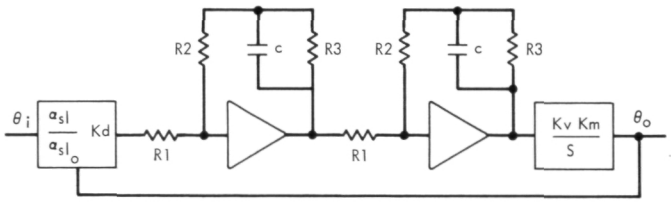

Since the loop filter has a transfer function of

$$F(s) = \left(\sqrt{K_a}\,\frac{1+T_2 s}{1+T_1 s}\right)^2 = \left(\left(\frac{R_2+R_3}{R_1}\right)\left(\frac{1+T_2 s}{1+T_1 s}\right)\right)^2$$

then

$$T_1 = R3C = \frac{360T_2^3\,\Lambda}{q\,\phi_{ss}} + \sqrt{\left(\frac{360T_2^3\,\Lambda}{q\,\phi_{ss}}\right)^2 + \left(\frac{360T_2^3\,(\Omega+\Lambda t)}{q\,\phi_{ss}}\right)}$$

$$T_2 = R2C = \frac{q_o\,(2q_o+3)}{2W1_o\,(2q_o-1)}$$

where

$$q = \alpha_{sl}\left(\frac{K_d\,K_v\,K_m\,K_a\,T_2^3}{T_1^2}\right) \approx \alpha_{sl}\,K_d\,K_v\,K_m \times \left(\frac{R_2+R_3}{R_3}\right)^2\left(\frac{R_2}{R_1}\right)^2 T_2$$

and

$$R_1 = R_2\left(\frac{R_2+R_3}{R_3}\right)\sqrt{\frac{\alpha_{sl_o}\,K_d\,K_v\,K_m\,T_2}{q_o}}$$

C. Loop Design Characterization

1. Loop noise bandwidth (two sided) (Ref. 3)

$$\mathcal{W}_l = \frac{q\,(2q+3)}{2T_2\,(2q-1)} = \frac{r\,(4r+3)}{T_2\,(4r-1)}$$

where

$$r_o = \frac{GT_2^3}{2T_1^2} = \frac{q}{2} = 3.375 \text{ (Ref. 3)}$$

$$r = r_o\,\frac{\alpha_{sl}}{\alpha_{sl_o}} \text{ (Ref. 3)}$$

Frequency acquisition can be accomplished by increasing the dc gain by a factor of 10 (bandwidth increase by a factor of 7.8) until frequency lock is accomplished and then logarithmically decreasing the gain to its nominal value.

2. Operating phase jitter. Theoretical phase noise of the subcarrier estimate is given by (Ref. 4):

$$\sigma_{\theta n}^2 = \Gamma_{sl}\left(\frac{1}{\alpha'}\right)^2\left(\frac{\pi}{2}\right)^2\left(\frac{N_o}{ST_{sy}} \times \frac{1}{2R_{sy}}\right) \times \left(\mathcal{W}_{l_o}\left(0.22447 r_o\,\frac{\alpha_{sl}}{\alpha_{sl_o}}\left(\frac{4r_o\,\alpha_{sl}+3\alpha_{sl_o}}{4r_o\,\alpha_{sl}-1\alpha_{sl_o}}\right)\right)\right)$$

where $r_o = 3.375$, and Γ_{sl} is the so-called soft limiter performance factor and may be taken as a constant 1.16 over the region of significant phase jitter (Ref. 5).

3. Signal-to-noise ratio degradation. Theoretical degradation of signal-to-noise ratio may be predicted as follows (Ref. 6):

$$\text{Degradation} = 20\log_{10}\left[1 - \left(\frac{2}{\pi}\right)^{1.5}\sigma_{\theta n} - \left(\frac{2}{\pi}\right) \times \phi_{ss}\,\text{erf}\left(\frac{\phi_{ss}}{\sqrt{2}\times\sigma_{\theta n}}\right)\right], \text{ in dB}$$

where $\sigma_{\theta n}$ is as specified above and erf is the error function. Table 3 illustrates the four bandwidths that are available. The loop, in the "nonacquisition" mode, is critically damped, and is overdamped in the acquisition mode.

4. SDA performance. A software program (written in PDP-11 BASIC) is available that allows the user to define a particular mission (ST_{sy}/N_o, Ω_o, Λ_o, mission time, R_{sy} and f_{sc}) and the particular loop configuration ($\mathcal{W}_{l_o}$) to obtain total SDA degradation. To demonstrate what performance could be expected, two subcarrier frequencies (20 and 400 kHz) were chosen and total SDA degradation as a function of doppler rate was computed as the symbol rate was changed from 5 to 500 ksps. (Figs. 3, 4, 5).

V. Block IV SDA Loop Filter Dc Offset Analysis

Dc offset is always of concern in a phase-locked loop (either second or third order) since it is an important parameter in the acquisition and static phase error characteristics. The improved doppler rate tracking performance obtained in the Block IV SDA has been purchased by designing a third-order phase-locked loop. The third-order loop has reduced the long term stability requirements for the VCOs (due to higher loop gain and an improved acquisition characteristic) but has initiated the requirement for much better engineering of the dc stability problem.

Analysis was performed by Tausworthe to determine the effect on the dc offset problem.[1] Figures 6 and 7 are

[1]Tausworthe, R. C., Jet Propulsion Laboratory, Pasadena, Calif. (private communication).

plots of dc imperfection (E in mV, referred to the phase detector output) vs frequency offset for various bandwidths and represents the maximum frequency offset (for a particular dc imperfection) that the loop will drive toward a zero beat condition for the proposed Block IV SDA design.

Measurements were made on the prototype loop filter. The test data indicated a stability of 10 μV (referred to the phase detector output) is possible.

If a margin is assumed to cover manufacturing and adjustment, a 1-mV offset would guarantee the following performance at design point: The narrow band loop ($\mathcal{W}_{L_0} = 0.03$ Hz) will acquire from an offset of $4.6 \times \mathcal{W}_{L_0}$ and narrow bandwidth using auto acquisition will acquire from an offset of $30 \times (\mathcal{W}_{L_0} = 0.03\,\text{Hz})$. The wide bandwidth ($\mathcal{W}_{L_0} = 0.5$ Hz) will acquire from an offset of $16 \times \mathcal{W}_{L_0}$ and wide bandwidth using auto acquisition will acquire from an offset of $112 \times (\mathcal{W}_{L_0} = 0.5\,\text{Hz})$.

VI. Calibration Sequence and Configuration Control

A. General

The Block IV SDA can be controlled by an operator through the manual control panel or by a computer through the 14-line standard interface. The control unit (Fig. 8) allows three functions to be performed:

1. Automatic system calibration. Built-in digital hardware has the calibration logic programmed into it so that the SDA sequences through the necessary adjustments and tests to verify its operational status.

2. Configuration control. This allows Manual (or computer) control of all calibration and operational configurations.

3. Fault location. There are four features of the Block IV SDA that permit rapid fault location:

(1) Module status indicators (one for each module) indicate that all configuration relay and reference circuits are operating correctly. These indicators are normally off, and turn on when a failure occurs.

(2) A 3-bit alpha-numeric error indicator on the front panel indicates the step in the calibration sequence when a failure occurs.

(3) A voltmeter has been incorporated to monitor key test points.

(4) To test the indicators on the front panel, a special test function was designed into the unit. The "in-lock" indicator can be depressed, which causes all light emitting diode indicators to turn on, thus giving a test to the fault location indicators.

The three controls at the top left corner of the front panel are calibration sequence controls, (INT CAL, RCV1 CAL, and RCV2 CAL) which the operator can use to initiate automatic system calibration. If a receiver is in a strong signal (continuous wave) test condition, the SDA will adjust its phase and gain to match the particular receiver.

The configuration controls that are available are MOD INDEX (modulation index), SUBCARRIER FREQUENCY (X4), SYM RATE (symbol rate), and METER SELECT.

The MODE control switch selects between MAN (manual) and COMP (computer) control of the SDA. The NORMAL/INTERPLEX switch controls interplex phasing and insertion of a notch filter when appropriate. The INPUT selector allows either RCV1 (receiver 1) or RCV2 (receiver 2) or TAPE/TEST to be used as the input to the SDA. The OUTPUT selection for the SDA is either DEMOD, which is the SDA output, or TAPE or TEST, which are signals bypassing all but the output circuitry of the SDA. The LOOP controls select the loop bandwidth, initiate AUTO ACQ (auto acquisition) and place the loop in SHORT or in TRACK configuration.

The METER control allows a meter check by putting the ground on it. Measurements can be made to monitor the data or quad channel output, dynamic phase error, correlation detector output (also available on an analog meter), static phase error output or receiver 1 or 2 AGC voltage. The control unit thus serves as input into, and receives feedback from, the SDA so that the indicators on the front panel reflect the static and dynamic status of the system.

B. SDA Control Unit Logic Description

The logic flow of the Block IV SDA is described in the following pages and is shown as a logic flow diagram in Fig. 9.

1. Momentary power loss. The SDA control unit contains a "power on" sensing circuit that is utilized to indicate a momentary loss of power. This feature is important because information stored in the SDA control registers

can be lost as a result of a power loss. The operation of the "power on" sensing electronics is as follows:

(1) When the power drops below an adequate level, the computer data-ready line is pulled down (grounded). This condition would be apparent on the control panel as erratic indications from indicator/switches.

(2) When the power comes back up to an acceptable level, the "power on" sensing circuit sends a signal to the computer and control panel ERROR WORD display, indicating there has been a power loss. This indicates to the computer or operator that there has been a power loss and the full calibration procedure must be initiated.

(3) The "power on" signal also initiates the following:

(a) Power on time delay (1 min).

(b) Internal voltage test. The control unit configures itself to measure internal voltages. The successful completion of this function provides an enable for the INT CAL command.

(c) Set configuration word flag to NO. This prevents the SDA from using the stored computer configuration word if there had been a momentary power loss. When the computer sends the configuration word the flag is changed to YES.

2. Calibration summary. The calibration of the SDA is composed of two major functions: internal calibration and receivers 1 and 2 calibration. Internal calibration is performed using no external input signals (except 5- and 10-MHz reference) and receivers 1 and 2 calibration utilizes a 10-MHz (continuous wave) signal from the receivers. The SDA control unit automatically performs the calibration procedure, adjusting SDA module parameters so the SDA is ready to receive the spacecraft signal. The sequencing of the SDA into and out of these major calibration functions is presented on the following pages. The tuning operations performed during calibrations are listed below.

a. Internal calibration

(1) Phase adjust: adjusts phase shifters for output null for the data channel, quad channel, and error channel.

(2) Gain adjust: adjusts attenuators for nominal output for the data channel and quad channel.

(3) Phase check: verifies output null for all gain/bandwidth settings for the data channel, quad channel, and error channel.

(4) Gain check: verifies nominal output for all gain/bandwidth settings for the data channel, quad channel, and error channel.

(5) Interplex test: verifies interplex 90-deg phase shifter is functioning.

(6) Loop check: generates subcarrier (f_{sc}) times data test signal to check loop acquisition performance.

(a) Normal acquisition: checks acquisition for the 0.5-Hz and 0.23-Hz bandwidths.

(b) Auto acquisition: checks auto acquisition in wide (3.9-Hz to 0.5-Hz) bandwidths.

b. Receivers 1 and 2 calibration

(1) Adjust phase: adjusts SDA phase for operation with receivers 1 and 2.

(2) Adjust gain: adjusts SDA gain for operation with receivers 1 and 2.

VII. Mechanical Design and Thermal Analysis

The required subassemblies, for two Block IV SDAs, are mounted in a standard DSN 209-cm (82.31-in.) high rack cabinet. The various units have been distributed with the largest heat dissipation assemblies located at the top. The two synthesizers and SDA modules have been located toward the bottom of the cabinet to optimize their local temperature environment to guarantee performance. The two Control Units and associated Manual Control Panels are located at eye height, for operator convenience (see Fig. 10).

The front door of the cabinet will be normally closed to prevent cooling air loss. A bezel and cutout in the front door provide operator access to the two manual control panels, without opening the door, and provide the necessary cooling air seal.

Cooling air will be provided by two standard DSN rack cabinet side ducts. These will be modified by removing 7.6 cm (3 in.) from the bottom of the inside face and angling an air scoop, at approximately 45 deg, from the rack bottom, into each side duct. It is anticipated that this modification will reduce air flow resistance into the side ducts. All other air flow into the cabinet will be blocked by the connector interface plate mounted in the cabinet bottom.

Dc power requirements have been measured or approximated based on breadboard measurements, and the power supply efficiency has been measured vs load. From

these, the total SDA power dissipation was estimated. Thermal analysis indicates that with cabinet heat dissipation of approximately 1230 W and 15°C station plenum inlet air temperature, the temperature at the cabinet top outlet will be approximately 25°C.

VIII. Status of Design and Engineering Model Development

A. Design Status

Seven out of the ten module types have been documented to the point of having printed circuit (PC) board masters and machine drawings. Photographic techniques are planned to make all subassembly and assembly drawings to reduce documentation costs. The three remaining modules are scheduled for completion of design by June 1973.

B. Engineering Model

All module types have been prototyped and present plans call for an engineering model (containing PC boards made from released documentation) in August 1973. This engineering model will be used to confirm the design and serve as an example at the bidders' conference to better describe the procurement package.

It is planned to be on contract by October 1973 and deliver two SDAs to DSS 14 in August 1974, and the remaining two SDAs to DSS 43 in November 1974.

References

1. Tausworthe, R. C., and Crow, R. B., *Practical Design of Third Order Phase-Locked Loop*. Document No. 900-450, Jet Propulsion Laboratory, Pasadena, Calif. (JPL internal document).
2. Brockman, M. H., "An Efficient and Versatile Telemetry Subcarrier Demodulator Technique for Deep Space Telecommunications," Paper A-7, 2, presented at the 4th Hawaii International Conference on System Science, University of Hawaii, Honolulu, Hawaii, Jan. 12, 1971.
3. Brown, D. H., "Third-Order Phase-Locked Loop Perspectives," in *The Deep Space Network Progress Report*, TR 32-1526, Vol. VIII, pp. 99–110. Jet Propulsion Laboratory, Pasadena, Calif., April 15, 1972.
4. Brockmann, M. H., "MMTS: Performance of Subcarrier Demodulator," in *The Deep Space Network*, Space Programs Summary 37-52, Vol. II, p. 134, Eq. (34). Jet Propulsion Laboratory, Pasadena, Calif., July 31, 1968.
5. Tausworthe, R. C., "Analysis of Narrow-Band Signals Through the Band-Pass Soft Limiter," in Supporting Research and Advanced Development, Space Programs Summary 37-53, Vol. III, pp. 209–214. Jet Propulsion Laboratory, Pasadena, Calif., Oct. 31, 1968.
6. Brockmann, M. H., "MMTS: Performance of Subcarrier Demodulator," in *The Deep Space Network*, Space Programs Summary 37-52, Vol. II, p. 134, Eq. (35). Jet Propulsion Laboratory, Pasadena, Calif., July 31, 1968.
7. Crow, R. B., Holmes, J. K., and Tausworthe, R. C., "Block IV Subcarrier Demodulator Assembly Acquisition Problem," in *The Deep Space Network Progress Report*, TR 32-1526, Vol. XIII, p. 42. Jet Propulsion Laboratory, Pasadena, Calif., Feb. 15, 1973.

Table 1. Functional comparison between Block III and Block IV SDA

Function	Block III	Block IV	Comments
Symbol rate	5.6 to 270 k symbols per second (sps)	5.6 to 500 ksps	Required for Mariner Jupiter/Saturn 1977 (MJS'77)
Subcarrier frequency	100 Hz to 1 MHz	100 Hz to 1 MHz	
Tracking loop type	2nd order	3rd order	Improves SDA performance in the presence of high loop stress due to doppler rate (i.e., Jupiter flyby)
Modulation index range	10 to 74 deg (2-dB resolution)	10 to 80 deg (1-dB resolution)	User requested mod index range increase
τ_0	5.6 to 5.6 ksps	5.6 to 120 sps	This output limited to 56 sps by the Telemetry and Command Processor Assembly (TCP)
SDA input bandwidth (−1 dB)	3 MHz	7 MHz	To be compatible with Block IV receiver
Interplex operation	Manual phasing, no monitor, no notch filter	Phasing, monitoring, notch filter controlled by firmware	To reduce operator involvement and improve performance
Controls	Manual	Manual/computer	To reduce operator involvement and improve performance
Monitor	Manual/computer	Manual/computer	
Alignment	Manual	Firmware	To reduce operator involvement and improve performance
Size	Full standard equipment rack	Half of standard equipment rack	Cost reduction
Auxiliary (acquisition)	Part of design	Not included	Not used on Block III
BER data feedthrough	Part of design	Not included	
1 MHz output	Part of design	Not included	
Reference frequency			
Input	5, 10 MHz	5, 10 MHz	
Output from synthesizer	5 MHz	5 and 10 MHz	
Internal frequency standard in synthesizer	Yes	(5-MHz stations reference to be used)	Cost reduction
Incidental SDA degradation	0.1 ±0.1 dB	0.1 ±0.1 dB	
DC offset and stability	0 ±5 mV (per day)	0 ±5 mV	Reduce calibration requirement

Table 2. Design differences between Block III and Block IV SDA

Function	Block III	Block IV	Comments
Loop bandwidth	0.03, 0.15, 0.375, 1.5 Hz	0.03, 0.234, 0.5, 3.9 Hz	
Acquisition scheme	0.15 to 0.03 Hz, automatic when loop locks, no acquisition for 0.375- or 1.5-Hz loop	0.234 to 0.03 Hz, or 3.9 to 0.5 Hz logarithm bandwidth reduction when loop lock; can operate in acquisition bandwidth as an operational configuration (Ref. 7)	
Soft limiter suppression factor ν	1/2	1/4	This increases the radio-frequency (RF) loop gain (therefore minimizes the dc loop gain) to optimize the total dc stability
Bandwidth of soft limiter	500 Hz	1.0 kHz	500-Hz bandwidth at 10 MHz has proven too costly in Block III SDA
Signal to subcarrier leakage ratio	16 dB at 110 kHz 9 dB at 1.1 MHz	27 dB at 110 kHz 19 dB at 1.1 MHz	Reduce unwanted (additive) subcarrier signal
Internal SDA signal-to-noise ratio			
Data channel	+17 dB	+21 dB	Better internal noise characteristics permit easier calibration and trouble diagnostics
Error channel	+40 dB	+58 dB	
IF system linearity			
Design point $\frac{ST_{sy}}{N_o}$	−1 dB (5.6 < R_{sy} < 270 ksps)	−1 dB (5.6 < R_{sy} < 480 sps) −4 dB (480 < R_{sy} < 500 ksps)	
Receiver 1/2 AGC voltage	Not required	Required by firmware control	
In-lock detector sensitivity $\left(\frac{ST_{sy}}{N_o}\right)$	−1 dB	−1 dB	

Table 3. Subcarrier tracking loop parameters

Loop bandwidth	$\mathcal{W}_{L_o}^{1,2}$, Hz	$G_o^{1,3}$, $\mathcal{W}$ 1/s	K_{DO}^{5}, V/90 deg	K_{VCO}, Hz/V	T_1, s	T_2, s
Narrow	0.03	56.8	0.034	1	5250	148.5
Narrow acquisition[5]	0.234	568	0.034	1	5250	148.5
Wide	0.5	263,020	0.143	10	5250	8.91
Wide acquisition	3.90	2,630,200	0.143	10	5250	8.91

[1]Design point chosen for uncoded limiter suppression factor, $\alpha_o' = 0.48$

[2]IF limiter-detector characteristics for $S/N_o = +8$ dB, +19 dB

[3]K_M (quadrature generator) = 0.25

[4]$\nu = \frac{1}{4}$; $K_{D_{strong\,signal}} = 4$ V/90 deg

[5]Acquisition mode can be used as a tracking bandwidth, or can be commanded to logarithmically reduce the bandwidth to its nominal value (i.e., narrow or wide). The acquisition amplifier has a nominal gain of 20, which is increased to 200 in the acquisition mode.

PAGE MISSING FROM AVAILABLE VERSION

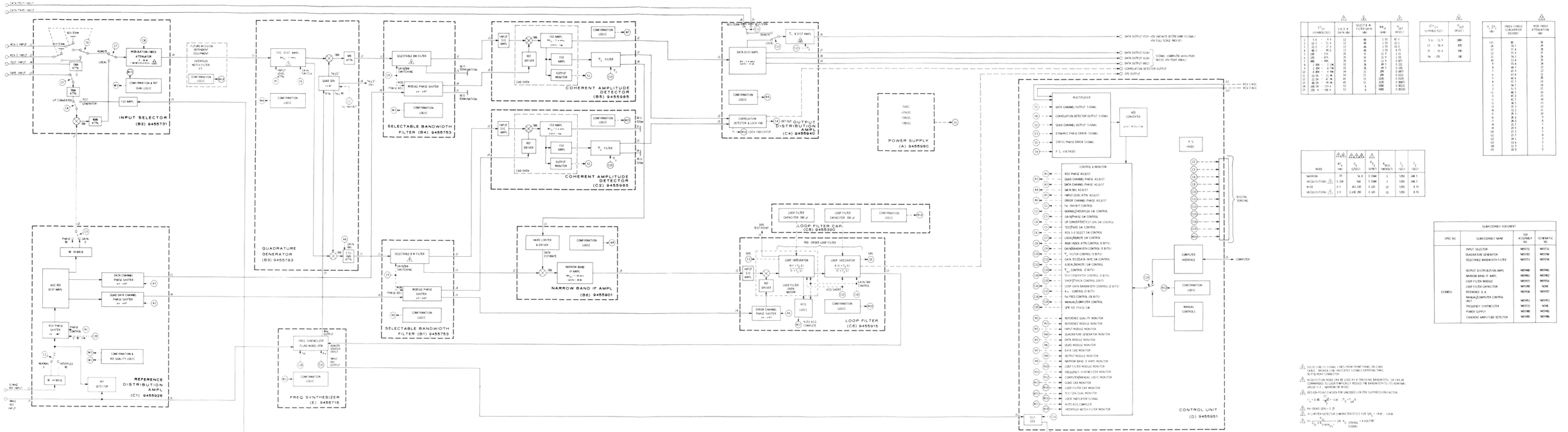

SUBASSEMBLY DOCUMENT				
SPEC NO.	SUBASSEMBLY NAME	TOP ASSEMBLY NO.	SCHEMATIC NO.
9455851	INPUT SELECTOR	9455731	9455732
	QUADRATURE GENERATOR	9455783	9455784
	SELECTABLE BANDWIDTH FILTER	9455753	9455754
	OUTPUT DISTRIBUTION AMPL	9455940	9455941
	NARROW BAND IF AMPL	9455901	9455902
	LOOP FILTER MODULE	9455915	9455916
	LOOP FILTER CAPACITOR	9455390	NONE
	REFERENCE D. A.	9455926	9455927
	MANUAL/COMPUTER CONTROL UNIT	9455951	9455952
	FREQUENCY SYNTHESIZER	9455715	NONE
	POWER SUPPLY	9455980	9455981
	COHERENT AMPLITUDE DETECTOR	9455985	9455986

Fig. 1. Block diagram of Block IV SDA

PAGE MISSING FROM AVAILABLE VERSION

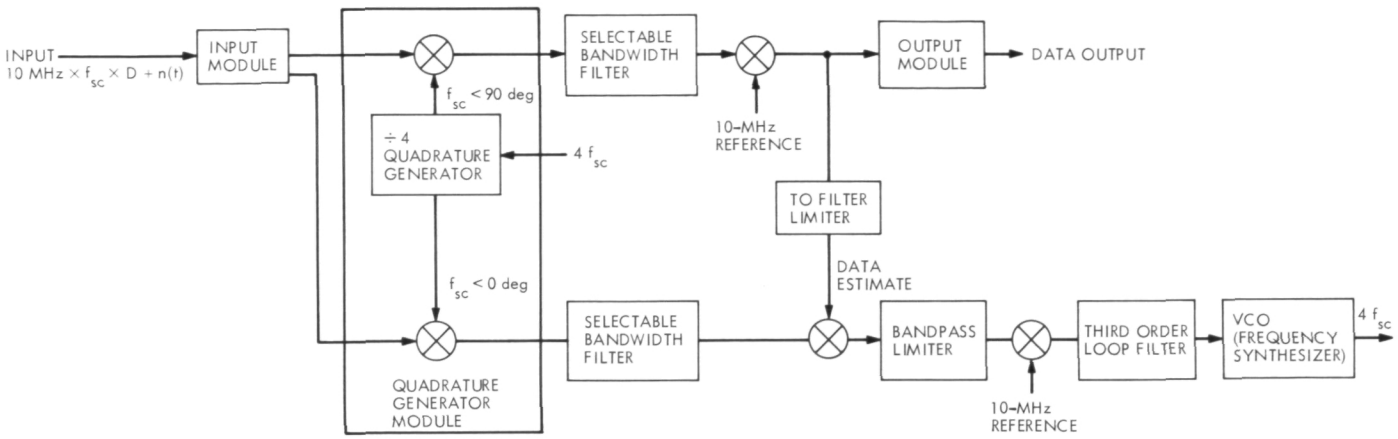

Fig. 2. Subcarrier tracking loop

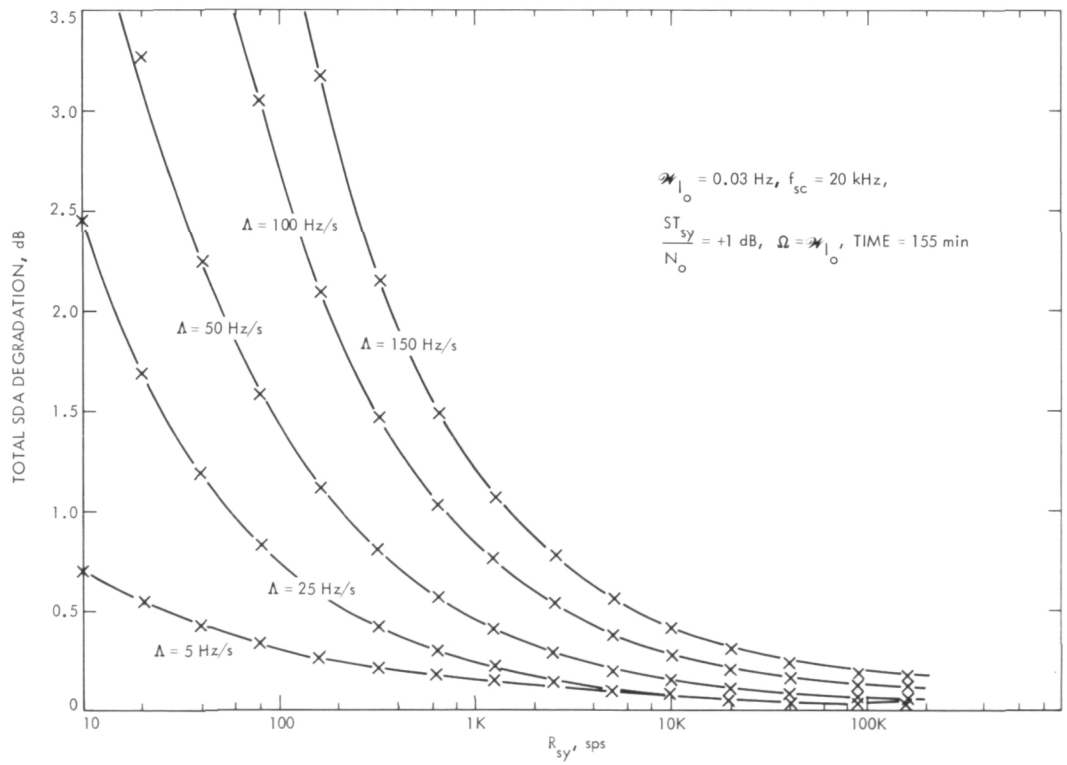

Fig. 3. Total SDA degradation vs R_{sy}; $\mathcal{W}_{l_o}$ = 0.03 Hz, f_{sc} = 20 kHz

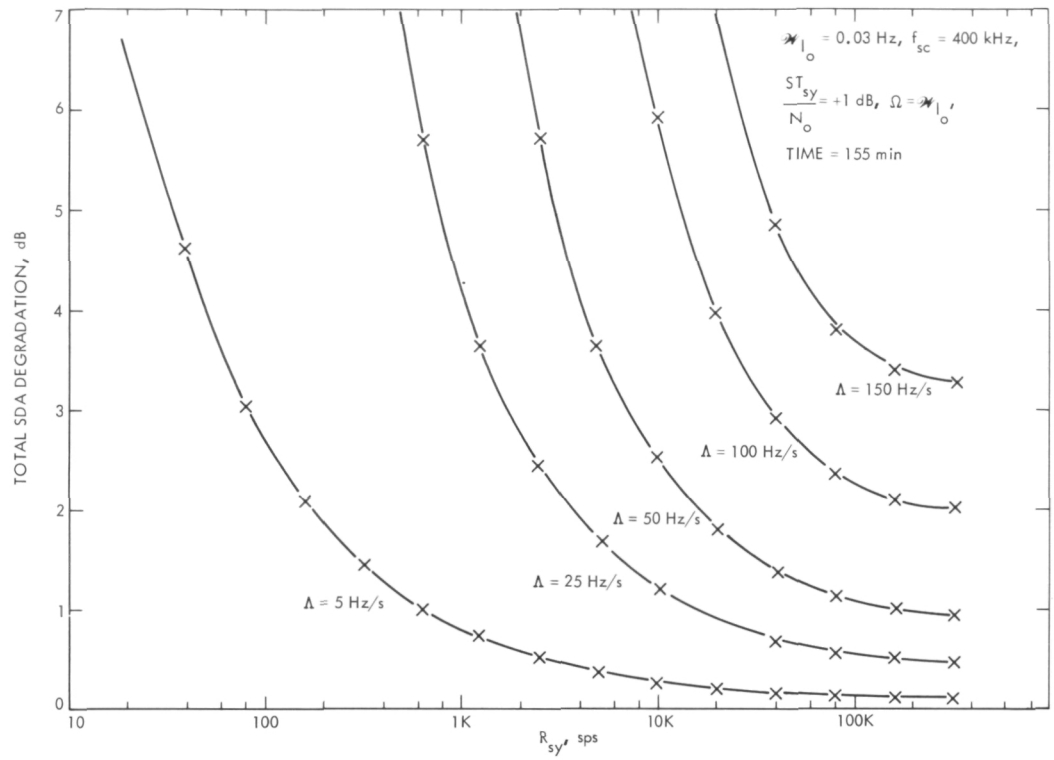

Fig. 4. Total SDA degradation vs R_{sy}; $\mathcal{W}_{l_o} = 0.03$ Hz, $f_{sc} = 400$ kHz

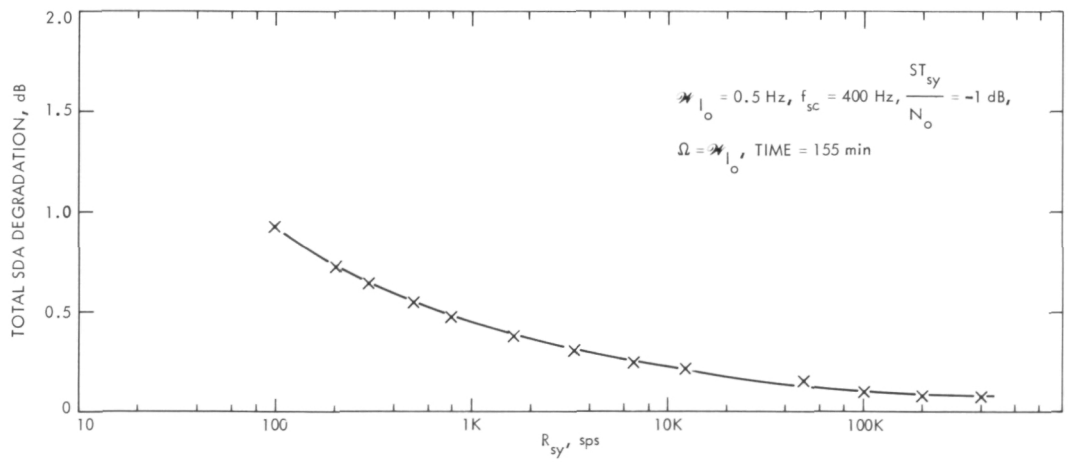

Fig. 5. Total SDA degradation vs R_{sy}; $\mathcal{W}_{l_o} = 0.5$ Hz, $f_{sc} = 400$ kHz

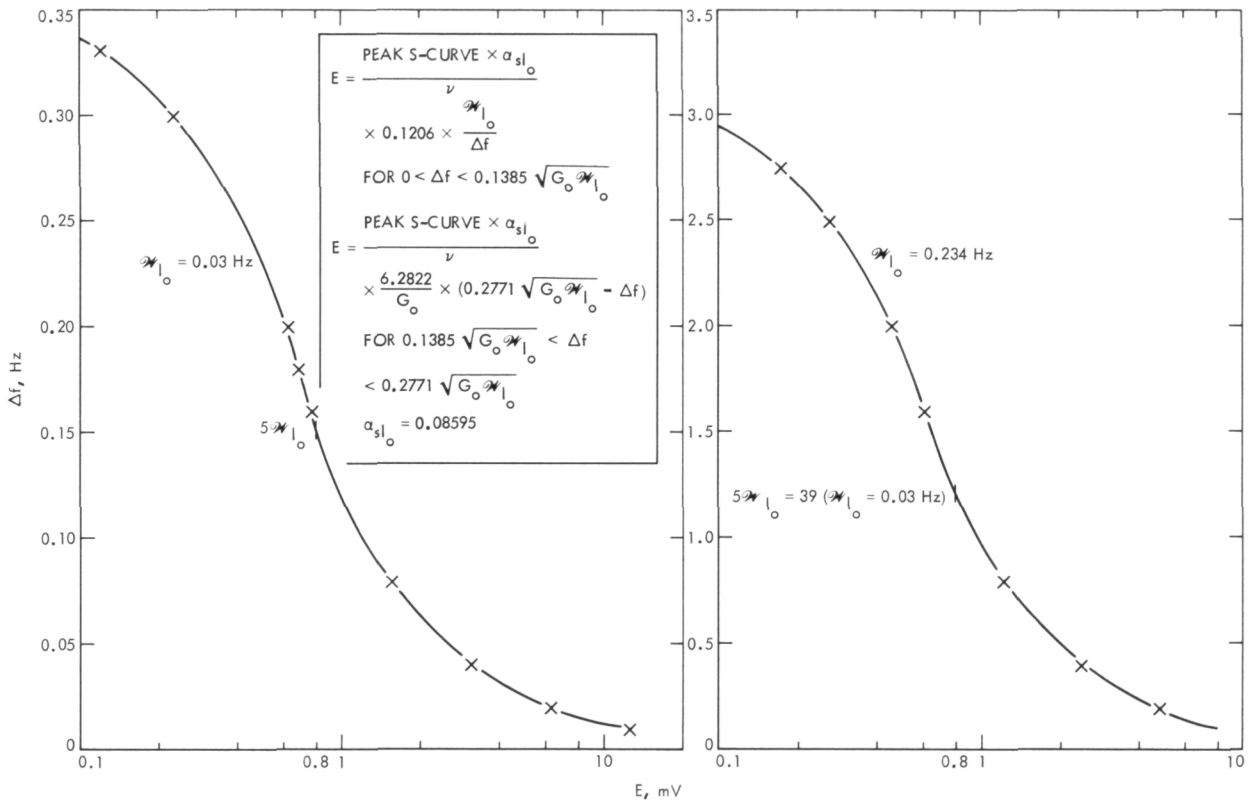

Fig. 6. Acquisition Range vs dc imperfection; $\mathscr{W}_{l_o} = 0.03$ Hz

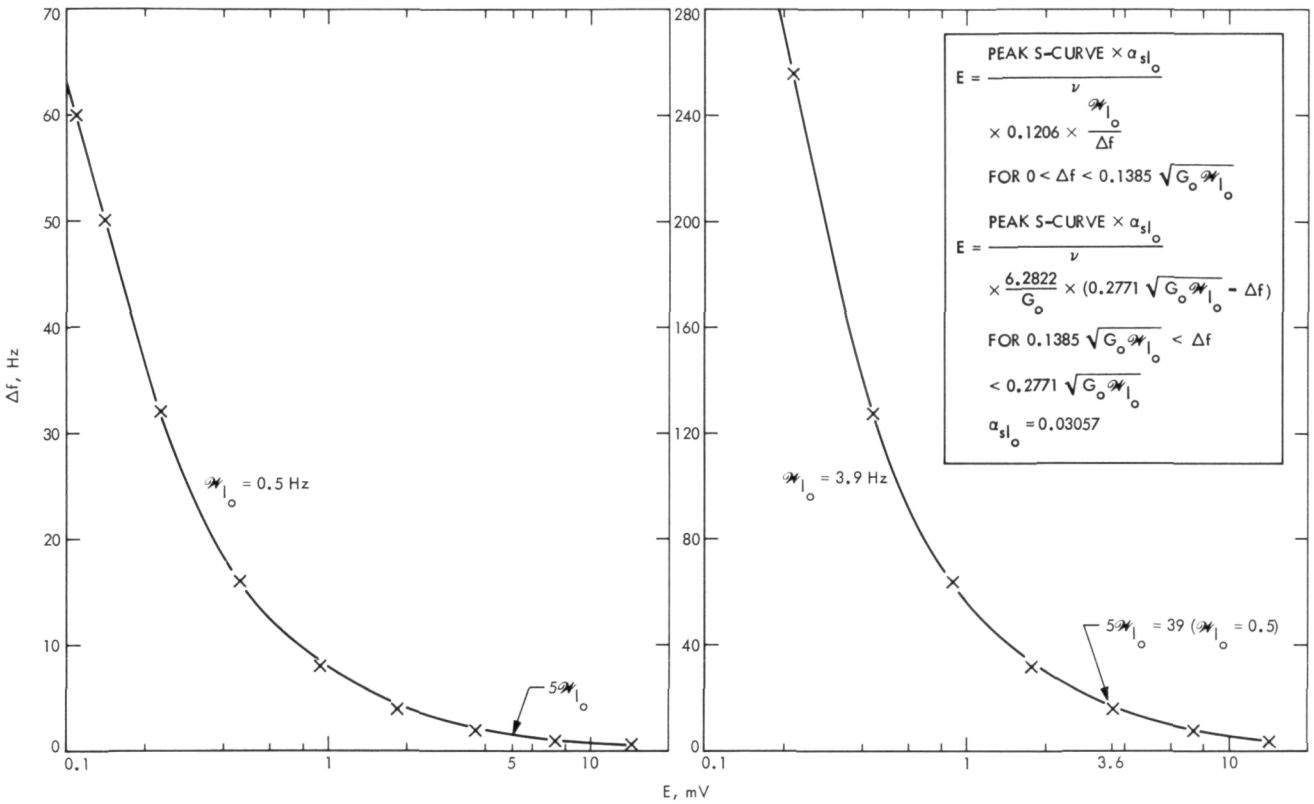

Fig. 7. Acquisition Range vs dc imperfection; $\mathscr{W}_{l_o}$ = 0.5 Hz

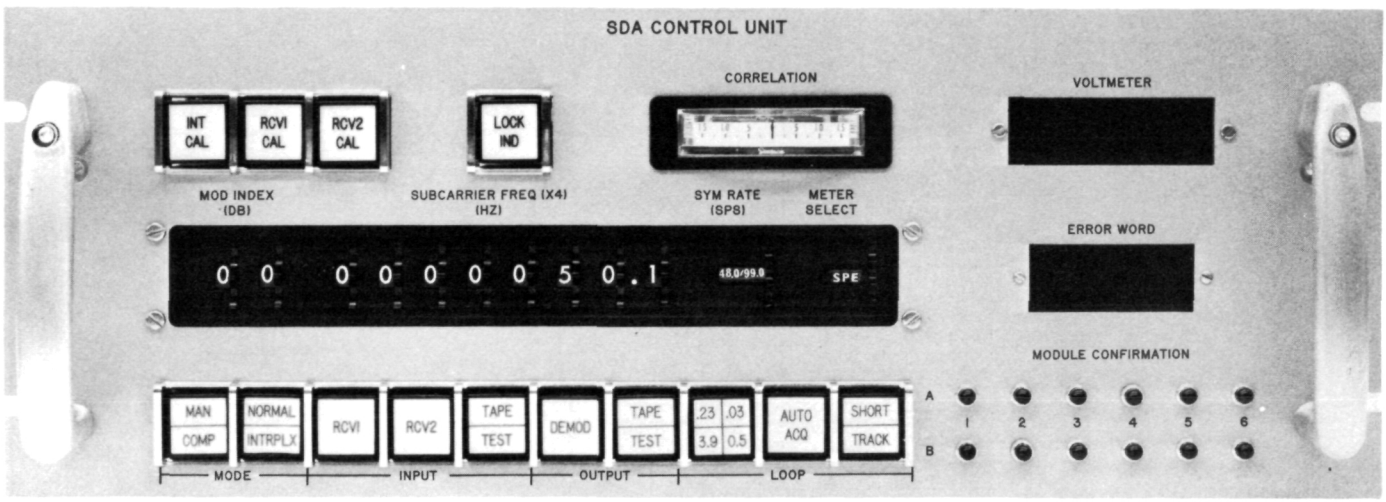

Fig. 8. Block IV SDA control panel

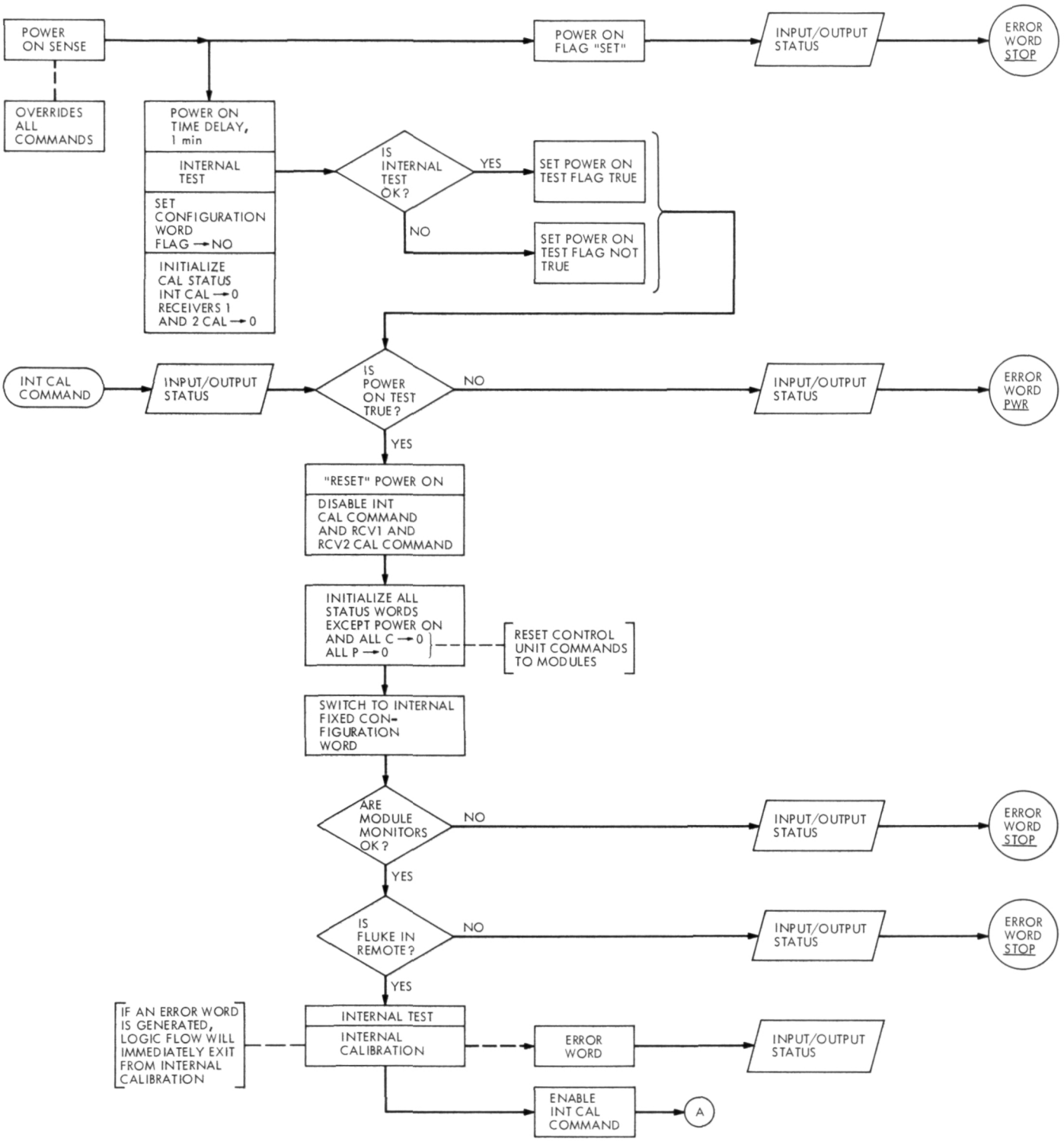

Fig. 9. Block IV SDA control unit logic flow diagram

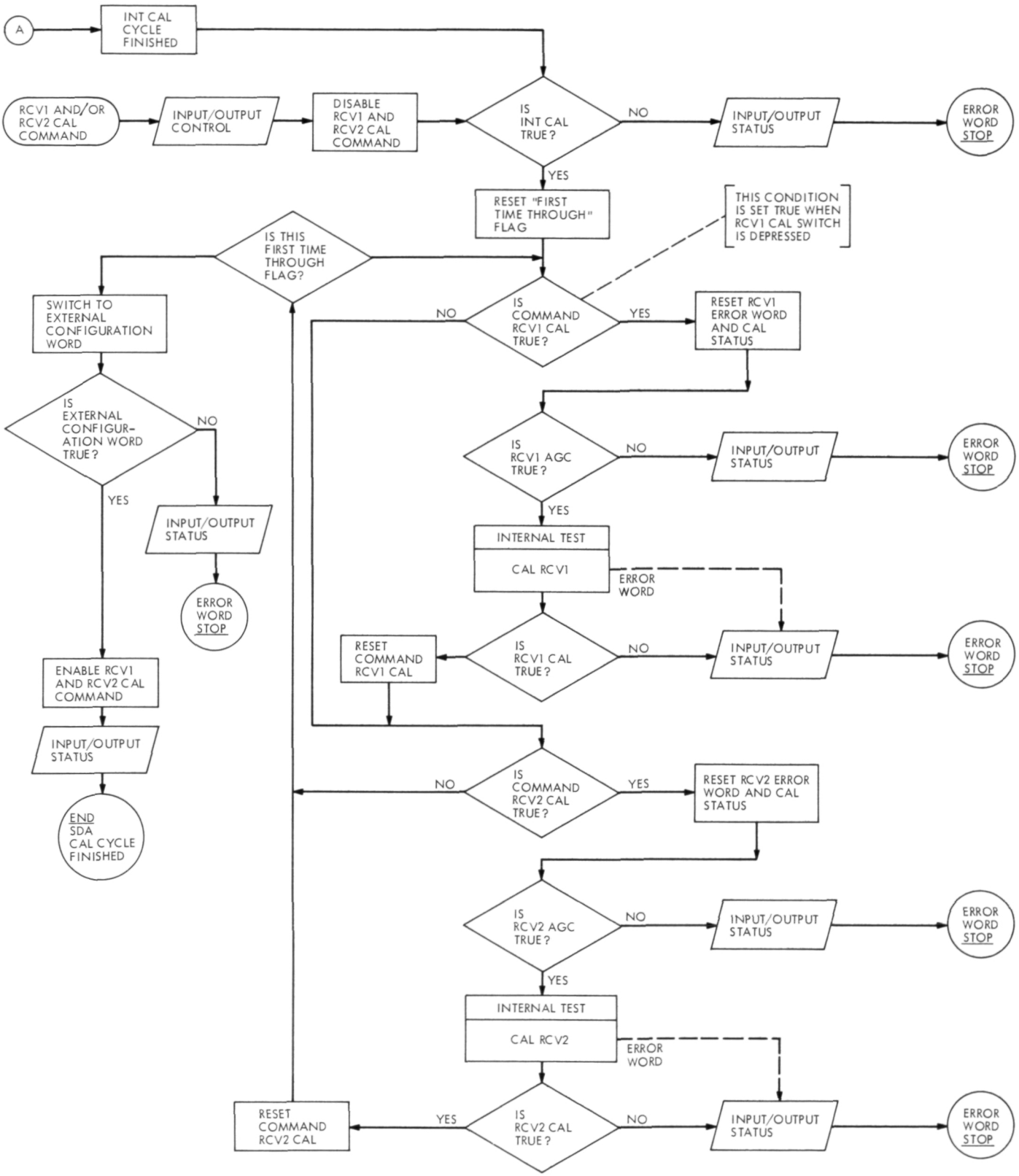
A
INT CAL CYCLE FINISHED
RCV1 AND/OR RCV2 CAL COMMAND
INPUT/OUTPUT CONTROL
DISABLE RCV1 AND RCV2 CAL COMMAND
IS INT CAL TRUE?
NO
INPUT/OUTPUT STATUS
ERROR WORD STOP
YES
RESET "FIRST TIME THROUGH" FLAG
THIS CONDITION IS SET TRUE WHEN RCV1 CAL SWITCH IS DEPRESSED
IS THIS FIRST TIME THROUGH FLAG?
SWITCH TO EXTERNAL CONFIGURATION WORD
IS COMMAND RCV1 CAL TRUE?
NO
YES
RESET RCV1 ERROR WORD AND CAL STATUS
IS EXTERNAL CONFIGUR-ATION WORD TRUE?
NO
YES
INPUT/OUTPUT STATUS
ERROR WORD STOP
IS RCV1 AGC TRUE?
NO
INPUT/OUTPUT STATUS
ERROR WORD STOP
YES
INTERNAL TEST
CAL RCV1
ERROR WORD
ENABLE RCV1 AND RCV2 CAL COMMAND
INPUT/OUTPUT STATUS
END SDA CAL CYCLE FINISHED
RESET COMMAND RCV1 CAL
IS RCV1 CAL TRUE?
NO
INPUT/OUTPUT STATUS
ERROR WORD STOP
IS COMMAND RCV2 CAL TRUE?
NO
YES
RESET RCV2 ERROR WORD AND CAL STATUS
IS RCV2 AGC TRUE?
NO
INPUT/OUTPUT STATUS
ERROR WORD STOP
YES
INTERNAL TEST
CAL RCV2
ERROR WORD
RESET COMMAND RCV2 CAL
YES
IS RCV2 CAL TRUE?
NO
INPUT/OUTPUT STATUS
ERROR WORD STOP

Fig. 9. (contd)

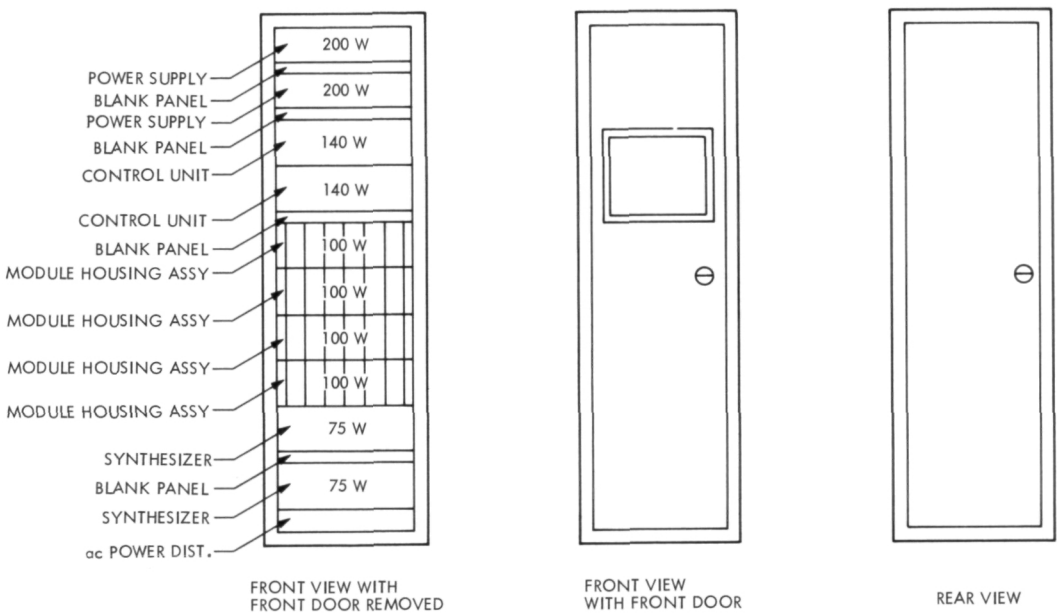

Fig. 10. SDA rack configuration

Block IV Receiver–Exciter Control and Monitoring

C. E. Johns
R. F. Systems Development Section

The Block IV Receiver–Exciter Subsystem has the capability of being configured and controlled either by a computer or manually. This report contains a brief discussion on the computer mode of control and a technical description of the manual controls and system monitor.

I. Introduction

Basic to the Block IV Receiver–Exciter (RE) Subsystem is its capability of being controlled by computer in the primary mode of operation, or manually in the secondary mode. Computer control provides complete receiver and exciter configuration, adjusts system operating frequencies, performs doppler tracking, and automatically acquires the receiver. It also performs pre- and post-calibrations on the receiver, and monitors and stores system performance test points, operating frequencies, and analog monitoring voltages in the computer. When being controlled manually, configuration data are stored within the RE Subsystem and are processed for distribution to the station monitors.

II. Computer Control

A block diagram of the overall Block IV Receiver–Exciter control and monitor is shown in Fig. 1. The Receiver–Exciter Subsystem will contain a minicomputer which will be controlled by a station computer when full station automation occurs. The interface between computers occurs in the computer distribution module. This computer distribution module also couples three separate control distribution modules to the receiver–exciter minicomputer for control of the receiver and exciter configuration, control of the receiver and exciter frequencies (programmed oscillators), and control of performance monitoring of the receiver–exciter. Two instruments are used for monitoring: a digital voltmeter to monitor analog signals and a counter to monitor frequencies. Each instrument is time-shared through the appropriate multiplexer. These instruments have been selected to provide output compatible with computer control.

The control lines from the computer distribution module to the station computer and the computer control distribution modules are the Network Control System standard 14-line interface. These control lines are bidirectional to allow system data to be stored within the computer.

III. Manual Control

Putting the receiver–exciter on manual control is accomplished by actuation of individual switches located on the front panel of the control assembly. The receiver manual control panel is shown in Fig. 2; the exciter manual control panel is similar. As shown in Fig. 1, the receiver and the exciter manual controls are essentially in parallel with the control lines to and from the computer.

The manual controls duplicate the computer functions in that they must be capable of addressing the individual control and configuration (C/C) registers, transmit control data to these registers, and then receive and compare the register data with transmitted data for confirmation. Also, the manual control stores the data received from the C/C registers in binary level format to make this information available for monitoring.

Figure 3 is a simplified block diagram of a receiver or exciter manual control. Binary voltage levels from the front panel switches are applied to the input of a data multiplexer. When the load switch is pressed, the sequencing counter generates a *new data ready* pulse causing the address/read counter to address the first C/C register. The C/C register generates and transmits, back to the manual control, a *respond* pulse. The manual control then transmits the first set of configuration data to the C/C register and puts the transmitted data into temporary storage. The C/C register again responds and retransmits the configuration data back to the manual control where they are compared with the stored data in the control. Also the data received back from the C/C register are stored in latches located within the manual control. This process continues until all of the C/C registers have been addressed and configured and then automatically stops.

Each successful comparison between the transmitted and received data causes the comparison counter to advance one count. After the configuration cycle is complete, a front panel light driven by the comparison counter output verifies that the system has been correctly configured.

The manual control also reads and stores the RF subassembly test point (power monitors) voltages, and these are applied to front panel indicators.

Loading the configuration data into the receiver or exciter C/C registers can also be done automatically. The automatic loading uses the station 1-s time tick to start the counters (in the manual control) through their address, read, and sequencing cycle. This feature assures that the configuration has not changed during a tracking period.

IV. Receiver and Exciter Monitors

Receiver and exciter monitors are used for distributing the configuration status to the station monitors. A typical monitor drawer block diagram is shown in Fig. 4. The data, stored within the manual control, are coupled to the input of the monitor drawer through a multiconductor cable. Each datum bit is applied to the input of a relay driver which controls several relay closures for external distribution. The C/C functions are also displayed on front panel lights.

V. Conclusion

A Block IV Receiver–Exciter Subsystem will be installed at DSS 14 to support the Mariner Venus/Mercury 1973 S–X-band experiment. A Block IV RE Subsystem will also be installed in each of the 64-m subnet stations as one of the primary radio subsystems for Viking 1975. Through the Viking 1975 period, computers will not be available and the RE Subsystem will be controlled manually. Present plans are to install computers after Viking 1975 to allow computer control of the RE Subsystems.

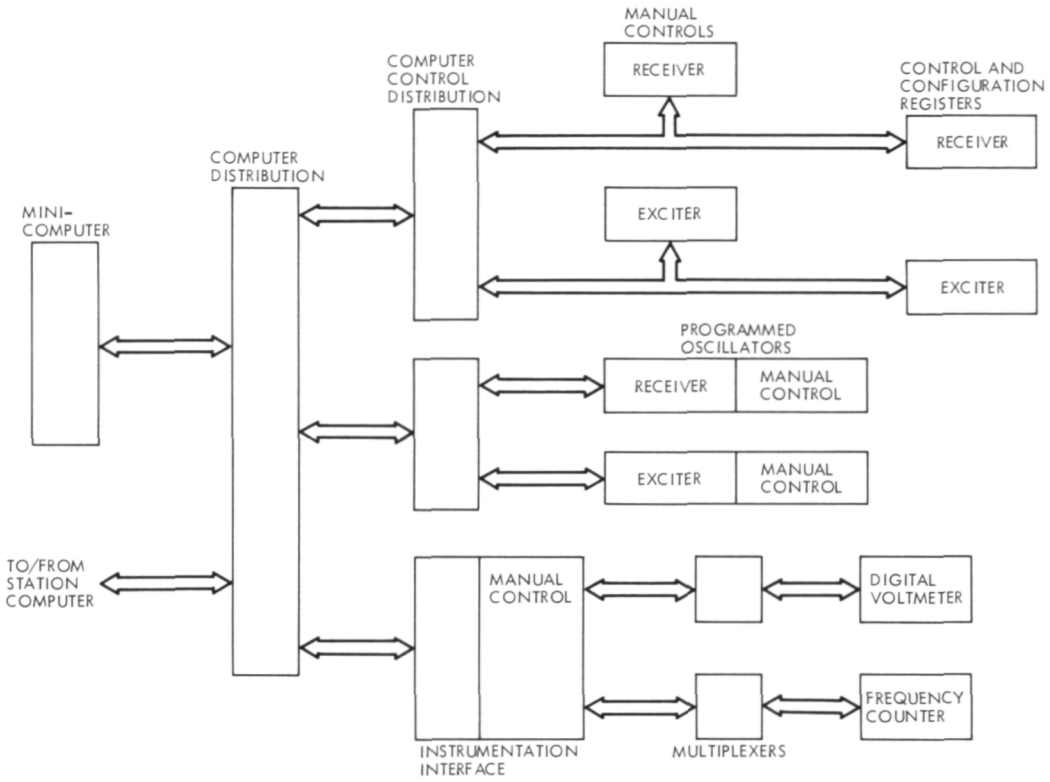

Fig. 1. Block IV Receiver–Exciter control

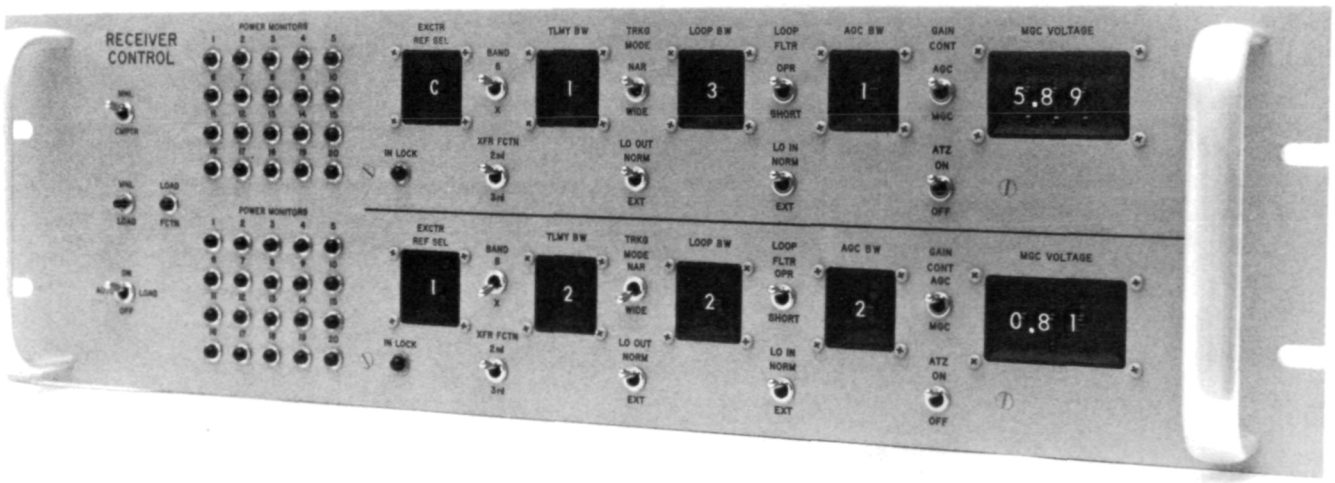

Fig. 2. Block IV receiver manual control panel

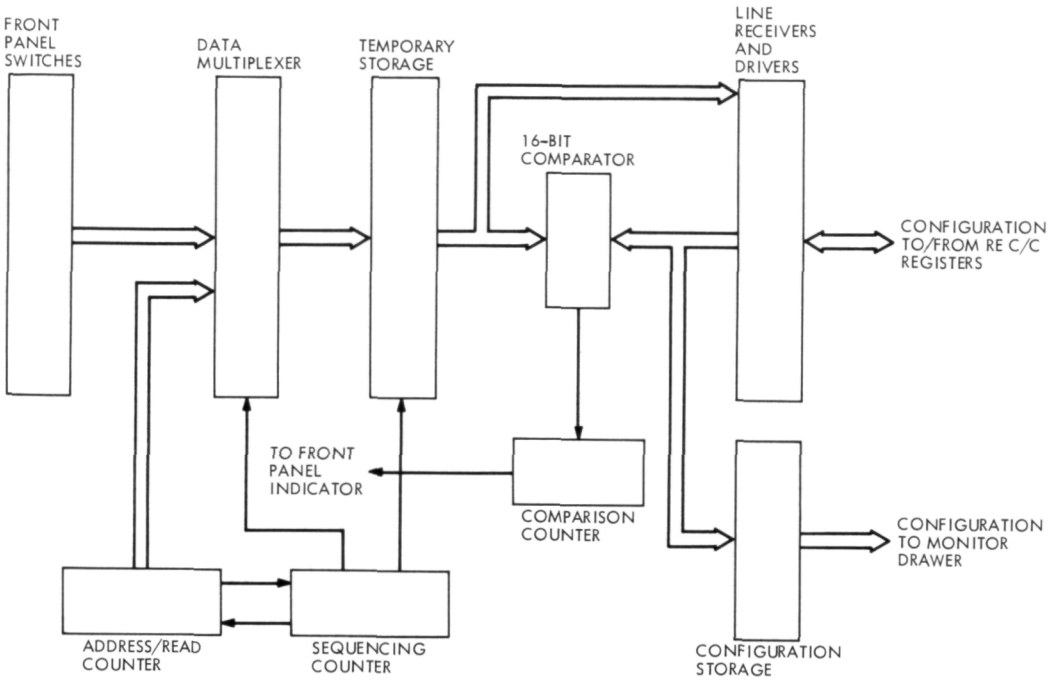

Fig. 3. Block IV Receiver–Exciter manual control block diagram

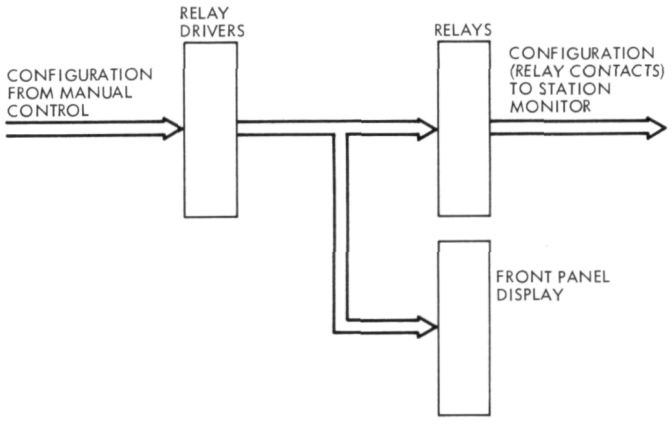

Fig. 4. Block IV configuration monitor drawer

Dual Carrier Investigations at the Mars Deep Space Station

S. S. Kent
R. F. Systems Development Section

Dual carrier transmission from a deep space station can result in receive-band interference signals. Investigations have been conducted at the Mars Deep Space Station to determine the impact of this interference on telemetry and doppler data in terms of the carrier-to-interference power ratio. These investigations were limited to uncoded data at 2048 bits/s and to a fixed (near zero) doppler frequency.

In general, it is seen that for carrier loop margins near 20 dB (typical of Viking orbital operations), the presence of detectable receive-band intermodulation interference will produce detectable data degradation.

I. Introduction

Receive-band interference resulting from high power diplexing with dual carrier uplink has been discussed in two previous reports (Refs. 1, 2). Previous investigations were primarily concerned with locating the sources and determining the signature of the interfering signals along with reduction of the level of the interference. This report will show, to some extent, the possible effect of the interference on telemetry and doppler data.

Two types of dual carrier interference were investigated (Ref. 2): (1) broadband noise bursts that occur in conjunction with intermodulation products (IMPs) and, (2) IMPs with negligible noise bursts. The first type of interference was achieved by irradiating the antenna surface, while the second type was achieved by transmitting into a water load located in the S-Band Polarization Diversity (SPD) feed cone at the antenna port of the diplexer.

II. Instrumentation for Interference

In order to characterize the interference so as to correlate it with the anticipated data degradation, the following instrumentation systems or assemblies were employed:

(1) Open-loop T_{op} instrumentation[1]

[1]This instrumentation actually measured $GkT_{op}B$ as a function of time where

G = total receiver gain to the detector
k = Boltzmann's constant
T_{op} = system operating temperature in kelvins
B = equivalent RF noise bandwidth of the detector

(2) Receiver No. 1 operating in narrow-band loop and narrow-band automatic gain control (AGC) modes

(3) Dual channel strip chart recorder for recording T_{op} and receiver No. 1 AGC voltage.

The T_{op} instrumentation was operated in the 1-MHz bandwidth mode with its output recorded on one channel of the strip chart recorder with receiver AGC voltage on the other. Channel 1 afforded a permanent recording of all noise burst activity of duration greater than 0.1 s (approximately). Typically the strip chart recorder was operated at a speed of 1.27 cm (0.5 in.)/min and was calibrated for 100 K full scale for antenna operation or 500 K for water load operation.

Channel 2 of the recorder was calibrated from −130 to −170 dBmW in terms of receiver 1 AGC voltage. Thus, any IMP sufficient to enable the receiver to acquire lock was characterized in terms of its mean and variance directly as related in time to the noise burst activity. Since the intent of the testing was to determine actual data degradation, the normal station configurations for on-site systems testing were employed. Operational test software was also used to facilitate use of station equipment and personnel. The telemetry system was tested in accordance with portions of TP 853-30/2A-04 while the doppler system was tested in accordance with TP 853-32/2B-08.

III. Test Description

In order to evaluate the effects of IMPs/noise bursts on the data, it was decided that three primary test modes would be satisfactory: (I) IMP frequency (Ref. 2) coinciding exactly with the simulated spacecraft carrier frequency; (II) IMP frequency coinciding exactly with the spacecraft subcarrier frequency; and (III) IMP frequency half-way between the spacecraft carrier and subcarrier frequencies. Other modes could be tested, but it was felt that III would be the typical case and I and II would be worst cases.

Figure 1 is a block diagram of the configuration employed to enable testing for telemetry and doppler data degradation simultaneously. It should be noted that receiver No. 1 received only the IMP/noise burst signal whereas receiver No. 2 received the test signal plus the IMP/noise burst signal. Also, the synthesizer/Iso Amp/$\times 3$ combination is required to enable doppler extraction within the usable bandwidth limits of the doppler extractor assembly.

The data outputs from this configuration are:

(1) Strip chart recorder:

(a) T_{op}

(b) IMP level, AGC in dBmW

(2) Bit error rate (BER)

(3) Doppler phase jitter, in deg rms (σ)

Time was recorded on the various data records so as to enable correlation of the data in terms of IMP/noise burst levels and BER or σ.

All the data discussed herein was obtained while transmitting on channels 6 and 23 and receiving on channel 17. These channels were deliberately chosen to produce an $N = 31$ (Ref. 2) interference signal which, in turn, creates the strongest IMP/NB levels for the channel crystallization available at the site (see Fig. 1 of Ref. 2 for IMP level versus N).

Table 1 is a listing of the various frequencies required in order to achieve operation in Modes I, II, and III. Note that each of the frequencies is tabulated as a VHF frequency—this is done because (1) all voltage-controlled oscillators (VCOs) are counted at this frequency, and, more importantly, (2) this enables achieving the frequency accuracies required to conduct the tests.

Due to the shortage of station time available for these tests (one 8-hour block per week), some of the doppler and telemetry testing had to be conducted simultaneously which somewhat restricted data taking for doppler degradation determination; i.e., when ST_B/N_o is set for telemetry, the margin (signal-to-noise ratio) for doppler becomes a dependent variable for any given modulation index. For these tests, the values of ST_B/N_o used were 3, 6, and 10 dB. These values resulted in doppler margins of 17, 20, and 24 dB, respectively.

Subsequent to the start of these tests, an IMP generator (Ref. 4) was developed as an aid in dual carrier investigations. Tests at the Venus Station (DSS 13) have demonstrated that the IMP generator is equivalent to an internal source (waveguide component) of IMPs in both amplitude and phase signature. It doesn't, however, simulate the noise burst signature encountered on the antenna surface. This generator was used to facilitate doppler data gathering in a more orderly and controllable manner.

As shown in Fig. 1, the IMP generator was connected in series with the water load for the doppler testing.

Thus, whenever operating into the water load, it was possible to control the level of the simulated IMPs from −120 dBm to well below receiver threshold (« − 174 dBmW).

IV. Telemetry Test Results

For all telemetry data, the bit rate was 2048 bps uncoded and the modulation index gave 8 dB carrier suppression. Figures 2 through 4 show the results of IMP/noise burst interference for each of the modes of operation tested.

Figure 2 is the result of transmitting the dual carrier signals into the water load. The interfering signal in this case consisted of IMPs with negligible noise bursts. Figure 3 is the result of irradiating the antenna surface with the dual carrier signals. The interfering signal in this case consisted of IMPs in conjunction with considerable noise bursts. Comparison of Figs. 2 and 3 shows that the presence of noise burst activity degrades the data significantly. The two probable reasons for the increased degradation are (1) increased variance of the IMP, and (2) increase in T_{op} during noise burst activity (Ref. 2).

Figure 4 shows the Mode II (IMP on subcarrier) operation degradation resulting from transmitting dual carriers into the water load. Comparison of Figs. 2 and 4 indicates that Mode I is more sensitive to IMP/noise burst interference. At this writing no attempt has been made to model the degradations measured to date.

Some attempts were made to gather data in the Mode III configuration, but time limitations generally precluded gathering of any really significant data. Scattered data points indicate, however, that Mode III is the least sensitive to IMPs/noise bursts, as would be expected.

V. Doppler Test Results[2]

A. General

Figures 5 through 9 show doppler degradation resulting from each of the modes tested. Data for Figs. 6, 7, and 8 were gathered through the use of the IMP generator. Figure 9 represents data resulting from irradiating the antenna surface with either dual 40-kW or single 400-kW carrier signals.

B. Model

An attempt was made to model the degradation for noise burst-free Mode I operations by assuming that the IMP spectrum is noise-like and constant over the receiver loop bandwidth, $2\beta_L$. The loop margin can be written as

$$m = \frac{P_c}{N_o 2\beta_{L_o}} \tag{1}$$

where

P_c = carrier power level

N_o = noise spectral density (one sided)

β_{L_o} = design point loop bandwidth (one sided)

The signal-to-noise ratio in the actual two-sided loop bandwidth, $2\beta_L$, is

$$\text{SNR} = \frac{P_c}{N_o 2\beta_L} \tag{2}$$

From Eq. (1) this can be rewritten as

$$\text{SNR} = m\frac{\beta_{L_o}}{\beta_L} \tag{3}$$

Defining the signal-to-IMP ratio as

$$\text{SIR} = \frac{P_c}{P_I} \tag{4}$$

and applying the factor β_{L_o}/β_L, an effective IMP margin, m_I, can be derived as

$$m_I = \frac{P_c}{P_I} \cdot \frac{\beta_L}{\beta_{L_o}} \tag{5}$$

Thus, the carrier to IMP ratio can be related in terms of loop margin. The total variance σ^2 of loop phase noise should then be the sum of the two individual variances, or

$$\sigma_T{}^2 = \sigma_m{}^2 + \sigma_{m_I}{}^2 \tag{6}$$

Equation (6) is plotted in Fig. 7 for P_c/P_I ratios of +5, +10, +20 and $+\infty$ dB.

The data points plotted on Fig. 7 represent those in which no cycle slippages occurred. Except for two points,

[2]All of the doppler phase jitter data is compared against Fig. 9 of the theoretical doppler model established by J. R. Lesh in Ref. 3.

the data are in good agreement with the simple model assumed.

It should be noted that Fig. 6 includes data points that had cycle slippage occur (the circled number indicates the number of cycles slipped). These points do not fit with the model derived as evidenced by a comparison with Fig. 7.

C. Cycle Slippage

Theory predicts large phase variance as the loop margin approaches 0 dB. This is indeed true to the point where cycle slippage actually occurs. The simple model used herein also predicts the same behavior as P_I approaches P_c, which also proved to be the case from actual tests. The test program counts the slipped cycles and gives a printout. Fig. 8 is a plot showing cycle slippage as a function of both loop margin m and P_c/P_I ratio.

D. Antenna Irradiation

Figure 9 is the phase jitter resulting from radiating dual 40-kW or single 400-kW carriers from the antenna. In the case of the dual 40-kW carriers, all data points except one had some cycle slippage occur during the averaging time. The computer program does not include cycle slippage in its calculations of phase variance so that the resultant variances are subject to considerable question as to validity. During this period of time, the noise burst activity could best be described as moderate in terms of frequency of occurrence, with T_{op} peak amplitudes of 29 K compared to a steady-state level of 22 K. The IMP variance for these data was as much as ± 12 dB as opposed to the usual 1 to 2 dB variance of the IMP generator.

The single carrier data indicates that light to moderate noise burst activity has no apparent effect on the doppler quality. The noise burst activity relating to the single carrier data points of Fig. 9 gave T_{op} amplitude peaks varying from 23 to 29 K (over a steady-state level of 22 K) and varying in occurrence from once to five times a minute.

VI. Conclusions

From the results of testing to date, it can be concluded that:

(1) Data degradation is directly related to the amount of IMP/noise burst activity.

(2) Data quality is most sensitive to IMPs interfering with the carrier signal.

(3) In the case of telemetry, some degradation does occur where IMPs interfere with the subcarrier.

(4) IMP activity sufficiently removed from both the carrier and subcarrier does not affect the data quality.

(5) Noise burst activity, by itself, is less detrimental to data quality than is combined IMP/noise burst.

(6) Measurable degradation of bit error rate and doppler jitter occur whenever the carrier to mean IMP ratio is 20 dB or less, but only if it occurs on or near the carrier or subcarrier frequencies.

(7) Even large noise burst activity ($\Delta T_{op} \sim 100$ K) does not completely destroy data under typical operating signal level margins.

References

1. Bathker, D. A., and Brown, D. W., "Dual Carrier Preparations for Viking," in *The Deep Space Network Progress Report,* Technical Report 32-1526, Vol. XIV, pp. 178–199. Jet Propulsion Laboratory, Pasadena, Calif., April 15, 1973.

2. Bathker, D. A., and Brown, D. W., "Dual Carrier Preparations for Viking," in *The Deep Space Network Progress Report,* Technical Report 32-1526, Vol. XI, pp. 146–149. Jet Propulsion Laboratory, Pasadena, Calif., Oct. 15, 1972.

3. Lesh, J. R., "Theoretical Analysis of the Doppler System Test," in *The Deep Space Network,* Technical Report 32-1526, Vol. XV, pp. 190–202. Jet Propulsion Laboratory, Pasadena, Calif., June 15, 1973.

4. Kolbly, R. B., "Intermodulation Products Generator," in *The Deep Space Network Progress Report,* Technical Report 32-1526, Vol. XV, Jet Propulsion Laboratory, Pasadena, Calif., June 15, 1973.

Table 1. Frequency predicts for data degradation tests

Mode	Exciter 1	Exciter 2	Receiver 1	Receiver 2	Test transmitter	Ext. synthesizer
I	22045604.00	21985251.00	23395713	23395713	19133237.60	22023153.70
II	22045604.00	21985251.00	23395713	23398214	19135237.60	22025455.78
III	22045604.00	21985251.00	23395713	23396964	19134237.60	22024304.74

All frequencies are in hertz.
Subcarrier frequency = 240,000 Hz.
Data rate = 2048 bits/s, uncoded.

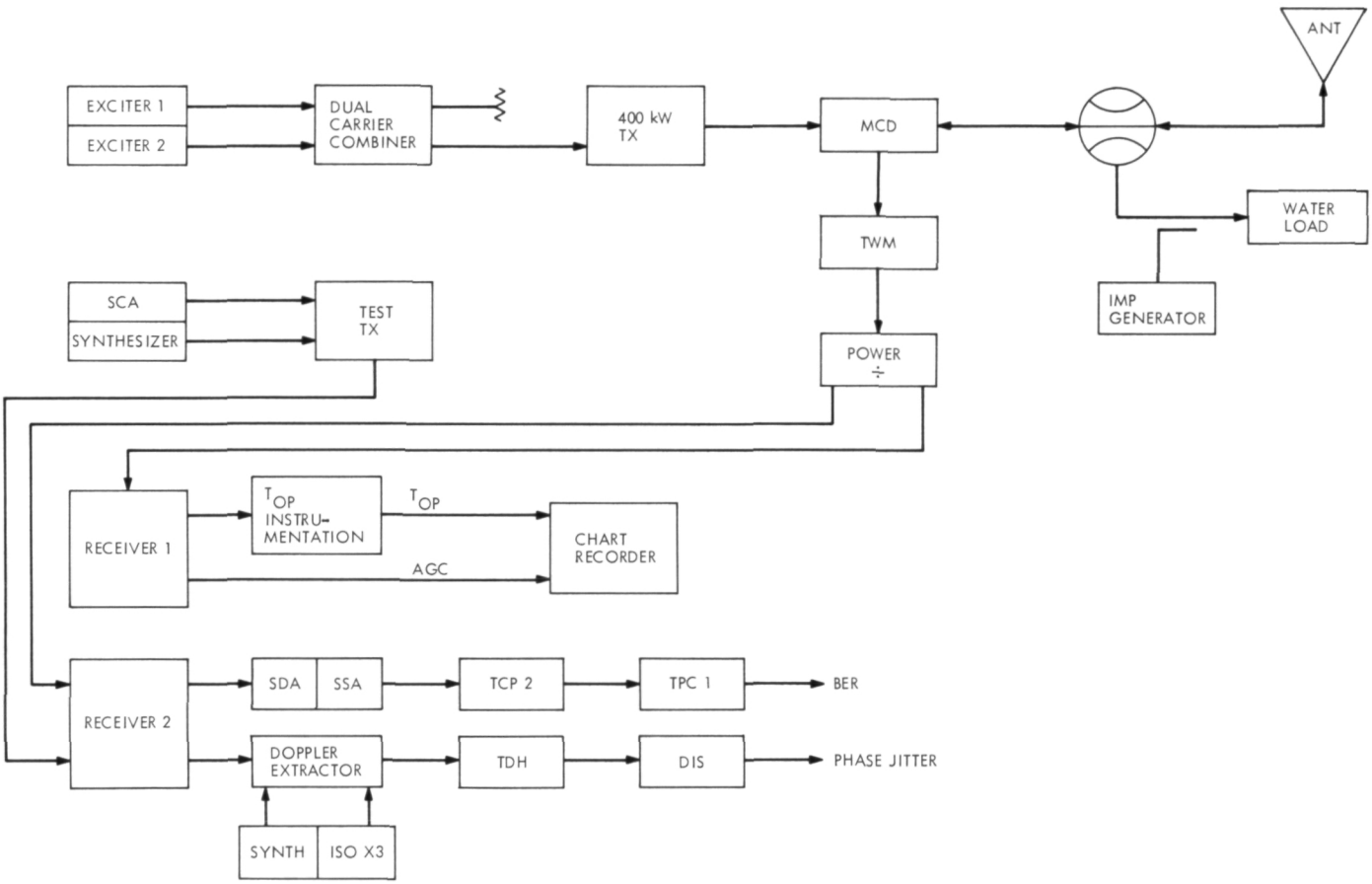

Fig. 1. Block diagram of DSS 14 dual carrier tests

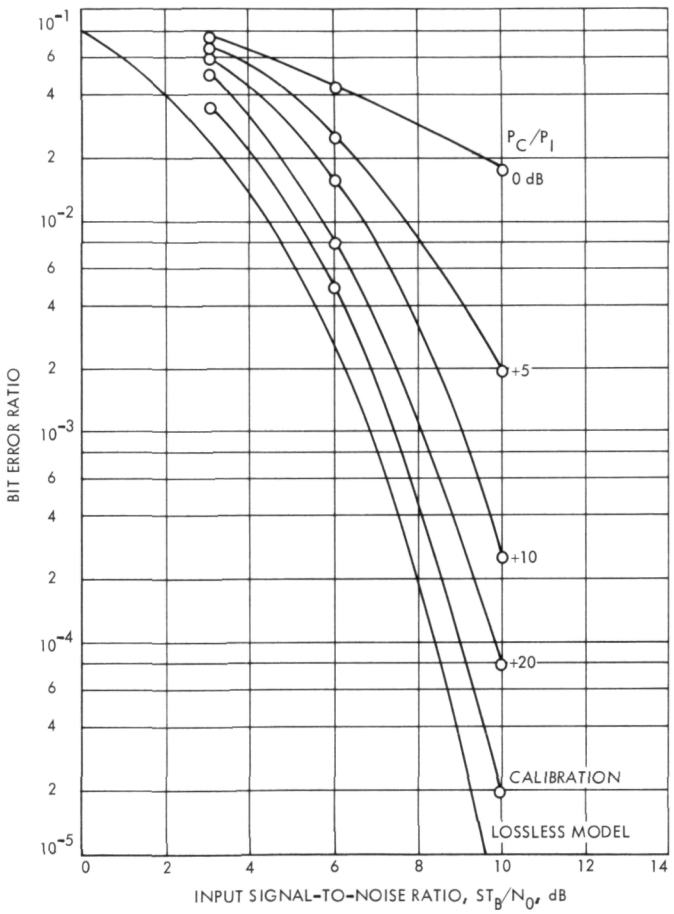

Fig. 2. Telemetry bit error rate as a function of carrier to mean IMP power ratio, Mode I operation. Cone water load configuration

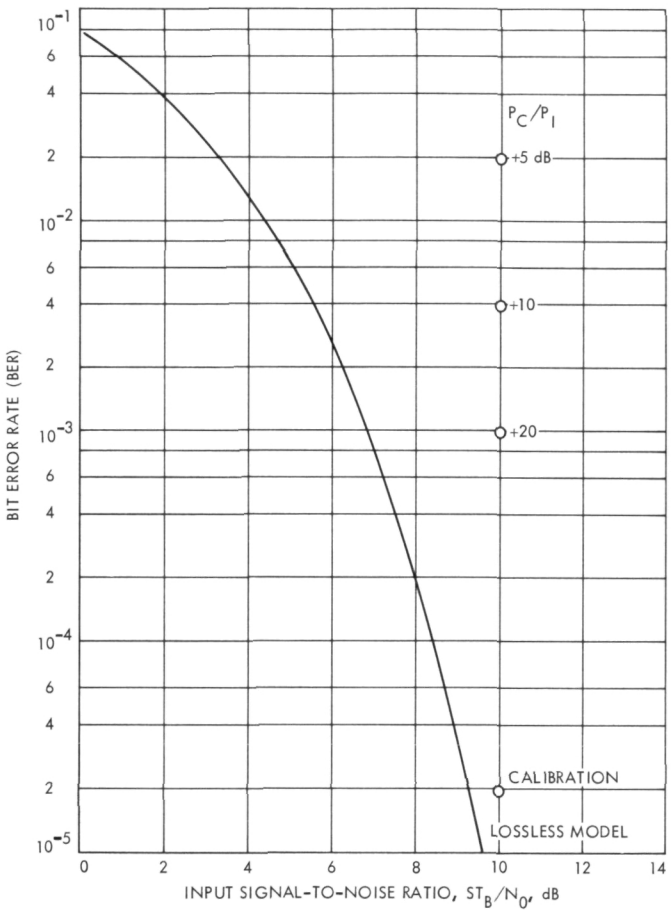

Fig. 3. Telemetry bit error rate as a function of carrier to mean IMP power ratio, Mode I operation. Antenna configuration

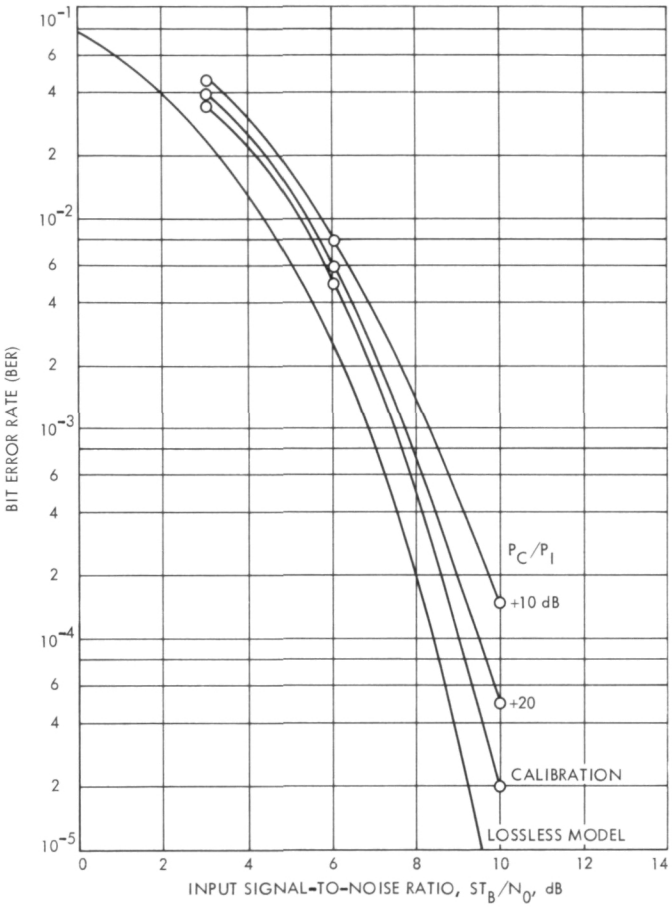

Fig. 4. Telemetry bit error rate as a function of carrier to mean IMP power ratio, Mode II operation. SPD cone water load configuration

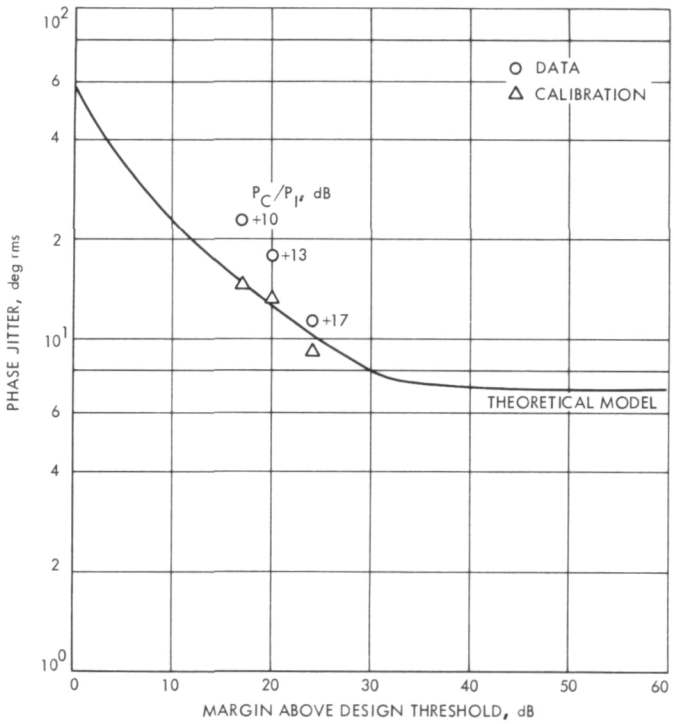

Fig. 5. Doppler phase jitter as a function of carrier to mean IMP power ratio. SPD cone water load configuration

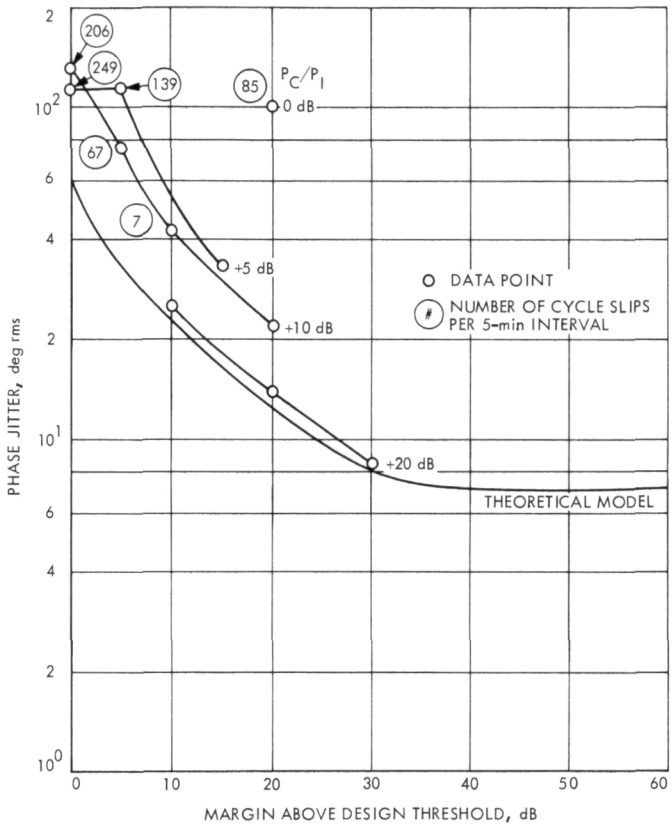

Fig. 6. Doppler phase jitter as a function of carrier to mean IMP power ratio, Mode I operation. SPD cone water load/IMP generator configuration

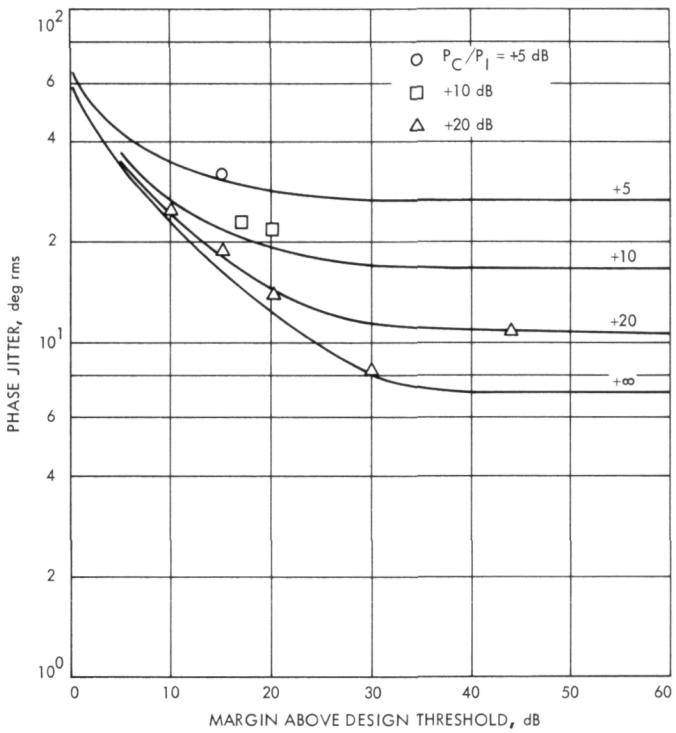

Fig. 7. Mathematical model vs actual doppler phase jitter as a function of carrier to mean IMP power ratio, Mode I operation. SPD cone water load/IMP generator configuration

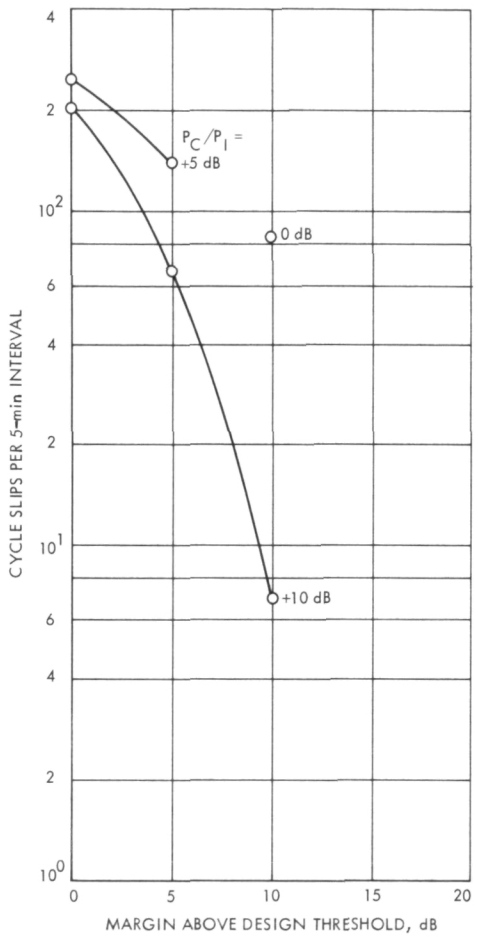

Fig. 8. Doppler cycle slips as a function of carrier to mean IMP power ratio, Mode I operation. SPD cone water load/IMP generator configuration

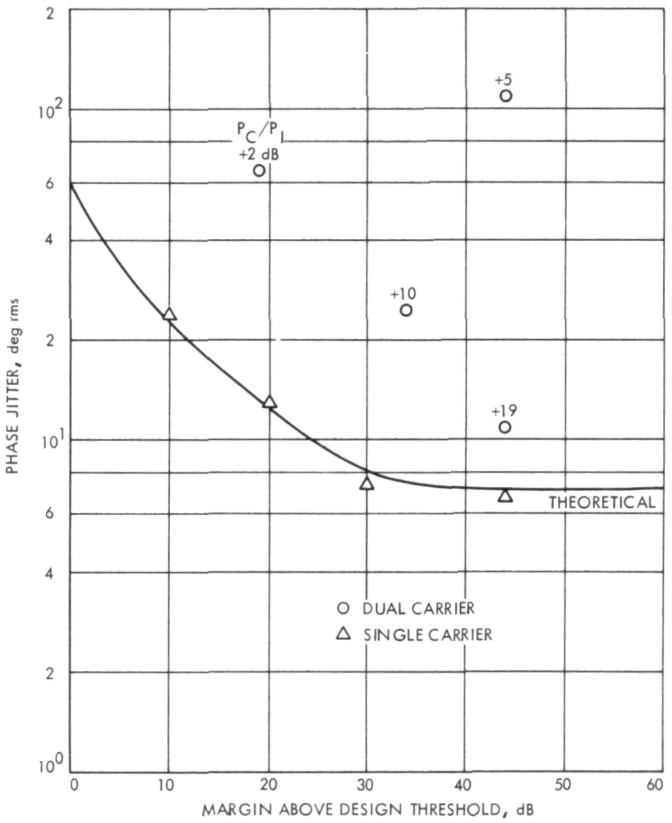

Fig. 9. Doppler phase jitter as a function of carrier to mean IMP power ratio, Mode I operation. Antenna configuration

Pioneer F & G Telemetry and Command Processor Core Dump Program

R. Chafin and M. Pancino
Network Operations Office

The Pioneer F & G Telemetry and Command Processor Assembly Core Dump Program, DOI-5365-SP-A, provides the tracking stations with the capability of obtaining a core dump of a faulted Telemetry and Command Processor operational program with a minimum loss of track time. The program dumps core onto the Spacecraft Telemetry and Command data tape. When the dump is completed, the operational program can be reloaded. The dump can be transferred from the data tape at a later time, and can be used to diagnose the program faulting condition.

I. Introduction

One of the most frustrating classes of software problems is that which occurs in a real-time operations program during tracking operations and is not easily repeatable. If a software problem is easily repeatable, the troubleshooting can be accomplished off-line by simulating the fault-forcing condition. However, if the problem is not easily repeatable and the time is not available for immediate troubleshooting, a method of recording the faulted conditions and restoring the tracking operations in a minimum of time is needed.

One of the standard troubleshooting techniques is to make core dumps of the computer in the faulted condition. A core dump is a record of the contents of each location of memory. From the core dump the person troubleshooting the program can deduce the state of the program in the faulted condition. He can examine the various flags used by the program as directors and the contents of various buffers that reveal the condition of the data being processed. With this tool, the source of the program problem can very often be determined.

During station tracking operations, the normal core dump capability is not available, because the primary station data processing TCP computer does not usually include a line printer onto which a core dump can be readily output. In addition, the tracking operational constraints preclude obtaining a core dump in the normal manner, even if a line printer were available, as the resumption of data acquisition from the spacecraft is the highest priority.

II. Program Description

The method described in this article was designed to provide a core dump within the capabilities and constraints of the existing tracking station network with a minimum impact on the spacecraft tracking operations. This can be accomplished by recording the core dump on magnetic tape in a format compatible with the data record format used by the operational program. A core dump of a software failure occurring during system operations can be placed on the same magnetic tape as the spacecraft telemetry and command data. Following the tracking operations, the core dump data can be separated from the telemetry and command data, and printed out on a line printer. The core dump can then be transmitted by high-speed data (HSD) to JPL for troubleshooting by the cognizant engineer.

As soon as the operational program fails, the operator records the computer display register values and then loads the Pioneer F & G Core Dump Program into the faulted TCP computer, using standard fill procedure. The Core Dump Program is loaded into a small portion of computer core. This results in the loss of any previous data in those locations. The program then halts while the operator reenters the recorded register values into the appropriate registers. The operator restarts the program. Various flags and routines are initialized (Fig. 1) and the program then samples the selected peripheral units associated with the TCP and records the state of the peripheral units in relation to the TCP. The peripheral units sampled are the station clock, Command Modulator Assembly (CMA), Symbol Synchronizer Assembly (SSA), Block Decoder Assembly (BDA), and Data Decoder Assembly (DDA). These data are then formatted into the standard block format along with selected other parameters. The core dump program then obtains the contents of the first 24 TCP core locations, i.e., 00000000 to 00000030 octal, and places them again into a block format. Subsequent core locations are placed in block formats until a total of five blocks (one mag tape record) are completed. The mag tape record is then written onto the original data record (ODR) tape forming a permanent record for later retrieval. The mag tape recording process uses the Y buffer interlace register. The interlace register is a unit which controls the writing of the mag tape data without supervision from the central processor. The core dump program loads the interlace register with the starting location of each data group and the amount of data (the number of words) to be formatted. The mag tape unit is then started and records the data defined in the interlace register. The completion of the writing of the mag tape record generates an end-of-transmission interrupt which instructs the central processor to continue.

The program returns to the formatting routine and creates another mag tape record (five-block formats, each containing the contents of 24 TCP core locations). Each succeeding five-block record is written on mag tape until all the TCP core locations are completely recorded. Two end-of-file (EOF) marks are written on the mag tape and the program halts (Fig. 2).

On the completion of the core dump, the TCP operator reloads and initializes the Operational Program which searches the original data record (ODR) magnetic tape for two EOF marks and then continues recording the normal spacecraft data from that point on the tape.

After the pass, the core dump data can be retrieved from the ODR tape by utilizing a post-track playback computer program. The playback program is initialized for the core dump data parameters, and the ODR tape is searched for the core dump data. These data are then sent by HSD line either to JPL for investigation or looped back to the station for local investigation.

III. Conclusion

The Core Dump Program could be used to investigate the core contents of any computer program resident in the TCP; however, each mission may require a "Mission-Dependent" Core Dump Program due to the necessity of formatting the core contents of the TCP to be compatible with the recorded data from the specific spacecraft. This necessity arises from the fact that the ODR tape, complete with received data and core dump, requires a uniform format for successful playback.

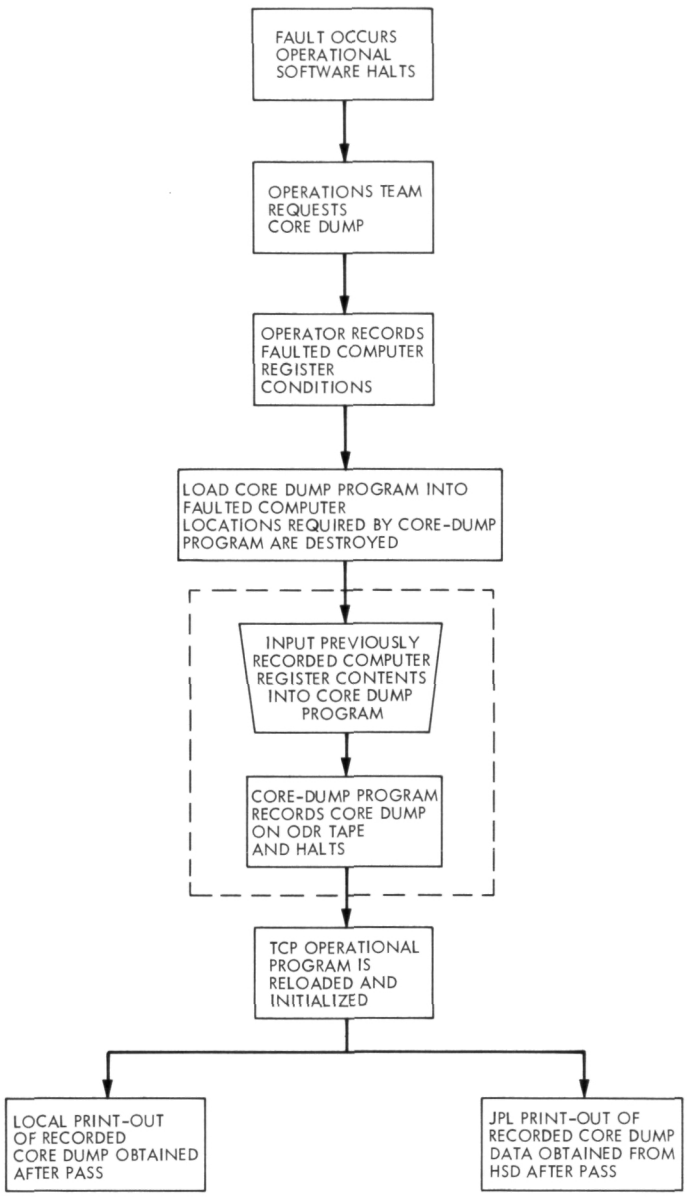

Fig. 1. Operations flow chart

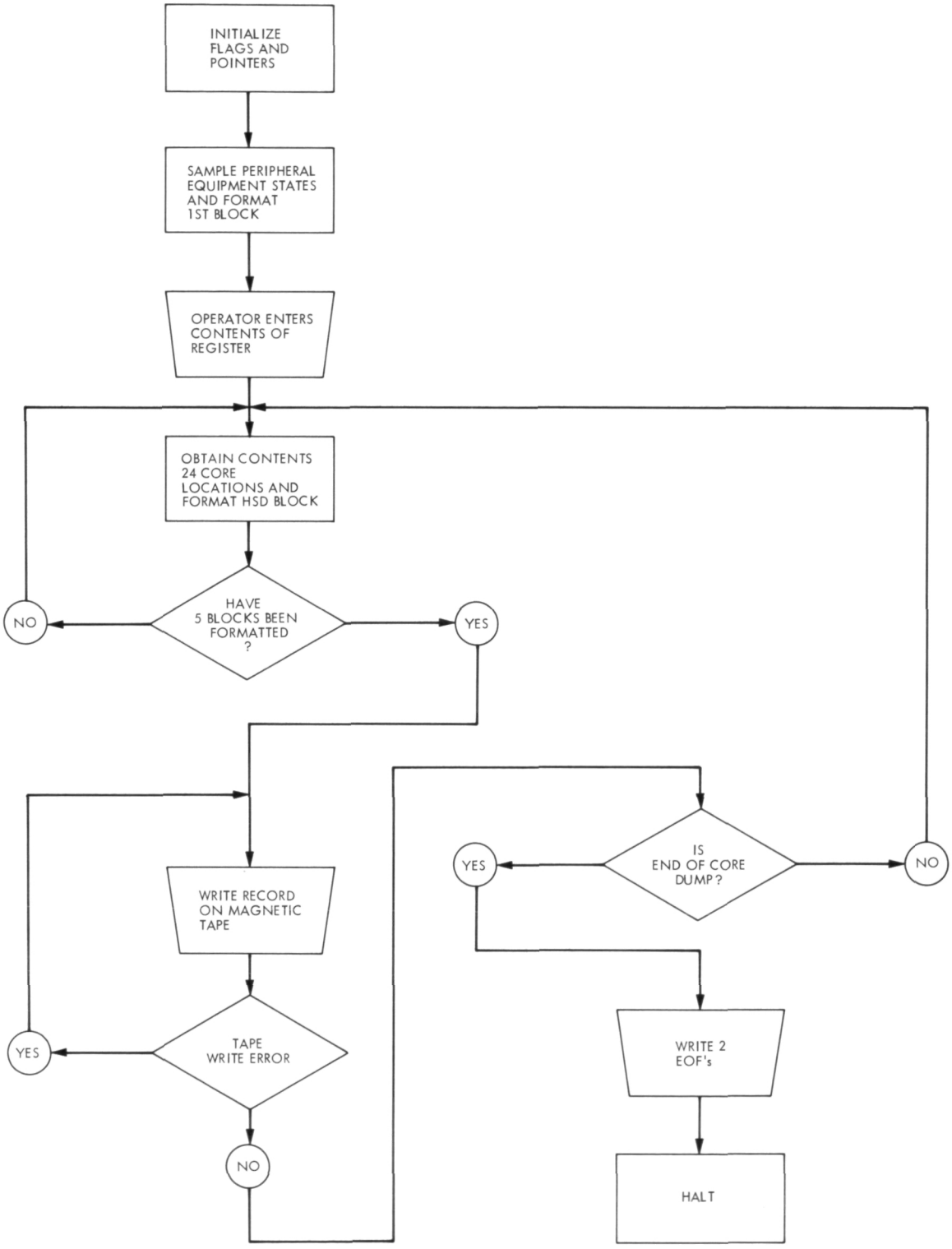

Fig. 2. Core dump functional flow chart (detail)

Error Probability of Binary Signals With Subcarrier Interference

J. R. Lesh
Network Operations Office

Expressions are presented for the symbol detection error probability of a binary data stream in the presence of an asynchronously related interfering squarewave. These expressions are useful in computing effective symbol energy-to-noise ratio degradation resulting from subcarrier interference.

I. Introduction

The emphasis toward higher data rates has resulted in a steady decrease in the ratios of subcarrier frequencies to data symbol rates. Systems which once employed ratios larger than 10 subcarrier cycles per data symbol are yielding to systems with as few as 1.5 subcarrier cycles per symbol. However, as this ratio decreases, the possibility of subcarrier interference becomes much greater.

Subcarrier interference occurs in the Subcarrier Demodulator Assembly (SDA) as a result of subcarrier and intermediate frequency (IF) mixing. For single subcarrier systems the received IF signal, which can be expanded into IF carrier and IF data components, is applied to the first mixer in the SDA. The purpose of this mixer is to demodulate (remove) the subcarrier signal from the received IF data component. However, this mixer also acts as a modulator to the IF carrier component, modulating onto the carrier the estimated subcarrier. If the ratio of the subcarrier frequency to symbol rate is sufficiently small, both components will pass through the data channel bandpass filter and will be present at the second SDA (coherent IF) mixer. Since the two components are in phase quadrature, the modulated carrier component will be blocked at this mixer provided the receiver phase error (which is also the IF phase error) is zero. When the receiver phase error is

nonzero (such as in extreme doppler environments), the second mixer extracts portions of both signals. The result is a baseband symbol stream corrupted by a squarewave subcarrier component, which is subcarrier interference.

In the case of dual-subcarrier modulation, the problem of subcarrier interference is potentially more serious. This is because dual-subcarrier modulation, either conventional or interplex modulation, produces a received signal expansion containing four terms, two of which are in phase while the other two are in the orthogonal direction. For example, with interplex modulation the channel 1 and channel 2 information terms are orthogonal with the intermodulation term in phase with the channel 1 term and the carrier term in phase with the channel 2 term. In this case subcarrier interference can occur (depending on power allocation and frequencies involved) even without a receiver phase error.

In this article expressions are determined for the error probability of a binary data stream corrupted by an additive squarewave. It is assumed that the squarewave is generated asynchronously relative to the data stream so that no fixed phase relationship exists between the two signals. By comparing the results of these expressions with the standard binary detection error probability, it is possible to determine the effective decrease in symbol energy-to-noise ratio resulting from subcarrier interference.

II. Error Probability

Consider a binary data stream $D(t)$ assuming values of $\pm V$ with a data symbol period T_s which is immersed in additive white gaussian noise. The noise $n(t)$ is assumed to be zero mean and have a one-sided spectral density of N_0 W/Hz. Also present is an interfering squarewave having a period T_{sq}. If we let $S(t)$ represent the unit amplitude squarewave, then the composite signal $y(t)$ is given by

$$y(t) = D(t) + \alpha S(t) + n(t) \tag{1}$$

where α is the amplitude of the interfering squarewave.

For maximum likelihood symbol detection, we form the quantity

$$z = \int_0^{T_s} y(t)\, dt \tag{2}$$

and compare the result with a threshold of zero. The corresponding symbol error probability is then given by

$$P_e = Q\left(\frac{\sqrt{2}\,x}{\sqrt{N_0 T_s}}\right) \tag{3}$$

where $Q(u)$ is the error probability integral defined by

$$Q(u) = \frac{1}{\sqrt{2\pi}} \int_u^{\infty} \exp\left[-\frac{\psi^2}{2}\right] d\psi \tag{4}$$

and x is defined by

$$x = \int_0^{T_s} [D(t) + \alpha S(t)]\, dt \tag{5}$$

In order to determine the expression for x, let us define the integer m to be the number of squarewave periods which can be totally contained in one symbol time. Then we have the relation

$$T_s = (m + \gamma)\, T_{sq} \tag{6}$$

where $0 \leq \gamma < 1$. Now, since the integral over complete squarewave periods gives zero contribution, we have (assuming $D(t) = +V$, $0 \leq t \leq T_s$)

$$x = VT_s + \int_0^{T_{sq}} \alpha S(t)\, dt \tag{7}$$

It is clear that the value of the integral term of Eq. (7) will depend on the phase of the squarewave relative to the symbol period. If we fix this phase for the moment by defining t_0 as the time from the beginning of the symbol period to the first leading edge of the squarewave (see Fig. 1), then the expression for x conditioned on t_0 is given by

$$x|_{t_0} = \left.\begin{cases} VT_s + \gamma T_{sq}\alpha - 2\alpha t_0; & 0 \leq t_0 < \gamma T_{sq} \\ VT_s - \gamma T_{sq}\alpha; & \gamma T_{sq} \leq t_0 < \dfrac{T_{sq}}{2} \\ VT_s - \alpha(\gamma + 1)\, T_{sq} + 2\alpha t_0; & \dfrac{T_{sq}}{2} \leq t_0 < \left(\gamma + \dfrac{1}{2}\right) T_{sq} \\ VT_s + \gamma T_{sq}\alpha; & \left(\gamma + \dfrac{1}{2}\right) T_{sq} \leq t_0 < T_{sq} \end{cases}\right\}; \quad 0 \leq \gamma < \frac{1}{2} \tag{8}$$

or

$$x|_{t_0} = \begin{cases} VT_s + \alpha(1-\gamma)T_{sq}; & 0 \leq t_0 < \left(\gamma - \frac{1}{2}\right)T_{sq} \\ VT_s + \gamma T_{sq}\alpha - 2\alpha t_0; & \left(\gamma - \frac{1}{2}\right)T_{sq} \leq t_0 < \frac{T_{sq}}{2} \\ VT_s - \alpha(1-\gamma)T_{sq}; & \frac{T_{sq}}{2} \leq t_0 < \gamma T_{sq} \\ VT_s - \alpha(1+\gamma)T_{sq} + 2\alpha t_0; & \gamma T_{sq} \leq t_0 < T_{sq} \end{cases}; \qquad \frac{1}{2} \leq \gamma < 1 \tag{9}$$

The conditional error probability $P_e|_{t_0}$ given the value of t_0 can be determined by substituting the appropriate relation from Eqs. (8) and (9) into Eq. (3). Then, since the data stream and squarewave were assumed to be asynchronous, the time interval t_0 will be uniformly distributed in the interval $(0, T_{sq})$, so that the average error probability is given by

$$P_e = \frac{1}{T_{sq}} \int_0^{T_{sq}} P_e|_{t_0}\, dt_0 \tag{10}$$

Performing this integration for $0 \leq \gamma < 1/2$ yields

$$P_e = \left(\frac{1}{2} - \gamma\right)\left\{Q\left[\frac{\sqrt{2}(VT_s - \gamma T_{sq}\alpha)}{\sqrt{N_0 T_s}}\right] + Q\left[\frac{\sqrt{2}(VT_s + \gamma T_{sq}\alpha)}{\sqrt{N_0 T_s}}\right]\right\} + \frac{1}{\alpha T_{sq}} \int_{VT_s - \gamma T_{sq}\alpha}^{VT_s + \gamma T_{sq}\alpha} Q\left(\frac{\sqrt{2}\,u}{\sqrt{N_0 T_s}}\right) du; \qquad 0 \leq \gamma < \frac{1}{2} \tag{11}$$

Now, let us define

$$R = \frac{V^2 T_s}{N_0}$$

as the input symbol energy-to-noise ratio without subcarrier interference and

$$\rho = \frac{\alpha}{V}$$

as the ratio of squarewave to data symbol amplitudes. Then form Eq. (6) and the identity

$$\int Q(\sqrt{2}\,ax)\, dx = xQ(\sqrt{2}\,ax) - \frac{e^{-a^2x^2}}{2a\sqrt{\pi}} \tag{12}$$

we have that the symbol error probability is given by

$$P_e = \frac{1}{2}\left\{Q\left[\sqrt{2R}\left(1 - \frac{\rho\gamma}{m+\gamma}\right)\right] + Q\left[\sqrt{2R}\left(1 + \frac{\rho\gamma}{m+\gamma}\right)\right]\right\} + \frac{(m+\gamma)}{\rho}\left\{Q\left[\sqrt{2R}\left(1 + \frac{\rho\gamma}{m+\gamma}\right)\right] - Q\left[\sqrt{2R}\left(1 - \frac{\rho\gamma}{m+\gamma}\right)\right]\right\} + \frac{(m+\gamma)}{\rho\sqrt{\pi R}} \exp\left\{-R\left[1 + \frac{\rho^2\gamma^2}{(m+\gamma)^2}\right]\right\} \times \sinh\left(\frac{2\gamma\rho R}{m+\gamma}\right); \qquad 0 \leq \gamma < \frac{1}{2} \tag{13}$$

By the same procedure we obtain for γ larger than 1/2,

$$P_e = \frac{1}{2}\left\{Q\left[\sqrt{2R}\left(1 + \frac{\rho(1-\gamma)}{m+\gamma}\right)\right] + Q\left[\sqrt{2R}\left(1 - \frac{\rho(1-\gamma)}{m+\gamma}\right)\right]\right\} + \frac{(m+\gamma)}{\rho}\left\{Q\left[\sqrt{2R}\left(1 + \frac{\rho(1-\gamma)}{m+\gamma}\right)\right] - Q\left[\sqrt{2R}\left(1 - \frac{\rho(1-\gamma)}{m+\gamma}\right)\right]\right\} + \frac{m+\gamma}{\rho\sqrt{\pi R}} \exp\left\{-R\left[1 + \frac{\rho^2(1-\gamma)^2}{(m+\gamma)^2}\right]\right\} \times \sinh\left[\frac{2\rho R(1-\gamma)}{m+\gamma}\right]; \qquad \frac{1}{2} \leq \gamma < 1 \tag{14}$$

III. An Example

As an example let us consider a 50-kHz subcarrier biphase modulated by a 33-kbps data stream. The sub-

carrier in turn phase modulates a carrier with a modulation index of 30 deg. Assume also that the received carrier has been shifted due to doppler such that the receiver static phase error is 30 deg. (It is also assumed that the receiver margin is sufficiently high so that the receiver dynamic phase error is negligible.) Also, let the data symbol energy-to-noise ratio at the SDA second mixer output be 5.0 dB. For this example $m = 1$, $\gamma = 0.515$ and $\rho = 1.0$. From Eq. (14) we find that the symbol error probability is 0.0113, which corresponds to an effective symbol energy-to-noise ratio of 4.1 dB. We conclude that the subcarrier interference alone has caused an effective degradation of 0.9 dB.

IV. Remarks

The above expressions were originally obtained for predicting subcarrier degradation resulting from interplex modulation on the Mariner Venus/Mercury 1973 (MVM'73) mission. When typical mission parameters were used in these expressions, it was found that the effective symbol energy-to-noise ratio degradation was less than 0.2 dB. This was true even in mode 1 for the low-rate channel, where the interfering subcarrier at the symbol detection matched filter has an amplitude 1.13 times that of the symbol amplitude (assuming that the notch filter tuned to the IF carrier is not used ahead of the SDA).

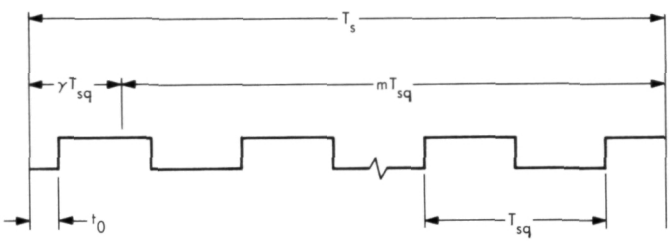

Fig. 1. Time relationship for data symbol and squarewave subcarrier

DSN Supply System Model

D. H. McClure
DSN Facility Operations Office

A model of the DSN Supply System was developed, using the Forrester approach, which describes the existing supply system material and paper flow. The model accurately depicts the system for typical situations involving items of supply normally stocked at a Complex Supply Depot. The model allows the user to study the effects of parameter variations such as procurement lead time, shipping time, reorder points, and user demand rates.

I. Introduction

The model of the DSN Supply System uses the Forrester approach. A flow chart was developed which depicts the existing DSN Supply System material and paper flow. Equations were then written to describe the various levels, rates, and system delays. The model accurately depicts the system for typical situations involving items of supply normally stocked at a Complex Supply Depot (CSD). The model allows the user to study the effects of parameter variations such as procurement lead time, shipping time, reorder points, and user demand rates.

II. Description of the Model

The current model consists of three loops:

(1) *User/Issue/Complex Supply Depot.* The user loop includes the user demand rate, and in/out-of-stock test, the stock issue rate, and the inventory level at the Complex Supply Depot.

(2) *Automatic Resupply.* The auto-resupply loop includes the inventory level at the Complex Supply Depot, the Material Issue Memos (MIMs), and their associated delay during return to the DSIF Supply Depot (DSD), the establishment of the reorder point (ROP), and the delays encountered in ordering and shipping material to the Complex Supply Depot.

(3) *Direct Turn Over (DTO).* The DTO loop includes the generation of the DTO request, the delay encountered in transmitting the DTO request to DSD, the issuance of material from DSD, and the delay encountered in shipping the material to the Complex Supply Depot.

Three runs are included to illustrate the model. The runs are based on a typical item of supply for which a normal user demand rate is four units per week and the maximum complex stock level is 108 units.

Run 1 (Fig. 1) illustrates the steady-state condition for a period of 100 weeks. This provides the baseline for comparison for the changes made in later runs. For this run the maximum complex stock level is calculated as 104 units and the reorder point (ROP) as 62.4 units.

Run 2 (Fig. 2) illustrates the effect of a 20% increase in the user demand rate (UDR) after week 13. Because of the higher usage rate, the stock level reaches zero at week 24. The DTO loop provided additional stock which resulted in an over-stock condition when the auto-resupply quantity arrived. However, by week 60, the system has adjusted and is in steady-state for the new usage rate. The new ROP is 78 and the maximum complex stock level readjusted to 130.

Run 3 (Fig. 3) illustrates the effect of a one-time large withdrawal from the Complex Supply Depot. This would be the case if an Engineering Change Order (ECO) modification kit required parts to be obtained from the supply system rather than being supplied with the modification kit. In the past it has been argued that drawing parts from the supply system for ECO modification kits would give a false indication of usage rate and result in an over-stock condition at the Complex Supply Depot. In Run 3 the user demand is increased from 4 to 25 at week 13, then returned to 4 for the remainder of the run. The DTO loop appears to have over-reacted resulting in an over-stocked condition. The net result is a 48-week supply rather than the desired 26.

Figure 4 is an updated version of the model flow chart. This model does not include the activity which supports the DSD. It assumes the DSD to be an infinite source.

This dynamic model of the DSN supply activity represents only key elements and is, at best, a crude approximation of the existing supply system. Nevertheless, it should provide a start for understanding the behavior of the system, and for identifying other elements to be included in the model.

The model is limited to those items of supply which are normally carried in stock at a Complex Supply Depot (CSD). Items currently out of stock are assumed to be special ordered as a DTO item. The system is further assumed to be operated on the "push" basis; this means that resupply is normally automatic. As items are issued at the CSD, MIMs are generated and copies forwarded to the DSD. This information is then used to change the inventory records file for the CSD. When these records indicate that the pre-established reorder point has been reached, a quantity of items is shipped to the CSD to return their stock level to the established maximum.

Some of the more obvious delays are included in the model. Future models will include a more complete analysis of the activities within DSD. The relationship between DSD and its vendors, and DTOs for normally nonstocked items need further exploration. The latest version of this model is identified as DYN10E.

The system equations are classified in three categories: (1) primary levels and associated rates, (2) derived values, and (3) input constants. The derived values are calculated using equations identified as auxiliary. Table 1 summarizes the three categories.

In the section that follows, the equations are described as they relate to the model diagram in Fig. 4.

III. System Equations

The symbols used to represent quantities in the equations have been chosen to have as much mnemonic significance as possible. Thus, a technician requesting an item from the stockroom represents the generation of an unfilled order. When the item is issued, the order is considered closed. The quantity (or level) of unfilled orders is given in Eq. (20.L):

$$UOL.K = UOL.J + (DT)\,(UDR.J - SIR.J) \qquad (20.L)$$

where

UOL = Unfilled order level at the CSD (units)

UDR = User demand rate (units/week)

SIR = Stock issue rate at the CSD (units/week)

DT = Solution time interval (weeks)

This equation states that the level of unfilled orders now (at time K) is equal to the level at the last time it was measured (at time J), plus the quantity that was received (user demand rate in units per week times the number of weeks between J and K) less the quantity closed out (as represented by the stock issue rate in units per week times the number of weeks between J and K). The number of weeks between J and K is denoted as DT. The user demand rate is given in Eq. (10.R):

$$UDR.K = UDP \qquad (10.R)$$

where

UDR = User demand rate (units/week)

UDP = User demand rate parameter (units/week)

This equation simply allows the rate to be controlled by a variable parameter.

Before stock can be issued it must be in stock. If it is not in stock, a DTO must be generated to order the material from DSD. Therefore, a test is made to determine if the issues are in or out of stock and to establish a value for the DTO order rate or stock issue rate. This test is shown in Eqs. (30.A) and (40.A):

$$\text{ISL.K} = \begin{cases} \text{UOL, if UOL} \leq \text{CSL} \\ \text{O, if UOL} > \text{CSL} \end{cases} \qquad (30.A)$$

where

ISL = In-stock level (units)

CSL = CSD stock level (units)

$$\text{OSL.K} = \begin{cases} \text{UOL, if UOL} > \text{CSL} \\ \text{O, if UOL} \leq \text{CSL} \end{cases} \qquad (40.A)$$

where

OSL = Out-of-stock level (units)

UOL = Unfilled order level (units)

CSL = CSD stock level (units)

The outcome of this test determines the path to be followed: DTO or immediate stock issue. If the item is out of stock, the UOL is used to establish the DTO order rate in Eq. (50.R):

$$\text{DOR.K} = \frac{\text{OSL.J}}{\text{DPD}} \qquad (50.R)$$

where

DOR = DTO order rate (units/week)

OSL = Out-of-stock level (units)

DPD = DTO preparation delay (weeks)

The constant DPD represents the delay due to the time it takes to prepare the DTO and transmit to the DSD.

A finite amount of time is required for the DTO to reach the DSD. The time is represented as a delay. The level of DTOs in transit is given by Eq. (60.L):

$$\text{UDT.K} = \text{UDT.J} + (\text{DT})\,(\text{DOR.J} - \text{TRR.J}) \qquad (60.L)$$

where

UDT = Unfilled DTO orders in transit (units)

DOR = DTO order rate (units/week)

TRR = DTOs received at DSD rate (units/week)

Since most DTOs are teletyped (TWX'd) to the DSD, the quantity UDT represents those waiting to be put on the TWX machine and those which have been received at DSD but not yet logged. The rate at which the DTOs are received at DSD is a function of the DTO order rate and the delay encountered. Equation (70.R) is a third-order delay equation which gives this rate:

$$\text{TRR.K} = \text{DELAY 3 (DOR.J, DXD)} \qquad (70.R)$$

where

TRR = DTOs received at DSD rate (units/week)

DOR = DTO order rate (units/week)

DXD = DTO TWX delay (weeks)

DELAY 3 = Third-order delay equation

The DTO log represents a level of unfilled DTOs. This level is affected not only by the incoming orders, but by the DTO issue rate at the CSD. The unfilled DTO level is given in Eq. (80.L):

$$\text{UDO.K} = \text{UDO.J} + (\text{DT})\,(\text{TRR.J} - \text{DCR.J}) \qquad (80.L)$$

where

UDO = Unfilled DTO level at DSD (units)

TRR = DTOs received at DSD rate (units/week)

DCR = DTO close-out rate (units/week)

The close-out rate is given in Eq. (90.R):

$$\text{DCR.K} = \frac{\text{CDL.J}}{\text{DCD}} \qquad (90.R)$$

where

DCR = DTO close-out rate (units/week)

CDL = Completed DTO level (units)

DCD = DTO close-out delay (weeks)

The auxiliary Eq. (100.A) gathers the DTOs that are ready for close-out as a result of their issuance at the CSD. Although there is a time delay in this path, it was not included because its significance is probably minor.

$$\text{CDL.K} = \text{CDL.J} + (\text{DT})\,(\text{CIR.JK} - \text{DCR.JK}) \qquad (100.A)$$

where

CDL = Completed DTO level (units)

CIR = CSF DTO issue rate (units/week)

DCR = DTOs close-out rate (units/week)

Auxiliary Eq. (105.A) sums the DTOs received from the Complex Supply Depot and controls the DTO issue rate:

$$DOL.K = DOL.J + (DT)\,(TRR.J - DIR.J) \qquad (105.A)$$

where

DOL = DTO order level (units)

TRR = DTOs received at DSD rate (units/week)

DIR = DTO issue rate (units/week)

The DTO issue rate is dependent on the level of the DTO order level and the time necessary to issue them. This rate assumes that the DSD inventory level always exceeds the unfilled order level. The fact that this it not necessarily true will be reflected in the next model.

Equation (110.R) represents the rate of DTO issues from DSD:

$$DIR.K = \frac{DOL.J}{DID} \qquad (110.R)$$

where

DIR = DTO issue rate at DSD (units/week)

DOL = DTO order level (units)

DID = DTO issue delay (weeks)

The level of DSD inventory is given in Eq. (120.L) and reflects the deletion of inventory due to DTO and automatic-resupply issues. Additions to inventory are governed by Eq. (130.R).

$$DIL.K = DIL.J + (DT)\,(VDR.J - DIR.J) - ASL.J \qquad (120.L)$$

where

DIL = DSD inventory level (units)

VDR = Vendor delivery rate (units/week)

DIR = DTO issue rate (units/week)

ASL = Automatic-supply level at CSD (units)

$$VDR.K = VDP \qquad (130.R)$$

where

VDR = Vendor delivery rate (units/week)

VDP = Vendor delivery rate parameter

The delivery of DTO issued material is delayed by the transportation time. Equation (140.L) equates the DTOs in transit as a function of the DIR and DRR. However, DRR is a function of the transportation delay and is given in Eq. (150.R).

$$DTC.K = DTC.J + (DT)\,(DIR.J - DRR.J) \qquad (140.L)$$

where

DTC = DTOs in transit to CSD (units)

DIR = DTO issue rate (units/week)

DRR = DTOs received at CSD rate (units/week)

$$DRR.K = DELAY\ 3\ (DIR.J,\ DTD) \qquad (150.R)$$

where

DRR = DTOs received at CSD rate (units/week)

DIR = DTO issue rate (units/week)

DTD = DTO transportation delay (weeks)

DELAY 3 = Third-order delay equation

Auxiliary Eq. (155.A) gives the level of units of supply added to the CSL by the DTO path:

$$DSL.K = DSL.J + (DT)\,(DRR.J - CIR.J) \qquad (155.A)$$

where

DSL = DTO stock level at CSD (units)

DRR = DTOs received at CSD rate (units/week)

CIR = CSD DTO issue rate (units/week)

Once the DTO material is received at the CSD, it can be issued to the user. The CSD DTO issue rate is given in Eq. (180.A). The in-stock issue is a similar function given in Eq. (190.A). These two auxiliary equations are summed to given the total stock issue rate, Eq. (200.R).

$$CIR.K = \frac{DSL.J}{HID} \qquad (180.A)$$

where

CIR = CSD DTO issue rate (units/week)

DSL = DTO stock level at CSD (units)

HID = Handling of issues delay (weeks)

$$IIR.K = \frac{ISL.J}{HID} \qquad (190.A)$$

where

IIR = In-stock issue rate (units/week)

ISL = In-stock level (units)

HID = Handling issues delay (weeks)

$$SIR.K = IIR.J + CIR.J \qquad (200.R)$$

where

SIR = Stock issue rate (units/week)

IIR = In-stock issue rate (units/week)

CIR = CSD DTO issue rate (units/week)

The CSD stock level is a function of the stock issues and the material arriving via the DTO path and the automatic-resupply path. Equation (210.L) gives the CSD stock level:

$$CSL.K = CSL.J + ASL.J + DSL.J - (DT)(SIR.J) \qquad (210.L)$$

where

CSL = CSD stock level (units)

DSL = DTO stock level at CSD (units)

ASL = Auto-resupply level at CSD (units)

SIR = Stock issue rate at CSD (units/week)

Each time an issue is made, a Material Issue Memo is prepared. Once a week these MIMs are forwarded to the DSD. The information on the MIM is keypunched and subsequently entered into the DSD Inventory Status Record files. When the stock level at the CSD reaches the predetermined reorder point, a quantity of material equal to the CSD maximum level is issued automatically.

Equation (220.L), which gives the MIM order level, is dependent upon the stock issue rate and the rate at which they are forwarded to DSD. Equation (230.R) gives the rate at which the MIMs are forwarded.

$$MOL.K = MOL.J + (DT)(SIR.J - MIR.J) \qquad (220.L)$$

where

MOL = MIM order level (units)

SIR = Stock issue rate at CSD (units/week)

MIR = MIM issue rate (units/week)

$$MIR.KL = \frac{MOL.J}{MRD} \qquad (230.R)$$

where

MIR = MIM issue rate (units/week)

MOL = MIM order level (units)

MRD = MIM release delay (weeks)

Since the MIMs are mailed to the DSD, there is a finite delay before they are received. Equations (240.L) and (250.R) inject the effect of this delay:

$$MTL.K = MTL.J + (DT)(MIR.J - MRR.J) \qquad (240.L)$$

where

MTL = MIMs in transit to DSD level (units)

MIR = MIM issue rate (units/week)

MRR = MIM received at DSD rate (units/week)

$$MRR.K = DELAY\ 3\ (MIR.J, MTD) \qquad (250.R)$$

where

MRR = MIM received at DSD rate (units/week)

MIR = MIM issue rate (units/week)

MTD = MIM transportation delay (weeks)

The MIMs received at DSD are considered closed out when they are keypunched. Equations (260.L) and (270.R) show these functions:

$$MRL.K = MRL.J + (DT)(MRR.J - MCR.J) \qquad (260.L)$$

where

MRL = MIMs received level at DSD (units)

MRR = MIMs received at DSD rate (units/week)

MCR = MIM close-out rate (units/week)

$$MCR.KL = \frac{MRL.J}{CKD} \qquad (270.L)$$

where

MCR = MIM close-out rate (units/week)

MRL = MIMs received level at DSD (units)

CKD = Keypunch delay (weeks)

The automatic-resupply issue rate is a function which only occurs when the reorder point has been reached.

The reorder point (ROP) is established at a level where the stock level is replenished before the stock level reaches zero. Figure 5 illustrates the ROP and its relationship to the maximum CSD stock level and the various delays in the system. From the figure, it can be seen that ROP is given by Eq. (290.A):

$$ROP = \frac{MCL.K\,(AOLD + AILD + TES)}{26 + TES} \qquad (290.A)$$

where

ROP = Reorder point (units)

MCL = Maximum CSD stock level (units)

AOLD = Automatic-resupply order level delay (weeks)

AILD = Automatic-resupply in-transit level delay (weeks)

TES = Time required for safety stock to be used (weeks)

The maximum CSD stock level is set at a sufficient quantity to last 6 months:

$$MCL.K = 26\,(AUDR.J) \qquad (295.A)$$

where

MCL = Maximum CSD stock level (units)

AUDR = Average user demand rate (units/week)

The average user demand rate is determined on the user demand rate for the previous 5 weeks. This allows smoothing to reduce the long-range effects of sudden changes in the user demands.

$$AUDR.K = UDR\,(K-1) + UDR\,(K-2) + UDR\,(K-3) + UDR\,(K-4) + UDR\,(K-5) \qquad (305.A)$$

where

AUDR.K = Average user demand rate (units/week)

UDR = User demand rate (units/week)

Since the automatic-resupply system depends on comparing the ROP with the CSD stock level, some means of monitoring that level must be established. Auxiliary Eq. (300.A) gives the pseudo-CSD stock level based on the MIMs received and the outgoing shipments:

$$PCSL.K = PCSL.J + ASL.J + (DT)\,(DIR.J - MRR.J) \qquad (300.A)$$

where

PCSL = Pseudo-CSL (units)

ASL = Auto-resupply level at CSD (units)

DIR = DTO issue rate (units/week)

MRR = MIMs received rate (units/week)

Once the ROP has been reached (as compared to the pseudo-CSL), an automatic order level is set equal to the current value of the MCL. A procurement lead time of AOLD holds the quantity until it is released as AIR. At this time the automatic in-transit level is set at the same quantity and held for the number of weeks corresponding to the shipping time. At the end of this time, ASL is set equal to AIL and the values of CSL and PCSL are increased accordingly.

Table 1. DSN supply system model DYN10E

Primary Levels and Rates:
Complex supply level
Stock issue rate
DTO received at CSD rate
Auto-resupply issue rate
DTO order level
DTO order rate
DTO issue rate
Auto-resupply order level
Pseudo-complex supply level
Reorder point
Auto-resupply issue rate
Derived Values:
Reorder point
Maximum complex supply level
Average user demand rate
Input Constants:
User demand parameter
Vendor delivery parameter
System delays

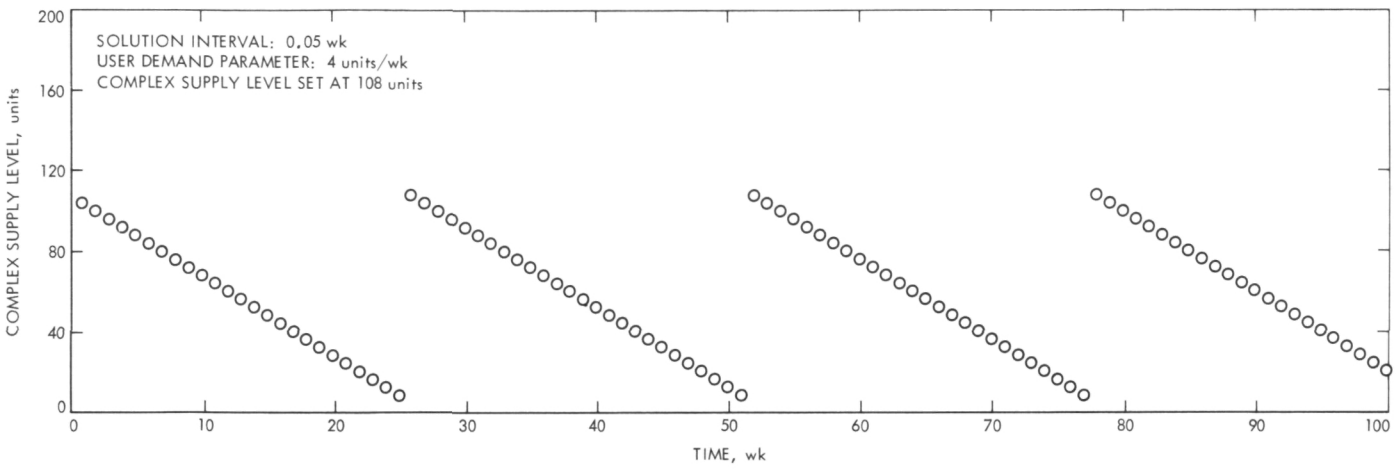

Fig. 1. Complex supply level vs time for steady-state conditions

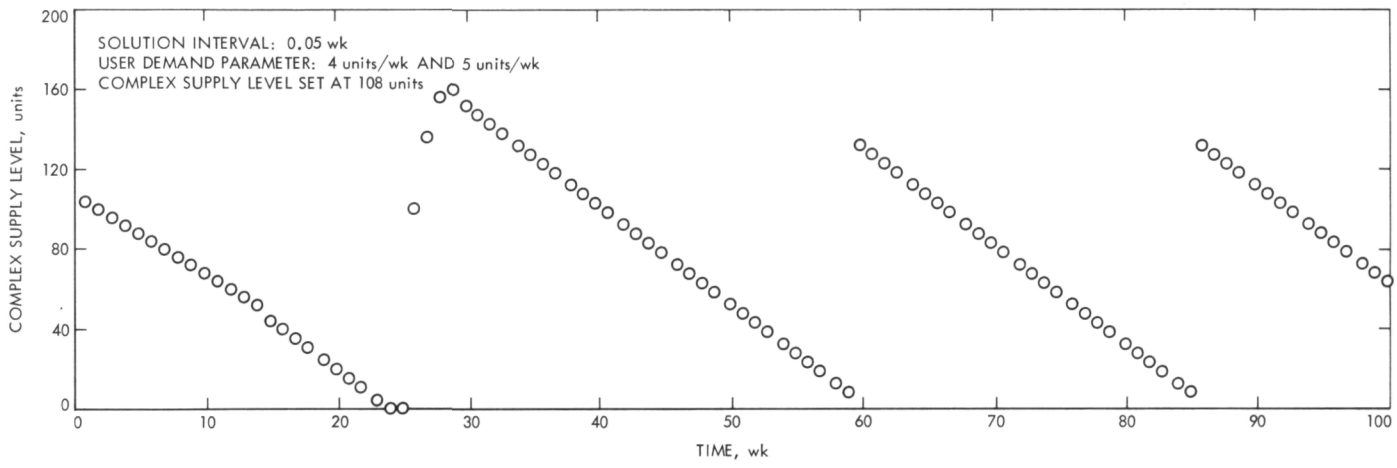

Fig. 2. Complex supply level vs time for 20% increase in UDR after week 13

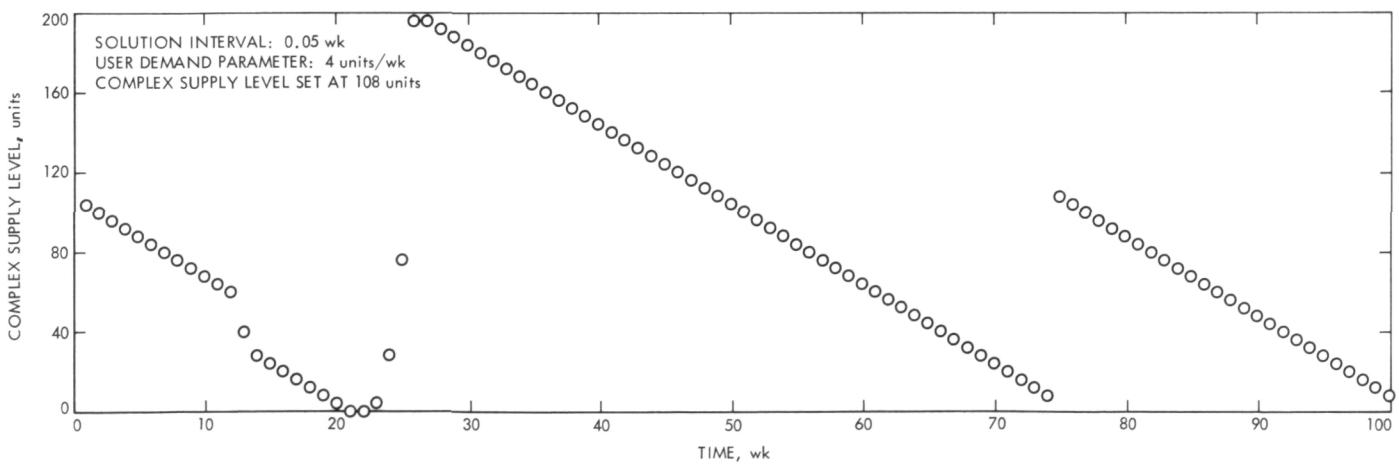

Fig. 3. Complex supply level vs time for one-time large withdrawal at week 13

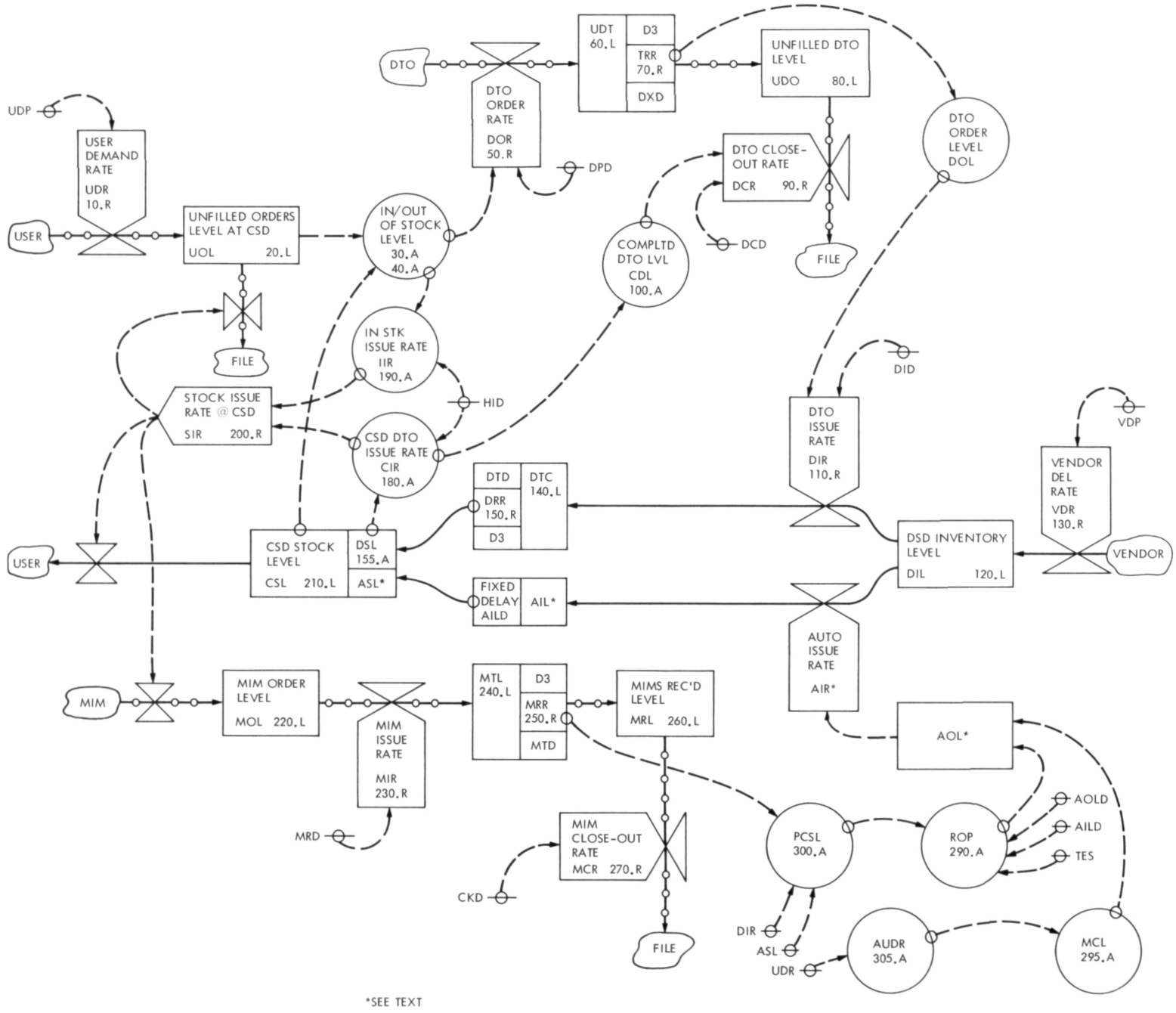

*SEE TEXT

Fig. 4. Model flow chart

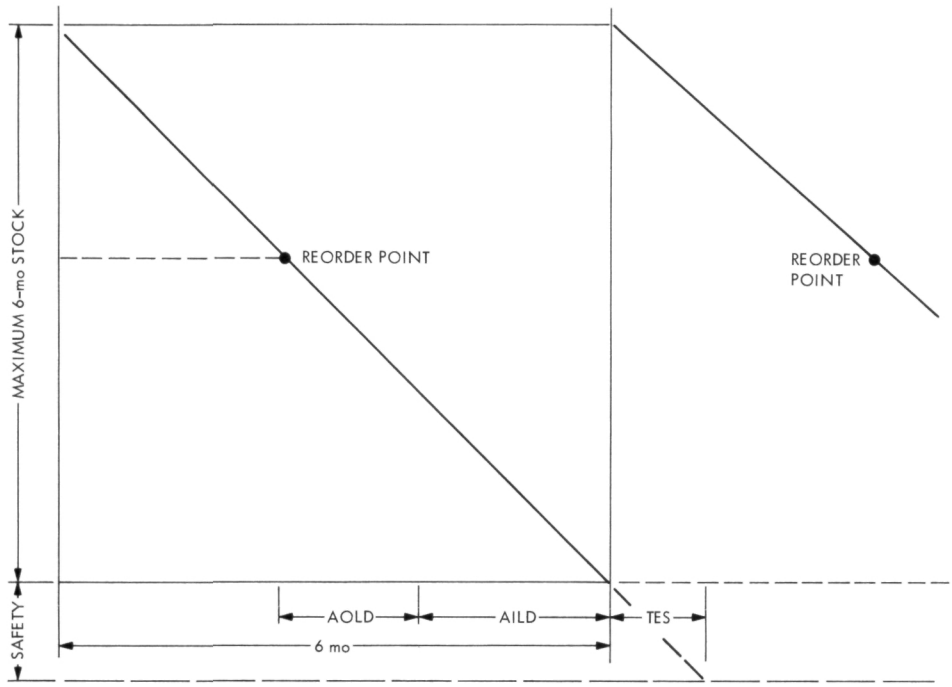

Fig. 5. Relationship of reorder point to maximum CSD stock level

Bibliography

Anderson, J. D., *Determination of the Masses of the Moon and Venus and the Astronomical Unit from Radio Tracking Data of the Mariner II Spacecraft*, Technical Report 32-816. Jet Propulsion Laboratory, Pasadena, Calif., July 1, 1967.

Anderson, J. D., et al., "The Radius of Venus as Determined by Planetary Radar and Mariner V Radio Tracking Data," *J. Atmos. Sci.*, pp. 1171–1174, Sept. 25, 1968.

Anderson, J. D., "Determination of Astrodynamic Constants and a Test of the General Relativistic Time Delay With S-Band Range and Doppler Data From Mariners 6 and 7," *Space Research*, Vol. XI, pp. 105–112, Akademie-Verlag, Berlin, 1971.

Barnum, P. W., et al., *Tracking and Data System Support for the Mariner Mars 1971 Mission: Orbit Insertion Through End of Primary Mission,* Technical Memorandum 33-523, Vol. III. Jet Propulsion Laboratory, Pasadena, Calif., May 15, 1973.

Bathker, D. A., *Predicted and Measured Power Density Description of a Large Ground Microwave System*, Technical Memorandum 33-433. Jet Propulsion Laboratory, Pasadena, Calif., Apr. 15, 1971.

Berman, A. L., *Tracking System Data Analysis Report, Ranger VII Final Report*, Technical Report 32-719. Jet Propulsion Laboratory, Pasadena, Calif., June 1, 1965.

Butman, S., "Rate Distortion Over Band-Limited Feedback Channels," *IEEE Trans. Inform. Theory*, Vol. IT-17, No. 1, pp. 110–112, Jan. 1971.

Butman, S., and Timor, U., "Interplex—An Efficient Multichannel PSK/PM Telemetry System," *IEEE Trans. Commun.*, Vol. COM-20, No. 3, pp. 415–419, June 1972.

Cain, D. L., and Hamilton, T. W., *Determination of Tracking Station Locations by Doppler and Range Measurements to an Earth Satellite*, Technical Report 32-534. Jet Propulsion Laboratory, Pasadena, Calif., Feb. 1, 1964.

Carey, C. N., and Sjogren, W. L., "Gravitational Inconsistency in the Lunar Theory: Confirmation by Radio Tracking," *Science*, Vol. 160, pp. 875–876, April–June 1968.

Chadwick, H. D., and Springett, J. C., "The Design of a Low Data Rate MSFK Communication System," *IEEE Trans. Commun. Technol.*, Vol. COM-18, No. 6, pp. 740–750, Dec. 1970.

Clark, B. G., et al., "High Resolution Observations of Compact Radio Sources at 13 cm," *Astrophys. J.*, Vol. 161, pp. 803–809, Sept. 1970.

Curkendall, D. W., and Stephenson, R. R., "Earthbased Tracking and Orbit Determination—Backbone of the Planetary Navigation System," *Astronaut. Aeronaut.*, Vol. 7, May 1970.

Curkendall, D. W., "Planetary Navigation: The New Challenges," *Astronaut. Aeronaut.*, Vol. 7, May 1970.

Bibliography (contd)

Downs, G. S., and Reichley, P. E., "Observations of Interstellar Scintillations of Pulsar Signals at 2388 MHz," *Astrophys. J.*, Vol. 163, No. 1, Pt. 2, pp. L11–L16, Jan. 1971.

Downs, G. S., et al., "Mars Radar Observation, A Preliminary Report," *Science*, Vol. 174, No. 4016, pp. 1324–1327, Dec. 24, 1971.

Efron, L., and Solloway, C. B., *Proceedings of the Conference on Scientific Applications of Radio and Radar Tracking in the Space Program, Technical Report* 32-1475. Jet Propulsion Laboratory, Pasadena, Calif., July 1970.

Flanagan, F. M., et al., *Deep Space Network Support of the Manned Space Flight Network for Apollo: 1962–1968*, Technical Memorandum 33-452, Vol. I. Jet Propulsion Laboratory, Pasadena, Calif., July 1970.

Flanagan, F. M., et al., *Deep Space Network Support of the Manned Space Flight Network for Apollo: 1969–1970*, Technical Memorandum 33-452, Vol. II. Jet Propulsion Laboratory, Pasadena, Calif., May 1, 1971.

Fjeldbo, G., and Eshleman, V. R., "Radio Occultation Measurements and Interpretations," in *The Atmospheres of Venus and Mars*, p. 225. Gordon and Breach, Science Publishers, Inc., New York, N.Y.

Georgevic, R. M., *Mathematical Model of the Solar Radiation Force and Torques Acting on the Components of a Spacecraft*, Technical Memorandum 33-494. Jet Propulsion Laboratory, Pasadena, Calif., Oct. 1, 1971.

Goldstein, R. M., "Radar Time-of-Flight Measurements to Venus," *Astron. J.*, Vol. 73, No. 9, Aug. 1968.

Goldstein, R. M., and Rumsey, H., Jr., "A Radar Snapshot of Venus," *Science*, Vol. 169, Sept. 1970.

Goldstein, R. M., "Radar Observations of Mercury," *Astron. J.*, Vol. 76, No. 10, pp. 1152–1154, Dec. 1971.

Gordon, H. J., et al., *The Mariner 6 and 7 Flight Paths and Their Determination From Tracking Data*, Technical Memorandum 33-469. Jet Propulsion Laboratory, Pasadena, Calif., Dec. 1, 1970.

Gray, R. M., and Tausworthe, R. C., "Frequency-Counted Measurements, and Phase Locking to Noise Oscillators," *IEEE Trans. Commun. Technol.*, Vol. COM-19, No. 1, pp. 21–30, Feb. 1971.

Gulkis, S., and Gary, B., "Circular Polarization and Total-Flux Measurements of Jupiter at 13.1 cm Wavelength," *Astron. J.*, Vol. 76, No. 1, pp. 12–16, Feb. 1971.

Hamilton, T. W., et al., *The Ranger IV Flight Path and Its Determination From Tracking Data,* Technical Report 32-345. Jet Propulsion Laboratory, Pasadena, Calif., Sept. 15, 1962.

Holmes, J. K., "First Slip Times Versus Static Phase Error Offset for the First and Passive Second-Order Phase-Locked Loop," *IEEE Trans. Commun. Technol.*, Vol. COM-19, No. 2, pp. 234–235, Apr. 1971.

Holmes, J. K., and Tegnelia, C. R., *Digital Command System Second-Order Subcarrier Tracking Performance*, Technical Report 32-1540. Jet Propulsion Laboratory, Pasadena, Calif., Oct. 1, 1971.

Bibliography (contd)

Holmes, J. K., "Performance of a First Order Transition Sampling Digital Phase-Locked Loop Using Random-Walk Models," *IEEE Trans. Commun.*, Vol. COM-20, No. 2, pp. 119–131, Apr. 1972.

Kliore, A., "Radio Occultation Measurements of the Atmospheres of Mars and Venus," in *The Atmospheres of Venus and Mars*, by J. C. Brandt and M. E. McElrow, p. 205. Gordon and Breach Science Publishers, Inc., New York, N.Y., 1968.

Kliore, A. J., et al., "Summary of Mariner 6 and 7 Radio Occultation Results on the Atmosphere of Mars," *Space Research*, Vol. XI, pp. 165–175, Akademie-Verlag, Berlin, 1971.

Labrum, R. G., et al., *The Surveyor V, VI, and VII Flight Paths and Their Determination from Tracking Data*, Technical Report 32-1302. Jet Propulsion Laboratory, Pasadena, Calif., Dec. 1, 1968.

Laeser, R. P., et al., *Tracking and Data System Support for the Mariner Mars 1971 Mission: Prelaunch Phase Through First Trajectory Correction Maneuver*, Technical Memorandum 33-523, Vol. I. Jet Propulsion Laboratory, Pasadena, Calif., Mar. 15, 1972.

Layland, J. W., and Lushbaugh, W. A., "A Flexible High-Speed Sequential Decoder for Deep Space Channels," *IEEE Trans. Commun. Technol.*, Vol. COM-19 No. 5, pp. 813–820, Oct. 1971.

Leavitt, R. K., *The Least-Squares Process of MEDIA for Computing DRVID Calibration Polynomials*, Technical Memorandum 33-542. Jet Propulsion Laboratory, Pasadena, Calif., May 15, 1972.

Lieske, J. H., and Null, G. W., "Icarus and the Determination of Astronomical Constants," *Astron. J.*, Vol. 74, No. 2, Mar. 1969.

Lindsey, W. C., and Simon, M. K., "The Effect of Loop Stress on the Performance of Phase-Coherent Communication Systems, *IEEE Trans. Commun. Technol.*, Vol. COM-18, No. 5, pp. 569–588, Oct. 1970.

Lindsey, W. C., and Simon, M. K., "Carrier Synchronization and Detection of Polyphase Signals," *IEEE Trans. Commun.*, Vol. COM-20, No. 3, pp. 441–454, June 1972.

Lorell, J., and Sjogren, W. L., *Lunar Orbiter Data Analysis*, Technical Report 32-1220. Jet Propulsion Laboratory, Pasadena, Calif., Nov. 15, 1967.

Lorell, J., *Lunar Orbiter Gravity Analysis*, Technical Report 32-1387. Jet Propulsion Laboratory, Pasadena, Calif., June 15, 1969.

Lorell, J., et al., "Celestial Mechanics Experiment for *Mariner*," *Icarus*, Vol. 12, Jan. 1970.

Ludwig, A. C., et al., *Gain Calibration of a Horn Antenna Using Pattern Integration*, Technical Report 32-1572. Jet Propulsion Laboratory, Pasadena, Calif., Oct. 1, 1972.

McNeal, C. E., *Ranger V Tracking Systems Data Analysis Final Report*, Technical Report 32-702. Jet Propulsion Laboratory, Pasadena, Calif., Apr. 15, 1965.

Bibliography (contd)

Melbourne, W. G., et al., *Constants and Related Information for Astrodynamical Calculations*, Technical Report 32-1306. Jet Propulsion Laboratory, Pasadena, Calif., July 15, 1968.

Melbourne, W. G., "Planetary Ephemerides," *Astronaut. Aeronaut.*, Vol. 7, May 1970.

Miller, L., et al., *The Atlas-Centaur VI Flight Path and Its Determination from Tracking Data*, Technical Report 32-911. Jet Propulsion Laboratory, Pasadena, Calif., Apr. 15, 1966.

Moyer, T. D., *Mathematical Formulation of the Double-Precision Orbit Determination Program (DPODP)*, Technical Report 32-1527. Jet Propulsion Laboratory, Pasadena, Calif., May 17, 1971.

Mulhall, B. D., et al., *Tracking System Analytic Calibration Activities for the Mariner Mars 1969 Mission*, Technical Report 32-1499. Jet Propulsion Laboratory, Pasadena, Calif., Nov. 15, 1970.

Mulholland, J. D., and Sjogren, W. L., *Lunar Orbiter Ranging Data*, Technical Report 32-1087. Jet Propulsion Laboratory, Pasadena, Calif., Jan. 6, 1967.

Mulholland, J. D., *Proceedings of the Symposium on Observation, Analysis, and Space Research Applications of the Lunar Motion*, Technical Report 32-1386. Jet Propulsion Laboratory, Pasadena, Calif., Apr. 1969.

Muller, P. M., and Sjogren, W. L., *Consistency of Lunar Orbiter Residuals With Trajectory and Local Gravity Effects*, Technical Report 32-1307. Jet Propulsion Laboratory, Pasadena, Calif., Sept. 1, 1968.

Muller, P. M., and Sjogren, W. L., *Lunar Mass Concentrations*, Technical Report 32-1339. Jet Propulsion Laboratory, Pasadena, Calif., Aug. 16, 1968.

Null, G. W., et al., *Mariner IV Flight Path and Its Determination From Tracking Data*, Technical Report 32-1108. Jet Propulsion Laboratory, Pasadena, Calif., Aug. 1, 1967.

O'Neil, W. J., et al., *The Surveyor III and Surveyor IV Flight Paths and Their Determination From Tracking Data*, Technical Report 32-1292. Jet Propulsion Laboratory, Pasadena, Calif., Aug. 15, 1968.

Otoshi, T. Y., and Stelzried, C. T., "A Precision Compact Rotary Vane Attenuator," *IEEE Trans. Micro. Theor. Technique*, Vol. MTT-19, No. 11, pp. 843–854, Nov. 1971.

Pease, G. E., et al., *The Mariner V Flight Path and Its Determination From Tracking Data*, Technical Report 32-1363. Jet Propulsion Laboratory, Pasadena, Calif., July 1, 1969.

Renzetti, N. A., *Tracking and Data Acquisition for Ranger Missions I–V*, Technical Memorandum 33-174. Jet Propulsion Laboratory, Pasadena, Calif., July 1, 1964.

Renzetti, N. A., *Tracking and Data Acquisition for Ranger Missions VI–IX*, Technical Memorandum 33-275. Jet Propulsion Laboratory, Pasadena, Calif., Sept. 15, 1966.

Bibliography (contd)

Renzetti, N. A., *Tracking and Data Acquisition Support for the Mariner Venus 1962 Mission*, Technical Memorandum 33-212. Jet Propulsion Laboratory, Pasadena, Calif., July 1, 1965.

Renzetti, N. A., *Tracking and Data Acquisition Report, Mariner Mars 1964 Mission: Near-Earth Trajectory Phase*, Technical Memorandum 33-239, Vol. I. Jet Propulsion Laboratory, Pasadena, Calif., Jan. 1, 1965.

Renzetti, N. A., *Tracking and Data Acquisition Report, Mariner Mars 1964 Mission: Cruise to Post-Encounter Phase*, Technical Memorandum 33-239, Vol. II. Jet Propulsion Laboratory, Pasadena, Calif., Oct. 1, 1967.

Renzetti, N. A., *Tracking and Data Acquisition Report, Mariner Mars 1964 Mission: Extended Mission*, Technical Memorandum 33-239, Vol. III. Jet Propulsion Laboratory, Pasadena, Calif., Dec. 1, 1968.

Renzetti, N. A., *Tracking and Data System Support for Surveyor: Missions I and II*, Technical Memorandum 33-301, Vol. I. Jet Propulsion Laboratory, Pasadena, Calif., July 15, 1969.

Renzetti, N. A., *Tracking and Data System Support for Surveyor: Missions III and IV*, Technical Memorandum 33-301, Vol. II. Jet Propulsion Laboratory, Pasadena, Calif., Sept. 1, 1969.

Renzetti, N. A., *Tracking and Data System Support for Surveyor: Mission V*, Technical Memorandum 33-301, Vol. III. Jet Propulsion Laboratory, Pasadena, Calif., Dec. 1, 1969.

Renzetti, N. A., *Tracking and Data System Support for Surveyor: Mission VI*, Technical Memorandum 33-301, Vol. IV. Jet Propulsion Laboratory, Pasadena, Calif., Dec. 1, 1969.

Renzetti, N. A., *Tracking and Data System Support for Surveyor: Mission VII*, Technical Memorandum 33-301, Vol. V. Jet Propulsion Laboratory, Pasadena, Calif., Dec. 1, 1969.

Renzetti, N. A., *Tracking and Data System Support for the Mariner Venus 67 Mission: Planning Phase Through Midcourse Maneuver*, Technical Memorandum 33-385, Vol. I. Jet Propulsion Laboratory, Pasadena, Calif., Sept. 1, 1969.

Renzetti, N. A., *Tracking and Data System Support for the Mariner Venus 67 Mission: Midcourse Maneuver Through End of Mission*, Technical Memorandum 33-385, Vol. II. Jet Propulsion Laboratory, Pasadena, Calif., Sept. 1, 1969.

Renzetti, N. A., *Tracking and Data System Support for the Pioneer Project. Pioneer VI. Prelaunch to End of Nominal Mission*, Technical Memorandum 33-426, Vol. I. Jet Propulsion Laboratory, Pasadena, Calif., Feb. 1, 1970.

Renzetti, N. A., *Tracking and Data System Support for the Pioneer Project. Pioneer VII. Prelaunch to End of Nominal Mission*, Technical Memorandum 33-426, Vol. II. Jet Propulsion Laboratory, Pasadena, Calif., Apr. 15, 1970.

Renzetti, N. A., *Tracking and Data System Support for the Pioneer Project. Pioneer VIII. Prelaunch Through May 1968*, Technical Memorandum 33-426, Vol. III. Jet Propulsion Laboratory, Pasadena, Calif., July 15, 1970.

Bibliography (contd)

Renzetti, N. A., *Tracking and Data System Support for the Pioneer Project. Pioneer IX. Prelaunch Through June 1969*, Technical Memorandum 33-426, Vol. IV. Jet Propulsion Laboratory, Pasadena, Calif., Nov. 15, 1970.

Renzetti, N. A., *Tracking and Data System Support for the Pioneer Project. Pioneer VI. Extended Mission: July 1, 1966–July 1, 1969*, Technical Memorandum 33-426, Vol. V. Jet Propulsion Laboratory, Pasadena, Calif., Feb. 1, 1971.

Renzetti, N. A., *Tracking and Data System Support for the Pioneer Project. Pioneer VII. Extended Mission: February 24, 1967–July 1, 1968*, Technical Memorandum 33-426, Vol. VI. Jet Propulsion Laboratory, Pasadena, Calif., Apr. 15, 1971.

Renzetti, N. A., *Tracking and Data System Support for the Pioneer Project. Pioneer VII. Extended Mission: July 1, 1968–July 1, 1969*, Technical Memorandum 33-426, Vol. VII. Jet Propulsion Laboratory, Pasadena, Calif., Apr. 15, 1971.

Renzetti, N. A., *Tracking and Data System Support for the Pioneer Project. Pioneer VIII. Extended Mission: June 1, 1968–July 1, 1969*, Technical Memorandum 33-426, Vol. VIII. Jet Propulsion Laboratory, Pasadena, Calif., May 1, 1971.

Renzetti, N. A., *Tracking and Data System Support for the Pioneer Project. Pioneers VI–IX. Extended Missions: July 1, 1969–July 1, 1970*, Technical Memorandum 33-426, Vol. IX. Jet Propulsion Laboratory, Pasadena, Calif., Aug. 15, 1971.

Renzetti, N. A., and Siegmeth, A. J., *Tracking and Data System Support for the Pioneer Project. Pioneers 6–9. Extended Missions: July 1, 1971–July 1 1972*, Technical Memorandum 33-426, Vol. XI. Jet Propulsion Laboratory, Pasadena, Calif., May 1, 1973.

Siegmeth, A. J., Purdue, R. E., and Ryan, R. E., *Tracking and Data System Support for the Pioneer Project. Pioneers 6–9. Extended Missions: July 1, 1970–July 1, 1971*, Technical Memorandum 33-426, Vol. X. Jet Propulsion Laboratory, Pasadena, Calif., Aug. 15, 1972.

Siegmeth, A. J., et al., *Tracking and Data System Support for the Pioneer Project: Pioneer 10—Prelaunch Planning Through Second Trajectory Correction December 4, 1969 to April 1, 1972*, Technical Memorandum 33-584, Vol. I. Jet Propulsion Laboratory, Pasadena, Calif., Apr. 1, 1973.

Simon, M. K., "Nonlinear Analysis of an Absolute Value Type of an Early-Late Gate Bit Synchronizer," *IEEE Trans. Commun. Technol.*, Vol. COM-18, No. 5, pp. 589–596, Oct. 1970.

Simon, M. K., and Lindsey, W. C., "Data-Aided Carrier Tracking Loops," *IEEE Trans. Commun. Technol.*, Vol. COM-19, No. 2, pp. 157–168, Apr. 1971.

Simon, M. K., "On the Selection of an Optimum Design Point for Phase-Coherent Receivers Employing Bandpass Limiters," *IEEE Trans. Commun.*, Vol. COM-20, No. 2, pp. 210–214, Apr. 1972.

Simon, M. K., "On the Selection of a Sampling Filter Bandwidth for a Digital Data Detector," *IEEE Trans. Commun.*, Vol. COM-20, No. 3, pp. 438–441, June 1972.

Bibliography (contd)

Sjogren, W. L., et al., *The Ranger V Flight Path and Its Determination From Tracking Data*, Technical Report 32-562. Jet Propulsion Laboratory, Pasadena, Calif., Dec. 6, 1963.

Sjogren, W. L., et al., *The Ranger VI Flight Path and Its Determination From Tracking Data*, Technical Report 32-605. Jet Propulsion Laboratory, Pasadena, Calif., Dec. 15, 1964.

Sjogren, W. L., *The Ranger III Flight Path and Its Determination From Tracking Data*, Technical Report 32-563. Jet Propulsion Laboratory, Pasadena, Calif., Sept. 15, 1965.

Sjogren, W. L., et al., *Physical Constants as Determined From Radio Tracking of the Ranger Lunar Probes*, Technical Report 32-1057. Jet Propulsion Laboratory, Pasadena, Calif., Dec. 30, 1966.

Sjogren, W. L., *Proceedings of the JPL Seminar on Uncertainties in the Lunar Ephemeris*, Technical Report 32-1247. Jet Propulsion Laboratory, Pasadena, Calif., May 1, 1968.

Sjogren, W. L., "Lunar Gravity Estimate: Independent Confirmation," *J. Geophys. Res.*, Vol. 76, No. 29, Oct. 10, 1971.

Sjogren, W. L., et al., "Lunar Gravity via Apollo 14 Doppler Radio Tracking," *Science*, Vol. 175, No. 4018, pp. 165–168, Jan. 14, 1972.

Spier, G. W., *Design and Implementation of Models for the Double Precision Trajectory Program (DPTRAJ)*, Technical Memorandum 33-451. Jet Propulsion Laboratory, Pasadena, Calif., Apr. 15, 1971.

Springett, J. C., and Simon, M. K., "An Analysis of the Phase Coherent-Incoherent Output of the Bandpass Limiter," *IEEE Trans. Commun. Technol.*, Vol. COM-19, No. 1, pp. 42–49, Feb. 1971.

Stelzried, C. T., *A Faraday Rotation Measurement of a 13-cm Signal in the Solar Corona*, Technical Report 32-1401. Jet Propulsion Laboratory, Pasadena, Calif., July 15, 1970.

Stelzried, C. T., et al., "The Quasi-Stationary Coronal Magnetic Field and Electron Density as Determined From a Faraday Rotation Experiment," *Sol. Phys.*, Vol. 14, No. 2, pp. 440–456, Oct. 1970.

Stelzried, C. T., "Operating Noise-Temperature Calibrations of Low-Noise Receiving Systems," *Microwave J.*, Vol. 14, No. 6, pp. 41–46, 48, June 1971.

Stelzried, C. T., et al., "Transformation of Received Signal Polarization Angle to the Plane of the Ecliptic," *J. Space. Rock.*, Vol. 9, No. 2, pp. 69–70, Feb. 1972.

Tausworthe, R. C., "Simplified Formula for Mean-Slip Time of Phase-Locked Loops With Steady-State Phase Error," *IEEE Trans. Commun.*, Vol. COM-20, No. 3, pp. 331–337, June 1972

Textor, G. P., Kelly, L. B., and Kelly, M., *Tracking and Data System Support for the Mariner Mars 1971 Mission: First Trajectory Correction Maneuver Through Orbit Insertion*, Technical Memorandum 33-523, Vol. II. Jet Propulsion Laboratory, Pasadena, Calif., June 15, 1972.

Bibliography (contd)

Thornton, J. H., Jr., *The Surveyor I and Surveyor II Flight Paths and Their Determination From Tracking Data*, Technical Report 32-1285. Jet Propulsion Laboratory, Pasadena, Calif., Aug. 1, 1968.

Timor, U., "Equivalence of Time-Multiplexed and Frequency-Multiplexed Signals in Digital Communications," *IEEE Trans. Commun.*, Vol. COM-20, No. 3, pp. 435–438, June 1972.

Vegos, C. J., et al., *The Ranger IX Flight Path and Its Determination From Tracking Data*, Technical Report 32-767. Jet Propulsion Laboratory, Pasadena, Calif., Nov. 1, 1968.

Winn, F. B., *Selenographic Location of Surveyor VI, Surveyor VI Mission Report: Part II. Science Results*, Technical Report 32-1262. Jet Propulsion Laboratory, Pasadena, Calif., Jan. 10, 1968.

Winn, F. B., "Post Landing Tracking Data Analysis," in *Surveyor VII Mission Report: Part II. Science Results*, Technical Report 32-1264. Jet Propulsion Laboratory, Pasadena, Calif., Mar. 15, 1968.

Winn, F. B., "Post Lunar Touchdown Tracking Data Analysis," in *Surveyor Project Final Report: Part II. Science Results*, Technical Report 32-1265. Jet Propulsion Laboratory, Pasadena, Calif., June 15, 1968.

Winn, F. B., *Surveyor Posttouchdown Analyses of Tracking Data*, NASA SP-184. National Aeronautics and Space Administration, Washington, D.C., p. 369.

Wollenhaupt, W. R., et al., *The Ranger VII Flight Path and Its Determination From Tracking Data*, Technical Report 32-694. Jet Propulsion Laboratory, Pasadena, Calif., Dec. 15, 1964.

NASA — JPL — Coml., L.A., Calif.